Università degli Studi di Ferrara

DOTTORATO DI RICERCA IN
"SCIENZE DELLA TERRA"

CICLOXXIV

COORDINATORE Prof. BECCALUVA Luigi

Lattice relaxation in solid solutions: long-range vs. short-range structure around Cr^{3+} and Co^{2+} in oxides and silicates

Settore Scientifico Disciplinare GEO/06

Dottorando
Dott. ARDIT Matteo

Tutore
Prof. CRUCIANI Giuseppe

Co-tutore
Dott. DONDI Michele

Anni 2008/2011

Contents

Abstract

This dissertation reports the results derived from the 3-year doctoral thesis project aimed at exploring some oxide and silicate structures as promising ceramic pigments with enhanced colorimetric properties with respect to the traditional colorants. Solid solutions of perovskite, alumoniobite, and melilite compounds were obtained by doping octahedral and tetrahedral coordination sites with transition metal ions (e.g. Cr^{3+}, Co^{2+}, and Zn^{2}) through a solid-state synthesis performed by means of an industrial-like process. The analytical techniques adopted to investigate the synthesized compounds allowed the determination of the "averaged" crystal structure, or the so termed *long-range* properties, and the *short-range* properties (i.e. the local structure around the substituting ions) through X-ray powder diffraction and electron absorption spectroscopy (EAS), respectively. As stated by Geiger (2001) "an understanding of the microscopic, mesoscopic and macroscopic properties and of the behaviour of solid solutions under different conditions is a challenge for all disciplines concerned with the solid state". As a matter of fact, the precise determination of a structure around impurities results fundamental to provide detailed information on their incorporation and on physical properties. For instance, in the case of the solid solutions here reported, the lattice incorporation of transition metal ions as impurities is the cause of their gradual coloration. Most of the times, such a coloration is more intense as greater is the impurity amount.

The final goal of this work, was attained by calculating the structural relaxation coefficient for each studied solid solution by combining the *mean* with the *local* bond distances achieved by XRPD and EAS, respectively.

Riassunto

In questa tesi sono riportati i risultati ottenuti durante il progetto triennale di dottorato volto ad esplorare strutture di ossidi e di silicati considerati dei promettenti pigmenti ceramici dalle proprietà colorimetriche migliorate rispetto ai coloranti tradizionali. Soluzioni solide di composti di perovskite, alumoniobite e melilite sono state ottenute dopando siti a coordinazione ottaedrica e tetraedrica con metalli di transizione (ad esempio Cr^{3+}, Co^{2+} e Zn^{2+}) attraverso una sintesi allo stato solido condotta seguendo il processo industriale per la realizzazione di pigmenti ceramici. Le tecniche di analisi adottate per studiare i composti sintetizzati hanno permesso sia la determinazione della struttura cristallina "media", o delle così dette proprietà a *lungo raggio*, mediante la diffrazione di polveri ai raggi-X (XRPD), che delle proprietà a *corto raggio* (cioè della struttura locale nell'intorno degli ioni sostituenti) attraverso la spettroscopia di assorbimento elettronico (EAS). Come affermato da Geiger (2001) "la comprensione delle proprietà microscopiche, mesoscopiche e macroscopiche e del comportamento di soluzioni solide in condizioni diverse è una sfida per tutte le discipline coinvolte nello studio dello stato solido". La precisa determinazione di una struttura nell'intorno di "impurità" risulta perciò fondamentale al fine di fornire informazioni dettagliate sulla loro incorporazione e sulle loro proprietà fisiche. Ad esempio, nel caso delle soluzioni solide riportate in questa tesi, l'incorporazione strutturale di ioni di metalli di transizione come impurità è la causa della loro graduale colorazione. Il più delle volte tale colorazione è tanto più intensa quanto maggiore è la quantità di impurità.

L'obiettivo finale di questo lavoro, è stato raggiunto mediante il calcolo del coefficiente strutturale di rilassamento di ogni soluzione solida studiata, combinando le distanze di legame medie, ottenute tramite XRPD, con quelle locali, derivate dalla spettroscopia EAS.

1.
INTRODUCTION

1.1. Solid solutions

The composition of a mineral or a synthetic compound is an internal variable, a characteristic intrinsic to each crystal (Hazen and Finger 1984). Most minerals exhibit a considerable range in chemical composition. Such variation mainly derives from ionic substitutions or solid solutions. A solid solution, therefore, can be defined as the result of the replacement of one ion or ionic group by another in a particular structure, and its importance ranges over a wide variety of cases. To give an example, studies on solid solutions allow the achievement of reliable phase diagrams for many types of materials, and family of minerals. Furthermore, the structural doping through the process of ion replacement can improve the electric, magnetic, or mechanical performances of a compound by modifying the physical and chemical properties of the pure "undoped" phase. It follows that the accommodation process and, therefore, the investigation of the structural environment around substitutional elements in solids is one of the key topics in several scientific fields such as metallurgy, chemistry, physics, material science, and the Earth science disciplines (Geiger 2001).

The formation of a solid solution can be explained by simple rules regarding atomic size, crystal structure, valence, and electronegativity factors. These rules were formulated by Victor Moritz Goldschmidt (1937), a mineralogist considered to be the founder of modern geochemistry and crystal chemistry. An important objective of Goldschmidt's work was to discover the laws of distribution of the chemical elements. Goldschmidt as well as Pauling (1927) pointed out that the internal structure of crystals could be understood in terms of the size and charge of the ions, and that an ion of one element can replace an ion of another if it is similar in size and charge. These considerations are summarized by a set of generalizations known as *Goldschmidt's rules of substitution* (Faure 1998).

(i) The ions of one element can extensively replace those of another in ionic crystals if their radii differ by less than about 15%.

(ii) Ions whose charges differ by one unit substitute readily for one another provided electrical neutrality of the crystal is maintained. If the charges of the ions differ by more than one unit, substitution is generally slight.

(iii) When two different ions can occupy a particular position in a crystal lattice, the ion with the higher *ionic potential* (the ratio of nominal valence to the radius of an ion) forms a stronger bond with the anions surrounding the site.

(iv) Substitution may be limited, even when the size and charge criteria are satisfied, when the competing ions have different *electronegativities* (the measure of the ability of an atom in a molecule to attract electrons to itself) and form bond of different ionic character.

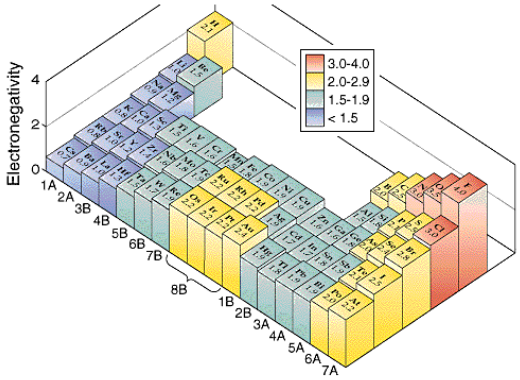

Figure 1.1. Schematic representation of the electronegativity values along the periodic table of elements.

The latter rule was formulated by Ringwood (1955) to explain the discrepancies that arose from the first three rules previously proposed by Goldschmidt. For example, according to Goldschmidt's rules, isovalent substitutions between Na^+ and Cu^+, or Ca^{2+} and Cd^{2+}, should be allowed. Hence, Cu^+ should replace Na^+ in sodium minerals such as albite ($NaAlSi_3O_8$) or halite (NaCl), but in reality this substitution does not occur. The reason of such impediment derives from the different nature of the bonds that copper and sodium usually adopt in a crystal structure in compliance with their electronegativities, i.e. copper forms more covalent bonds than sodium (Faure 1998).

Other factors, as the "external" variables temperature and pressure, can play a significant role in determining the extent of a ionic substitution (e.g. the temperature at which crystals grow). The higher the temperature, the more extensive is the thermal allowance in the crystal structure and the less strict are the spatial requirements for the ion replacement. As a result, ionic substitutions that could not have occurred in crystals grown at low temperatures may be present in those grown at higher ones. For instance, the high-temperature form of K-feldspar, $KAlSi_3O_8$ (sanidine), can accommodate more sodium in place of potassium than microcline,

its low-temperature counterpart (see Table 1.1). On the other hand, a pressure increasing can also affect the size of both the crystallographic sites and (to a lesser degree) of the ions, thus resulting that different substitutions might take place at higher pressure.

Typically, solid solutions are classified as substitutional, interstitial and omissional.

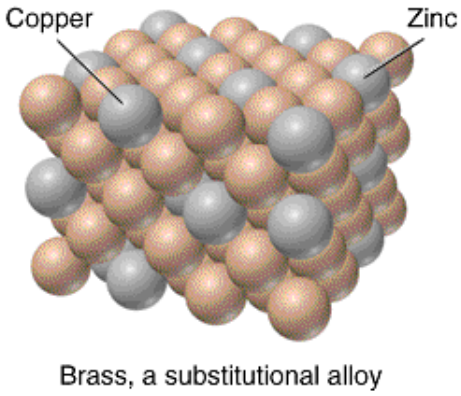

Figure 1.2. Example of a substitutional solid solution occurring in brass, a copper-zinc alloy.

► ***Substitutional solid solutions*** – This is the most widespread ionic substitution. It can imply an isovalent exchange of atoms, meaning that ions of equal charge and nearly equal size substitute for one another (i.e. the so-called *simple* solid solutions, as the example reported in Figure 1.2), or involve a *coupled* substitution if an ion of different charge is substituted. In this case, a multiple substitution is need in order to maintain the charge balance (see the Table1 for some examples).

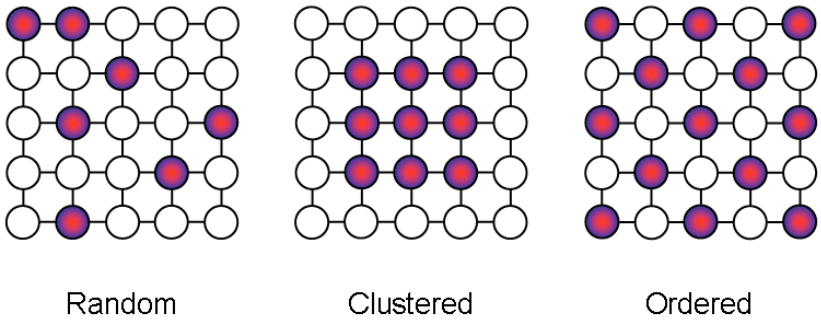

Figure 1.3. Sub-classification of a *simple* substitutional solid solution based on the arrangement of the atoms. From left to right: random, clustered and ordered distribution of the atomic species.

Furthermore, substitutional solid solutions can be *complete* or *partial*, if the ions replacement occur over the complete range of possible compositions or the compositional range of substitution is limited, respectively. Some very common examples of substitutional solid solutions occurring in minerals are reported in Table 1.1.

Table 1.1. Common examples of substitutional solid solutions in Earth science.

Substitution	Ionic Radii		Type	Examples
Simple:				
$Fe^{2+} \leftrightarrow Mg^{2+}$	$^{[VI]}Fe^{2+} = 0.78$	$^{[VI]}Mg^{2+} = 0.72$	complete	olivines $Mg_2SiO_4 – Fe_2SiO_4$
$Fe^{2+} \leftrightarrow Mn^{2+}$	$^{[VI]}Fe^{2+} = 0.78$	$^{[VI]}Mn^{2+} = 0.83$	theoretically complete	siderite – rhodochrosite $Fe(CO)_3 – Mn(CO)_3$
$Na^{+} \leftrightarrow K^{+}$	$^{[VIII]}Na^{+} = 1.18$	$^{[VIII]}K^{+} = 1.51$	complete (HT) partial (LT)	alkali feldspars $NaAlSi_3O_8 – KAlSi_3O_8$
$Fe^{3+} \leftrightarrow Al^{3+}$	$^{[VI]}Fe^{3+} = 0.65$	$^{[VI]}Al^{3+} = 0.54$	limited	alkali feldspars
$Br^{-} \leftrightarrow Cl^{-}$	$^{[VI]}Br^{-} = 1.96$	$^{[VI]}Cl^{-} = 1.81$	complete	KBr – KCl
Coupled:				
$Na^{+}Si^{4+} \leftrightarrow Ca^{2+}Al^{3+}$	$^{[VIII]}Na^{+} = 1.18$ $^{[IV]}Si^{4+} = 0.26$	$^{[VIII]}Ca^{2+} = 1.12$ $^{[IV]}Al^{3+} = 0.39$	complete	plagioclase $NaAlSi_3O_8 – CaAl_2Si_2O_8$
$Ca^{2+}Mg^{2+} \leftrightarrow Na^{+}Al^{3+}$	$^{[VIII]}Ca^{2+} = 1.12$ $^{[VI]}Mg^{2+} = 0.72$	$^{[VIII]}Na^{+} = 1.18$ $^{[VI]}Al^{3+} = 0.54$	limited	diopside – jadeite $CaMgSi_2O_6 – NaAlSi_2O_6$

Among the *coupled* solid solutions there is a particular one that involves the filling of a site that is normally vacant. For example, in order to achieve the charge neutrality in the amphibole mineral tremolite, $\square Ca_2Mg_5Si_8O_{22}(OH)_2$, when one Al^{3+} replaces for one of the Si^{4+} ions, then also Na^{+} is usually hosted into the site that is normally vacant ($\square$). The resulting mineral is the so-called sodic amphibole, $NaCa_2Mg_5AlSi_7O_{22}(OH)_2$.

► ***Interstitial solid solutions*** − Ionic substitutions of this type take place when atoms, ions, or molecules fill the interstices (voids that are not structural) found between the atoms, ions, or ionic groups of a crystal structure (Figure 1.4). The interstices may take the form of channel-like cavities in certain crystals, such as in the cyclosilicate beryl $Be_3Al_2(SiO_3)_6$. In this case, potassium, rubidium, cesium, and water, as well as helium, are some of the large ions and gases that could be found in the tubular voids of the beryl structure.

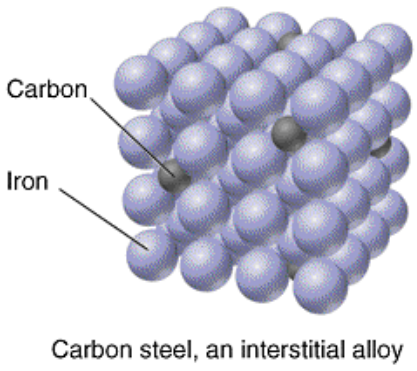

Figure 1.4. Carbon steel is an example of interstitial solid solution, where carbon fills the non-structural voids between carbon atoms.

► ***Omissional solid solutions*** − Another less common way in which minerals or compounds can vary their composition is by omission solid solution, characterized by having structural vacancies that are not occupied by atoms. Examples are exhibited by the minerals wüstite $Fe_{1-x}O$ and pyrrhotite ($Fe_{1-x}S$), both referred to have a defective structure. In pyrrhotite for instance, cation vacancies result in a range of compositions from FeS and Fe_7S_8, the overall charge balance in the structure being maintained by converting some of the Fe^{2+} ions to Fe^{3+} (Putnis 1992).

1.2. From the additivity law of Vegard to the phenomenological theory of Urusov

In an early application of X-ray diffraction to the analysis of crystal structure, Vegard (1921) observed that in many cubic ionic salts the lattice constant linearly scaled with the composition. This consideration found further confirms when Vegard and Dale (1928) proposed a same relationship for isomorphous compounds, which differ only in ionic substitution on a specific site. Since the begin of 1920's this empirical rule, now known as "Vegard's law", has become accepted by many as of general validity, and consequently employed in several scientific fields of mineralogy, metallurgy and materials science to extrapolate structural values in ideal binary solid solutions. At the same time, numerous deviations from this law are witnessed (e.g. Zen 1956; Denton and Ashcroft 1991; Urusov 1992). Vegard's law works well for many end-member compounds of isomorphous series, but intermediate compositions within a solid solution series often display more complex behaviour and deviations from this law usually become as bigger as higher is the structural complexity of the examined systems.

Studies on solid solutions increased as much as the importance of solid solutions grew, and both theoretician and experimentalist scientists started formulating a number of different theoretical approaches to describe and calculate structural relaxation, energetic and mixing properties of solid solutions, such as mixing energy, mixing volume, configurational and vibrational entropies, excess free energy and stability, i.e. solubility limits as a function of temperature and pressure (Urusov 2001). These theories are classified as:

- Semi-empirical phenomenological models;
- Semi-classical atomistic approaches;
- First principle (*ab initio*) calculations.

One of the widespread model used to calculate the structural relaxation occurring around a substituting ion along a solid solution is that based on the phenomenological theory formulated by Urusov (1992).

1.3. The concept of structural relaxation

In the last decades, several experimental studies have demonstrated that the stability of isostructural solid solutions, at the atomic scale, is affected by a structural relaxation around substituting cations (for example, Galoisy 1996; Langer 2001; Langer et al. 2004; Taran et al. 2004; Andrut et al. 2004; Gaudry et al. 2006; Juhin et al. 2007, 2008; Cruciani et al. 2009; Hålenius et al. 2010; Urusov and Taran 2011). As mentioned above, the formation of a solid solution, its compositional extent and its thermodynamic properties depend on the properties of the substituting ions, and on the intrinsic characteristics of the host structure in allowing atomic substitution at one or more structural sites (e.g. the way as the coordination polyhedra are connected to each other). Along a binary join, the information obtained by the "averaging" diffraction methods (i.e. the *long-range* properties) does not give any indication on the local distances between the central ion and its surrounding oxygen-based polyhedron (i.e. the *short-range* properties). The lack of such an information may be overcome by the use of spectroscopic methods. The spectroscopic technique used can concern the environment of a single atom as well as its first or second coordination shell or correlate lengths over hundreds of angstroms (Oberti 2001).

As a matter of fact, structural data achieved through diffraction methods along a solid solution usually obeys Vegard's rule, and both the lattice parameters and the average bond lengths might be found from the same addivity rule. For the hypothetic case of a *A*O–*B*O solid solution, with mean bond lengths $\langle A\text{–O}\rangle$ and $\langle B\text{–O}\rangle$ for the *A* and *B* end-members, respectively, the Vegard's rule applied to the bond distance of any intermediate term of composition $A_{1-x}B_x\text{O}$, will be:

$$\langle A_{1-x}B_x\text{–O}\rangle = (1\text{-}x) \cdot \langle A\text{–O}\rangle + x \cdot \langle B\text{–O}\rangle$$
$$= \langle B\text{–O}\rangle - (1\text{-}x) \cdot (\langle B\text{–O}\rangle - \langle A\text{–O}\rangle)$$
$$= \langle A\text{–O}\rangle + x \cdot (\langle B\text{–O}\rangle - \langle A\text{–O}\rangle) \quad (1.1)$$

where x is the amount of the replacing cation.

As proposed by Urusov (1992), the deviation from Vegard's rule can be quantified, on a geometrical basis, through the relaxation coefficient (ε), as:

$$\varepsilon = (\langle B\text{–O}\rangle_x - \langle A\text{–O}\rangle) \cdot (\langle B\text{–O}\rangle - \langle A\text{–O}\rangle)^{-1} \quad (1.2)$$

where the mean polyhedral distances $\langle A\text{–O}\rangle$ and $\langle B\text{–O}\rangle$ are measured by diffraction methods (e.g. single crystal X-ray diffraction, SC-XRD, or X-ray powder diffraction, XRPD), and $\langle B\text{–O}\rangle_x$ is the local mean distance for the sample $A_{1-x}B_xO$, with $x \rightarrow 0$ estimated by spectroscopy (e.g. electronic absorption spectroscopy, EAS, or extended X-ray absorption fine structure spectroscopy, EXAFS).

Looking at both the equations 1.1 and 1.2, it appears obvious that the behaviour of exchanging cations in a solid solution falls between two extreme cases (see Figure 1.5). The assumption that all of the individual bond lengths in the mixed crystal are equal to their average values implies that the relaxation is completely absent (ε = 0). This case corresponds to the so-called virtual crystal approximation (VCA), and it means that $\langle B\text{–O}\rangle_x = \langle A\text{–O}\rangle$. Under another assumption, all the atoms in the solid solution preserve their initial size. This case of full relaxation, instead, implies the hard sphere (*HS*) model (ε = 1) meaning that the

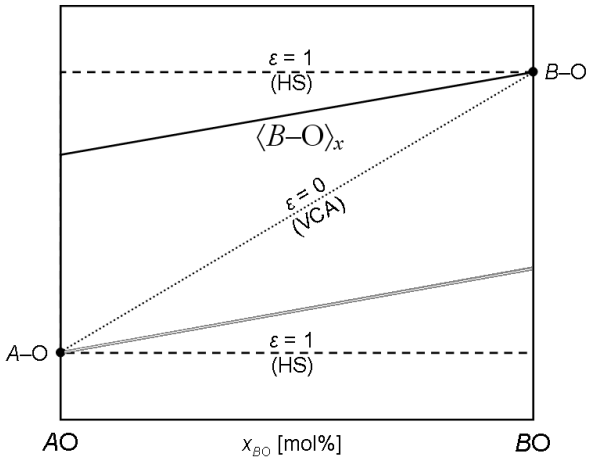

Figure 1.5. Dependence of the individual bond lengths in a binary solid solution $A_{1-x}B_xO$ according to different approaches. See text for explanation. Real changes of the individual local bond length, $\langle B\text{–O}\rangle_x$, is visualized by the black straight line between the VCA (ε = 0) and the HS (ε = 1) models.

interatomic $\langle B\text{–O}\rangle_x$ distance will not change with composition: $\langle B\text{–O}\rangle_x = \langle B\text{–O}\rangle$. Therefore, the individual bond lengths are equal to the bond lengths found in the doped end-member (Urusov 1992, 2001; Wildner et al. 2004; Andrut et al. 2004).

1.4. Structural relaxation from electronic absorption spectroscopy

As already pointed out in the preface, the studies that will be presented and discussed in the third section of this dissertation are fundamentally based on the combined approach X-ray powder diffraction/electronic absorption spectroscopy with the purpose to calculate the structural relaxation coefficient along several kinds of solid solution. For this reason, in this paragraph is described the procedure to achieve the structural relaxation coefficient used in every solid solution reported afterward.

The most popular method to achieve the local metal–oxygen distances in a solid solution investigated through electronic absorption spectroscopy is by means of the crystal field parameter $10Dq$, a measure of the length of a metal–oxygen bond related to the shift of the main optical bands of a transition metal ion (*TMI*) as a function of the amount of the *TMI* itself along a solid solution (e.g. Langer 2001; Langer et al. 2004; Taran et al. 2004; Cruciani et al. 2009; Hålenius et al. 2010). According to the crystal field theory (Dunn 1965, Burns 1993), for the previously adopted hypothetical *A*O–*B*O solid solution, the $10Dq$ value depends on the mean metal–oxygen bond distances by a relationship, that in the point charge approximation is close to the inverse fifth power of the mean distance $\langle B\text{–O}\rangle$:

$$10Dq = 5/3 \cdot Q \cdot \langle r^4\rangle \cdot \langle B\text{–O}\rangle^{-5} \qquad (1.3)$$

where both the effective charge on the ligands Q and the average radius of d orbitals $\langle r\rangle$ can be considered constant for the same metal ion in the same ligand environment (Dunn 1965; Marfunin 1979; Burns 1993; Langer 2001). The latter equation 1.3 can therefore be simplified as:

$$10Dq = \text{const} \cdot \langle B\text{–O}\rangle^{-5}. \qquad (1.4)$$

The local ions–oxygen distance (i.e. $\langle B\text{–O}\rangle_x$) achieved by optical spectroscopy can be determined by means of previous equations as:

$$\langle B\text{–O}\rangle_x = \langle B\text{–O}\rangle_{x=1} \cdot [(10DqB)_{x=1} / (10DqB)_x]^{1/5} \quad (1.5)$$

Concluding, the so obtained latter value will lead to a easy calculation of the relaxation coefficient (ε) along the AO–BO solid solution by means of the equation 1.2. To remember, the relaxation coefficient ε is usually calculated as infinite dilution (i.e. ε, with $x \rightarrow 0$) of the metal ion in the solid solution (Langer 2001).

1.5. Technological perspective

Physical formalisms are able to explain in general colour of minerals and synthetic analogues, but some chromatic features are not fully understood in detail. An in-depth insight into the dependence of optical properties on the local structural environment of a given ion is essential to go beyond the current knowledge.

The industry of inorganic pigments is very static and, especially in the ceramic sector, a new viewpoint is needed to comprehend the behaviour of current pigments and to develop novel colorants.

For these reasons in the third section of the "Results and discussion" chapter two of the three works that are going to be presented are exclusively devoted to give the technological viewpoint of this dissertation.

2.
EXPERIMENTAL METHODS

2.1. Synthesis procedures

Materials under any kind of investigation can pertain to two categories: natural and synthetic. The samples, object of the studies that are going to be presented in the following chapter, have been obtained through synthetic routes; no natural samples (i.e. minerals) were employed. The almost totality of the obtained compounds were synthesized via solid-state reaction, the conventional synthesis of ceramic powders. Just in one case a different synthesis procedure was adopted (i.e. the sol-gel combustion synthesis in order to obtain the $YAlO_3$−$YCrO_3$ perovskite solid solution). The reason of such choices stems from the following considerations:

(i) natural samples not always exist (for instance $YCrO_3$ perovskite, $AlNbO_4$ alumoniobite, and $Ba_2MgSi_2O_7$ melilite are exclusively synthetic compounds), and if available, they not always provide a complete solid solution and/or the samples have a very heterogeneous chemistry (i.e. most of the constituent ions are partially replaced by isomorphs);

(ii) a synthetic route provides samples almost or fully monophasic, and guarantees a well defined stoichiometry, meaning that each consideration made over the chemical variation along a solid solution is more reliable;

(iii) the conventional solid-state reaction procedure is fast and, in most cases, good enough in terms of purity of the realized compounds and chemistry reliability. Furthermore, the choice of such a synthesis was made on the hypothesis of a direct industrial reproducibility, meaning that every sample previously "created" in laboratory could be successfully developed at industrial scale with no substantial loss of the product quality.

► ***Solid-state reaction*** − As already stated, the solid-state reaction between oxide and/or carbonate precursors is the conventional synthesis for multicomponent ceramic powders (Segal, 1997). The process of synthesis followed to prepare the samples, object of the studies reported in the next chapter, was performed through:

- wet mixing and homogenization by ball milling in acetone of high purity raw materials;
- drying in oven at 100 °C (Figure 2.1a);
- pulverization in agate mortar;
- pelletizing by using a piston cylinder press till ~80 MPa (Figure 2.1b);
- calcination in alumina crucible using an electric kiln in static air (Figure 2.1c) at maximum temperature of typically 1200 °C for several hours and with a heating rate of 3 °C/min, and natural cooling to room temperature.

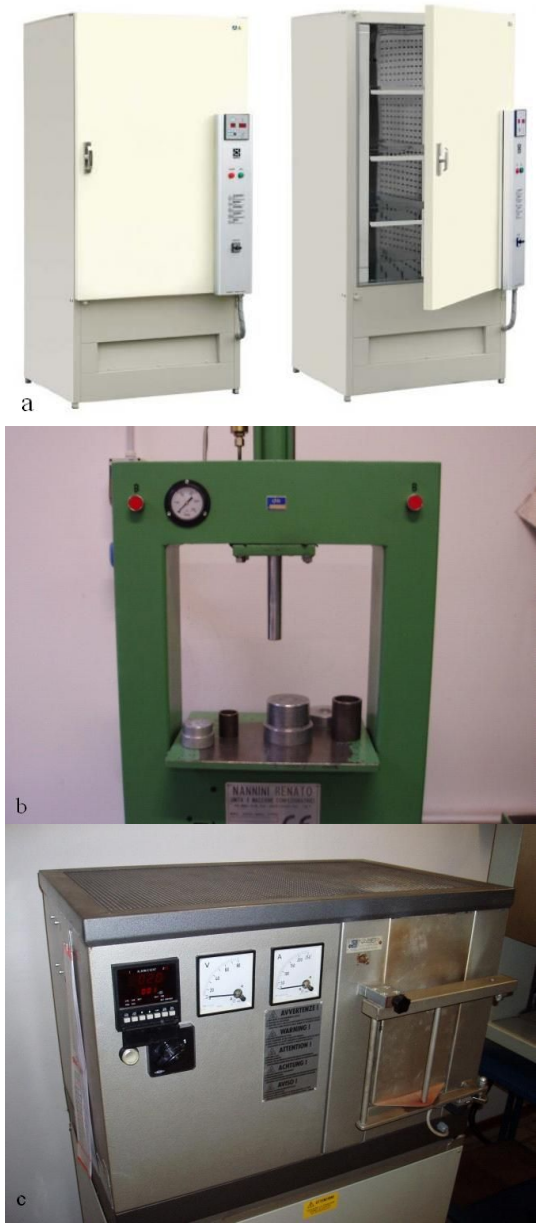

Figure 2.1. Main devices used during the synthesis process. (a) airing force oven (Nannetti); (b) piston cylinder press (Nannini); and (c) electric kiln (Naber).

Structure-type, stoichiometry, concentration of the substituting cations, number of sample(s) synthesized, temperature of calcination, and time of permanence at the maximum temperature in the electric kiln of the compounds here studied are listed in Table 2.1.

Reiterated cycles of milling and calcination were sometimes necessary to improve the reaction yield and to minimize any possible occurrence of undesired phases (i.e. secondary or accessory phases) in order to achieve a unique, nearly monophasic, compound. In fact, a minor disadvantage of this method is the common formation of undesirable phases, mainly due to firing at high temperature and poor chemical homogeneity, particularly when dopant

oxides are introduced in small amounts during the synthesis of electroceramics (Segal, 1997). On the other hand, the ready availability of oxides as precursors and the low cost for powder production on the laboratory- and industrial-scale preparations, make the solid-state reaction one of the most used synthesis procedure.

Table 2.1. Structure-type, stoichiometry, concentration of the substituting cations, number of sample(s), temperature of calcination, and hours of permanence at the maximum temperature in electric kiln of the compounds here studied and synthesized via solid-state reaction. In the last column (reference to work) is indicated the number of the corresponding work described in the next chapter.

Synthesized structure	stoichiometry	*x* (apfu)	no. of sample(s)	calcination *T* (°C)	hours of permanence	ref. work
YCr-perovskite	$YCrO_3$	–	1	1300	8	***3.SI.A***
alumoniobite (+Cr)	$(Al_{1-x}Cr_x)NbO_4$	0, 0.06, 0.125, 0.25, 0.375, 0.5	6	1200	8	***3.SI.C***
Sr-åkermanite – Ba-åkermanite	$(Sr_{2-x}Ba_x)MgSi_2O_7$	0, 1, 1.5, 1.6, 1.75, 2	6	1200	6	***3.SII.D***
Ca- – Sr- – Ba-åkermanite (+Co)	$(x)_2(Mg_{0.7}Co_{0.3})Si_2O_7$	Ca, CaSr, Sr, SrBa, $Sr_{0.5}Ba_{1.5}$, $Sr_{0.25}Ba_{1.75}$	6	1200	6	***3.SII.E***
hardystonite – Co-åkermanite	$Ca_2(Zn_{1-x}Co_x)Si_2O_7$	0, 0.25, 0.5, 0.75, 1	5	1300	24	***3.SIII.G***
hardystonite (+Co)	$Ca_2(Zn_{1-x}Co_x)Si_2O_7$	0.05, 0.1, 0.2, 0.3, 0.4	5	1200	4	***3.SIII.H***
willemite (+Co)	$Zn_{2-x}Co_xSiO_4$	0, 0.05, 0.1, 0.2, 0.3	5	1300	3	***3.SIII.I***

► ***Sol-gel combustion*** – Samples belonging to the $YAlO_3$–$YCrO_3$ join [*see the first work in the first section of the following chapter,* ***3.SI.A***] were prepared by sol-gel combustion, a technique combining the polymeric gel action with the fast combustion reaction, which is suitable to synthesize multicomponent systems in which the stoichiometry must be strictly maintained (Montanari et al. 2005). Seven samples were synthesized with an increasing chromium content, in order to cover the $YAlO_3$–$YCrO_3$ join till the chromium content of 0.75 apfu. The $YCrO_3$ end member was differently achieved by means of a solid-state reaction synthesis (see the former paragraph). $Al(NO)_3{\cdot}9H_2O$, $Y(NO)_3{\cdot}6H_2O$, $Cr(NO)_3{\cdot}9H_2O$, NH_4NO_3, anhydrous citric acid, NH_4OH were used as precursors. The two steps involved in this technique, xerogel formation and combustion, are described in details by Blosi and co-workers (2009). The combusted precursor, a black fluffy powder, was ball milled in ethanol for 24 h, sieved under 75 µm and calcined in electric kiln at 1300 °C in static air (200 °C/h heating rate, 4 h soaking time, natural cooling) in unsealed alumina crucible.

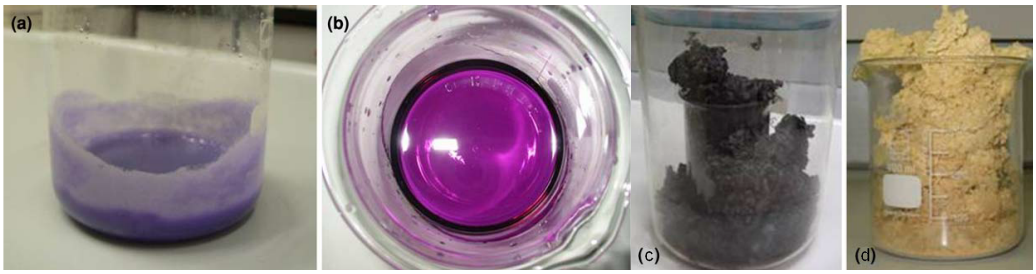

Figure 2.2. Effect on gel stability of the citrate-metal cations ratio. Stoichiometric ratio (a), stable and transparent gel achieved with an excess of citrate (b), and pictures of powders combusted at different temperatures: 300 °C (c) and 500 °C (d).

2.2. X-ray diffraction (XRD)

The use of the X-rays for crystallographic analysis is based on few basic principles:

(i) There are many types of secondary effects that occur when X-rays interact with matter (e.g. photoelectric and Compton effects), but the dominant effect is *scattering* (i.e. the fraction of the outcoming radiation that deviates from the incident direction without change in wavelength). In this process, an electron in the path of the X-ray beam vibrates with the frequency of the incoming radiation thus becomes a secondary point source of X-rays of the same energy as the incident X-rays.

(ii) In crystalline materials (i.e. single crystal or polycrystalline), some X-rays are scattered "in-phase", meaning that the amplitude scattered from a crystal is non-zero only in specific directions and at discrete sets of points spanning the reciprocal space. The phenomenon described by this "in-phase" scattered X-rays is called *diffraction*. The directions of possible diffractions depend only on the size and shape of the unit cell. Certain classes of diffraction are systematically extinct due to the occurrence of translational operations in the space-group (lattice centring, screws, and glides).

(iii) Size of periodic unit cell and atom arrangement in the crystal structure (i.e. bond distances and angles) can be established by measuring the angular relationships between the incident and diffracted X-rays, and by collecting the intensities of diffracted X-rays. Hence, the intensities of the diffracted waves depend on the kind and arrangement of atoms in the crystal structure.

In order to obtain essential information on the crystal structure of a material, the wavelength of the incident X-rays should be roughly similar to the interatomic spacing of the analyzed sample.

► ***X-ray powder diffraction* (*XRPD*)** − The expression "powder diffraction" denotes the phenomenon of diffraction of a specimen that is in the form of a polycrystalline powder. The X-ray powder diffraction method was developed by P. Debye and P. Scherrer (1916), and, marginally later, by A. Hull (1917) just four years after the discovery of the phenomenon of single-crystal diffraction made in 1912 by W. Friedrich, P. Knipping and M. von Laue and developed from 1912 by W. H. Bragg and his son W. L. Bragg (Paszkowicz 2006).

Despite its large potentialities, powder diffraction has been used for nearly half a century almost exclusively for *quantitative* or *semi-quantitative phase analyses*. After the Second World War, rapid progresses were made in terms of data speed collection and quality of results in response to the fast development of technology and instrumentation (e.g. automated diffractometers, goniometers, X-ray generator tubes, detectors...), and powder diffraction started to increase its popularity. However, the global view on the powder diffraction and its applications was revolutionized when, at the end of the 1960s, H. Rietveld devised a method to extract information on the *crystal structure* from neutron powder diffraction (NPD) data by refining a model against the whole diffraction profile (Rietveld 1967 and 1969). The Rietveld's idea arose at early days of the era of digitised data, and led to a computational method which yields information on the crystal structure of materials which cannot be prepared in the form of single crystals (Paszkowicz 2006). The method uses a least squares approach to refine a theoretical line profile until the measured profile is matched, and gives the exclusive possibility to extract structural information on the components of mono- or poly-phase materials. A decade later its appearance, the Rietveld method was re-designed and extended for X-ray studies [*a more detailed description of the Rietveld method will be given in the next paragraph*]. Nowadays, the most widespread use of powder diffraction include:

- the traditional application for phase identification of single- or multiple-phase materials, minerals, chemical compounds, ceramics or other engineered materials. A diffraction pattern is typically in the form of a graph of diffraction angle (or interplanar spacing)

against diffracted line intensity. The pattern is thus made up of a series of superimposed diffractograms, one for each unique phase in the specimen. Each of these unique patterns can act as an empirical "*fingerprint*" for the identification of the various phases, using pattern recognition techniques based on a file of standard single-phase patterns (Jenkins 2000);

- *ab initio* crystal structure determinations;
- Rietveld crystal structure refinements;
- the accurate quantitative phase analysis (QPA) by line intensity or the Rietveld method;
- quantitative determinations of microstructural properties such as lattice strain and residual stress measurements;
- recognition of amorphous materials in partially crystalline mixtures;
- domain size and disorder;
- the analysis of textured samples;
- the kinetic and structural analyses of materials and reaction processes *in situ* at non-ambient conditions (i.e. high-temperature or high-pressure) also performed in real time, etc.

Many of these investigations are routinely performed in several academic or industrial laboratories, while the most cutting-edge applications still require the use of non-conventional radiation sources.

Laboratory X-ray diffraction suffers from limitations connected with restricted wavelength selection and slow data collection. On the hand, large scale facilities provide ultrahigh beam intensity, high coherence, high collimation, and infinitesimal pulse duration. Synchrotron laboratories significantly contribute to the physics and chemistry of condensed matter, to materials science, medicine, geology, etc. Diffraction techniques available at some specialised beam lines permit the investigation of samples of extremely small sizes for single crystals (studies of submicrometer-size crystals can be found in literature) and down to about five micrometers for powder samples. The latter opportunity is used, in particular, for diffraction at the highest accessible pressures (up to 300−400 GPa - i.e. at the conditions existing at any depth in the interior of the Earth (Paszkowicz 2006, and literature therein).

► ***Whole Powder Profile Fitting* (*WPPF*) *- the Rietveld method*** − The Rietveld method is based on the approach of the Whole Powder Profile Fitting (WPPF), i.e. all categories of observables (line position, line intensity, line profile, and background) are considered together in order to build a model which is then used to generate a full powder diffraction pattern. The (initial) calculated pattern is then compared to the observed pattern and modified by least square in order to minimize the differences between observed and calculated. This refinement procedure (hence, Rietveld refinement) is conceptually very close to the single-crystal structure refinement with a fundamental difference: instead of comparing the calculated and observed intensities of individual Bragg reflections (i.e. $F^2_{hkl,\mathrm{calc}}$ vs. $F^2_{hkl,\mathrm{obs}}$), in the Rietveld method the intensity of each i^{th} point ($y_{i,\mathrm{obs}}$) at a given $2\theta_i$ step in a powder profile is modelled (i.e. $y_{i,\mathrm{calc}}$ vs. $y_{i,\mathrm{obs}}$). The other important difference in powder data refinement, with respect to single crystal, is that the model must account for line position and profile broadening, and for the background. The function, which is minimized by least squares, can be expressed as:

$$S_y = \sum_{i=1}^{N} w_i \left(y_{oi} - y_{ci}\right)^2 \qquad 2.1$$

where: y_{oi} and y_{ci} is the observed and calculated intensity of the i^{th} step, respectively; w_i is the weight according to the Poisson statistics (i.e. $w_i = 1/\sigma_{oi}^2 = 1/y_{oi}$). The summation is over the N measured datapoints in the 2θ region included in the refinement.

In the case of polycrystalline samples formed by a single phase, the calculated intensity at the i^{th} step, y_{ci}, is obtained according to the formula:

$$y_{ci} = b_{ci} + S \sum_{hkl=h1k1l1}^{HKL} K_{hkl} \Phi\left(2\theta_i - 2\theta_B\right)_{hkl} O_{hkl} AE_{hkl} \qquad 2.2$$

where:

b_{ci} = background intensity calculated at the i^{th} step;

S = scale factor = $K_e K_s$, in which:

- K_e = experimental constant,

- K_s = "sample" constant;

K_{hkl} = can be defined as a structural constant of diffraction line (*hkl*) and depends on:

- unit-cell volume,
- the structure factor of diffraction line corrected by the Debye-Waller factor and for anomalous scattering,
- multiplicity factor of diffraction line,
- Lorentz-polarization factor;

$\Phi(2\theta_i - 2\theta_B)_{hkl}$ = profile shape function which itself dependent on FWHM, peak asymmetry and shape parameter(s);

A_{hkl} = absorption factor; E_{hkl} = primary extinction factor; O_{hkl} = preferred orientation factor.

The summation to achieve the y_{ci} is calculated over all the HKL diffraction lines which may contribute to the i^{th} intensity step, according to the profile shape function.

In the case of a polycrystalline sample made of a multiphase mixture, the previous equation is modified to account for different phases; the calculated intensity at the i^{th} step, y_{ci}, is expressed as:

$$y_{ci} = b_{ci} + \sum_{\alpha=1}^{\#phases} S_\alpha \sum_{hkl=h1k1l1}^{HKL} K_{(hkl)\alpha} \Phi\left(2\theta_i - 2\theta_B\right)_{(hkl)\alpha} O_{(hkl)\alpha} A_\alpha E_{(hkl)\alpha} \qquad 2.3$$

where the definitions are very similar to those given for the previous formula, with the difference that most terms are also specific for each different phase present in the mixture, in particular the scale factor (S_α). The latter summation is extended to all the phases whose diffraction lines contribute to the intensity of the i^{th} step.

Under the assumptions that the mixture is made of crystalline phases only (i.e. $\sum_j w_j = 1$), and being all phases considered in the refinement, the weight fraction of each phase is readily obtained from the refined scale factors (S_α), i.e.

$$w_\alpha = \frac{S_\alpha \rho_\alpha}{\sum_j S_j \rho_j} \qquad 2.4$$

The Rietveld quantitative phase analysis based on the latter equation is a truly standardless analysis and allows to overcome the limitations which are encountered with the quantitative phase analysis methods based on line intensities.

2.3. X-ray powder diffraction (data collection) at ambient condition

X-ray powder diffraction data were collected at room temperature using a Bruker D8 Advanced diffractometer (Figure 2.3, on the left) equipped with a Sol-X Si(Li) solid state detector set to discriminate Cu$K\alpha_{1,2}$ radiation (Figure 2.3, on the right). Data collection parameters for each series of compounds here studied is reported in Table 2.2, including: 2θ measuring range, step width, and counting time per step.

Table 2.2. Data collection parameters i.e. (2θ measuring range, step width, and counting time per step) for each series of compounds here studied. In the last column (reference to work) is indicated the number of the corresponding work described in the next chapter.

Structure	formula	measuring range (°2θ)	step width (°2θ)	counting time per step (s)	ref. work
YAl-perovskite (+Cr)	$Y(Al_{1-x}Cr_x)O_3$	15−130	0.02	10	***3.SI.A***
alumoniobite (+Cr)	$(Al_{1-x}Cr_x)NbO_4$	05-130	0.02	10	***3.SI.C***
Sr-åkermanite − Ba-åkermanite	$(Sr_{2-x}Ba_x)MgSi_2O_7$	15-130	0.02	10	***3.SII.D***
Ca- − Sr- − Ba-åkermanite (+Co)	$(x)_2(Mg_{0.7}Co_{0.3})Si_2O_7$	15-130	0.02	10	***3.SII.E***
hardystonite − Co-åkermanite	$Ca_2(Zn_{1-x}Co_x)Si_2O_7$	05-130	0.015	10	***3.SIII.G***
hardystonite (+Co)	$Ca_2(Zn_{1-x}Co_x)Si_2O_7$	15-130	0.02	10	***3.SIII.H***
willemite (+Co)	$Zn_{2-x}Co_xSiO_4$	15-130	0.02	10	***3.SIII.I***

Figure 2.3. On the left, panoramic (top) and detailed (bottom) views of the Bruker D8 Advance diffractometer with a θ:θ Bragg-Brentano geometry settles at the department of mineralogy, petrology and geophysics of the university of Ferrara. On the right, detail of the Bruker Sol-XE energy dispersive X-ray Si-solid state detector (top) and external box of the X-ray tube (bottom).

► ***Rietveld refinement strategies for data collected at ambient condition***

− The structural refinements were accomplished by the Rietveld method (Young 1995) using the GSAS-EXPGUI software package (Larson and Von Dreele 1988; Toby 2001). The presence of impurity phases (if any) was accounted for by carrying out multiphase refinements in which only the scale factors and the cell parameters were varied for the minor phases. Starting atomic models for the studied structure were taken from literature as indicated in Table 2.3. The refinements included cell parameters, atomic coordinates,

isotropic atomic displacement parameters, a shifted Chebyshev polynomial to reproduce the background (the number of the coefficients varied from 15 to 18), zero-point, a scale factor (or phase fraction, in the case of samples with presence of impurity phases). The diffraction peak profiles were modeled by a pseudo-Voigt function. The refined profile parameters included:

- the (θ)-independent Gaussian term (GW);
- ($\cos\theta^{-1}$)- and (tanθ)-dependent Lorentzian terms (LX and LY, respectively);
- an asymmetry contribution due to axial divergence (asym).

The only exception is represented by the parameters used to fit the peak profiles of the samples belonging to the $YAlO_3$−$YCrO_3$ perovskite solid solution. Besides those previously listed, further refined parameters were:

- ($\tan^2\theta$)- and (tanθ)-dependent Gaussian terms (GU and GV, respectively);
- two terms to account for profile asymmetry due to axial divergence [*S*/*L* (*S*: sample size; *L*: distance between sample and detector) and *H*/*L* (*H*: detector height; *L*: distance between sample and detector)] instead of the unique term "asym";
- six additive terms for the anisotropic peak broadening (L_{11}, L_{22}, L_{33}, L_{12}, L_{13}, and L_{23}).

Table 2.3. Starting atomic model and their space group for the studied structure and their space group. In the last column (reference to work) is indicated the number corresponding to the work described in the next chapter.

Solid solution	starting atomic model, space group (work reference)	ref. work
$Y(Al_{1-x}Cr_x)O_3$	$YAlO_3$, *Pnma* (Cruciani et al. 2009)	***3.SI.A***
$(Al_{1-x}Cr_x)NbO_4$	$AlNbO_4$, *C*2/*m* (Greis et al. 1996) $CrNbO_4$, $P4_2/mnm$ (Petersen and Müller-Buschbaum 1992)	***3.SI.C***
$(x)_2MgSi_2O_7$	$Ca_2MgSi_2O_7$, $P\text{-}42_1m$ (Kimata and Ii 1981) $Sr_2MgSi_2O_7$, $P\text{-}42_1m$ (Kimata 1983a) $Ba_2MgSi_2O_7$, *C*2/*c* (Aitasalo et al. 1996)	***3.SII.D and 3.SII.E***
$Ca_2(Zn_{1-x}Co_x)Si_2O_7$ $Zn_{2-x}Co_xSiO_4$	$Ca_2ZnSi_2O_7$, $P\text{-}42_1m$ (Bindi et al. 2001) Zn_2SiO_4, *R*-3H (McMurdie et al. 1986)	***3.SIII.G and 3.SIII.H*** ***3.SIII.I***

2.4. X-ray powder diffraction (data collection) and Rietveld refinement strategies at non ambient condition

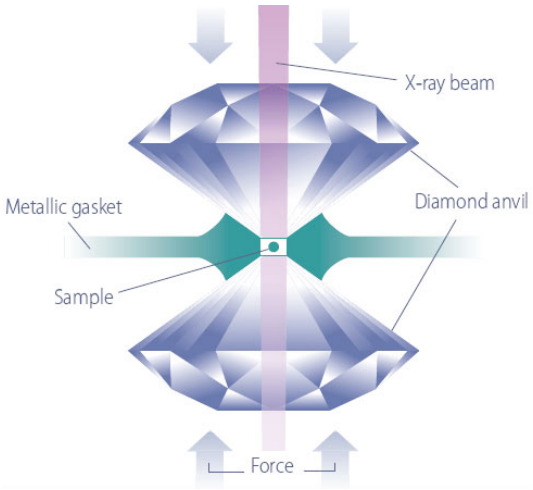

Figure 2.4. Picture of a stylized diamond anvil cell (DAC). (www.esrf.eu/AboutUs/Upgrade/science/extremeconditions).

► ***High pressure synchrotron data collection*** – High-pressure X-ray powder diffraction data of $YCrO_3$ perovskite [*see the second work in the first section of the following chapter,* ***3.SI.B***], and $Sr_2MgSi_2O_7$ melilite-type and $Ba_2MgSi_2O_7$ melilite-related compounds [*see the second work in the second section of the following chapter,* ***3.SII.E***] were collected *in situ* at the ID27 beam line (ESRF, Grenoble). Both the sample and the ruby grain for pressure calibration were loaded into a membrane-type diamond anvil cell (see Figure 2.4), with the gasket filled with helium and with a 4 : 1 methanol-ethanol mixture (for the perovskite and the melilite samples, respectively) as pressure-transmitting medium in order to achieve quasi-hydrostatic pressure conditions (Mezouar et al. 2005).

Diffraction patterns were collected using monochromatic X-rays (λ = 0.3738 Å) at room temperature, and both the sample-to-detector distance and detector tilt were calibrated using silicon. The pressure cell was allowed to relax for several minutes at each pressure. All patterns, collected on a Mar245 CCD detector (see Figure 2.5) till a maximum pressure of 60.4 and 11.2 GPa (for the perovskites and the melilite samples, respectively), were subsequently integrated over the full rings using the Fit2D program (Hammersley et al. 1996), masking all the diffraction peaks of diamond and solid He (in the case of the $YCrO_3$ perovskite), in order to obtain the conventional intensity versus 2θ step

Figure 2.5. Detail of a MAR-type CCD detector (in the image the model no. 225).

angle patterns. The intensity variation along each diffraction ring was used to estimate the statistical error of step counts. As mentioned above, the pressure was measured using the ruby fluorescence method (Forman et al. 1972), with estimated precision of ±0.05 GPa for the measured pressures.

● ***Notes on Rietveld refinement strategies (HP)*** − Refinement software, space groups and starting atomic parameters used to refine the structures at high pressure conditions were the same as those used for the refinements of the samples collected at ambient conditions (see Table 2.3). In the case of $YCrO_3$ orthorhombic perovskite, the diffraction peak profile was modeled by a pseudo-Voigt function with one Gaussian and one Lorentzian broadening coefficients. Besides the 15 shifted Chebyshev polynomial coefficients to reproduce the background, the refinement included a scale factor, the cell parameters, and the atomic coordinates.

In the case of $Sr_2MgSi_2O_7$ and $Ba_2MgSi_2O_7$ compounds, instead, the refinements included the unit cell parameters and 20 Chebyshev polynomial coefficients to calculate the background function. The diffraction peak profiles were modeled by a pseudo-Voigt function with one Gaussian and two Lorentzian broadening coefficients plus a shift contribution.

► ***High temperature data collection***

− High temperature X-ray powder diffraction data of the monoclinic $Ba_2MgSi_2O_7$ melilite-related compound [*see the third work in the second section of the following chapter,* ***3.SII.F***] were performed *in situ* at the ISTEC-CNR laboratory of diffraction (Faenza). Data collection was carried out using a Bruker D8 Advanced equipped with a 1-dimensional LynxEye (Figure 2.6), and a hot chamber (MRI BASIC, see Figure 2.7) with a Type-S thermocouple (Pt/Pt10Rh). A small amount of the sample, previously mixed with a 15% in weight of CeO_2 (National Bureau of Standards, Gaithersburg, Maryland, USA), was mounted on a Pt20Rh stage-heating element. Cerium oxide was selected as internal standard for temperature calibration because no peaks of its cubic lattice overlap with those of our sample, and because CeO_2 is an extensively studied material at high-temperature conditions, and the volumetric and lattice parameter thermal expansion are determined with extreme accuracy (e.g. Körner et al. 1989; Shuk and Greenblatt 1999; Sameshima et al. 1999; Mathews et al. 2000; Chavan et al. 2003; Chavan et al. 2004; and many others). The XRD patterns were recorded every 100 °C from ambient temperature to 1000 °C in air with a heating rate of 0.17 °C·s^{-1} in the 10−80° 2θ range, with a counting time of 0.5 s per 0.02° 2θ step.

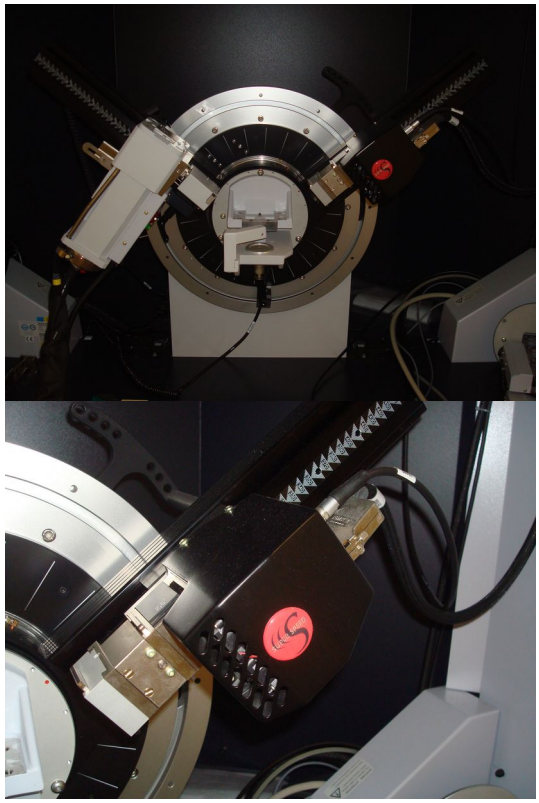

Figure 2.6. (on the top) Bruker D8 Advance diffractometer equipped with a 1-dimensional LynxEye detector; (on the bottom) Detail of the LynxEye detector based on a silicon strip technology (BRUKER Spec Sheet XRD 27).

Figure 2.7. External view of the MRI-BASIC hot chamber.

● ***Notes on Rietveld refinement strategies (HT)*** − While the line positions in the powder patterns were accurately determined with the above experimental set-up, the measured line intensities were not accurate enough to allow a series of full structure refinements due to the "infinitively-thick sample" condition not being met. Therefore, the structural model refined for monoclinic $Ba_2MgSi_2O_7$ at ambient conditions was used and kept fixed for all the temperature steps of the high-temperature measurements. Besides the unit cell parameters, all Rietveld refinements included one Gaussian and two Lorentzian broadening coefficients of the pseudo-Voigt function to model the peak profiles, a sample-shift contribution to account for its changing height with respect to the focussing circle, and 20 Chebyshev polynomial coefficients to reproduce the background.

2.5. Coordination polyhedron variations under different conditions (*X*, *T*, *P*): the distortion indices

A detailed description of a crystal structure must provide several pieces of information, the most significant are:

- space group (s.g.);
- unit-cell parameters (lattice, *l*, and volume, *V*);
- atomic coordinates (*x*, *y*, *z*);
- atomic displacement parameters (*U*, or *B*).

On the other hand, a stand-alone description of a crystal structure through the above listed parameters is often unfruitful; to consider a set of data in absolute terms is, most of the times, meaningless. Hence, in order to better describe and understand how a structure evolves with the variation of internal (i.e. chemical composition) or external (i.e. temperature and pressure) conditions, or how it could be related with structures having common features, a comparative analysis of data is done. The most widely reported continuous structural variation with composition, temperature and pressure are those associated with the unit-cell parameters (Hazen and Finger 1984). However, the most challenging comparisons are those related to the variations occurring in the coordination polyhedra (e.g. starting with bond lengths, *M*−O, and bond angle, *M*−O−*M* and O−*M*−O, variations) which, on the other hand, affect directly the optical properties (see paragraphs 2.6 and 2.7).

In order to help the comparison and, consequently, the description of such polyhedra variations, several indices of distortion and deviation from the geometrically regular starting form adopted from the literature. Those most used in this dissertation are illustrated below (other, less common or specific for a particular compound, are described in the proper sections).

► ***Quadratic elongation* (λ)** − this polyhedral distortion index is based of values of bond distances. $\langle\lambda\rangle$ is defined for tetrahedra, octahedra, cubes, dodecahedra, and icosahedra as:

$$\langle\lambda\rangle = \frac{1}{n}\sum_{i=1}^{n}\left(\frac{l_i}{l_0}\right)^2 \qquad 2.5$$

where l_0 is the centre-to-vertex distance of a regular polyhedron of the same volume, n is the coordination number of the central atom, and l_i is the distance from the central atom to the i^{th} coordinating atom. Hence, a regular polyhedron will have $\lambda = 1$, whereas a distorted one will have λ values greater than 1 (Robinson et al. 1971; Hazen and Finger 1984).

► ***Bond angle variance* (σ^2)** − calculated for the same kind of polyhedra as for the previous index, the bond angle variance is defined as:

$$\sigma^2 = \frac{1}{m-1}\sum_{i=1}^{m}(\theta_i - \theta_0)^2 \qquad 2.6$$

where m is (number of faces in the polyhedron) × 3/2 (i.e. number of bond angles), θ_0 is the ideal bond angle for a regular polyhedron (e.g. 90° for an octahedron or 109.47° for a tetrahedron), and θ_i is the i^{th} adjacent bond angle. Hence, a regular polyhedron will have $\sigma^2 = 0$, whereas a distorted one will have values greater than 0 (Robinson et al. 1971; Momma and Izumi 2008).

In order to achieved a more detailed characterization of the internal distortion of a polyhedron other distortion indices can be adopted.

► ***Bond length distortion* (*BLD*)** − distortions occurring to the bond distances can be detected through the bond length distortion parameter (Baur 1974; Griffen and Ribbe 1979), defined as:

$$BLD = \frac{100}{n}\sum_{i=1}^{n}\frac{\left|(M_i - O) - \langle M - O\rangle\right|}{\langle M - O\rangle} \qquad 2.7$$

where n is the coordination number of the central atom, (M_i−O) is the i^{th} bond distance, and ⟨M−O⟩ is the mean bond length.

► ***Edge length distortion* (*ELD*)** − similarly to the previous parameter the distortion related to the edge of a polyhedra is defined as:

$$ELD = \frac{100}{n}\sum_{i=1}^{n}\frac{\left|(O - O)_i - \langle O - O\rangle\right|}{\langle O - O\rangle} \qquad 2.8$$

where n is the edges number of the polyhedron (e.g. in the case of an octahedron n = 12), (O−O)$_i$ is the i^{th} edge length, and ⟨O−O⟩ is the mean edge length (Griffen and Ribbe 1979).

► ***Effective coordination number* (*ECoN*)** − The effective coordination number (Hoppe 1979; Hoppe et al. 1989) is defined as:

$$ECoN = \sum_i w_i \qquad 2.9$$

where the quantity

$$w_i = \exp\left[1 - \left(\frac{l_i}{l_{av}}\right)^6\right] \qquad 2.10$$

is called the "bond weight" of the i^{th} bond. The variable l_{av} represents a weighted average bond length defined as

$$l_{av} = \frac{\sum_i l_i \exp\left[1-\left(\frac{l_i}{l_{\min}}\right)^6\right]}{\sum_i \exp\left[1-\left(\frac{l_i}{l_{\min}}\right)^6\right]} \qquad 2.11$$

where l_{min} is the smallest bond length in the coordination polyhedron, and l_i is the i^{th} bond distance.

2.6. Spectroscopic methods

Spectroscopic methods provide information about local structure (e.g. site symmetry, coordination number, *local* chemical and crystallographic environment) and, differently to what happens during X-ray diffraction analyses, they do not depend on the *long-range* periodicity of a crystal structure. Although there are a lot of spectroscopic methods, they all work on the same basic principle: to measure the difference between energy levels in a material by measuring the energy of the absorbed or emitted radiation when the material is excited to a higher energy state, or as it decays back to the ground state. Both absorption and emission of energy are provoked when an incident radiation of the appropriate frequency induces changes in the energy levels in the material, and their intensity depends on the number of molecules, atoms, or electrons moving between energy

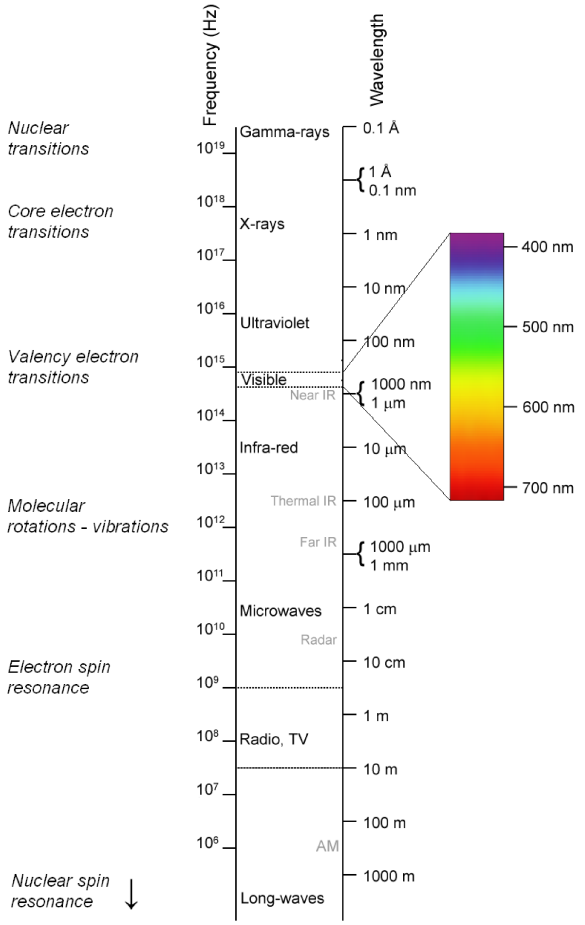

Figure 2.8. The electromagnetic spectrum and phenomena causing absorption.

levels (Putnis 1992). A wide range of phenomena (i.e. nuclear spin resonance, electron spin resonance, molecular rotations and vibrations, valence electron transitions, core electron transitions, and nuclear transitions) contribute to the energy of a material at temperatures above absolute zero, and it is usual to describe these individual phenomena as if they possessed distinct reservoirs of energy. Each phenomenon is then associated with a range of energy that varies from the *ground state* (i.e. zero energy) to the *excited states* (i.e. at higher energy). The energy range is expressed in terms of frequency or wavelength, related by the equation

$$E = h\nu = hc/\lambda \qquad 2.12$$

where h is the Planck's constant (6.6×10^{-34} Js), c is the velocity of light (3×10^{8} ms^{-1}), ν is the frequency (Hz or cycles/s) and λ is the wavelength (cms). E is the energy in joules.
The energy difference between ground and excited states cover the entire range of the electromagnetic spectrum from radiofrequency (~10^{6} Hz) to X-ray and γ-ray frequencies (up to ~10^{20} Hz) (Putnis 1992).

► ***Electronic absorption spectroscopy*** **(*EAS*)** − Optical spectroscopy is concerned with qualitative and quantitative measurements of the absorption, reflection, and emission of light on matter in the spectral range from near infra-red, through visible, to ultra-violet. In the studies reported in the next chapter the measurement of the absorption spectra was performed by diffuse reflectance (R_∞) then converted to absorbance (K/S) by the Kubelka-Munk equation (Marfunin 1979; see Figure 2.9 caption). Among the many processes which contribute to the absorption spectra of investigated materials (e.g. ligand–metal and metal–ligand charge transfer, metal–metal charge transfer, color centers, band gap transitions and others), crystal field *d–d* transitions process plays a decisive role. The physical nature of this process is related to the transitions within the *d* (or *f*) states localized at cations and split by the crystal field due to surrounding ligands. The formalism developed to describe the latter process is termed crystal field theory (CFT).

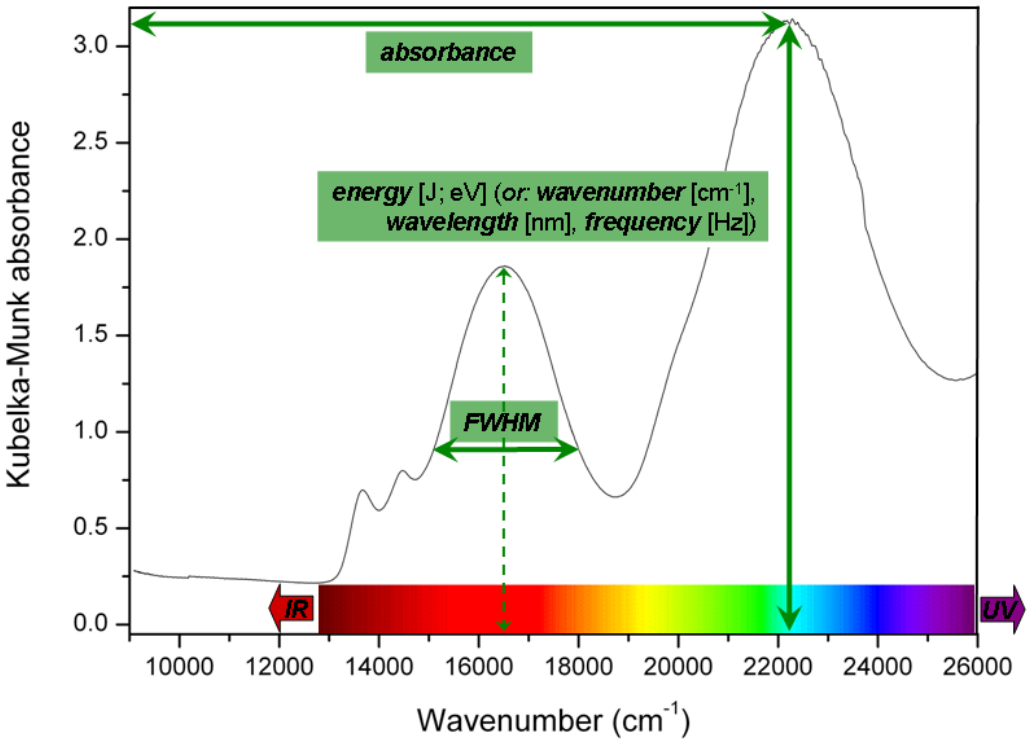

Figure 2.9. Optical spectra of octahedrally coordinated Cr^{3+} in $YCrO_3$ perovskite structure. In the x-axis the wavenumber (mathematically related to the energy, the wavelength, and the frequency), whereas in the b-axis the absorbance treated with the Kubelka-MunK function. Generally used for the analysis of diffuse reflectance spectra obtained from weakly absorbing samples, such polycrystalline samples, the Kubelka-Munk theory provides a correlation between reflectance and concentration of an absorbing species by:

$$K/S=(1-R_\infty)^2\cdot(2R_\infty)^{-1}$$

where, K = the absorption coefficient (i.e. the limiting fraction of absorption of light energy per unit thickness, as thickness becomes very small); S = the scattering coefficient (i.e. the limiting fraction of light energy scattered backwards per unit thickness as thickness tends to zero); R = reflectance.

► ***Crystal field theory* (*CFT*)** − Pioneered by Bethe (1929) and van Vleck (1932), the CFT is a model of chemical bonding applicable to transition metal and lanthanide ions, and it describes the origin and consequences of interactions between the *d* (or *f*) orbitals with the electrostatic fields originating from negatively charged anions or dipolar groups coordinating the central ion (Wildner et al. 2004, and literature therein). The most important problems solved by application of crystal field theory in geosciences include:

- concepts of colour and pleochroism;
- interpretation of electronic structure and bonding;
- partitioning of transition metal ions;

- evaluation of thermodynamic properties of minerals influenced by CFSE (e.g. electronic entropy or enthalpy of mixing);
- mantle geochemistry of transition elements (e.g. polyhedral bulk moduli from high-pressure spectra, and phase transition);
- detection of structural details (e.g. cation ordering, and dynamic or static Jahn-Teller distortions).

The description of the interaction of the *d* (or *f*) electrons of a transition ion with the crystal field generated by the surrounding ligands requires background knowledge of quantum mechanics (QM). Basic idea on QM is shortly given in the following paragraph aimed to clarify some of the rule that govern electron systems.

● ***One-electron systems*** **–** Time-independent one-electron Schrödinger equation to describe the energy of a localized *d* electron is

$$\mathbf{H}\Psi = E\Psi \qquad 2.13$$

where **H** is the Hamiltonian (i.e. the operator of the total energy of the system), and E is the total energy corresponding to the state Ψ under consideration. In the case of a *d* electronic configuration in a transition metal ion, the motion of the *d* electron referred to a spherical coordinate system (r, θ, φ) can be described by

$$\left[-\left(\hbar^2/2m\right)\nabla^2 - eV(r)\right]\Psi(r,\theta,\varphi) = E\Psi(r,\theta,\varphi) \qquad 2.14$$

where the first term in the square brackets is the Hamiltonian in Eq. 2.13 and it represents the kinetic energy of the electron, where $\hbar = h/2\pi$ is the Planck's number, m is the electron mass, and ∇^2 is the Laplacian operator. The second term represents the potential energy of the *d* electron due to the nucleus and all other electrons in the ion. In a spherical approximation and for a one-electron system (i.e. hydrogen atom) the former wavefunction can be solved as it follows (see an example in Figure 2.10):

$$\Psi(r,\theta,\varphi) = R_n(r)Y_{lm_l}(\theta,\varphi)\chi_{m_s} \qquad 2.15$$

Equation 2.15 comprises the radial function $R(r)$, the spherical harmonics $Y(\theta, \varphi)$, and the spin function χ, which is independent from the spatial coordinates of the electron. The various solutions describing the possible state of one-electron system are parameterized by the *four quantum numbers*:

- n = the *principal quantum number*, an integer corresponding to the electron orbits or shells (e.g. K: $n = 1$; L: $n = 2$; M: $n = 3$; N $n = 4$; ...);
- l = the *orbital quantum number*, corresponding to the orbital type and equal to n-1 (e.g. *s*: $l = 0$; *p*: $l = 1$; *d*: $l = 2$; *f*: $l = 3$; ...);
- m_l = the *magnetic quantum number*, that describes the orientation of the orbital with respect to a reference direction. Its value can be comprises between -l, -l+1, ..., 0, ...l-1, and l;
- m_s = the *spin quantum number*, corresponding to the parallel or antiparallel orientation of the electron spin angular moment. m_s can be equal to $+^1/_2$ or to $-^1/_2$.

- ***Crystal field splitting*** – If a free transition metal ion is placed into a hypothetical field of negative charges evenly distributed on a sphere, the five *d* orbitals will be raised in energy (i.e. destabilized) due to the interaction of the *d* electrons with the negative field, but remain degenerate. However, in the case when the negative charges are more or less localized at certain ligand atoms in a crystal, the resulting (non-spherical) crystal field (CF) potential will split the five *d* orbitals into the orbital groups or single orbitals of different energy. These energy splittings are described by the CF parameter Δ_i (or $10Dq$) where the subscript i refers to the polyhedral type (i: c = cube; t = tetrahedron; o = octahedron). The magnitude and type of such crystal field splittings within the five *d* orbitals

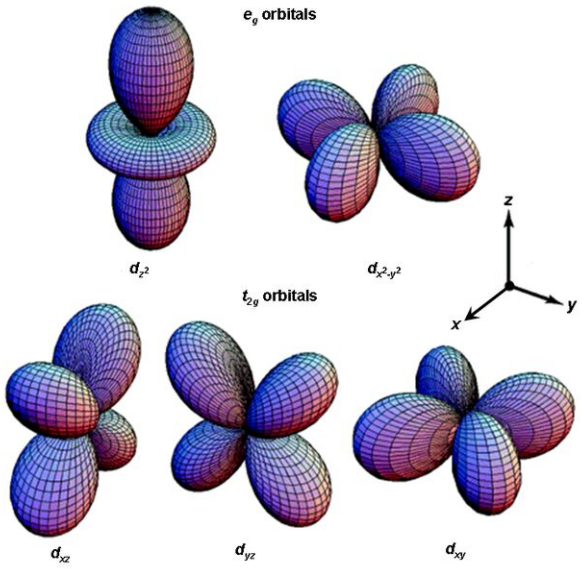

Figure 2.10. Shape and orientation of the *d* orbitals with respect to the reference Cartesian axes. These are the orbitals solution of the one-electron Schrödinger equation.

depend on the symmetry and geometry of the coordination polyhedron as well as on the actual type of the central transition ion and the ligand atoms.

For example, in octahedral symmetry the *d*-orbitals split into two sets with an energy difference Δ_o (see Figure 2.11 on the top). The d_{xy}, d_{xz} and d_{yz} orbitals have a lower energetic level than that of the spherical field described when the ion is "free", while d_{z2} and d_{x2-y2} orbitals have a higher energetic level. Indeed, the former group of orbitals is more apart from the ligands than the latter and therefore are subjected to a lower repulsion. The three lower-energy orbitals are collectively referred to as t_{2g}, and the two higher-energy orbitals as e_g. (These labels are based on the theory of molecular symmetry).

In tetrahedral symmetry (Figure 2.11 on the bottom) the crystal field of the *d*-orbitals again splits into two groups, with an energy difference Δ_t. Opposite to the octahedral case, the lower energy orbitals will be d_{z2} and d_{x2-y2}, whereas the higher energy orbitals will be d_{xy}, d_{xz} and d_{yz}. Furthermore, since the ligand electrons in tetrahedral symmetry are not oriented directly towards the *d*-orbitals, the energy splitting will be lower than in the octahedral case.

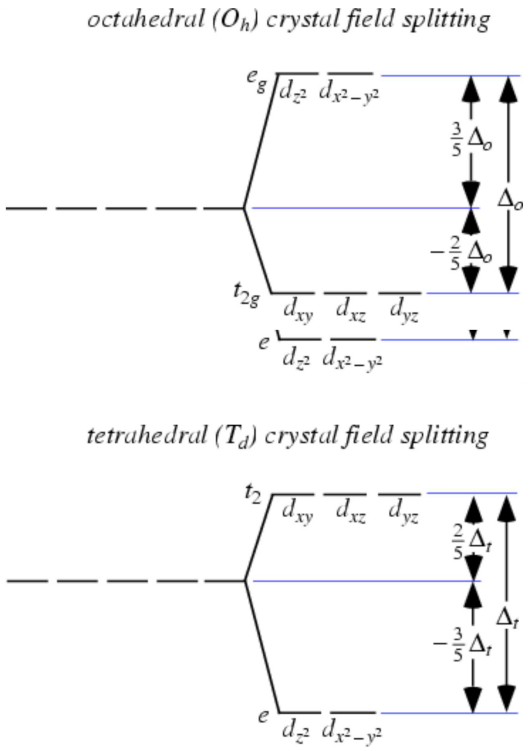

Figure 2.11. Relative 3*d* orbital energy levels of a transition metal ion in low-symmetry distorted sites. Octahedral crystal field splitting (on the top); tetrahedral crystal field splitting (on the bottom).

● ***Multi-electron systems*** – Differently to the theoretical notions reported for cases on one-electron systems, the methodical interpretation of optical absorption spectra of transition element compounds requires a many-electron d^N system, taking into account the inter-electron interactions (i.e. repulsions) between the *d* electrons within an open-shell orbital set. Therefore, for real cases, further perturbations into the many-electrons Schrödinger equation must be introduced in addition to the crystal field (CF). The full Hamiltonian for the d^N electrons in crystals, instead of that in Equation 2.14, has the form (Wildner et al. 2004):

$$\mathbf{H} = \mathbf{H}_{spher} + \mathbf{H}_{ee} + \mathbf{H}_{CF} + \mathbf{H}_{SO,SS} \qquad 2.16$$

where:

$\mathbf{H}_{spher}$ = the free-ion Hamiltonian in the spherical approximation (this Hamiltonian can be estimated from the *A* Racah parameter*);

$\mathbf{H}_{ee}$ = electron-electron repulsion effects within the nd^N configuration not included in $\mathbf{H}_{spher}$ (the contribution of this Hamiltonian is usually estimated from *B* and *C* Racah parameters* that provide information on covalence degree and polarizability of the metal–anion bond);

$\mathbf{H}_{CF}$ =crystal field interactions (this contribution derives from the crystal field parameter 10*Dq* as explained above);

$\mathbf{H}_{SO,SS}$ = spin orbit and electronic spin-spin interaction.

*[*see explanation in the next paragraph*]

● ***Tanabe-Sugano diagrams*** – Tanabe-Sugano (T/S) diagrams are used to predict absorptions in the UV and visible electromagnetic spectrum of coordination compounds. They are qualitatively useful and can be used to approximate the value of the crystal field strength 10*Dq*. Bethe's crystal field theory and Racah parameters are used in T/S diagrams to explain the absorption spectra of octahedral complex ions in a more quantitative way.

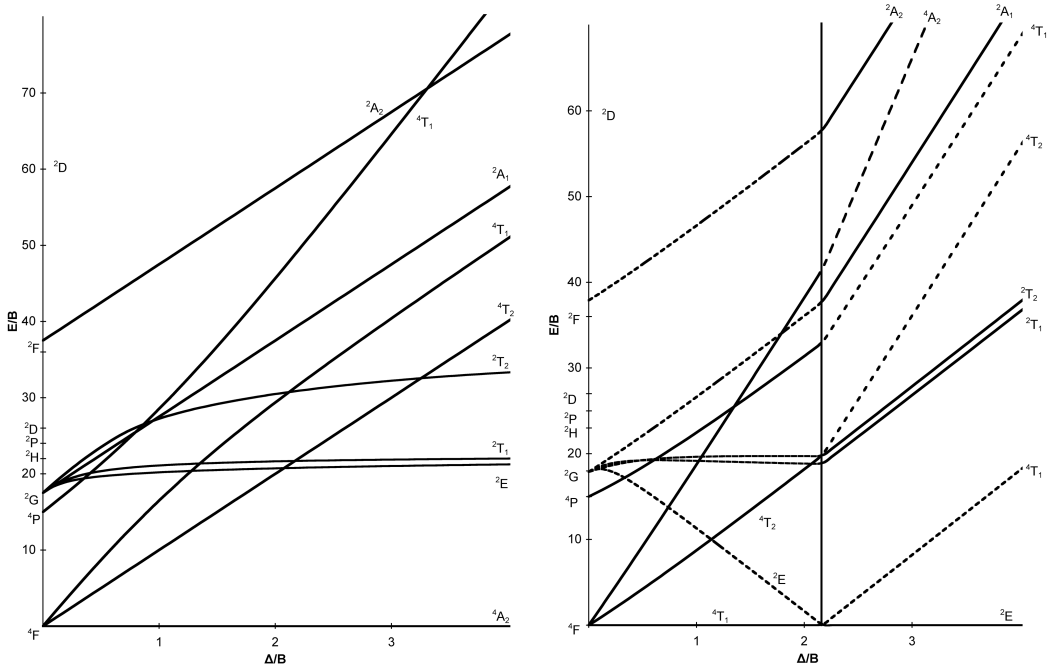

Figure 2.12. Examples of d^3 (on the left side) and d^7 (on the right side) of Tanabe-Sugano diagrams.

The *x*-axis of a T/S diagram is expressed in terms of the crystal field parameter, $10Dq$, or Δ, divided by the Racah parameter B (Figure 2.12). The *y*-axis is in terms of energy, E, also scaled by B. *Three Racah parameters exist, A, B, and C, which describe various aspects of interelectronic repulsion. A is an average total interelectron repulsion, and being constant among *d*-electron configuration, it is not necessary for calculating relative energies (i.e. it is absent from Tanabe and Sugano's studies of complex ions), while B and C correspond with individual *d*-electron repulsions (B is the most important of Racah's parameters). One line corresponds to each electronic state. The bending of certain lines is due to configuration interactions of the excited states. Although electronic transitions are only "allowed" if the spin multiplicity remains the same (i.e. electrons do not change from spin up to spin down or vice versa when moving from one energy level to another), energy levels for "spin-forbidden" electronic states are included in the diagrams. Each state is given and labelled by its symmetry (e.g. A_{1g}, T_{2g}, etc.). Term symbols (e.g. ^3P, ^1S, etc.) for a specific d^N free ion are listed, in order of increasing energy, on the *y*-axis of the diagram.

According to the Russell-Saunders coupling scheme (LS) of the orbital and spin momenta: $L = \sum_{i=1}^{N} m_l$ and $S = \sum_{i=1}^{N} m_s$ spectroscopic terms are labelled ^{2S+1}L

2.7. UV-visible-NIR spectroscopy

Electronic absorption spectroscopy (EAS) was performed by diffuse reflectance at room temperature by means a Perkin Elmer spectrophotometer with $BaSO_4$ integrating sphere (Figure 2.13), and $BaSO_4$ as white reference material. As stated before [*Paragraph 2.6, Electronic absorption spectroscopy (EAS)*] reflectance (R_∞) was converted to absorbance (K/S) by the Kubelka-Munk equation.

Figure 2.13. Perkin Elmer spectrophotometer.

The model of spectrophotometer (λ19 or λ35), range of smoothing, measured wavenumber ranges, number of collected points, and scan rates of the collected spectra for each solid-solution reported in this dissertation are listed in Table 2.4.

Table 2.4. The model of spectrophotometer (λ19 or λ35) range of smoothing, measured wavenumber ranges, number of collected points, and scan rates of the collected spectra. In the last column (reference to work) is indicated the number of the corresponding work described in the next chapter.

Structure	formula	λ-type	range of smoothing	wavenumber range $\times 10^{-3}$ (cm^{-1})	no. of points	scan rate ($nm \times min^{-1}$)	ref. work
YAl-perovskite (+Cr)	$Y(Al_{1-x}Cr_x)O_3$	35	2	09−26	1281	480	*3.SI.A*
YAl-perovskite (+Cr) - *spin forbidden*	$Y(Al_{1-x}Cr_x)O_3$	35	2	13−15	1501	120	*3.SI.A*
alumoniobite (+Cr)	$(Al_{1-x}Cr_x)NbO_4$	35	2	09-26	2077	120	*3.SI.C*
Ca- − Sr- − Ba-åkermanite (+Co)	$(x)_2(Mg_{0.7}Co_{0.3})Si_2O_7$	19	4	04-40	~5000	480	*3.SII.E*
hardystonite − Co-åkermanite	$Ca_2(Zn_{1-x}Co_x)Si_2O_7$	19	4	04-40	4000 1000	480	*3.SIII.G*
hardystonite (+Co)	$Ca_2(Zn_{1-x}Co_x)Si_2O_7$	19	4	04-40	794 +3268 +1021	480	*3.SIII.H*
willemite (+Co)	$Zn_{2-x}Co_xSiO_4$	19	4	04-30	2355 +459	480	*3.SIII.I*

► ***Quantitative spectra analysis*** − Absorbance bands were deconvoluted by Gaussian function (PFM, OriginLab) starting from peak maxima by automatic fitting to convergence, in order to obtain band energy (centroid) and band width (FWHM) which experimental errors, including background correction and reproducibility, are around 2% and 5%, respectively. In some cases, the accurate deconvolution of low intensity peaks, occurring as shoulders on the main bands, required a 0.01 nm step size with background subtraction and asymmetrical double sigmoidal function.

- ***Cr^{3+}*** − Crystal field strength $10Dq$ was calculated by fitting the energy of spin-allowed transitions in the d^3 Tanabe-Sugano diagram (Tanabe and Sugano 1954; Andrut et al. 2004) or simply taking the wavenumber of the $^4T_{2g}(^4F)$ band = $10Dq$. Interelectronic repulsion Racah parameters were calculated by

spin-allowed t → T

$$B_{35} = \frac{1}{3}\frac{\left[\left(2\cdot{}^4t_{2g}\right)-{}^4t_{1g}\right]\cdot\left({}^4t_{1g}-{}^4t_{2g}\right)}{\left(9\cdot{}^4t_{2g}\right)-\left(5\cdot{}^4t_{1g}\right)} \qquad 2.17$$

or spin-forbidden t → T

$$B_{55} = \sqrt{\frac{-10Dq\left[\left(3 \cdot^2 t_{2g}\right) - \left(5 \cdot^2 E\right)\right]}{278}} \qquad 2.18$$

$$C = \frac{1}{5}\frac{^2t_{2g} - \left(15 \cdot B_{55}\right) + \left(176 \cdot B_{55}{}^2\right)}{10Dq} \qquad 2.19$$

t → T

transitions (Lever 1984; Wildner et al. 2004). The correspondent nephelauxetic ratios β_{35} and β_{55} (considered to express the covalent degree and polarizability of the Cr–O bonding, respectively) were calculated as $\beta = B/B_0$, where B is experimental and B_0 is the value of the free ion (Lever 1984; Burns 1993; Wildner et al. 2004).

- ***Co*$^{2+}$** − Similarly to the Cr^{3+} case, crystal field strength $10Dq$ for Co^{2+} ion (d^7) was calculated by fitting the energy of spin-allowed transitions in the d^3 Tanabe-Sugano diagram that is used, according to the d^{10-x} rule, in the case of ions in fourfold coordination (Tanabe and Sugano 1954; Andrut et al. 2004). In this case, it was not possible to determine directly the $10Dq$ value from the $^4T_{2g}(^4F)$ band, as it is three-fold split and two out of three subbands fall out of the measured range. The effect of spin-orbit coupling, inducing a three-fold splitting of the spin-allowed transitions, was accounted by both averaging values of split bands and the baricenter method (Burns 1993): results so obtained differ for less than 0.5%. Interelectronic repulsion Racah B parameter was evaluated by spin-allowed transitions using equation 2.17 (Lever 1984; Wildner et al. 2004) and the correspondent nephelauxetic ratio β (considered to express the covalent degree of the Co–O bonding) was calculated as $\beta = B/B_0$, where B is experimental and B_0 is the free ion value (Lever 1984; Burns 1993).

The parameters used in the deconvolution, i.e. number of Gaussian bands, treatment of the background, goodness of fit, and preliminary data treatment of the deconvolute spectra, are listed in Table 2.5.

Table 2.5. Parameters of deconvolution: number of Gaussian bands, treatment of the background, goodness of fit (χ^2), and preliminary data treatment. In the last column (reference to work) is indicated the number of the corresponding work described in the next chapter.

Structure	formula	no. Gaussian bands	background treatment	χ^2	preliminary data treatment	ref. work
YAl-perovskite (+Cr)	$Y(Al_{1-x}Cr_x)O_3$	5	LB	$2\text{-}3\cdot10^{-4}$	No	*3.SI.A*
YAl-perovskite (+Cr) - *spin forbidden*	$Y(Al_{1-x}Cr_x)O_3$	2	manual	$0.5\text{-}1.5\cdot10^{-6}$	No	*3.SI.A*
alumoniobite (+Cr)	$(Al_{1-x}Cr_x)NbO_4$	8	manual	$1\text{-}3\cdot10^{-4}$	rutile contribution subtracted	*3.SI.C*
Ca- − Sr- − Ba-åkermanite (+Co)	$(x)_2(Mg_{0.7}Co_{0.3})Si_2O_7$	13	linear	−	No	*3.SII.E*
hardystonite − Co-åkermanite	$Ca_2(Zn_{1-x}Co_x)Si_2O_7$	13	linear	−	No	*3.SIII.G*
hardystonite (+Co)	$Ca_2(Zn_{1-x}Co_x)Si_2O_7$	2 + 3 + 4 = 9	linear	$0.1\text{-}1\cdot10^{-3}$	No	*3.SIII.H*
willemite (+Co)	$Zn_{2-x}Co_xSiO_4$	2 + 4 + 5 = 11	linear	$0.2\text{-}1\cdot10^{-3}$	No	*3.SIII.I*

2.8. Technological tests to ceramic pigments

Technological behaviour was assessed by adding pigment into different ceramic glazes (S1, S2 and S5) and glassy coatings (F1, F2 and F5) for porous wall and floor tiles, whose chemical and physical properties are reported in Table 2.6. The pigment under investigation was contrasted with high-quality industrial colorants, having care to compare the same amount of cobalt or chromium in the coating (e.g. 0.35% CoO). For instance, by this way, the hardystonite pigment H30 was added into coatings at 5 wt.%, while spinel and olivine additions were 1.2% and 0.5%, respectively. Coating application was carried out by wet mixing, sprinkling the slip on a porous ceramic tile, that was dried in oven and fast fired in an electric roller kiln (maximum temperature = maturing temperature T_1 of Table 2.6, 45−50 min cold-to-cold). Colour was measured by diffuse reflectance spectroscopy (HunterLab Miniscan MSXP4000, 400−700 nm, D_{65} standard illuminant, 10° observer, white glazed tile reference x = 31.5, y = 33.3) and expressed as CIE-Lab coordinates.

Table 2.6. Chemical and physical properties of glassy coatings (F1, F2 and F5) and glazes (S1, S2, S3 and S5) used in technological tests.

Component Property	Unit	F1	F2	F5	S1	S2	S3	S5
SiO_2	% wt.	63.9	57.1	59.0	53.5	51.1	49.7	48.0
ZrO_2		<0.1	<0.1	<0.5	<0.1	<0.1	8.1	2.0
B_2O_3		11.7	8.9	2.0	<0.1	1.2	2.4	2.0
Al_2O_3		9.5	9.0	9.0	25.2	22.6	19.7	16.0
MgO		<0.1	1.1	2.0	3.4	1.4	0.2	1.0
CaO		0.5	7.9	12.0	8.9	13.5	12.6	11.0
ZnO		1.0	5.0	11.0	<0.1	5.1	<0.1	5.0
BaO		<0.1	1.4	<0.5	<0.1	1.4	3.2	7.0
PbO		5.5	2.7	<0.5	<0.1	0.9	<0.1	<0.5
Li_2O		<0.1	<0.1	<0.5	<0.1	<0.1	<0.1	<0.5
Na_2O		6.1	2.0	1.0	5.6	2.6	2.2	2.0
K_2O		1.1	4.1	4.0	3.0	0.6	1.3	3.0
Zircon $ZrSiO_4$	% wt.	–	–	–	–	–	~5	1100
Quartz a-SiO2		–	–	–	<1	~10	~5	1175
Anorthite $CaAl_2Si_2O_8$		–	–	–	~5	~15	~5	1230
Wollastonite $CaSiO_3$		–	–	–	~5	~10	–	4.57
Gehlenite $Ca_2Al_2SiO_7$		–	–	–	<1	~10	–	371
Maturing temperature (softening) T_1	°C	930	940	1010	1210	1150	1100	1.558
Temperature of half sphere T_2		1265	1180	1170	1275	1200	1195	6.44
Temperature of melting T_3		1290	1230	1220	1305	1235	1230	2.948
Viscosity at T_1	kPa s	4.90	4.93	4.28	4.65	4.97	5.24	4.57
Surface tension at T_1	mN m^{-1}	293	326	363	378	394	383	48.0
Refractive index	1	1.503	1.539	1.546	1.526	1.547	1.561	2.0
Coeff. thermal expansion $a_{20\text{-}400°C}$	MK^{-1}	4.96	5.59	6.21	6.83	5.54	4.97	2.0
Theoretical density	g cm^{-3}	2.504	2.642	2.719	2.680	2.775	2.824	16.0

3.
RESULTS and DISCUSSION

Premise

This chapter is organized in three sections. Each section provides a series of "*key*" studies developed under a common goal: to assess the relaxation coefficient ε around an impurity (i.e. the doping transition metal ion, such as Cr^{3+} and Co^{2+}) hosted in different coordination site (i.e. octahedra and tetrahedra) along solid solutions of oxide and silicate structures, for instance, perovskite, alumoniobite, and melilite structures. The methodology of investigation for the compounds belonging to the examined series comprises both X-ray powder diffraction (XRPD) and electronic absorption spectroscopy (EAS) approaches.

Furthermore, in order to have a deeper and different perspective on the structural properties of the oxide and silicates investigated, other "*satellite*" works will be also included. These latter works will provide, for example, the high-pressure (HP) and the high-temperature (HT) behaviour of some of the end-members (i.e. the HP behaviour of the $YCrO_3$, $Sr_2MgSi_2O_7$ and $Ba_2MgSi_2O_7$ end-members, and the HT behaviour of the $Ba_2MgSi_2O_7$ compound), or will illustrate the technological performance of a solid solution (e.g. the effect of the cobalt incorporation in the hardystonite and willemite structures), trying to provide, in that way, a comprehensive viewpoint of the investigated solid solutions.

The almost totality of the studied cases were previously published or they are in submission to peer-reviewed international scientific journal (e.g. *American Mineralogist*, *Journal of Physical Chemistry* B, *Journal of the American Ceramic Society*, *Journal of the European Ceramic Society*, *Periodico di Mineralogia*, *Physical Review* B, *Physics and Chemistry of Minerals*). The title of each paragraph strictly reflects that of the corresponding study as published or as communicated to the journal during the submission process. Part of these studies could result rearranged in the text order and form, or implemented with further data for a more exhaustive description. On the other hand, the scientific meaning of the content

will be maintain and no data variation will be applied. In order to avoid redundant part (e.g. in some cases the experimental methodologies could be very similar) some paragraphs could be condensed in a general one, then specifying any difference case after case. Further information, when necessary, will be given.

Table 3.1. Reference to works presented in this chapter.

Section	Work label	Title
I - *Structural relaxation around six-fold coordinated Cr^{3+}: the cases of the $YAlO_3$–$YCrO_3$ perovskite and of the $AlNbO_4$–$CrNbO_4$ solid solutions*.	**A** (*k*)	– Structural relaxation around Cr^{3+} in $YAlO_3$–$YCrO_3$ perovskites from electronic absorption spectra.
	B (*s*)	– Elastic properties of $YCrO_3$ up to 60 GPa.
	C (*k*)	– Structural stability, cation ordering, and local relaxation along the join $AlNbO_4$–$Al_{0.5}Cr_{0.5}NbO_4$.
II - *Structural relaxation around four-fold coordinated Co^{2+}: the case of the $Sr_2MgSi_2O_7$–$Ba_2MgSi_2O_7$ melilite solid solution*.	**D** (*s*)	– Melilite-type and melilite-related compounds: structural variations along the join $Sr_{2-x}Ba_xMgSi_2O_7$, ($0 \le x \le 2$) and high-pressure behaviour of the two end-members.
	E (*k*)	– Local structural investigation along the Ca–Sr–Ba-åkermanite solid solution doped with a fixed amount of tetrahedrally coordinated Co^{2+}.
	F (*s*)	– The inverse high temperature/high pressure relationship in the monoclinic $Ba_2MgSi_2O_7$ melilite-related structure.
III - *Structural relaxation around four-fold coordinated Co^{2+}: the cases of the $ZnAl_2O_4$–$CoAl_2O_4$ spinel and $Ca_2ZnSi_2O_7$–$Ca_2CoSi_2O_7$ melilite solid solutions*.	**G** (*k*)	– Structural relaxation in tetrahedrally-coordinated Co^{2+} along the hardystonite–Co-åkermanite melilite solid solution.
	H (*s-t*)	– Co-doped hardystonite, $Ca_2(Zn,Co)Si_2O_7$, a new blue ceramic pigment.
	I (*s-t*)	– Co-doped willemite ceramic pigments: technological behaviour, crystal structure and optical properties.

Note: the letters "*k*" and "*s*" after each work label stand for "*key*" and "*satellite*" study, respectively. "*t*" stands for technological.

3. Section I.

Structural relaxation around six-fold coordinated Cr^{3+}: the cases of the $YAlO_3$–$YCrO_3$ perovskite and of the $AlNbO_4$–$CrNbO_4$ solid solutions.

► ***Perovskite*** − First discovered in the Ural mountains by Gustav Rose in 1839 and named after Russian mineralogist Lev Aleksevich von Perovski (1792–1856), perovskite is nowadays described as a ternary compounds with general formula $^{[XII]}A^{[VI]}BO_3$. The perovskite archetype, is a compact structure with a cubic symmetry (s.g. *Pm*-3*m*) composed by an un-tilted framework of corner-sharing octahedra, which contain the B cations, and extra-framework dodecahedral sites in which are placed the A cations (see Figure 3.I.1).

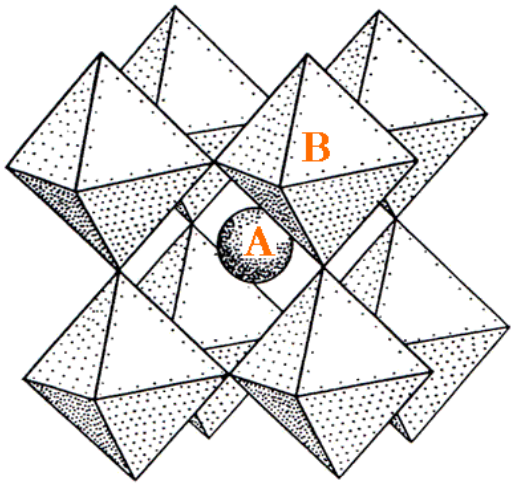

Figure 3.I.1. Schematic illustration of the perovskite archetype (s.g. *Pm*-3*m*).

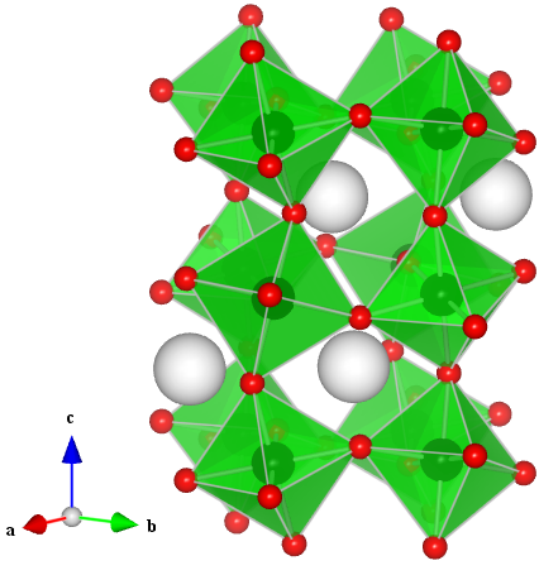

Figure 3.I.2. Polyhedral representation of an orthorhombic perovskite (s.g. *Pbnm*) as viewed parallel to the *ab* plane.

Depending on the chemical nature of the A and B cations (i.e. size, valence, electronic configuration, etc.), and on the pressure and temperature conditions, the ideal cubic symmetry is often lowered, and the resulting structure is described by tilted octahedra and more distorted polyhedra, in which the coordination numbers of A cation is usually reduced (Mitchell, 2002). In many cases the result of such tilting and distortion system is a perovskite with an orthorhombic symmetry, space group *Pbnm* (see Figure 3.I.2).

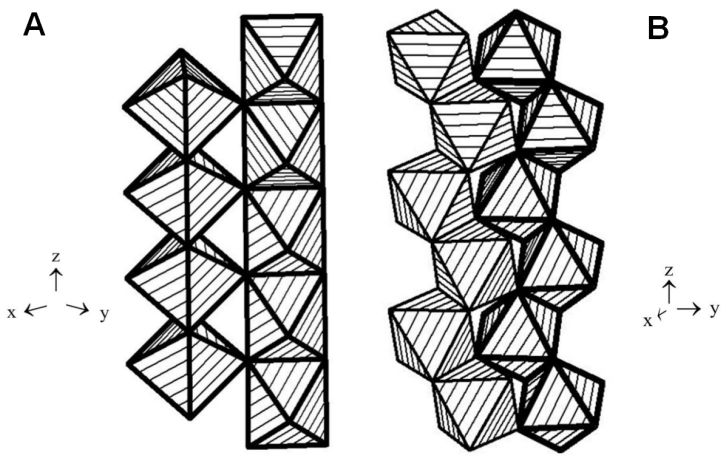

Figure 3.I.3. Polyhedral representation of the $CrNbO_4$, s.g. $P4_2/mnm$ (A) and of the $FeNbO_4$, s.g. $P2/c$ (B) structures. (Images reproduced "as in" from Tabero 2007).

► ***Alumoniobite*** – Ternary oxides with general formula $M^{3+}Nb^{5+}O_4$ (where M = Al, Cr, Fe, and Ga) are octahedral structures characterized by a large variety of polymorphs based upon sequences of closest-packed oxygen atoms.

$CrNbO_4$ has been reported as crystallizing with a rutile-type structure (s.g. $P4_2/mnm$) with a disordered distribution of Cr and Nb over the edge-sharing octahedral chains parallel to the c axis and corner connected in the (001) plane (Christensen et al. 1976; Petersen and Müller-Buschbaum 1992; see the polyhedral arrangement depicted in Figure 3.I.3A). This model has been recently questioned by Smirnov and Zvereva (2003) who suggested that a cation ordering, with non-equivalent octahedral chains connected to each other by corner-sharing as in the $AlWO_4$-type structure (s.g. $C2/m$), occurs in $CrNbO_4$. Such an octahedral arrangement would ensure the maximal distance between the same and equally charged cations, limiting the probability of charged cluster formation in the crystal.

An even more complex situation is delineated for the $FeNbO_4$ compound which crystallizes with the monoclinic wolframite-type structure (s.g. $P2/c$) up to 1385 K, then evolves through other three structural modifications with increasing temperature. Indeed, between 1385 and 1653 K, the wolframite-type structure, based on zig-zag chains of edge-sharing octahedra (see Figure 3.I.3B), is modified into an orthorhombic α-PbO_2-type phase, in which the separate chains of the former polymorph become identical. At higher temperature, the structure undergoes a further change to a rutile-type polymorph, taking the polyhedral arrangement of the $CrNbO_4$ compound, and finally to the monoclinic $AlNbO_4$-type structure (Tabero 2007, and literature therein).

At variance with the two polymorphs described above, isostructural $AlNbO_4$ and $GaNbO_4$ crystallize in the monoclinic *C*2/*m* space group. Their crystal structure, originated from the ReO_3-type structure by means of crystallographic shear operations, is made by sub-units of four distorted edge-sharing MO_6 octahedra (see Figure 3.I.4). These sub-units are connected to each other by sharing edges along the *a* and *b* directions and corners parallel to the *c* axis, forming a three-dimensional network (Pedersen 1962; Morosin 1965). Early described with a fully ordered distribution of Al and Nb over two non-equivalent octahedra, *M*1 and *M*2 respectively (Pedersen 1962), the structure of $AlNbO_4$ was later refined revealing a partially disordered occupation of the metal sites (Efremov et al. 1981; Greis et al. 1996) with about 20% of inversion degree between the two octahedra (i.e. $Al_{0.8}Nb_{0.2}O_6$ and $Al_{0.2}Nb_{0.8}O_6$ for *M*1 and *M*2 sites, respectively).

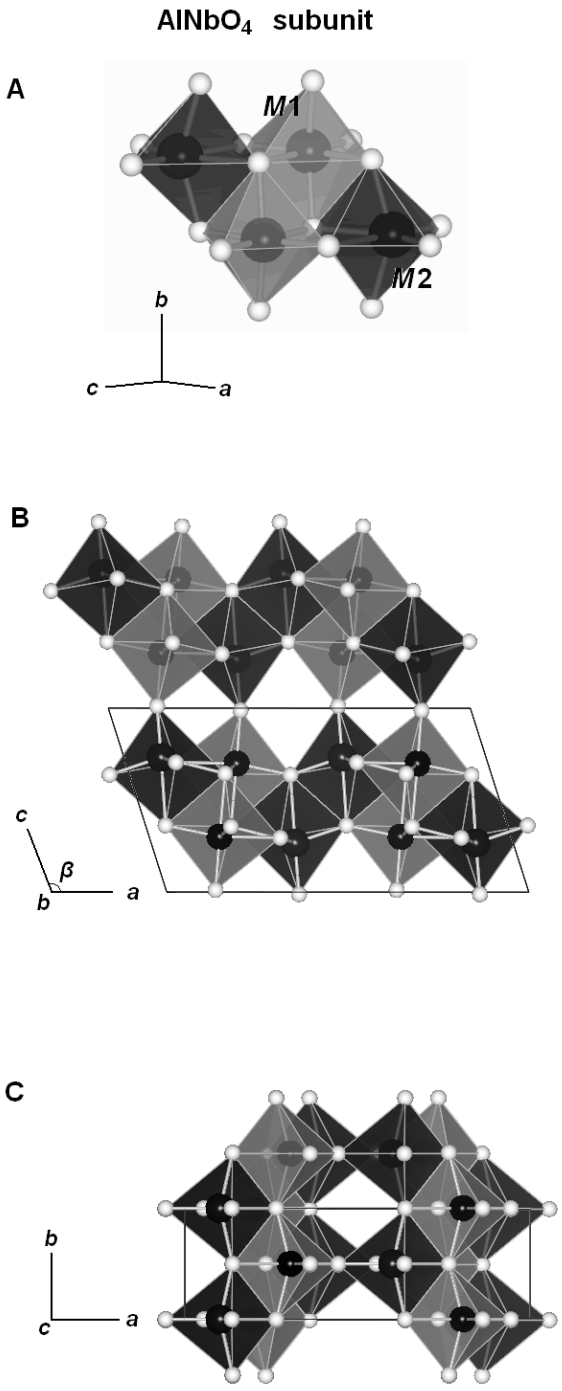

Figure 3.I.4. Schematic illustration of the $AlNbO_4$ subunit (A), and polyhedral representation of the $AlNbO_4$ structure (s.g. *C*2/*m*) as viewed parallel to the *ac* plane (B) or along the *c*-axis (C).

3. Section I. A. ♦ Structural relaxation around Cr^{3+} in $YAlO_3$–$YCrO_3$ perovskites from electronic absorption spectra

Note: This is a "*key*" study written in the 2009 by Cruciani, G., Ardit, M., Dondi, M., Matteucci, F., Blosi, M., Dalconi, M.C., and Albonetti, S., reported as published (with few variations, if any, as described in the premise of this section) in the "*Journal of Physical Chemistry A*, 113, 13772–13778".

Abstract

The structural relaxation around Cr^{3+} in $YAl_{1-x}Cr_xO_3$ perovskites was investigated and compared with analogous Cr–Al joins (corundum, spinel, garnet). Eight compositions ($x_{Cr^{3+}}$ from 0 to 1) were prepared by sol-gel combustion and were analyzed by a combined X-ray diffraction (XRD) and electronic absorption spectroscopy (EAS) approach. The unit cell parameters and the XRD averaged octahedral (Cr,Al)–O and $^{[VIII]}$Y–O bond distances scale linearly with the chromium fraction. The optical parameters show an expected decrease of crystal field strength (10*Dq*) and an increase of covalency (B_{35}) and polarizability (B_{55}) towards $YCrO_3$, but a nonlinear trend outlines some excess 10*Dq* below $x_{Cr^{3+}}$ ~0.4. The local Cr–O bond lengths, as calculated from EAS, indicate a compression from 1.98 Å ($x_{Cr^{3+}}$ = 1.0) down to 1.95 Å ($x_{Cr^{3+}}$ = 0.035) so that the relaxation coefficient of perovskite (ε = 0.54) is the lowest in comparison with garnet (ε = 0.74), spinel (ε = 0.68) and corundum (ε = 0.58) in contrast with its structural features. The enhanced covalent character of the Cr^{3+}–O–Cr^{3+} bond in the one-dimensional arrangement of corner-sharing octahedra can be invoked as a factor limiting the perovskite polyhedral network flexibility. increased probability of Cr–O–Cr clusters for $x_{Cr^{3+}}$ greater than ~0.4 is associated to diverging trends of nonequivalent interoctahedral angles. bond The relatively low relaxation degree of $Y(Al,Cr)O_3$ can be also understood by considering an additional contribution to 10*Dq* because of the electrostatic potential of the rest of lattice ions upon the localized electrons of the CrO_6 octahedron. Such an "excess" 10*Dq* increases when the point symmetry of the Cr site is low, as in perovskite, and would be affected by the change of yttrium effective coordination number observed by XRD for $x_{Cr^{3+}}$ greater than ~0.4. This would justify the systematic underestimation of local Cr–O bond distances, as inferred from EAS, compared to what is derived from X-ray absorption (XAS) studies implying a stronger degree of relaxation around Cr^{3+} of all the structures considered and supporting the hypothesis that 10*Dq* from EAS contains more

information than previously retained particularly an additional contribution from the next nearest neighbouring ions.

► ***Introduction*** − Perovskites belonging to the $YCrO_3$–$YAlO_3$ system have orthorhombic symmetry with aluminium and chromium accommodated in a slightly distorted octahedral site and Y hosted in a 8-fold coordinated site (Mitchell 2002; Cruciani et al. 2005). The peculiarity of these perovskites is their application in several fields, for example, optic-electrical in solid oxide fuel cells (Tachiwaki et al. 2001), high-temperature electrode and thermoelectric materials (Armstrong et al. 1998), or as ceramic pigment (Baldi and Dolen 1999; Marinova et al. 2003; Matteucci et al. 2006). Analogously to what happens along the Al_2O_3–Cr_2O_3 join (Poole and Itzel 1963; Gaudry et al. 2006), the colour ranges from bright green ($YCrO_3$) to red ($YAl_{0.97}Cr_{0.03}O_3$) passing through almost uncoloured compositions ($YAl_{0.87}Cr_{0.13}O_3$). Such chromatic changes depend on the shift of the main optical bands of Cr^{3+} ions, occurring as a consequence of varying both crystal field strength ($10Dq$) and covalence degree of Cr–O bond (Burns 1993; Gaudry et al. 2006).

The goal of this paper is to assess the relaxation coefficient ε around Cr^{3+} in the $Y(Cr,Al)O_3$ perovskite series through a combined X-ray diffraction (XRD) and electronic absorption spectroscopy (EAS) study [*for a detailed description on the concept of structural relaxation and on its relationship to the crystal field theory readers are requested to refer to paragraphs* ***1.3*** *and* ***1.4*** *of the dissertation introduction*]. The discussion will be addressed to crystal structural constraints on relaxation by comparing analogous investigations on other Cr–Al joins, such as eskolaite–ruby (Neuhaus and Richartz 1958; Schmitz-DuMont and Reinen 1959; Poole and Itzel 1963; Reinen 1969), grossular–uvarovite (Andrut and Wildner 2001; Langer et al. 2004), and spinel–magnesiochromite (Reinen 1969), taking into account recent criticism to this approach on the basis of X-ray absorption (XAS) studies and *ab initio* electronic structure calculations. This insight into the interdependence of colour on crystal structure is a key point to understand in depth the colour mechanism and design new and more efficient pigments exploiting the different chromatic spectra from the chromium end member (green) to the Cr-doped aluminium end member (red).

► ***Experimental*** – [*for the experimental details (including: synthesis procedure, X-ray powder diffraction data collection, Rietveld refinements, and optical spectroscopy) readers are requested to refer to the chapter **2** of the present dissertation*].

► ***Results and discussion***

● *Crystal structure* – The amount of perovskite varies from 100% (the end members Cr1000 and Cr0 as well as the sample Cr750) to a minimum of 93.7% in the sample Cr75 (Table A1).

Table A1. Batch and Phase Composition, X-ray Diffraction Details, Unit Cell Parameters, Metal−Oxygen Distances, Site Distortion, and Effective Volume and Coordination Number of Polyhedra in Perovskite Structures Analyzed[a]

sample label	Cr1000	Cr750	Cr500	Cr250	Cr135	Cr75	Cr35	Cr0
				Batch Composition (Molar Ratios) and Color of Powders				
Cr/(Cr+Al)	1.000	0.750	0.500	0.250	0.135	0.075	0.035	0.000
color	deep green	green	green	light green	gray	pink	pink	white
				Quantitative Phase Analysis				
perovskite (% wt)	100.0(0)	100.0(0)	97.6(1)	98.3(1)	97.0(1)	93.7(1)	97.0(1)	100.0(1)
				other phases (% wt):				
Y_2O_3			2.4(1)					
$Y_4Al_2O_9$				1.7(1)		4.6(1)	1.4(1)	
$Y_3Al_5O_{12}$					3.0 (1)	1.7(1)	1.6(1)	
				Agreement Factors and Refinement Details				
R_{wp}	0.159	0.172	0.132	0.127	0.141	0.137	0.143	0.150
R_p	0.106	0.130	0.089	0.083	0.099	0.100	0.105	0.105
no. of data	6000	5749	4749	4749	4749	5749	5749	6000
R_F^2	0.066	0.074	0.040	0.041	0.049	0.064	0.069	0.071
no. of reflections	402	398	283	281	279	384	383	380
no. of variables	27	28	32	32	30	42	42	27
				Unit Cell Parameters				
a (Å)	5.5242(1)	5.4815(1)	5.4316(1)	5.3833(1)	5.3581(1)	5.3458(1)	5.3356(1)	5.3298(1)
b (Å)	7.5356(1)	7.4973(1)	7.4534(1)	7.4140(1)	7.3929(1)	7.3844(1)	7.3763(1)	7.3724(1)
c (Å)	5.2434(1)	5.2306(1)	5.2137(1)	5.1983(1)	5.1895(1)	5.1858(1)	5.1820(1)	5.1806(1)
unit cell volume (Å^3)	218.27	214.96	211.07	207.48	205.56	204.71	203.95	203.57
				Chromium Fraction				
$x(Cr^{3+})$	1.00	0.73(1)	0.48(1)	0.24(1)	0.13(1)	0.06(1)	0.02(1)	0.00
probability of Cr−O−Cr bonds (%)	100	56	25	6	2	0.6	0.1	0
				Metal−Oxygen Mean Distances (Å)				
$^{[VIII]}$A−O	2.417	2.414	2.410	2.406	2.404	2.403	2.402	2.402
$^{[XII]}$A−O	2.738	2.718	2.696	2.676	2.666	2.661	2.656	2.655
$^{[VI]}$B−O	1.984	1.967	1.946	1.929	1.920	1.917	1.912	1.911
				Distortion Indices of Site A (Δ_8) and Site B (Δ_6) and Tolerance Factor				
Δ_8	4.448	3.933	3.408	3.107	3.046	3.086	2.928	2.925
Δ_6	0.044	0.056	0.066	0.046	0.064	0.062	0.039	0.048
$^{(VIII)}t_0$	0.861	0.868	0.876	0.882	0.885	0.886	0.888	0.889
				Polyhedral Volume, V (Å^3), and Effective Coordination Number, ECoN, of Site A				
V_A	23.52	23.30	23.04	22.78	22.64	22.57	22.53	22.52
V_B	10.40	10.14	9.82	9.57	9.44	9.39	9.32	9.3
$ECoN_A$	6.59(4)	6.67(5)	6.84(2)	6.91(2)	6.94(3)	6.91(4)	6.95(4)	7.00(5)

[a] Figures in parentheses are standard deviations in the last decimal figure. R_F^2 is only referred to perovskite reflections. The distortion indices are defined by

$$10^3 \cdot \frac{\sum_{i:1}^{n} ((M-O)_i - <M-O>)^2}{n \cdot (<M-O>)^2}$$

The observed tolerance factor is $^{(VIII)}t_0 = {}^{[VIII]}A-O/[2^{1/2}({}^{[VI]}B-O)]$. The effective coordination number is defined as $ECoN = \Sigma_i w_i$ (i), where $w_i = \exp[1 - (l_i/l_{av})^6]$ (ii) is called the "bond weight" of the ith bond. In eq ii, l_{av} represents a weighted average bond length defined as $l_{av} = (\Sigma_i l_i \exp[1 - (l_i/l_{min})^6]) (\Sigma_i \exp[1 - (l_i/l_{min})^6])^{-1}$ (iii), where l_{min} is the smallest bond length in the coordination polyhedron.

This implies that samples with intermediate composition (i.e., from Cr500 to Cr35) are not strictly monophasic but contain minor phases, such as yttrium oxide (Y_2O_3) and two kinds of yttrium–aluminum oxides: YAG ($Y_3Al_5O_{12}$) and YAM ($Y_4Al_2O_9$). The occurrence of secondary phases (2.4% on average) has no significant effects on the incorporation of Cr^{3+} in the dominant perovskite phase because both Y_2O_3 and YAM have no octahedral sites in which Cr^{3+} could be accommodated, while YAG is well-known to host essentially a small amount of Cr^{4+} in fourfold coordination (Henderson et al. 2000; Grinberg et al. 2003). This is confirmed by the refined chromium fractions reported in Table A1 (x_{Cr3+}) which are very close to the designed values in batch compositions.

The unit cell parameters (*a*-, *b*-, and *c*-cell edges and cell volume) scale linearly with the refined chromium fraction (x_{Cr3+}) along the $YAlO_3$–$YCrO_3$ join (Figure A1) in apparent agreement with the Vegard's law. Analogously, both the average octahedral ⟨Cr,Al–O⟩ and the ⟨$^{[VIII]}$Y–O⟩ bond distances, the latter being averaged on the shortest eight Y–O distances, show linear and positive trends with x_{Cr3+} (Figure A2a).

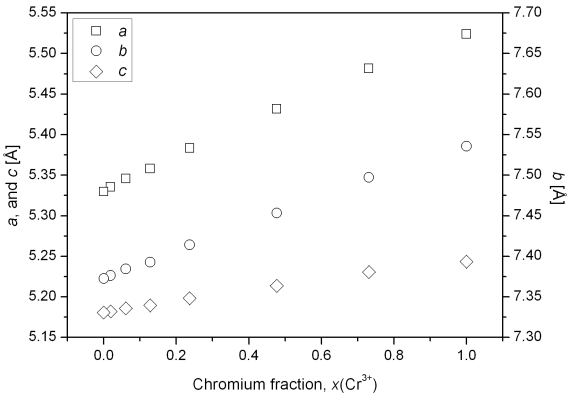

Figure A1. Variation of the unit cell parameters as a function of the refined chromium fraction (x_{Cr3+}).

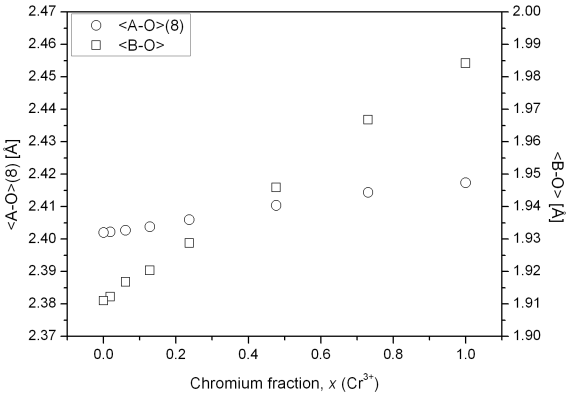

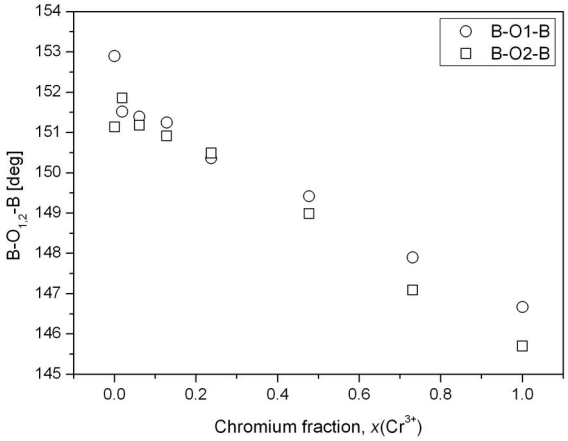

Figure A2. Variation of (a) mean metal–oxygen distances and (b) B–$O_{1,2}$–B bond angles as a function of the refined chromium fraction, x_{Cr3+}.

Such a parallel behavior of ⟨A–O⟩ and ⟨B–O⟩ is opposite to what is observed in the series of (Y,REE)AlO_3 perovskites, where an increase of the ⟨$^{[VIII]}$A–O⟩ distance, because of incorporation of larger REE ions in the A site, is associated to a decrease of the ⟨B–O⟩ distance resulting in a partial conservation of the unit cell volume (Cruciani et al. 2005). A similar mechanism is not effective along the $YAlO_3$–$YCrO_3$ join likely because of the narrower range of bond distance variation. This is evident from the relatively small changes of the polyhedral volumes of both the A and B sites (Table A1) whose ratio shows that the volume increasing of (Cr,Al)O_6 octahedra, connected with the increased ionic radius from Al^{3+} to Cr^{3+} (i.e. from 0.535 to 0.615 Å, Shannon 1976), is only ~5% more than that of YO_8 polyhedra. This suggests that the octahedral volume expansion is not directly transferred to the whole unit cell, but it is partially compensated by the well-known tilting phenomena occurring in perovskites (Mitchell 2002). The observed change of ⟨A–O⟩ and ⟨B–O⟩ distances is also seen in the linear decrease of the tolerance factor (see Table A1) suggesting that Y(Cr,Al)O_3 perovskites become more distorted from the cubic prototype with increase of x_{Cr3+}. Figure A2b shows the change of (Al,Cr)–$O_{1,2}$–(Al,Cr) bond angles along the studied $YAlO_3$–$YCrO_3$ join. The two symmetrically nonequivalent bond angles vary in a similar way up to a Cr fraction close to 0.4 while their trends start to diverge above this value. Another important feature, which occurs along the $YAlO_3$–$YCrO_3$ join when the chromium content increases above approximately x_{Cr3+} = 0.4, is the significant change of the effective coordination number (*ECoN*) of yttrium ions in the A site (Figure A3).

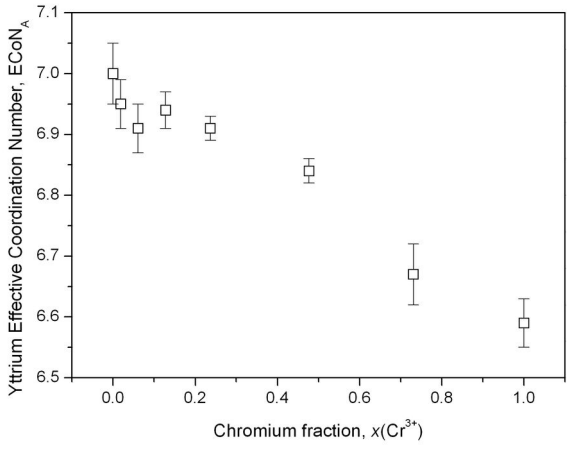

Figure A3. Variation of the effective coordination number of yttrium ions in function of the refined chromium fraction (x_{Cr3+}).

The *ECoN* parameter is particularly useful to revel the subtle variations of the effective charge contribution that each ligand provides to the coordination shell of a central cation (Hoppe 1979; Hoppe et al. 1989). It appears from Figure A3 that while the sevenfold effective coordination of Y gradually decreases as a function of Cr^{3+} content reaching a value of 6.5 in the $YCrO_3$ end member. The rate of decrease is larger above x_{Cr3+} = 0.4. This suggests the

existence of a threshold value above which the lattice strain induced by the incorporation of Cr^{3+} in the octahedral sites of $YAlO_3$ can no longer be accommodated by octahedral expansion and the strain is released by a more significant rearrangement of the A-site coordination environment.

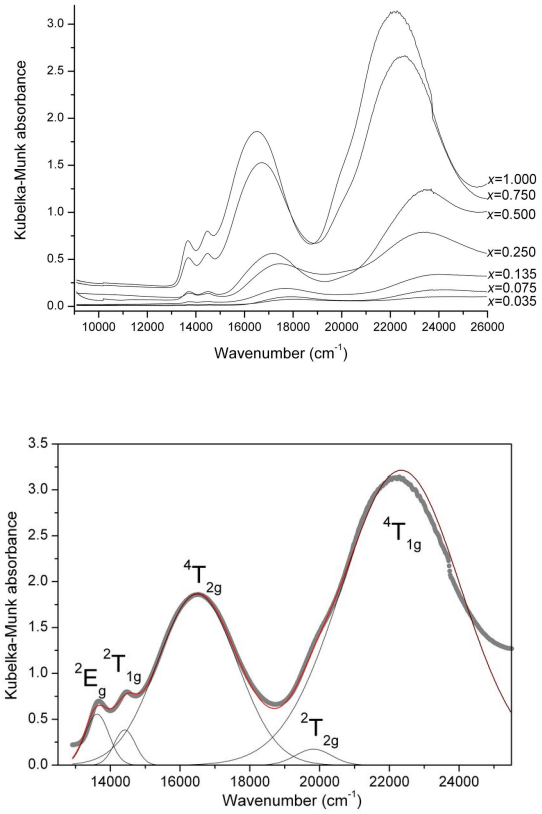

Figure A4. Diffuse reflectance spectra of $Y(Cr,Al)O_3$ perovskites (a) and example of spectrum deconvolution (b).

● *Optical properties* – $Y(Cr,Al)O_3$ perovskites exhibit the typical optical spectra of Cr^{3+} in octahedral coordination (Figure A4a) involving *d–d* electronic transitions (Taran et al. 1994; Langer et al. 1997; Andrut and Wildner 2001; Langer et al. 2004; Taran et al. 2004). Band absorbance increases almost linearly with $x_{Cr^{3+}}$, while band energy undergoes a gradual shift because of the changing crystal field strength along the $YAlO_3$–$YCrO_3$ join (Marfunin 1979; Burns 1993; Wildner et al. 2004).

The most intense bands are attributed to the parity-forbidden and spin-allowed transitions from the ground level $^4A_{2g}$ (^4F) to $^4T_{2g}$ (^4F) and $^4T_{1g}$ (^4F) at 16000–18000 cm^{-1} and 22000–24000 cm^{-1}, respectively. Minor bands, because of the parity- and spin-forbidden transitions $^4A_{2g}$ (^4F) → ^2E_g (^2G), → $^2T_{1g}$ (^2G) and → $^2T_{2g}$ (^2G), are observed at approximately 13700 cm^{-1}, 14300 cm^{-1} and 19500 cm^{-1}, respectively. Diffuse reflectance spectra were successfully deconvoluted using five Gaussian bands for the Cr^{3+} transitions (Figure A4b) whose values of energy, splitting and optical density are listed in Table A2.

Table A2. Energy (Peak), Band Splitting (fwhm), and Intensity (Area) of the Optical Bands of Cr^{3+} in $Y(Cr,Al)O_3$ Perovskites

	$^4A_{2g} \rightarrow$	$\rightarrow {}^4T_{2g}$ (^4F)			$\rightarrow {}^4T_{1g}$ (^4F)			$\rightarrow {}^2E_g$ (^2G>)	$\rightarrow {}^2T_{1g}$ (^2G)	$\rightarrow {}^2T_{2g}$ (^2G)
sample	$x_{Cr^{3+}}$	peak (cm^{-1})	fwhm (cm^{-1})	area (au)	peak (cm^{-1})	fwhm (cm^{-1})	area (au)	peak (cm^{-1})	peak (cm^{-1})	peak (cm^{-1})
Cr35	0.02	17 870	1920	40	24 100	3150	50	13 745	14 795	19 415
Cr75	0.06	17 880	2240	150	23 910	4070	250	13 735	14 570	19 520
Cr135	0.13	17 610	2160	220	23 695	2900	340	13 715	14 435	19 540
Cr250	0.24	17 340	2130	310	23 240	2930	1010	13 750	14 435	19 280
Cr500	0.48	16 980	2285	740	23 110	3310	4140	13 720	14 435	19 380
Cr750	0.73	16 630	2100	2390	22 410	3010	5730	13 695	14 385	20 080
Cr1000	1.00	16 410	2140	3190	22 140	2960	7030	13 640	14 360	20 215

Table A3. Optical Parameters of Cr^{3+} in $Y(Cr,Al)O_3$ Perovskites: Crystal Field Strength ($10Dq$), Interelectronic Repulsion Racah B_{35}, B_{55}, and C Parameters, Nephelauxetic Ratios β_{35} and β_{55}, and Local Cr−O Distance Calculated by Eq 2

sample	$x_{Cr^{3+}}$	$10Dq$ (cm^{-1})	B_{35} (cm^{-1})	B_{55} (cm^{-1})	C (cm^{-1})	β_{35} (1)	β_{55} (1)	$<Cr-O>^{local}$ (Å)
Cr35	0.02	17 867	609	805	2883	0.66	0.88	1.950 ± 0.005
Cr75	0.06	17 864	588	790	2904	0.64	0.86	1.950 ± 0.005
Cr135	0.13	17 616	593	787	2928	0.65	0.86	1.956 ± 0.005
Cr250	0.24	17 349	573	811	2886	0.62	0.88	1.962 ± 0.005
Cr500	0.48	16 968	576	797	2899	0.63	0.87	1.971 ± 0.005
Cr750	0.73	16 627	565	686	3060	0.62	0.75	1.979 ± 0.006
Cr1000	1.00	16 405	560	654	3116	0.61	0.71	1.984 ± 0.006

The main optical parameters, calculated on the basis of the Cr^{3+} transitions energy, are reported in Table A3. The crystal field strength $10Dq$ decreases regularly with $x_{Cr^{3+}}$, but its trend is not linear all along the join (Figure A5a). In good agreement with results from XRD analysis (e.g. variation of B–$O_{1,2}$–B angles and $ECoN_A$), we interpret the $10Dq$ versus $x_{Cr^{3+}}$ relationship on the basis of two linear trends changing their slopes at approximately $x_{Cr^{3+}}$ = 0.4. This fact, already observed in the corundum–eskolaite join (Andrut et al. 2004), is attributable to different slopes versus $x_{Cr^{3+}}$ of the three components in which the $^4A_{2g} \rightarrow {}^4T_{2g}$ (O_h) transition is split ($^4A \rightarrow {}^4A$, $^4A \rightarrow {}^4A$, $^4A \rightarrow {}^4A$) as a consequence of the low point symmetry (C_1) of the octahedral site in the orthorhombic perovskite lattice. However, such splitting of the main Cr^{3+} band is too small to be appreciable in terms of bandwidth in diffuse reflectance spectra (e.g. König–Kremer diagrams, 1977). As a matter of fact, FWHM values of $^4T_{2g}$ and $^4T_{1g}$ transitions remain almost constant all along the join (Table A2) as the distortion Δ_6 randomly fluctuates from 0.04 to 0.07 (Table A1).

The Racah parameters exhibit similar trends versus $x_{Cr^{3+}}$ (Figure A5b). The nephelauxetic ratio β_{55} rapidly increases from Cr1000 (0.71) to Cr500 (0.87) and then remains stable fluctuating in the 0.86–0.88 range towards Cr0. These high β_{55} values imply relatively strong π-bonds for Cr–O in perovskite (Reinen 1969), although a diminished polarizability of oxygens around Cr^{3+} in the Al-rich terms may be also invoked for analogy with other Al–Cr

oxides (Langer 2001). Both reasons are consistent with the known magnetic ordering of Cr–Cr pairs in orthochromates persisting down to Cr750 compositions (Lenglet and Hochu 2000). On the other hand, the nephelauxetic ratio β_{35} increases rather regularly from 0.61 (Cr1000) to 0.66 (Cr35); this limited variation of β_{35} confirms preliminary literature data on yttrium chromium perovskites (Reinen 1969). Such a growing trend of β_{35} indicates a slightly reduced covalency of the Cr–O bonding, which has been also observed along other Cr–Al joins, such as Cr_2O_3–Al_2O_3 (Poole and Itzel 1963; Reinen 1969), and $MgCr_2O_4$–$MgAl_2O_4$ (Reinen 1969). Overall, the covalent degree of the Cr–O bonding in $Y(Cr,Al)O_3$ perovskites is higher ($0.61 < \beta_{35} < 0.66$) with respect to the spinel $MgCr_2O_4$–$MgAl_2O_4$ series ($0.69 < \beta_{35} < 0.73$) and the garnet $Ca_3Cr_2Si_3O_{12}$–$Ca_3Al_2Si_3O_{12}$ join ($0.69 < \beta_{35} < 0.77$; Andrut and Wildner 2001; Langer et al. 2004), but falls within the wide variation range ($0.50 < \beta_{35} < 0.72$) of the Cr_2O_3–Al_2O_3 join (Neuhaus and Richartz 1958; Schmitz-DuMont and Reinen 1959; Poole and Itzel 1963; Reinen 1969; Gaudry et al. 2006).

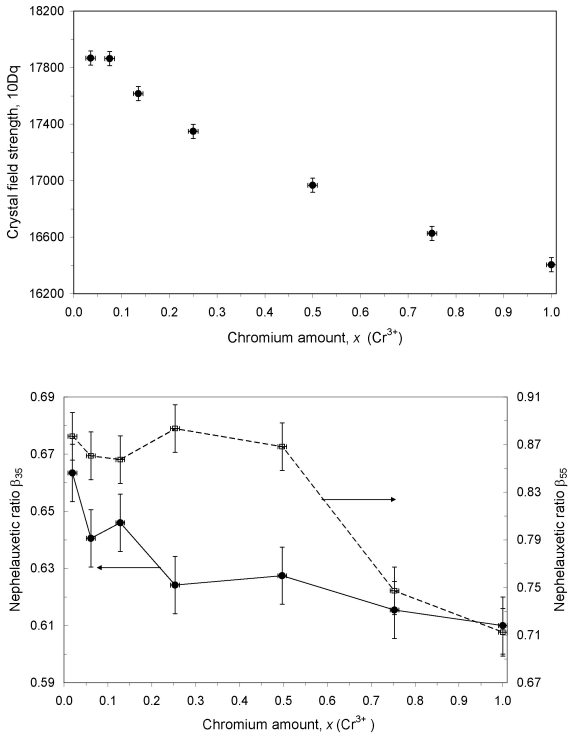

Figure A5. Variation along the $YAlO_3$–$YCrO_3$ join of (a) crystal field strength $10Dq$ and (b) Racah B_{35} and B_{55} parameters.

● *Structural relaxation* – The local Cr–O mean bond lengths were calculated from electronic absorption spectra *according to Eq. (1.5)* [*reported in the introductive chapter of this dissertation*], and the obtained results are listed in Table A3. The relaxation of the perovskite structure around Cr^{3+} can be appreciated plotting $\langle Cr–O\rangle^{local}$ versus x_{Cr3+} (Figure A6a). The relaxation coefficient, calculated *according to Eq.(1.2)* [*see the introductive chapter of this dissertation*], yields $\varepsilon_{lim\ xCr\to 0} = 0.54$, which implies a degree of structural relaxation approximately halfway between the HS and the VCA models. Such a relatively low relaxation coefficient does not necessarily imply that the perovskite structure behaves as an inflexible

one. Perovskites are known to display very large structural flexibility (Mitchell 2002). Comparison with other dense oxide structures will help to clarify this issue.

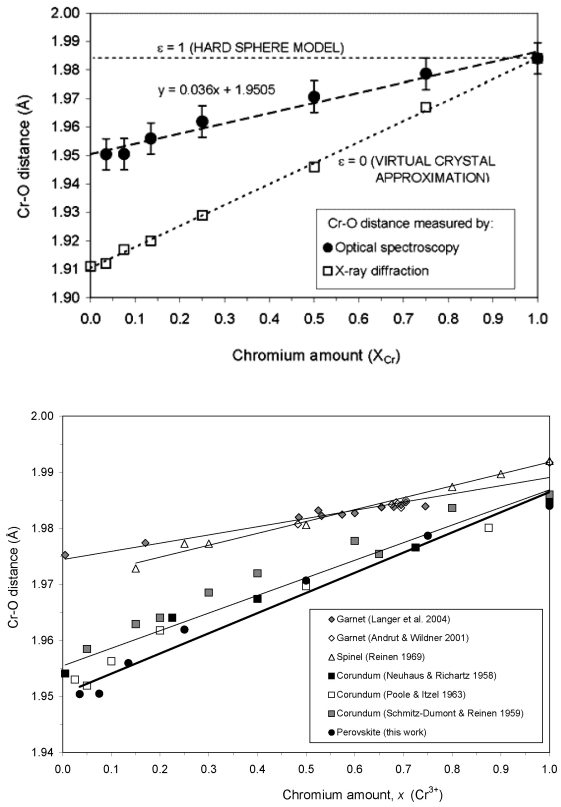

Figure A6. Coefficient of structural relaxation around Cr^{3+} in the $Y(Cr,Al)O_3$ perovskites (a) and comparison with other crystal structures (b).

As a matter of fact, the value found here for the ε coefficient in $Y(Cr,Al)O_3$ perovskites is the lowest among $(Al,Cr)O_6$ polyhedra as appreciable by comparison with the well-studied series of uvarovite–grossular (Andrut and Wildner 2001; Langer et al. 2004), magnesiochromite–spinel (Reinen 1969), and eskolaite–corundum (Neuhaus and Richartz 1958; Schmitz-DuMont and Reinen 1959; Poole and Itzel 1963; Reinen 1969). Available EAS data allow the calculation of the correspondent value of $\varepsilon_{\lim\, x\mathrm{Cr}\to 0}$, which is 0.74 for garnet, 0.68 for spinel, and 0.58 for corundum (Figure A6b). This ranking can be interpreted as because of a progressive decrease of polyhedral network flexibility when moving from garnet (isolated octahedra, edge-shared to tetrahedra), to spinel (edge-sharing octahedra, corner-shared to tetrahedra), to corundum (corner-, edge-, and face-sharing octahedra). More in detail, Juhin et al. 2008 concluded that a complete relaxation in pyrope is achieved through deformation of MgO_8 dodecahedra and SiO_4 tetrahedra, the former to a greater extent, which surround the central CrO_6 octahedron. On the other hand, bond buckling and angular tilts of Mg-centered tetrahedra around the CrO_6 octahedra have been recognized as the strain-accommodating mechanism in spinel (Juhin et al. 2007), while the extension of the relaxation process up to the second shell has not been observed in corundum because of the reduced degrees of freedom of its structure (Gaudry et al. 2003).

From a purely geometrical point of view, the polyhedral connectivity in the perovskite network (corner-sharing octahedra) would suggest a relatively large flexibility, as also

testified by the complex tilting systems and the ability to host a large variety of elements well-known for this structure (Mitchell 2002). This appears to be somewhat in contrast with the lowest ε value found in the $Y(Cr,Al)O_3$ perovskites under study. However, it has been suggested that the presence of *M*–O–*M* (e.g. *M* = a transition metal ion) one-dimensional chains formed by corner-sharing octahedra in perovskites will lead to an enhanced covalency accompanying the *M*3*d*–O2*p* hybridization thus explaining the large discrepancies found between observed and calculated total polarizabilities (Shannon and Fischer 2006). Such an enhanced covalency can also act as a constraint on the *M*–O–*M* bond angle, limiting to some extent the degrees of freedom in the perovskite network. The probability of occurrence of Cr–O–Cr bridges has been calculated under the assumption of random distribution for Cr^{3+} in $Y(Cr,Al)O_3$ (see Table A1). Interestingly, the nonlinear relationship of probability versus x_{Cr3+} can be approximated by two linear trends changing their slopes at x_{Cr3+} ~0.4. Cr–O–Cr clusters can be responsible for the diverging trends of $B–O_{1,2}–B$ bond angles observed in Figure A2b for x_{Cr3+} greater than ~0.4. They will act as a local structural constraint forcing the O1 and O2 hinges of octahedral chains to be no longer equivalent.

To better understand the significance of the EAS-based ε value found in our work, we recall some recent papers (Garcia-Lastra et al. 2006 and 2007; Moreno et al. 2007) disclosing that the crystal field strength relationship [*as expressed in the Eq.(1.4) of the introductive chapter of this dissertation*] is better defined as the sum of two terms: the first is actually the 10*Dq* as given in *Eq.(1.4)*, while the second, $V_R(\mathbf{r})$, accounts for the electrostatic potential of the rest of lattice ions upon the localized electrons of the CrO_6 octahedron (Moreno et al. 2007). This additional contribution was observed to increase when the point symmetry of the Cr site decreased (Garcia-Lastra et al. 2006), and is largely affected by the covalency of the Cr–O bond (Moreno et al. 2007) also mentioned above. In particular, the polarization-dependent part of $V_R(\mathbf{r})$ is associated to a change in covalency of the Cr–O bonding (Moreno et al. 2007), in line with the conclusions reached on the basis of combined EAS and XAS results on the corundum–eskolaite join (Gaudry et al. 2006). Following this line of reasoning, the as-measured 10*Dq* values should be subtracted by a correction term equal to $V_R(\mathbf{r})$ before being used for calculation of the local Cr–O bond distances. The larger derived distances lead to a greater calculated relaxation coefficient.

This interpretation would justify the systematic underestimation of local Cr–O bond distances, as inferred from optical spectra, compared to what derived from XAS studies (Gaudry et al. 2003; Juhin et al. 2007 and 2008). As a consequence, the ε coefficients calculated by EXAFS (~1 for garnet (Juhin et al. 2008), 0.83 for spinel (Juhin et al. 2007), 0.76 for corundum (Gaudry et al. 2003 and 2006), and ~0.8 for perovskite [*the author of the present work, in preparation*] are larger than the ones calculated by EAS, implying a stronger degree of relaxation around Cr^{3+} of all the structures considered. The relaxation ranking defined by XAS corresponds to that given by EAS, but for the perovskite series. Interestingly, a perfect correspondence should be obtained if the relaxation coefficient of $Y(Cr,Al)O_3$ would be calculated by using the samples from Cr1000 to Cr250: in this case, the resulting $\varepsilon = 0.61$ is intermediate between those of corundum and spinel. It is significant that samples from Cr250 to Cr35, showing an "excess" of crystal field strength responsible for the non linearity of the relationship $x_{Cr^{3+}}$ vs. $10Dq$ (Figure A5a), are characterized by a different arrangement of the second nearest neighbours, that is, yttrium effective coordination number close to 7 (Figure A3), which is likely to play an appreciable effect on the electrostatic potential $V_R(\mathbf{r})$.
The discrepancies between EAS and XAS data have induced a vivacious discussion and a criticism about the capacity of EAS to determine the actual Cr–O local distances (Gaudry et al. 2006; Juhin et al. 2007 and 2008), and the ligand field theory to describe accurately the electronic properties of transition-metal impurities in wide gap materials (Garcia-Lastra et al. 2006 and 2007; Moreno et al. 2007). The picture arising from our study substantially confirms that the local Cr–O distances and the related ε relaxation coefficients, as measured by EAS, are not reliable in absolute terms, but should be used to compare different structures. The crystal field strength derived from electronic absorption spectra appears to contain more information than previously retained particularly an additional contribution from the second nearest neighbouring ions, for example, yttrium in the $Y(Cr,Al)O_3$ perovskites.

► ***Conclusion*** − The expected decrease of crystal field strength along the $YAlO_3$–$YCrO_3$ join occurs with a nonlinear trend suggesting a change of chromium environment toward the Al end term with some excess $10Dq$ with respect to what is predictable by the tendency constructed with samples Cr1000→Cr250. The local Cr–O bond lengths, as calculated from EAS, go from 1.98 Å (Cr1000) down to 1.95 Å (Cr35) indicating an

unexpectedly low relaxation coefficient of perovskite (ε = 0.54) in comparison with garnet (ε = 0.74), spinel (ε = 0.68), and corundum (ε = 0.58) whose ranking is connected with a progressive decrease of polyhedral network flexibility. The low relaxation of perovskite network is explained by the increased probability of covalent-enhanced Cr^{3+}–O–Cr^{3+} bonds for x_{Cr3+} greater than ~0.4; the occurrence of Cr–O–Cr clusters is responsible for the diverging trends of nonequivalent (Al,Cr)–O–(Al,Cr) angles and the change of yttrium coordination. Considering now the systematic underestimation of local Cr–O bond distances inferred from EAS, compared to those from XAS, an additional contribution to 10*Dq* originating from the electrostatic potential of the rest of the lattice ions upon the localized electrons of the CrO_6 octahedron has to be invoked. This interpretation would justify the excess 10*Dq*, coming from a changed electronic potential on Cr^{3+} ions, because of a variation of the yttrium effective coordination number close to the $YAlO_3$ end term. This effect is enhanced in perovskites because of the low point symmetry of the Cr site. These results support the hypothesis that electronic absorption spectra, as well as crystal field strength values derived from them, contain more information than previously acknowledged especially some additional contribution to the electronic potential from the next nearest neighboring ions. However, further investigations are needed, particularly the combination of structural (XRD) and spectroscopic data (XAS, EAS) with *ab initio* electronic structure calculations.

3. Section I. B. ♦ Elastic properties of $YCrO_3$ up to 60 GPa

Note: This is a "*satellite*" study written in the 2010 by Ardit, M., Cruciani, G., Dondi, M., Merlini, M., and Bouvier, P., reported as published (with few variations, if any, as described in the premise of this section) in the "*Physical Review B*, 113, 13772–13778".

Abstract

The high pressure evolution of the $YCrO_3$ perovskite structure (space group *Pbnm*) has been investigated using synchrotron powder diffraction, up to 60 GPa. The results show an anisotropy in the elastic moduli of the individual crystallographic axes: the *b* axis is appreciably less compressible than both *a* and *c* axes [K_{a0} = 195(5) GPa, K_{b0} = 223(7) GPa, and K_{c0} = 200(6) GPa, respectively]. This implies that $YCrO_3$ becomes more distorted with increasing pressure, which is similar to what was previously found in $YTiO_3$ but opposite to the behavior reported for $YAlO_3$. Such contrasting trends are explained by the stronger confinement of Y ions in $YAlO_3$ due to the smaller size of octahedral network in the orthoaluminate compared to the orthochromate.

► ***Introduction*** − Perovskites are of great interest in Earth sciences because, at the high pressure and temperature conditions of the Earth's lower mantle, the pyroxene enstatite, $MgSiO_3$, transforms into a denser perovskite-structured polymorph (Navrotsky and Weidner 1989).

The group of 3:3 perovskites (trivalent cations in both A and B sites) has gained much interest in several technological fields due to their peculiar electric, magnetic, piezoelectric and optical properties (Ishihara 2009; Wolfram and Ellialtioglu 2006). Industrial applications of the $YCrO_3$ perovskite, subject of this study, include its use as interconnection for the solid oxide fuel cells (Wang et al. 2009) while in pure science it has been applied to develop model for defective structures (Carini II et al. 1991).

Furthermore, its multifunctional biferroic behaviour (i.e. possessing both ferromagnetic and ferroelectric properties) has been reported and explained by a local non-centrosymmetry arising from ~0.01 Å displacement of Cr^{3+} ions along the *c*-axis with respect to the centre of B octahedra (Serrao et al. 2005) The orthorhombic symmetry is maintained for the average crystallographic structure (Ramesha et al. 2007).

The first work presented in the ***Section I*** *of this dissertation* establishes the structural relaxation along the $YAlO_3$–$YCrO_3$ join (Cruciani et al. 2009). Compared to garnet, spinel, and corundum, the lowest relaxation around Cr^{3+} found in perovskite was in contrast with the lattice flexibility expected on the basis of its corner-sharing octahedral framework. Possible explanations involved the role of covalency in Cr–O bonds or the different elastic properties of the two end members.

In the last decade, many studies have been devoted to assess the high pressure behavior of both 2:4 and 3:3 orthorhombic perovskites (Ross 1998; Ross and Angel 1999; Loa et al. 2001 and 2007; Bouvier and Kreisel 2002; Ross and Chaplin 2003; Ross et al. 2004a,b; Angel et al. 2005; Knight et al. 2005; Sugahara et al. 2006; Wu et al. 2006; Zhao et al. 2006; Lufaso et al. 2007), and a general rule has been formulated (Angel et al. 2005). It predicts that at high pressures the octahedral tilting and perovskite distortion will increase in the 2:4 group (e.g. $CaTiO_3$) and decrease in the 3:3 group of perovskites (e.g. $YAlO_3$). No data have been reported so far on the high-pressure behavior of $YCrO_3$ belonging to the 3:3 group.

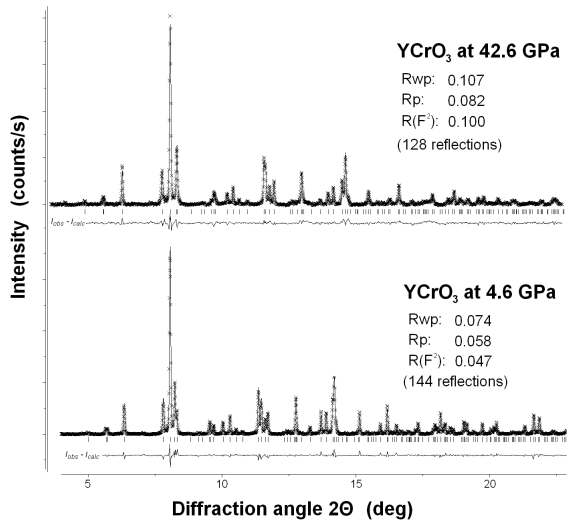

Figure B1. Plot of the Rietveld refinements for $YCrO_3$ at 4.6 GPa (at the bottom) and 42.6 GPa (on the top) at room temperature (λ = 0.3738 Å). The experimental data are indicated by crosses, the calculated pattern is the continuous line, whereas the lower curve is the weighted difference between the observed and calculated patterns. Vertical ticks mark the position of reflections for $YCrO_3$ in the *Pbnm* space group.

This study is aimed at determining the elastic properties of the orthochromate perovskite up to 60 GPa by means of *in situ* synchrotron powder diffraction. Comparison with the high pressure behavior of orthoaluminate will help to understand the low relaxation around Cr^{3+} in the $YAlO_3$–$YCrO_3$ perovskite system.

► ***Experimental*** – [*for the experimental details (including: sample preparation, Synchrotron X-ray diffraction data collection, and Rietveld refinements) readers are requested to refer to chapter* ***2***].

Two representative Rietveld plots at low (4.6 GPa) and high (42.6 GPa) pressure are given in Figure B1. Refined unit cell parameters, final atomic coordinates, and isotropic atomic displacement parameters of $YCrO_3$ perovskite at ambient pressure (Cruciani et al. 2009), 4.6

GPa, and 42.6 GPa are reported in Table B1. Previously reported crystal structure determinations of $YCrO_3$ (at ambient conditions) include an early model with not refined atomic coordinates (Geller and Wood, 1956), and the more recent study by Ramesha et al. (2007) using neutron powder diffraction and pair distribution function analysis. The results of our structure refinement at room pressure are identical, within the standard error, to those obtained from the latter study (see Table B2 for comparison).

Table B1. Unit cell parameters, final atomic coordinates, and isotropic atomic displacement parameters of $YCrO_3$ perovskite at ambient pressure, 4.6 GPa, and 42.6 GPa.

	P=0 GPa	*P=4.6 GPa*	*P=42.6 GPa*
a (Å)	5.2434(1)	5.2028(1)	4.9403(2)
b (Å)	5.5242(1)	5.4872(1)	5.2767(2)
c (Å)	7.5356(1)	7.4808(1)	7.1995(2)
Volume (Å^3)	218.27(1)	213.57(1)	187.16(1)
x_Y	-0.0167(2)	-0.0170(3)	-0.0205(5)
y_Y	0.0664(1)	0.0673(2)	0.0713(3)
$Ueq._Y$ (Å^2×100)	1.39(2)	1.16(4)	1.40(4)
$Ueq._{Cr}$ (Å^2×100)	1.26(4)	1.05(10)	1.33(9)
x_{O1}	0.101(1)	0.097(1)	0.105(2)
y_{O1}	0.465(1)	0.458(1)	0.470(2)
$Ueq._{O1}$ (Å^2×100)	1.7(2)	1.8(4)	1.6(4)
x_{O2}	0.693(1)	0.679(1)	0.686(2)
y_{O2}	0.302(1)	0.297(1)	0.299(2)
z_{O2}	0.055(1)	0.055(1)	0.053(1)
$Ueq._{O2}$ (Å^2×100)	1.6(1)	1.5(3)	1.5(3)

Fixed coordinates: $z_Y = ¼$; $x_{Cr} = 0$, $y_{Cr} = z_{Cr} = ½$; $z_{O1} = ¼$

Table B2. Comparison of selected parameters for $YCrO_3$ models at ambient pressure. ([*]Cruciani et al. 2009; [°]Ramesha et al. 2007)

	$YCrO_3$,[*]	$YCrO_3$,[°]
$<^{VIII}Y–O>$ (Å)	2.417	2.415
$<^{XII}Y–O>$ (Å)	2.738	2.735
Cr–O1 (Å)	1.967(2)	1.971(1)
Cr–O2' (Å)	1.988(4)	1.983(1)
Cr–O2" (Å)	1.998(4)	1.993(1)
<Cr–O> (Å)	1.984	1.982
M_A / M_B	1.18	1.18
$^{VIII}V_A$ (Å^3)	23.52	23.44
$^{XII}V_A$ (Å^3)	46.18	46.05
$^{VI}V_B$ (Å^3)	10.40	10.37
Cr–O1–Cr (°)	146.7(3)	145.6(1)
Cr–O2–Cr (°)	145.7(2)	146.3(1)

O2' and O2" coordinates obtained from O2 (x,y,z) in Table B1 by the following relations:
$x_{O2'} = ½+x_{O2}$; $y_{O2'} = ½-y_{O2}$; $z_{O2'} = ½+z_{O2}$
$x_{O2''} = 1-x_{O2}$; $y_{O2''} = 1-y_{O2}$; $z_{O2''} = ½+z_{O2}$
M_A / M_B: ratio of total estimated variation of bond valence in a polyhedral site due to change of average bond distance (Angel et al. 2005; Zhao et al. 2006).

$M_i = \frac{R_i N_i}{B} \exp\left(\frac{R_0 - R_i}{B}\right)$ where R_i = average bond length; N_i = coordination number of the cation site at ambient condition; R_0 = bond valence parameter (Brown and Altermatt 1985); B = universal constant (0.37).

V_A and V_B = volumes of A and B polyhedra, respectively; superscript is the assumed coordination number.

► *Results and discussion*

● *Elastic properties of $YCrO_3$* – The pressure dependence of the unit cell volume of $YCrO_3$ perovskite is plotted in Figure B2. The volume reduction is about 17.5% in the studied pressure range. No evidences for phase transitions were found up to 60.4 GPa.

The P-V data, fitted with a third-order Birch–Murnagham equation of state (EoS) [Eq. (B1)],

$$P = \frac{3K_{T0}}{2}\left[\left(\frac{V_0}{V}\right)^{\frac{7}{3}} - \left(\frac{V_0}{V}\right)^{\frac{5}{3}}\right] \times \left\{1 + \frac{3}{4}\left(K_0^{'} - 4\right)\cdot\left[\left(\frac{V_0}{V}\right)^{\frac{2}{3}} - 1\right]\right\} \qquad \text{(B1)}$$

give a V_0 = 218.23(4) Å^3, equal to the value obtained for the same sample refined at room pressure (Cruciani et al. 2009), and to a volumetric bulk modulus K_{T0} = 208.4(5) GPa with a $K_0^{'} = 3.7(1)$.

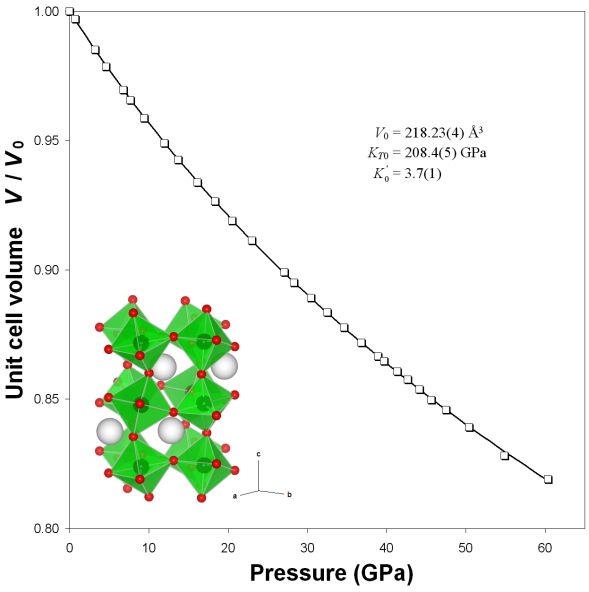

Figure B2. Variation of the unit cell volume of $YCrO_3$ perovskite between room pressure and 60.4 GPa. The inset displays the structure of $YCrO_3$ perovskite along the [110]. Line refers to the EoS calculated value.

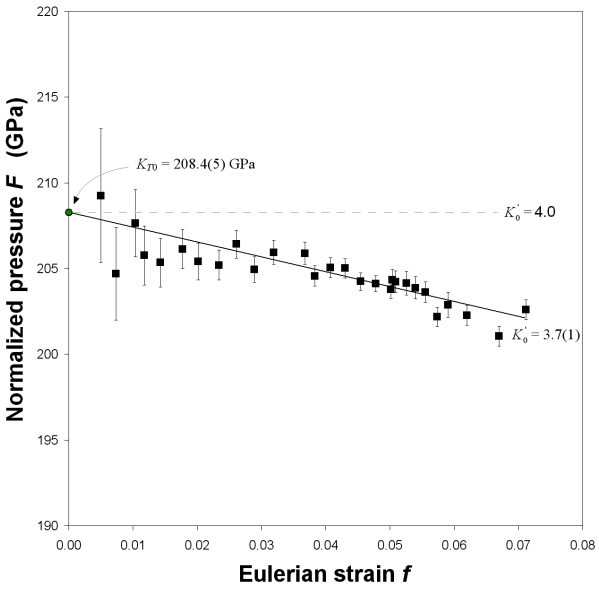

Figure B3. Normalized stress-strain (*F*–*f*) plot derived from the measured volumes for a third order Birch-Murnagham EoS. The normalized pressure stress *F* is defined as $F = P/3f\,(1 + 2f)^{5/2}$, while the finite eulerian strain *f* is defined as $f = [(V_0/V)^{2/3} - 1]/2$.

Normalized stress-strain (*F*–*f*) plot (Figure B3) provides a visual indication of how the $K_0^{'}$ term is significant in the EoS fitting (Angel 2000). If the EoS was truncated at second-order all data points could lie on a horizontal line of constant F ($K_0^{'} = 4$),

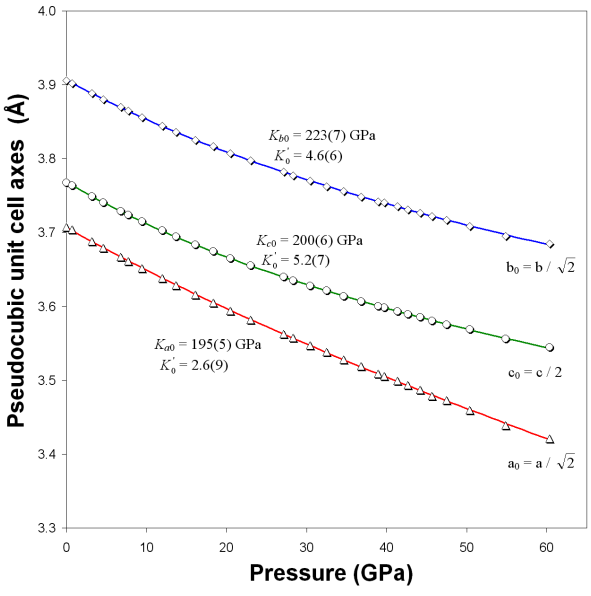

Figure B4. Variation of the pseudocubic unit cell axes of $YCrO_3$ perovskite between room pressure and 60.4 GPa.

whereas in the case of $YCrO_3$ the data lie on an inclined line, correctly described by a third-order truncation of the Birch-Murnagham EoS.

The elastic moduli of the individual crystallographic axes are obtained by fitting the measured data with the same EoS [Eq. (1)] to the cubes of each of the cell axes. The resulting axial moduli: K_{a0} = 195(5) GPa, K_{b0} = 223(7) GPa, and K_{c0} = 200(6) GPa, highlight how the *b* axis is appreciably less compressible than both *a* and *c* axes, which have similar compressibilities (Figure B4). The direct result is that the $YCrO_3$ perovskite structure becomes more distorted with increasing pressure.

Such a behavior is different compared to what was reported for the orthorhombic $YAlO_3$ perovskite, in which the *b* axis is significantly more compressible than both *a* and *c*, given the corresponding axial moduli: K_{a0} = 219(7) GPa, K_{b0} = 157(3) GPa, and K_{c0} = 212(2) GPa (Ross et al. 2004b). Consequently the two structures show a different anisotropic behavior along [010] and [101].

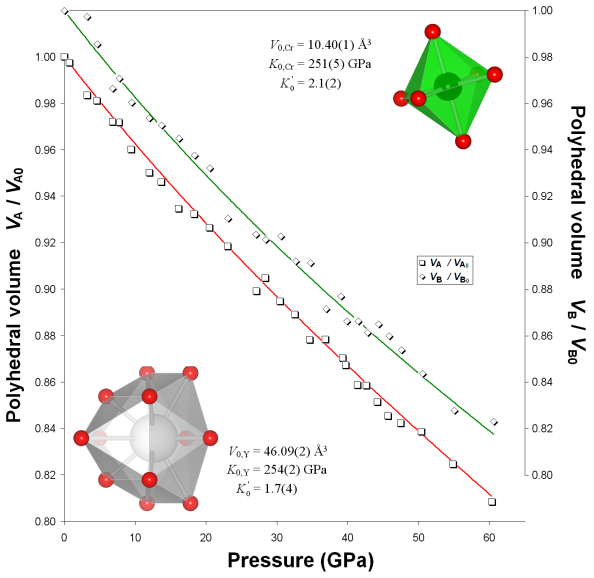

Figure B5. Variation of the polyhedral volume of $YCrO_3$ perovskite between room pressure and 60.4 GPa. Continuous lines define the EoS calculated to fit the data sets.

The polyhedral bulk moduli for YO_{12} and CrO_6 polyhedra (see Figure B5 for pressure dependence) were calculated using the same formalism applied to fit the P-V data, obtaining $V_{0,poly}$, K_{p0}: 46.09(2) Å^3, 254(2) GPa for YO_{12}, and 10.40(1) Å^3, 251(5) GPa for CrO_6. The volume compressibilities of the YO_{12} and CrO_6 sites are therefore equivalent, whereas for the $YAlO_3$ perovskite the compressibility of the cubic site is ~15% less than that of the AlO_6 octahedron (Ross et al. 2004b).

Besides the overall polyhedral compression, information about pressure-driven electronic changes in transition metal perovskites can be inferred from the changes of octahedral distortion as a function of pressure. For instance, the variation of Ti–O bond distances in $YTiO_3$ indicated the possibility of a pressure-induced spatial reorientation of the occupied t_{2g} orbitals in Ti^{3+} ions [electron configuration $3d^1(t_{2g})$] (Loa et al. 2007). Considering that Cr^{3+} (configuration $3d^3(t_{2g})$) is also a non-Jahn-Teller ion,

the pressure-driven orbital reorientation can be evaluated, in analogy to $YTiO_3$, by inspecting the changes in Cr–O bond lengths in the selected pressure range up to 35 GPa (Figure B6).

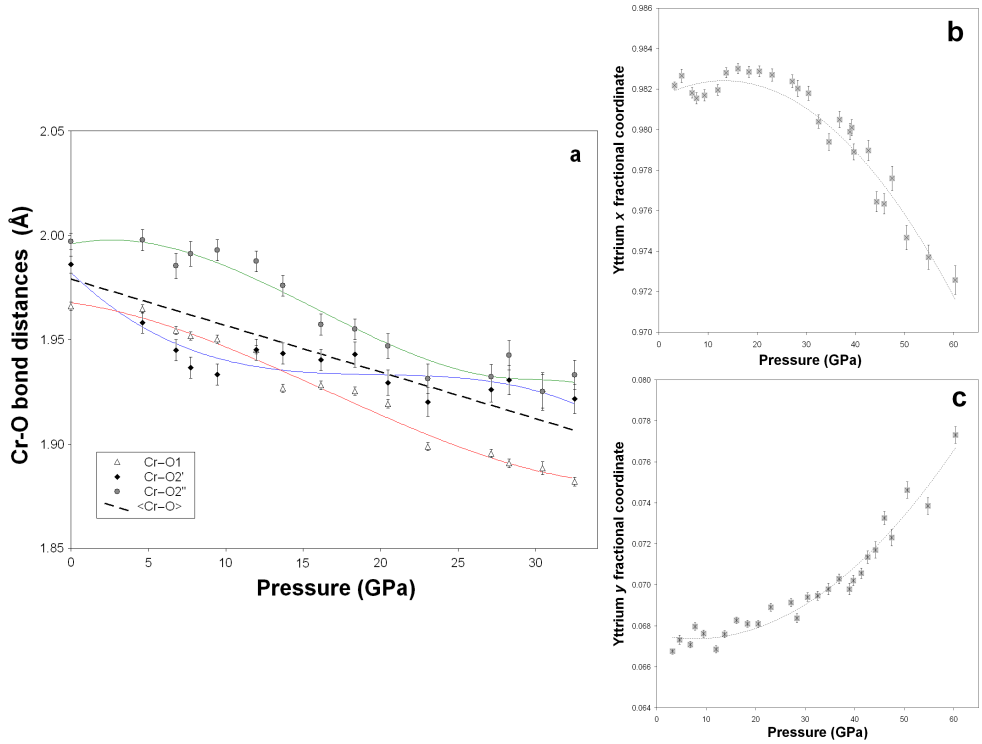

Figure B6. (a) Variation of the Cr–O bond lengths in $YCrO_3$ as a function of pressure up to 35 GPa. This upper limit is selected in order to evaluate the octahedral distortion as much as possible unaffected by the variations within the YO_{12} polyhedra. In fact, the displacement of Y ions (*x* and *y* coordinates in (b) and (c), respectively) away from the center of the dodecahedron is very close to the initial value in the 0-35 GPa pressure range.

The variation of Cr–O2', Cr–O2'', and Cr–O1 distances, respectively along the *x*, *y*, and *z* directions of the local coordinate system at Cr site, resembles very much what was found in $YTiO_3$. In both cases, at a given pressure (13 GPa for $YTiO_3$ and about 28 GPa for $YCrO_3$) two almost equal B–O2 and one shorter B–O1 distances occur, implying that the B octahedra are compressed along *z* and that the orbital reorientation has taken place. The distinct pressure of the orbital reorientation in $YTiO_3$ and $YCrO_3$ can be ascribed to the different electron configuration of the transition metal ions and to the lattice elastic properties.

As far as the effects of pressure on the biferroic character of $YCrO_3$, given that it is caused by the off-centre shift of Cr ions along *z* direction of octahedra, we expect that compression up to 28 GPa would also lead to disappearance of both the ferromagnetic and ferroelectric properties. Experimental confirmation of this suggestion needs further work which is beyond the scope of the present study.

● *Pressure dependence of cell distortion* – In order to better appreciate how the pressure influences the behavior of the three isotypic $YM^{3+}O_3$ (M^{3+} = Cr^{3+}, Al^{3+}, and Ti^{3+}) perovskites, the unit cell parameters of $YCrO_3$, $YAlO_3$ and $YTiO_3$ were compared through the relation $a \approx b \approx \sqrt{2}\, a_p$, and $c \approx 2a_p$ (a_p: a pseudocubic subcell parameter). Consequently, the cell distortion factor, d [Eq. (B2)], was calculated from that sub-lattice parameters in the same pressure range,

$$d = \frac{\left[\left(\frac{a}{\sqrt{2}} - a_p\right)^2 + \left(\frac{b}{\sqrt{2}} - a_p\right)^2 + \left(\frac{c}{2} - a_p\right)^2\right]}{3a_p{}^2 \times 10^4}, \qquad \text{(B2)}$$

where

$$a_p = \frac{\left(\frac{a}{\sqrt{2}} + \frac{b}{\sqrt{2}} + \frac{c}{2}\right)}{3}$$

obtaining a useful estimation of the departure from an ideal cubic model, for which $d = 0$ (Sasaki et al. 1983).

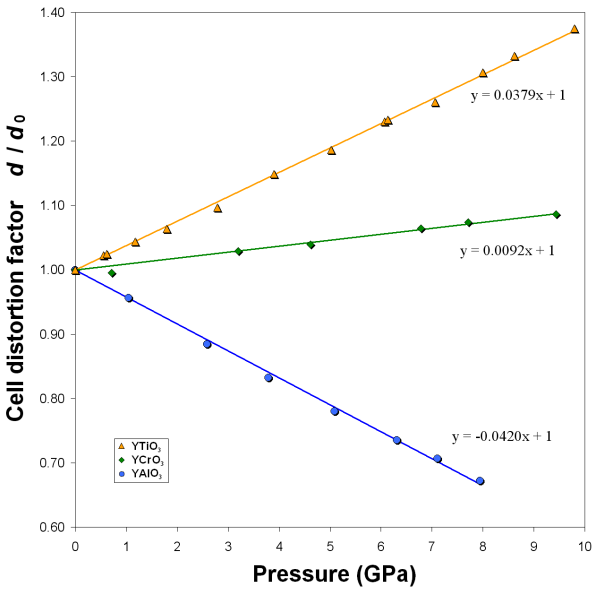

Figure B7. Cell distortion parameter (d / d_0) of $YCrO_3$, $YCrO_3$ and $YAlO_3$ perovskites versus pressure.

Figure B7 shows the clear antithetic behavior of $YCrO_3$ and $YTiO_3$ with respect to $YAlO_3$ orthorhombic perovskite under pressure: while the orthochromate and the orthotitanate become more distorted and are characterized by an increase of the d / d_0 ratio, the orthoaluminate data describe an opposite trend characterized by a decreasing of the d / d_0 ratio towards a structure with higher symmetry. The slopes of the linear relationships in Figure B7 inversely scale with room pressure ⟨B–O–B⟩ angles which in turn linearly decrease

with increasing ionic radii of octahedral B ions (i.e. slopes for d / d_0 vs. P: -0.0420_{YAlO3} < 0.0092_{YCrO3} < 0.0379_{YTiO3}; ⟨B–O–B⟩: 152.2_{YAlO3} > 146.2_{YCrO3} > $140.8°_{YTiO3}$; Shannon ionic radii of $^{VI}M^{3+}$ ions in B: 0.54_{Al} < 0.62_{Cr} < 0.67_{Ti} Å; Shannon 1976). These trends suggest that the pressure-induced distortion of perovskite framework can be related to both the initial octahedral tilt angles and to the ionic radii of octahedral cations for 3:3 perovskites, irrespective of the difference in electron configuration of trivalent ions in B sites. Based on this concept it can be predicted that a $YM^{3+}O_3$ perovskite with the ionic radius of M^{3+} ion in the B site equal to ~0.59 Å (e.g. Ni^{3+} or As^{3+}), thus a ⟨B–O–B⟩ angle at room pressure around 147.4°, will exhibit, upon compression, a d / d_0 ratio close to 1.0 in the whole pressure range, meaning it will neither increase nor decrease its lattice distortion.

► ***Concluding remarks*** – The above considerations show that the contrasting evolution under pressure of $YCrO_3$ and $YTiO_3$ (increasing distortion) vs. $YAlO_3$ (decreasing distortion) can be simply explained on the basis of the ionic radii of B cations. In fact, the mesh size of the octahedral network is reduced in $YAlO_3$, as compared to $YCrO_3$ and $YTiO_3$, with the ionic size of A cation (yttrium) remaining constant. As known from previous work (Cruciani et al. 2009), the decrease of mean octahedral bond distance, ⟨B–O⟩, from $YCrO_3$ to $YAlO_3$ is accompanied by a shortening of the average ⟨A–O⟩ distance, with a net increase of the effective coordination number of Y in $YAlO_3$. This is also associated to a linear decrease of interoctahedral tilting and rotation angles from 152.9° and 151.1° in $YAlO_3$ to 146.7° and 145.7° in $YCrO_3$ at room pressure (Cruciani et al. 2009). Conversely, the decrease in perovskite framework distortion upon increasing the A cation size, with the same cation in the B site, has been previously reported and discussed (Cruciani et al. 2005; Wu et al. 2006). As

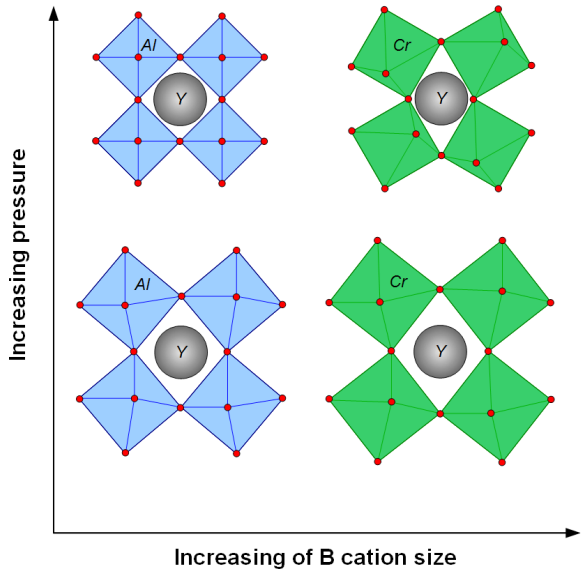

Figure B8. Sketch illustrating the effects of B cation size and pressure on distortion of $YCrO_3$ and $YAlO_3$ perovskites. Actual differences in size and distortion are exaggerated for the sake of clarity.

illustrated in Figure B8 (only $YAlO_3$ and $YCrO_3$ are sketched for the sake of simplicity), the more confined space of Y in $YAlO_3$ is responsible for the higher incompressibility of the A site compared to the B site in the orthoaluminate (Ross et al. 2004b).

The relatively larger shortening of the B–O bonds under pressure in $YAlO_3$ exerts an equivalent effect of the network mesh size reduction at room pressure, as discussed above, leading to a more regular structure of $YAlO_3$ at high pressures. The Y cation in $YCrO_3$ (and $YTiO_3$) does not exhibit the same strong confinement effect as in $YAlO_3$ where the A site is easier to compress and does not hamper the increase of octahedral tilting and rotation in $YCrO_3$ and $YTiO_3$ at high pressures.

These considerations confirm that the pressure-induced distortion of perovskite lattice is primarily controlled by the compressibility ratio of the B and A sites (β_B / β_A), in agreement to what suggested by several authors (Andrault and Poirier, 1991; Thomas 1998). However, the general rule which models β_B / β_A through the ratio of the bond valence difference parameters (M_A / M_B) calculated for the A and B polyhedra (i.e. β_B / β_A = M_A / M_B) (Angel et al. 2005), fails to predict the increasing distortion of both $YCrO_3$ and $YTiO_3$. As a consequence, either the β_B / β_A ratio cannot be accurately estimated from bond valence calculations or the assumption that M_A / M_B = 1.0 is the boundary between perovskites evolving under pressure to higher-symmetry (M_A / M_B > 1.0) or to lower-symmetry (M_A / M_B < 1.0) structures, is not valid.

3. Section I. C. ♦ Structural stability, cation ordering, and local relaxation along the join $AlNbO_4$–$Al_{0.5}Cr_{0.5}NbO_4$

Note: This is a "*key*" study written in the 2011 by Ardit, M., Dondi, M., and Cruciani, G., reported as submitted (with few variations, if any, as described in the premise of this section) to the "*American Mineralogist*" (accepted for publication).

Abstract

$(Al_{1-x}Cr_x)^{3+}Nb^{5+}O_4$ (with $0 \leq x \leq 0.5$) compounds have been investigated through combination of X-ray powder diffraction (XRPD) and electronic absorption spectroscopy (EAS). In spite of the natural occurrence of $AlTaO_4$, the lack of a mineral with composition $AlNbO_4$ contrasts with the strong geochemical affinity between Nb and Ta elements. Rietveld refinements of XRPD data showed that the effective coordination numbers of both the two non-equivalent octahedral sites (*M*1 and *M*2) in the $AlNbO_4$ structure are much lower than expected, especially the one mainly occupied by Nb, in agreement with the very low crystal field strength values (10*Dq*) found by EAS for Cr^{3+} replacing Al at site *M*2. These findings imply that an unfavorable bonding situation occurs for Nb, Al and Cr ions in the $AlNbO_4$ structure which can be regarded as substantially strained compared to $AlTaO_4$, thus explaining the lack of a natural $AlNbO_4$ isomorph. The observed long local Cr–O distances (low 10*Dq*) reveal that the $AlNbO_4$ lattice is not relaxed as a consequence of the Cr–Al substitution (the relaxation coefficient ε is close to zero) and the $AlNbO_4$ structure appears to follow the Vegard's law. This is due to the fact that the Cr^{3+} for Al^{3+} substitution, for the limited range of solid solution (up to 0.2 apfu at site *M*2), does not induce any additional octahedral strain in a lattice already significantly strained.

► ***Introduction*** − The niobium and tantalum elements mainly occur in nature in the form of accessory minerals in granitic pegmatites. On account of their close chemical affinity, these two elements typically give rise to isomorphous series of oxides. The most widespread and abundant family is that of columbite–tantalite minerals (AB_2O_6, with $A = Fe^{2+}$, Mn^{2+}, Mg^{2+} and $B = Nb^{5+}$, Ta^{5+}), but many other niobium- and tantalum-bearing groups exist, such as pyrochlores (pyrochlore, microlite, and betafite), fergusonites, euxenites (euxenite-(Y), tanteuxenite-(Y), and polycrase), aeschynites (aeschynite-(Y,Ce,Nd), nioboaeschynite-(Ce),

tantalaeschynite-(Ce), vigezzite-(Ce), and rynersonite), and others. On the other hand, contrary to the natural occurrence of the orthorhombic alumotantite, $AlTaO_4$ (Voloshin et al. 1981; Ercit et al. 1992), only synthetic materials are reported for niobium compounds with the same stoichiometry, therefore a niobium isomorph of $AlTaO_4$ does not occur in nature, to the best of our knowledge.

From the overview on the $M^{3+}Nb^{5+}O_4$ structures proposed at the begin of this section emerges that, even at room conditions, the chemical nature of the metal cations M^{3+} strongly affects the octahedral connectivity, the cation ordering, and the crystal structure of these oxides.

In order to better understand and disclose the substitution mechanisms, the cationic ordering among octahedral sites, the structural stability, and therefore the phase transition processes for $M^{3+}Nb^{5+}O_4$ compounds, a series of synthetic samples along the $AlNbO_4$–$(Al_{0.5}Cr_{0.5})NbO_4$ join were synthesized and investigated by means of a X-ray powder diffraction (XRPD) and electronic absorption spectroscopy (EAS) combined approach.

The rationale in focusing on the $(Al_{1-x}Cr_x)^{3+}Nb^{5+}O_4$ join and its aluminum end-member was threefold: i) we seek to understand the lack of natural $AlNbO_4$, in contrast with the occurrence of mineral alumotantite, $AlTaO_4$, in spite of the strong geochemical affinity between niobium and tantalum; ii) we aim to clarify the cation order-disorder scheme in $AlNbO_4$, being the only structure among the $M^{3+}Nb^{5+}O_4$ compounds with contrasting ordering models reported in the literature; iii) this study is also devoted to assess the degree of structural relaxation around Cr^{3+} by determining the relaxation coefficient, ε, in the range of chromium for aluminum substitution where the alumoniobite structure maintains the same symmetry. The latter topic has recently attracted much attention. In particular, the response of oxide structures to Cr^{3+} replacing Al has been investigated by combining spectroscopy (local structure) and diffraction (long range structure) method. Results from the present study will be compared with those of previous works on the corundum–eskolaite solid solution *ss* (Neuhaus and Richartz 1958; Schmitz-DuMont and Reinen 1959; Poole and Itzel 1963), grossular–uvarovite (Andrut and Wildner 2001; Langer et al. 2004) garnets *ss*, spinel–magnesiochromite (Reinen 1969; Hålenius et al. 2010) spinels *ss*, and $YAlO_3$–$YCrO_3$ perovskites *ss* (Cruciani et al. 2009).

► ***Experimental*** − [*for the experimental details (including: sample preparation, powder diffraction measurements and structural refinements, and optical spectroscopy) readers are requested to refer to chapter* ***2***].

The preferred orientation effect, caused by the relatively large particle size of powder sample, was corrected by applying a 4 order spherical harmonics. The results from structural refinement of the aluminum end-member, $AlNbO_4$, are in excellent agreement with those obtained from the previous study by Greis et al. (1996). Quantitative phase analysis, agreement factors and refinement details, and unit cell parameters are listed in Table C1, while the Rietveld refinement plot of the sample N50 is reported in Figure C1.

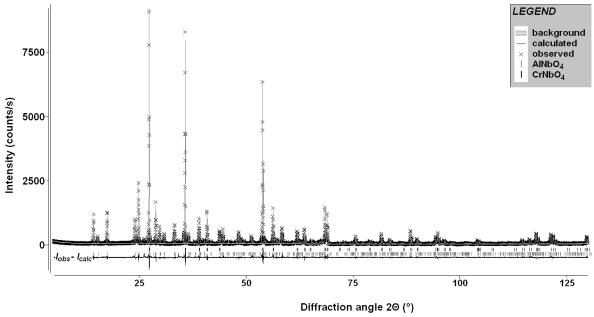

Figure C1. Rietveld plot of the powder diffraction pattern for sample N50. Both $AlNbO_4$ (s.g. *C*2/*m*) and $CrNbO_4$ (s.g. $P4_2/mnm$) occur in this sample with a phase fraction of 35.7 and 64.3%, respectively (see Table C1). The experimental data are indicated by crosses, the calculated pattern is the continuous line, and the lower curve is the weighted difference between the calculated and observed pattern intensities. Vertical ticks mark the position of reflections for the two phases.

Table C1. Quantitative phase analysis, agreement factors and refinement details, and unit cell parameters with their standard deviations (in parentheses).

Sample label	**N00**	**N06**	**N12**	**N25**		**N37**		**N50**	
Nominal chromium content (x_{Cr})	0.00	0.06	0.125	0.25		0.375		0.50	
Phases s.g.	*C*2/*m*	*C*2/*m*	*C*2/*m*	*C*2/*m*	$P4_2/mnm$	*C*2/*m*	$P4_2/mnm$	*C*2/*m*	$P4_2/mnm$
Phase fraction	100.00	100.00	100.00	94.97(3)	5.03(20)	77.09(11)	22.91(21)	35.73(24)	64.27(71)
Agreement factors and refinement details									
R_{wp}	0.1238	0.1122	0.1107	0.1201		0.1286		0.1268	
R_p	0.0918	0.0852	0.0833	0.0893		0.0958		0.0934	
No. of data	6250	6250	6250	6250		6250		6250	
No. of variables	54	54	54	76		76		76	
$R(F)$	0.0392	0.0321	0.0259	0.0324	–	0.0283	–	–	0.0236
$R(F^2)$	0.0644	0.0529	0.0449	0.0559	–	0.0530	–	–	0.0406
No. of reflections	562	564	565	569	81	569	81	569	81
Unit cell parameters									
a (Å)	12.1545(1)	12.1620(1)	12.1724(2)	12.1881(1)	–	12.1886(2)	–	12.1870(2)	4.6235(1)
b (Å)	3.7350(1)	3.7454(1)	3.7550(1)	3.7726(1)	–	3.7748(1)	–	3.7731(1)	4.6235(1)
c (Å)	6.4884(1)	6.4910(1)	6.4957(1)	6.5033(1)	–	6.5033(1)	–	6.5026(1)	2.9958(1)
β (°)	107.62(1)	107.64(1)	107.67(1)	107.70(1)	–	107.72(1)	–	107.69(1)	–
V (Å^3)	280.73(1)	281.77(1)	282.90(1)	284.88(1)	–	284.96(1)	–	284.86(1)	64.04(1)

► *Discussion of results*

● *XRD - Properties of the* $Al_{1-x}Cr_xO_4$ *join* – In our synthesis conditions, the only phases occurring along the $Al_{1-x}Cr_xNbO_4$ join have the monoclinic $AlNbO_4$- and the tetragonal rutile-type structures. The amount of these phases, reported in Table C1, varies as a function of the nominal chromium content (x_{Cr}) with an estimated phase fraction ratio $AlNbO_4/CrNbO_4 = 1$ for a sample with $x_{Cr} = 0.45$. Up to a nominal chromium amount of 0.125 a.p.f.u. the samples are monophasic with an $AlNbO_4$-type structure (i.e. samples N00, N06 and N12), whereas the samples become biphasic (composed with both $AlNbO_4$- and $CrNbO_4$-type structures) for a greater amount of the transition metal ion, $x_{Cr} > 0.125$ (i.e. samples N25, N37, and N50). Samples exclusively composed by a rutile-type structure are estimated for a $x_{Cr} > 0.75$. This phase fractions trend provides at least a first and clear indication on the incomplete solid-solution between $(Al,Cr)NbO_4$ oxides.

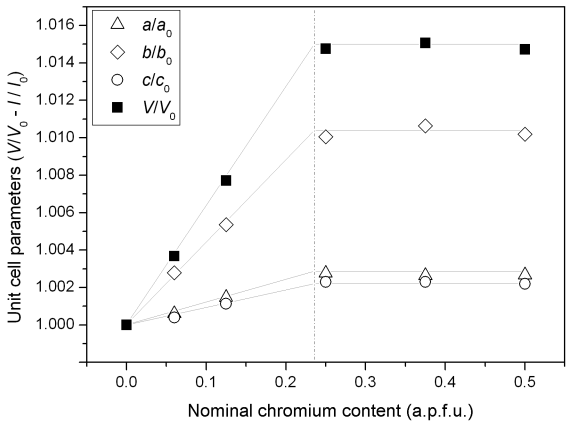

Figure C2. Normalized unit cell volume (V/V_0: black squares) and lattice parameters (a/a_0: triangles; b/b_0: diamonds; c/c_0: circles) of alumoniobitic compounds along the join $Al_{1-x}Cr_xO_4$ as a function of nominal chromium content.

● *XRD - Unit cell parameters* – The lattice parameters a, b, c, β, and the unit cell volume V, for the monoclinic structure along the $Al_{1-x}Cr_xO_4$ join are listed in Table C1. The normalized unit-cell axes and volume, plotted in Figure C2, show a linear increase as a function of substitution of the larger Cr^{3+} cation in the octahedral sites (ionic radius 0.615 Å; Shannon 1976) for the smaller Al^{3+} cation (0.535 Å), until all parameters become constant with a chromium content greater than ~0.24 a.p.f.u. (grey lines on Figure C2). This lattice expansion limit can be ascribed to the maximum chromium fraction that a $AlNbO_4$-type structure can accept. The anisotropic variation of cell parameters due to the replacement of Al by Cr can be also observed in Figure C2. In fact, the *b*-axis grows about 5 times faster than the *a*- and *c*-axis, respectively. Noteworthy, a similar but reversed anisotropic behavior has been found by Tabero (2007) for the lattice thermal expansion of the $AlNbO_4$ end-member. In this case the minimal and maximal thermal expansion along the *b*- and *c*-axis, respectively, can be understood considering the different

ratio of shared to unshared O–O edges in the different directions and the smaller expansion of the shared compared to the unshared edges. A similar effect was invoked by Burdett *et al*. (1987) to explain the thermal anisotropic behavior of anatase and rutile structures in which the coordination environment of the octahedral cations is largely controlled by the O–O repulsive forces, partially balancing the attractive Ti–O forces.

● *XRD - Cation ordering model* – As mentioned in the introduction section, $AlNbO_4$ can be described as a mixed oxide structure with partially ordered distribution of Al and Nb over the two non-equivalent octahedral sites. In order to identify the most accurate partition model for the Cr^{3+} ion along the join $Al_{1-x}Cr_xNbO_4$, the cation ordering scheme was assessed first for the $AlNbO_4$ end member (sample N00) by three different methods.

Following a first approach, the atomic occupancy fractions of aluminum and niobium were refined till convergence, under constraints $Al_{M1} + Al_{M2} = Nb_{M2} + Nb_{M1} = 1$ and $Al_{M1} = Nb_{M2}$, along with cell parameters, atomic coordinates, and atomic displacement parameters in the Rietveld refinement of sample N00. The resulting octahedral *M*1 aluminum fraction obtained from this refinement was very close to 0.80 a.p.f.u. Due to the strong correlation between the atomic displacement parameters and the occupancy fractions of the *M*1 and *M*2 octahedral sites, a further check was made. A sequence of Rietveld refinements, with fixed degree of octahedral cationic order, were performed according to the scheme $^{[M1]}(Al_{1-x}Nb_x)^{[M2]}(Al_xNb_{1-x})O_4$, where x was varied from 0.5 to 0.

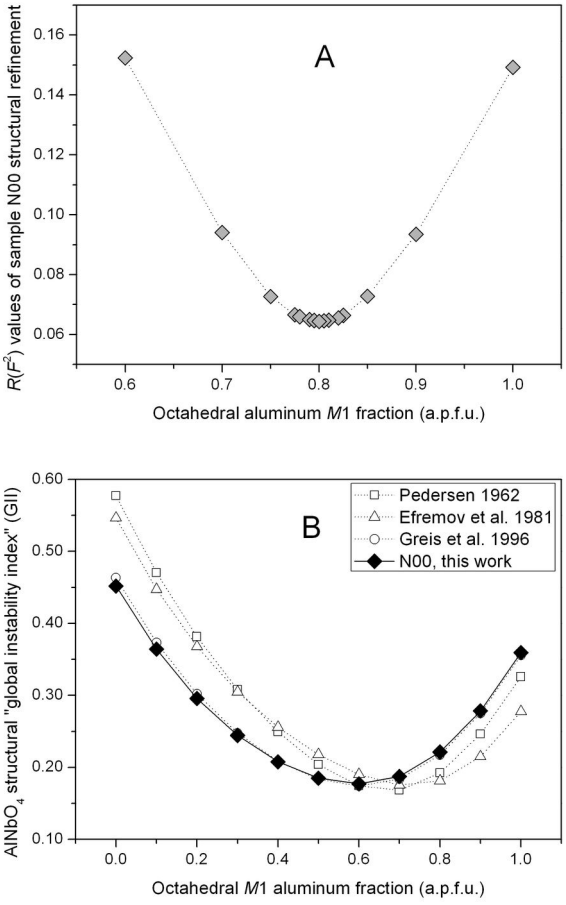

Figure C3. Octahedral *M*1 aluminum fraction against Rietveld refinement $R(F^2)$ agreement factor, (A), and "global instability index", *GII*, for the undoped $AlNbO_4$ structures (B). See legend for reference details.

In Figure C3A the $R(F^2)$ factors, achieved after each structural refinement, are plotted against the fraction of aluminum in the *M*1 octahedral site (Al_{M1}). The best agreement factors were found in the $0.75 \leq Al_{M1} \leq 0.85$ a.p.f.u. range, centered around $Al_{M1} = 0.80$ a.p.f.u., in agreement with the result from occupancy refinement. These findings also confirm the ordering models previously suggested by other authors (Efremov et al. 1981; Greis et al. 1996).

A third approach in order to assess the most reliable cation ordering scheme for the $AlNbO_4$ end-member was performed by calculating the lattice strain through the bond valence method. The bond valence calculations were carried out by using the equation

$$s_{ij} = \exp\left(\frac{R_0 - R_{ij}}{B}\right) \tag{C1}$$

where s_{ij} is the bond valence, R_{ij} the experimental cation-anion bond length, R_0 the characteristic bond valance parameter for the cation-anion pair, and *B* an empirical parameter with a constant value of 0.37 (Brown 2002). The root mean square of the bond valence sum deviations for all the atoms present in the asymmetric unit is defined by Salinas-Sanchez et al. (1992) as "the global instability index", *GII*. The *GII* values, expressed as valence units, v.u., compare the calculated bond valences and the formal valence (V_i) for all the species (*N*), suggesting the degree of structural strain [Eq. (C2)].

$$GII = \sqrt{\sum_{i=1}^{N}\left[\left(\sum_j s_{ij} - V_i\right)^2 \cdot N^{-1}\right]} \tag{C2}$$

Values of the *GII* less than 0.05 v.u. imply unstrained structures, while values greater than ~0.20 v.u. suggest that structures become strained (Salinas-Sanchez et al. 1992; Brown 2002). In Figure 3B are plotted the *GII* values obtained by varying the Al/Nb ratio in the octahedral sites for the structure refined with an initial cationic fraction $Al_{M1} = 0.80$, and for other structures taken from the literature for comparison (see the Figure C3B legend for the reference details). All structures show similar trends with a minimal value of *GII* between

0.60 and 0.70 a.p.f.u. of octahedral *M*1 aluminum fraction. It is noteworthy that the range of minimal values of *GII* for each structure model occurs around the limit of 0.20 v.u. above which the structure is considered strained. As a double check, a structural refinement was performed by fixing the aluminum fraction at *M*1 to 0.60 a.p.f.u. (i.e. $Al_{0.6}Nb_{0.4}O_6$ and $Al_{0.4}Nb_{0.6}O_6$ for *M*1 and *M*2, respectively). Both the refinement agreement factor (i.e. $R(F^2)$ = 0.152) and the *GII* (0.51 v.u.) indicate that the structure with such a cationic ordering is highly implausible.

Therefore, considering that the Al_{M1} range which corresponds to the minimal *GII* values is far from what found in our Rietveld refinements and the literature, this can be taken as a sign of structural instability possibly explaining why $AlNbO_4$ does not occur as a mineral in contrast to the geochemically related $AlTaO_4$. To check for this possibility the *GII* values were also calculated for both the orthorhombic and tetragonal models reported for the natural (Voloshin et al. 1981; Ercit et al. 1992) and synthetic (Jasper-Tönnies and Müller-Buschbaum 1983) forms of $AlTaO_4$, respectively. Surprisingly enough, both orthorhombic and tetragonal alumotantite exhibit high *GII* values (0.25 and 0.23, respectively), comparable to those found in $AlNbO_4$. This led us to conclude that the *GII* approach is not a suitable approach to model the charge distribution in $Al(Nb,Ta)O_4$ phases. In order to gain further insights on the structure instability issue, the effective coordination number (*ECoN*) was calculated for the octahedral cation sites in both $(Al,Cr)NbO_4$ and $AlTaO_4$. The effective cation coordination, as defined in *ECoN*, is estimated on the basis of a bond-valence like "bond weight" instead of using an arbitrary cut-off on the cation-ligand bond distances (Hoppe 1979; Hoppe et al. 1989). Table C2 shows that the *ECoN*s of *M*1 and *M*2 sites in $(Al,Cr)NbO_4$ are are much lower than expected with regard to the nominal coordination for an ideal octahedra (i.e. C.N. = 6). In particular, the *ECoN*s of *M*1 and *M*2 sites in $AlNbO_4$ (sample N00) are equal to ~5.1 and ~3.9, respectively. At variance with $AlNbO_4$, the *ECoN*s calculated for both structure models of $AlTaO_4$ are very close to the ideal values (6.00 for *M* in the tetragonal structure; 5.73 and 5.94 for *M*1 and *M*2, respectively, in the orthorhombic structure). This comparison confirms that the cation bonding situation is indeed much more unfavorable in $AlNbO_4$ compared to $AlTaO_4$. From the previous considerations emerge that the deficiency of a $AlNbO_4$ natural occurrence is ascribable to its particularly strained structure.

● *XRD - M1 and M2 octahedra as a function of* Cr → Al *substitution* – The refined metal-oxygen bond distances, M_i–O, polyhedral volumes, MO_6, bond length distortions, are listed in Table C2 along with the effective coordination numbers for both the *M*1 and *M*2 octahedra as a function of Cr → Al substitution.

Table C2. Metal-oxygen bond distances, polyhedral volumes, bond length distortions, and effective coordination numbers for the MO_6 octahedra of the AlNbO4-type structure along the $Al_{1-x}Cr_xO_4$ join. The standard deviations are reported in parentheses.

Sample label	**N00**	**N06**	**N12**	**N25**	**N37**
Octahedral M1O₆ chromium fraction (a.p.f.u.)					
	0.00	0.00	0.00	0.04	0.04
Octahedral metal-oxygen bond distances, *M*1–O (Å)					
*M*1–O1	1.806(6)	1.787(6)	1.807(6)	1.850(7)	1.869(9)
*M*1–O2	1.832(6)	1.849(6)	1.851(6)	1.869(7)	1.879(9)
*M*1–O3	2.046(6)	2.042(6)	2.018(6)	2.019(6)	2.021(8)
*M*1–O4	2.121(5)	2.122(5)	2.117(6)	2.089(6)	2.090(8)
*M*1–O4'	1.947(2)	1.943(2)	1.944(2)	1.945(2)	1.939(2)
*M*1–O4'	1.947(2)	1.943(2)	1.944(2)	1.945(2)	1.939(2)
⟨*M*1–O⟩	1.950(5)	1.948(5)	1.947(5)	1.953(5)	1.956(7)
V_{M1}(Å³)	9.42(4)	9.44(4)	9.46(5)	9.60(5)	9.69(6)
BLD (*M*1)	4.57(6)	4.60(6)	4.13(6)	3.45(7)	3.39(8)
ECoN (*M*1)	5.13	5.07	5.26	5.56	5.63
Octahedral M2O₆ chromium fraction (a.p.f.u.)					
	0.00	0.06	0.125	0.20	0.20
Octahedral metal-oxygen bond distances, *M*2–O (Å)					
*M*2–O1	1.726(6)	1.755(6)	1.751(6)	1.743(7)	1.731(9)
*M*2–O2	2.283(6)	2.260(5)	2.275(6)	2.281(6)	2.274(7)
*M*2–O2'	1.841(6)	1.858(5)	1.859(6)	1.854(6)	1.851(8)
*M*2–O3	1.942(2)	1.941(2)	1.951(2)	1.957(2)	1.954(2)
*M*2–O3	1.942(2)	1.941(2)	1.951(2)	1.957(2)	1.954(2)
*M*2–O4	2.185(5)	2.178(5)	2.172(6)	2.175(6)	2.194(8)
⟨*M*2–O⟩	1.987(5)	1.989(4)	1.993(5)	1.995(5)	1.993(7)
V_{M2}(Å³)	9.61(4)	9.67(4)	9.72(4)	9.76(5)	9.75(6)
BLD (*M*2)	8.31(6)	7.72(5)	7.70(6)	7.80(6)	8.06(8)
ECoN (*M*2)	3.85	4.14	4.07	3.97	3.83

Notes: *The octahedral bond length distortion (BLD) and the effective coordination number (ECoN) are calculated as previously defined in the fifth paragraph of the second chapter,* ***2.5****.*

Based on the previous assessment of the cation ordering scheme and on the preliminary analysis of bond distance variations, the chromium partitioning model over the two non-equivalent octahedral sites as reported in Table C2 was assumed in the final Rietveld refinements. More in detail, chromium was found to first replace aluminum in the larger *M*2 site until the limit for Al–Cr substitution in *M*2 (i.e. x_{Cr} = 0.20 a.p.f.u.), and then being further incorporated into the smaller *M*1 site, till the maximum nominal chromium content that the $AlNbO_4$ structure can accept (i.e. x_{Cr} = 0.24 a.p.f.u.) was reached.

Both the mean metal–oxygen bond distances and the octahedral volumes, across the $AlNbO_4$–$(Al_{0.5}Cr_{0.5})NbO_4$ join, well describe the chromium incorporation at the octahedral sites.

The relation between the mean ⟨*M*–O⟩ metal-oxygen distances for both *M*1 and *M*2 sites and the chromium site partitioning is displayed in Figure C4 to illustrate this behavior. Data sets evolution can be subdivided in two trends. Till a nominal chromium amount of 0.20 a.p.f.u., only the *M*2 site incorporates the transition metal ion whereas the *M*1 site is not involved. According to the different ionic radii of Al^{3+} and Cr^{3+}, that causes a linear expansion of the ⟨*M*2–O⟩ bond lengths as a function of the chromium increase, while the *M*1 site maintains the same metal-oxygen distances (within the standard deviation) or shows a slight contraction. For samples doped with higher percentage of chromium (from 0.20 up to 0.24 a.p.f.u.), both the data trends are constants with ⟨*M*2–O⟩ bond lengths characterized by lengthened distances compared to those observed before 0.20 a.p.f.u. From the *ECoN* variation in Table C2, it is clear that the Cr → Al substitution does not improve significantly the unfavorable bonding condition of the octahedral site in (Al,Cr)NbO_4 phases.

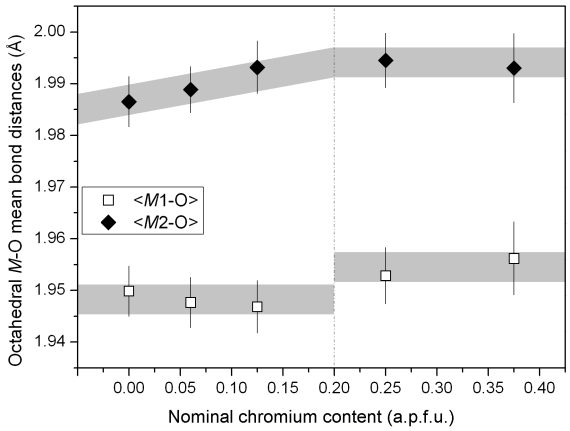

Figure C4. Octahedral ⟨*M*–O⟩ mean metal-oxygen bond distances vs. nominal chromium amount of $Al_{1-x}Cr_xNbO_4$.

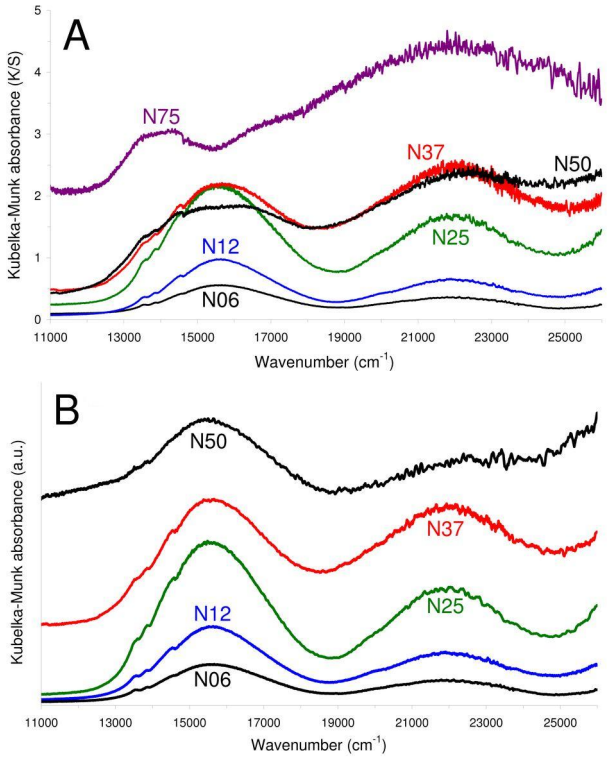

Figure C5. Diffuse reflectance spectra along the (Al,Cr)NbO_4 join: A) raw spectra; B) spectra where the contribution from the $CrNbO_4$ phase was subtracted.

● *Optical spectroscopy* – Electronic absorption spectra change in a complex way along the $AlNbO_4$–$CrNbO_4$ join (Figure C5A) due to multiple contributions from Cr^{3+} in different octahedral sites, involving d-d electronic transitions (Tanabe and Sugano 1954; Marfunin 1979; Lever 1984; Burns 1993; Andrut et al. 2004; Wildner et al. 2004). From the structural analysis, chromium is expected to be accommodated at both the octahedral sites of the $AlNbO_4$ lattice and at the strongly disordered octahedron of the rutile-type $CrNbO_4$ phase (Matteucci et al. 2006; Dondi et al. 2006). Once the contribution from such rutile-type phase was removed by subtraction, the typical spectral features of Cr^{3+} appeared all along the half join (Figure C5B). The most intense bands stem from the parity-forbidden and spin-allowed transitions from the ground level $^4A_{2g}(^4F)$ to $^4T_{2g}(^4F)$ at ~15700 cm^{-1} and to $^4T_{1g}(^4F)$ at ~21900 cm^{-1}. The parity-forbidden and spin-forbidden transitions $^2E_g(^2G)\leftarrow{}^4A_{2g}(^4F)$, $^2T_{1g}(^2G)\leftarrow$ and $^2T_{2g}(^2G)\leftarrow$ are responsible for minor bands observed at approximately 13600 cm^{-1}, 14400 cm^{-1} and 19800 cm^{-1}, respectively. The ^2E_g transition is split into two bands ($\bar{E}$ and $2\bar{A}$) due to spin-orbit coupling effect (Milos et al. 2008) enhanced by the strong distortion of site *M*2 where chromium is accommodated (Figure C6A). The deconvolution, based on the bands of Cr^{3+} at site *M*2 only, was not fully satisfactory; by introducing further contributions – centered at ~17000 and ~23000 cm^{-1}, respectively – the fitting was improved from $\chi^2=2.5\times10^{-3}$ to $\chi^2=1.4\times10^{-4}$ (N25). These additional bands are coherent with the $^4T_{2g}\leftarrow{}^4A_{2g}$ and $^4T_{1g}\leftarrow{}^4A_{2g}$ transitions of Cr^{3+} at site *M*1, in agreement with structural data for samples N25, N37 and N50 (Figure C6B). The energy and width of optical bands, as obtained by deconvolution, are listed in Table C3, together with crystal field strength and Racah *B* parameters, calculated for both

*M*1 and *M*2 sites. The optical spectrum of sample N50, after subtraction, has a low quality: good enough to reliably evaluate the value of 10*Dq*, but insufficient to get out further parameters, which were just estimated.

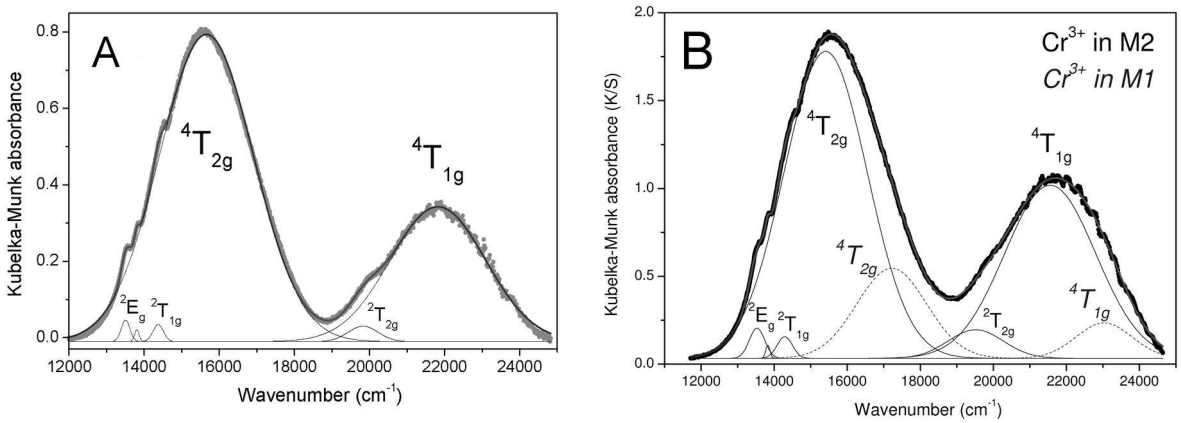

Figure C6. Example of deconvolution of DRS spectra for (A) sample N12 (Cr^{3+} at site *M*2) and (B) sample N25 (Cr^{3+} at both *M*1 and *M*2).

The energy of spin-allowed transitions, related to Cr^{3+} at site *M*2, is gradually lowering along the $AlNbO_4$–$CrNbO_4$ join from N06 to N25, then it keeps constant to N50, within the experimental error. This trend indicates a progressive decrease of the crystal field strength for the *M*2 site while for the *M*1 site no significant change occurs. On the other hand, the Racah parameters fluctuate in rather narrow ranges ($613 < B_{35} < 628$ cm^{-1}, $654 < B_{55} < 669$ cm^{-1}) and the trend of nephelauxetic ratios implies no significant change in the degree of covalency and polarization of the Cr–O bond (Table C3). The decreasing values of 10*Dq* for the site *M*2 suggest an elongation of the local Cr–O distance due to the increasing occupancy of Cr^{3+} till saturation occurs at about 0.20 a.p.f.u., fitting well the structural data on the long-range ⟨*M*2–O⟩ distance. The difference of crystal field strength between the *M*2 and *M*1 sites (1541 *vs.* 1720 cm^{-1}, respectively, for sample N25) is consistent with the different average M–O distance (1.995 Å for *M*2 *vs.* 1.953 Å for *M*1).

Optical data of the $AlNbO_4$–$CrNbO_4$ join can be compared with those of well studied joins, where chromium replaces aluminum in sixfold coordination (Figure C8): corundum–eskolaite (Neuhaus and Richartz 1958; Schmitz-DuMont and Reinen 1959; Poole and Itzel 1963), grossular–uvarovite (Andrut and Wildner 2001; Langer et al. 2004), spinel–magnesiochromite (Reinen 1969; Hålenius et al. 2010), and $YAlO_3$–$YCrO_3$ perovskite (Cruciani et al. 2009). The Racah B_{35} values of both sites of the $AlNbO_4$ structure fluctuate in the common field of variation for Cr-bearing minerals, implying a similar degree of covalency of the Cr–O bond. Only the value for *M*1 in N25 is an outlier, but it suffers from a noticeable uncertainty.

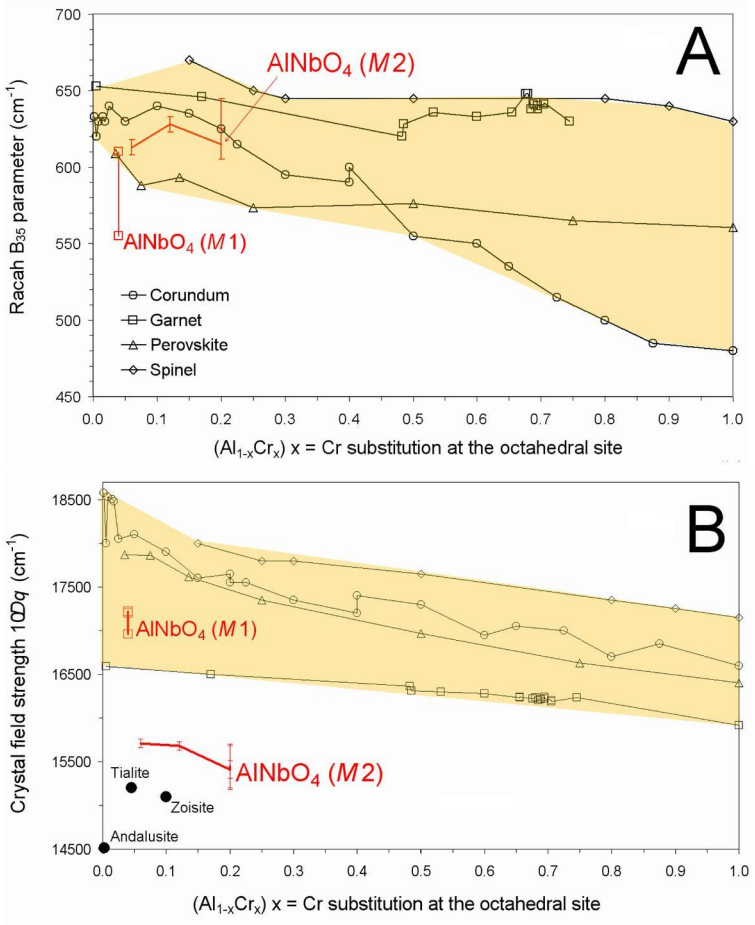

Figure C7. Trends of optical parameters vs nominal chromium amount in various structures with (Al,Cr) substitution in octahedral coordination. (A) Racah B_{35} parameter, (B) Crystal field strength. The color field is that of common variation of optical data.

In the case of crystal field strength, while values of site *M*1 fall within the usual variation range, the site *M*2 exhibits a remarkably low 10*Dq*. Similar values are not exceptional, as in the literature a 10*Dq* around 15500 cm^{-1} is recorded for diopside and enstatite (Burns 1993), i.e. the largest octahedral sites where Cr^{3+} is accommodated in substitution of Mg ion (with long-range *M*–O distance of about 2.08 Å). Interestingly, there is another class of structures with such anomalous low 10*Dq* values, where chromium is after aluminum at octahedra with small to intermediate long-range *M*–O distances. These structures, having strongly distorted octahedral sites, exhibit crystal field strength as low as 14300 cm^{-1} for andalusite (Carlson and

Rossman 1988), 15100 cm^{-1} for zoisite (Schmetzer and Berdesinski 1978) and 15200 cm^{-1} for "tialite" (Dondi et al. 2009).

Table C3. Diffuse reflectance data of Cr^{3+} in different octahedral sites in the $AlNbO_4$ and $CrNbO_4$ structures. Experimental band energy (peak, cm^{-1}), band width (FWHM, cm^{-1}), crystal field strength (10*Dq*), Racah B_{35}, B_{55} and *C* parameters, and nephelauxetic ratios β_{35} and β_{55}.

Sample Label	N06	N12	N25	N37	N50
***M*2 site**					
Cr^{3+} molar fraction	0.06	0.125	0.20	0.20	0.20
$^4T_{2g}$ (peak, cm^{-1})	15710	15680	15410	15450	15430
$^4T_{2g}$ (FWHM, cm^{-1})	3170	3200	2690	2640	2860
$^4T_{1g}$ (peak, cm^{-1})	21875	21960	21560	21680	*(21940)*
$^4T_{1g}$ (FWHM, cm^{-1})	4420	4640	2930	2420	*(3000)*
$^2E_g(\bar{E})$ (peak, cm^{-1})	13510	13490	13490	13510	13480
$^2E_g(\bar{E})$ (FWHM, cm^{-1})	190	230	300	410	430
$^2E_g(2\bar{A})$ (peak, cm^{-1})	13800	13785	13790	13715	13815
$^2E_g(2\bar{A})$ (FWHM, cm^{-1})	170	190	190	320	*n.d.*
$^2T_{1g}$ (peak, cm^{-1})	14375	14370	14380	14380	14375
$^2T_{1g}$ (FWHM, cm^{-1})	340	280	280	300	330
$^2T_{2g}$ (peak, cm^{-1})	19905	19880	19830	19730	19725
$^2T_{2g}$ (FWHM, cm^{-1})	470	400	460	740	850
Crystal field strength (10*Dq*, cm^{-1})	15710	15680	15410	15450	15430
Racah B_{35} (cm^{-1})	613	628	615	625	*(664)*
Nephelauxetic ratio β_{35} (adim.)	0.67	0.68	0.67	0.68	*(0.72)*
Racah B_{55} (cm^{-1})	665	664	669	667	654
Nephelauxetic ratio β_{55} (adim.)	0.72	0.72	0.73	0.73	0.71
Racah *C* (cm^{-1})	2977	2973	2967	3004	3023
***M*1 site**					
Cr^{3+} molar fraction			0.04	0.04	0.04
$^4T_{2g}$ (peak, cm^{-1})			17220	16960	17200
$^4T_{2g}$ (FWHM, cm^{-1})			2250	1580	1750
$^4T_{1g}$ (peak, cm^{-1})			23030	23210	*(23760)*
$^4T_{1g}$ (FWHM, cm^{-1})			1800	2100	*(1930)*
Crystal field strength (10*Dq*, cm^{-1})			17220	16960	17200
Racah B_{35} (cm^{-1})			555	610	*(646)*
Nephelauxetic ratio β_{35} (adim.)			0.60	0.66	*(0.70)*

Notes: *M*1 and *M*2 = octahedral sites in the $AlNbO_4$ lattice. *n.d.* = not determined.

According to the Crystal Field Theory (Burns 1993) such a low 10*Dq* indicates a long local Cr–O distance, coherent with, *e.g.*, the octahedral sites in pyroxenes or the 6-fold coordinated interstitial sites in andalusite and tialite. In the case of $AlNbO_4$, the *M*2 site is large, as its ⟨*M*2–O⟩ ~2.01 Å is longer than in Cr end-terms, like eskolaite, uvarovite, magnesiochromite or $YCrO_3$, where the ⟨Cr–O⟩ is around 1.98 Å. This circumstance turns Al^{3+} and Cr^{3+} ions rather "underbonded", as confirmed by the effective coordination numbers.

● *Structural relaxation around Cr^{3+} ions* – The coefficient of structural relaxation ε along the $AlNbO_4$–$CrNbO_4$ join cannot be calculated following the conventional procedure (e.g. Langer 2001) because:

- the $AlNbO_4$ phase is not stable all along the join, so the reference for the Cr–O distance in the isostructural chromium end-term is lacking;
- the solubility of chromium in the $AlNbO_4$ lattice is limited to ~20% at site *M*2;
- the Al–Cr substitution is complicated by the occurrence of two octahedral sites, where a partial occupancy is by niobium.

In order to overcome these hindrances, the investigation was limited to the structural relaxation along the $AlNbO_4$–$Al_{0.5}Cr_{0.5}NbO_4$ half join (nominal composition, corresponding to $AlNbO_4$–$Al_{0.8}Cr_{0.2}NbO_4$ as Cr^{3+} solubility at site *M*2). In this interval, the relative variation of the long-range *M*–O distance (measured by XRD) is close to the relative change of the short-range Cr–O distance (measured by EAS). This circumstance suggests that the $AlNbO_4$ lattice has a limited propensity to relax as a consequence of the Cr–Al substitution. If the reference Cr–O distance was assumed as the *M*–O distance, as measured by XRD in the sample N37, it would be possible to estimate a coefficient of structural relaxation ε around chromium at site *M*2. By this way, ε results close to zero and the $AlNbO_4$ structure follows the Vegard's law (Figure C8A).

The explanation why no relaxation occurs – in contrast with the well known Al–Cr joins in garnets, spinels, perovskites and corundum (Figure C8B) – relates with the limited extent of solid solution and the fact that the $AlNbO_4$ structure is strongly constrained by other factors, like cation ordering and electrostatic charge balance. As a matter of fact, Al^{3+} is hosted in a strongly underbonded and strained site and, consequently, the Cr^{3+} replacing at the M2 site occurs without significant strain and the lattice does not need to relax around this bigger ion.

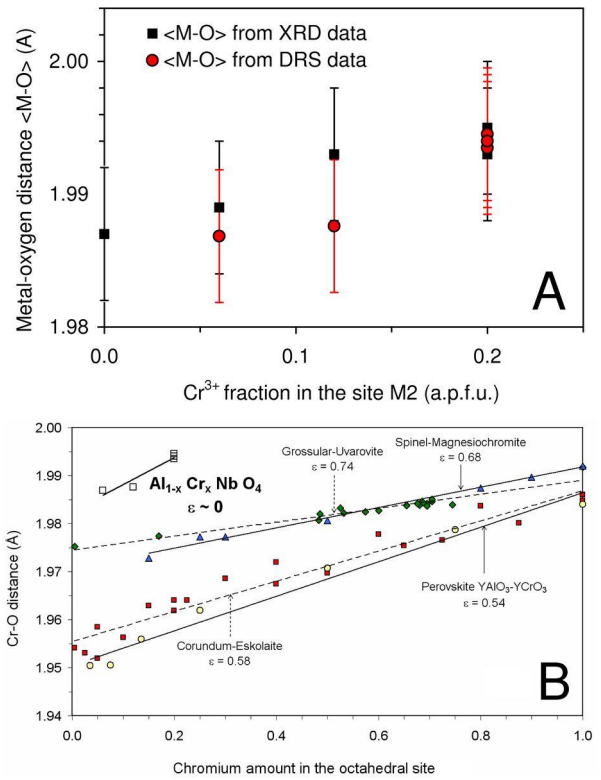

Figure C8. (A) Structural relaxation around Cr^{3+} at site *M*2 and (B) comparison with other Al–Cr joins in terms of coefficient of structural relaxation ε (see text for references).

We suggest that the role of O–O interactions recognized by Burdett *et al*. (1987) as controlling the octahedral cation bonding in oxygen closest packing ABAB structures like anatase and rutile is even stronger in the $AlNbO_4$ structure, where the competition between repulsive O–O forces and the attractive *M*–O forces introduce a cause of instability and make the local structure more rigid with regard to Cr for Al substitution.

3. SECTION II.

Structural relaxation around four-fold coordinated Co^{2+}: the case of the $Sr_2MgSi_2O_7$–$Ba_2MgSi_2O_7$ melilite solid solution

► ***Melilite-type*** − Minerals of the melilite group, having general formula $X_2T1T2_2A_7$ (where X is a large mono- to divalent cation: Na, Ca, Sr, Ba, …; $T1$ and $T2$ are small di- to tetravalent cations: $T1$ = Be, Mg, Al, Co, Zn, …; $T2$ = Al, Si, Ge, …; and A is an anion, frequently O, but also F or S), are typical constituents of ultramafic rocks, for instance alnöites and melilitites, and also occur in carbonaceous chondrites (Deer et al. 1986).

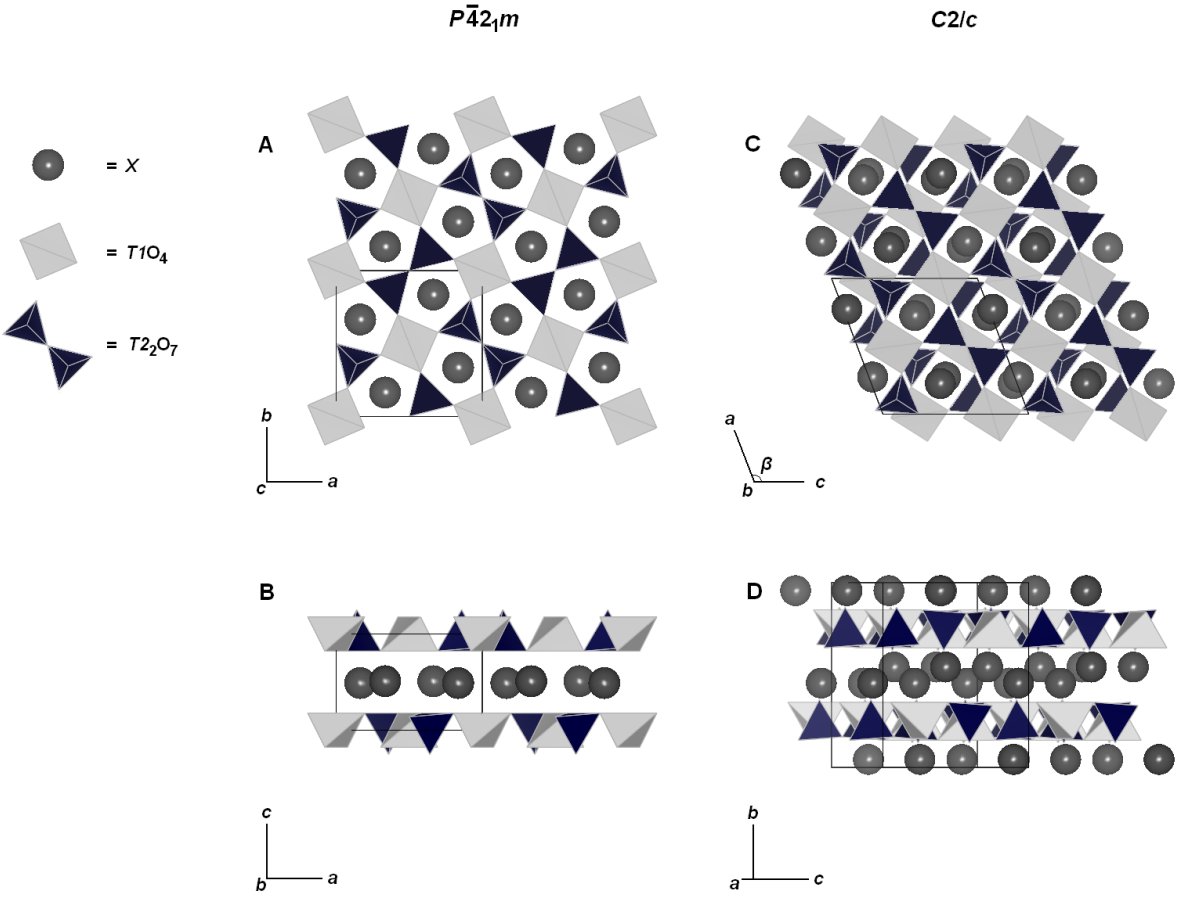

Figure 3.II.1. Polyhedral representations of the melilite-type structure (s.g. *P*-42$_1$*m*) - as viewed along the *c*-axis (A) or parallel to the *ab* plane (B) - and of the melilite-related structure (s.g. *C*2/*c*) - as viewed along the *b*-axis (C) or parallel to the *ac* plane (D).

The crystal structure of the minerals belonging to this group was solved for the first time by Warren (1930) in the *P*-42$_1$*m* space group, and described as sheets of linked tetrahedra ($T2_2O_7$

dimers and four-coordinated *T1* cations) connected together by *X* cations accommodated in a distorted eight-coordinated antiprismatic polyhedron (Figure 3.II.1 A and B).

Since the independent recognition by Hemingway et al. (1986) and Seifert et al. (1987) of a phase transition from an incommensurate phase (*IC*) to a normal structure (*N*) in åkermanite, many studies were devoted to the physical and chemical phenomena associated with displacively modulated phases. In 1990 Röthlisberger et al. pointed out that *IC* structure occurs in all $Ca_2T1Si_2O_7$ melilites (with *T1* = Mg, Mn, Fe, Co, Zn, and their solid solutions) but not in $Ca_2BeSi_2O_7$. It is generally accepted that an *IC* phase is an intermediate state between an unmodulated structure (*N*), typically the high-temperature phase, and a commensurate superstructure (so called "lock-in phase") at low-temperature (Yang et al. 1997).

► ***Melilite-related*** − Solved in 1984 by Malinovskii, the monoclinic $Ba_2CuSi_2O_7$ (s.g. *C*2/*c* and *Z* = 4) is the archetype form for $Ba_2T1Si_2O_7$ melilite-related compounds. Other silicates with this structure include $Ba_2CoSi_2O_7$ (Adams et al. 1996), $Ba_2ZnSi_2O_7$ (Kaiser and Jeitschko 2002), and $Ba_2MgSi_2O_7$ (Aitasalo et al. 2006). Although suggested as structures that should not crystallize with a tetragonal melilite-type structure (Rothlisberger et al. 1990), the above listed Mg, Co, and Cu melilite-related compounds were also solved in the $P\text{-}42_1m$ space group (*Z* = 2): $Ba_2MgSi_2O_7$ (Shimizu et al.1996), $Ba_2CoSi_2O_7$ (El Bali and Zavalij 2003), and $Ba_2CuSi_2O_7$ (Du et al. 2003) single crystals were successfully refined as melilite-type compounds.

Although with the same stoichiometry ($Ba_2T1Si_2O_7$), the monoclinic and tetragonal polymorphs exhibit substantial differences. Similarly to the extensively studied melilite-type structures, the monoclinic polymorphs consist of Si_2O_7 dimers connected by $T1O_4$ tetrahedra to form tetrahedral sheets parallel to the *ac* plane, instead of the *ab* plane in the $P2_1m$ structures (see Figure 3.II.1).

The first major difference concerns the coordination polyhedron of the barium cation, that in the tetragonal feature is a distorted square antiprism with "4 above + 4 below" ligands, whereas in the monoclinic form it is a bicapped trigonal prism with an alternated "5 + 3" and "3 + 5" ligands configuration (see Figure 3.II.2 A and B). However, as already pointed out by Armbruster et al. (1990) the main difference is in the arrangement of the tetrahedral sheet

topology (see Figure 3.II.2 C and D): there are only five-membered rings of tetrahedra in the tetragonal form, while four- and six-membered rings are present in the monoclinic structure. The change in the tetrahedral sheet arrangement promotes a new setting of the Si_2O_7 dimers laying in the same layer: in the melilite-type dimers are alternatively disposed along [110] and [-110], whereas in the melilite-related compounds all the dimers are arranged along [-101].

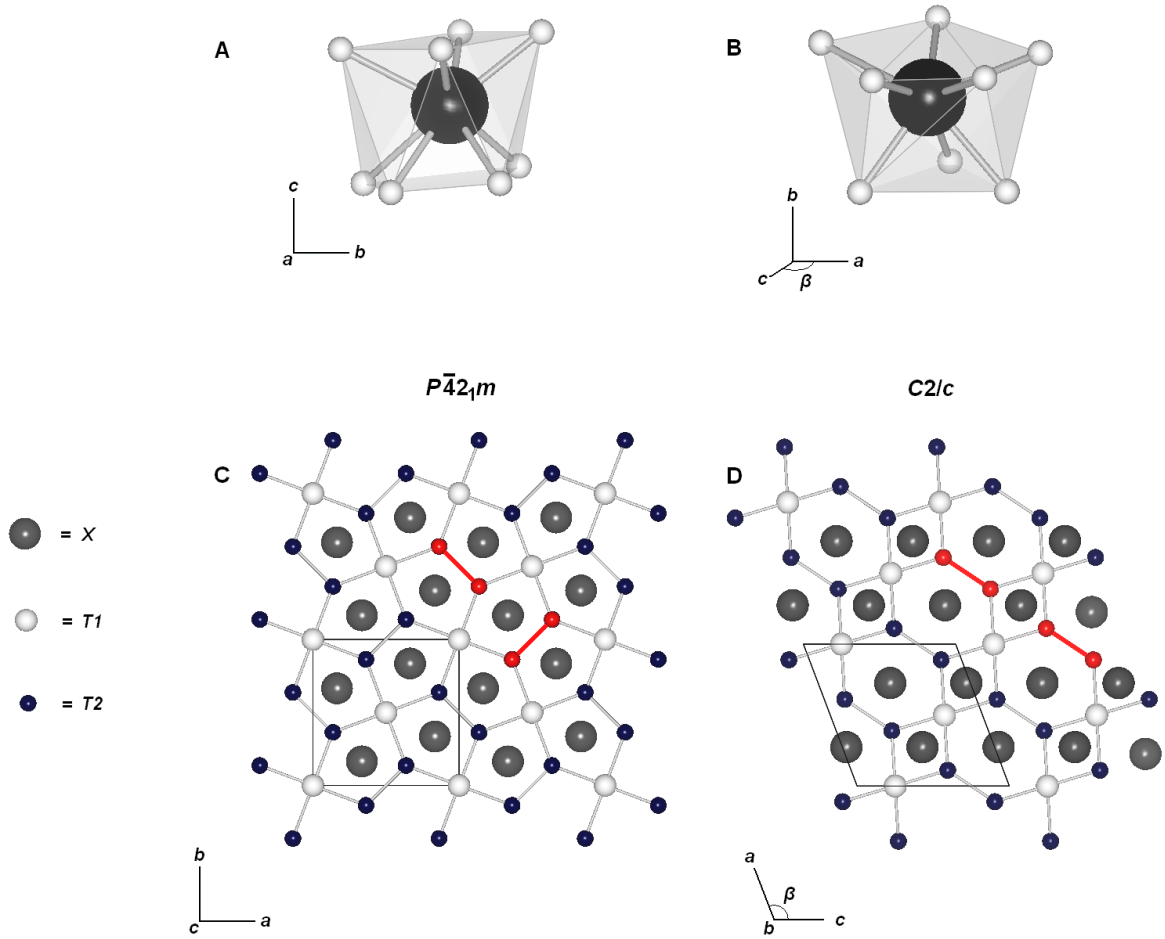

Figure 3.II.2. Eight-coordinated *X* cation in melilite-type (A) and melilite-related (B) compounds, and sheet topologies along [001] for the melilite-type structure (C) and along [010] for the melilite-related one (D). The different arrangements of the $T2_2O_7$ dimers for the two topologies are shown by highlighted *T2*–*T2* bonds.

3. Section II. D. ♦ Melilite-type and melilite-related compounds: structural variations along the join $Sr_{2-x}Ba_xMgSi_2O_7$, ($0 \leq x \leq 2$) and high-pressure behaviour of the two end-members

Note: This is a "*satellite*" study written in the 2011 by Ardit, M., Dondi, M., and Cruciani, G., reported as published (with few variations, if any, as described in the premise of this chapter) in the "*Physics and Chemistry of Minerals*, DOI 10.1007/s00269-011-0475-7".

Abstract

The structural variations along the solid solution $Sr_{2-x}Ba_xMgSi_2O_7$ ($0 \leq x \leq 2$), combined to the high pressure characterization of the two end-members, have been studied. A topological change from the tetragonal (melilite-type) to the monoclinic (melilite-related) structure along the join $Sr_2MgSi_2O_7$ (s.g. $P\text{-}42_1m$) – $Ba_2MgSi_2O_7$ (s.g. $C2/c$) occurs with a Ba content higher than 1.6 apfu. Favored in the crystallization from a melt, the tetragonal form has a tetrahedral sheet topology exclusively based on five-membered rings which provide a regular "4 up + 4 down" ligand arrangement. In contrast, the melilite-related structure, favored by solid-state reaction synthesis, is made by alternating six- and four-membered tetrahedral rings, that give an asymmetric arrangement of alternated "5 up + 3 down" and "3 up + 5 down" ligands around Sr or Ba. This latter configuration is characterized by an additional degree of freedom with Ba polyhedra hosted in the interlayer with a more irregular and compact coordination and longer Ba–O bond distances. Further insights into the relationships between the two melilite typologies were achieved by investigating the *in situ* high pressure behavior of these systems. The synchrotron high-pressure experiments allowed to calculate the elastic moduli for the Sr melilite-type end-member and for the Ba monoclinic polymorph ($Sr_2MgSi_2O_7$: K_{T0} = 107, $K_{a=b}$ = 121, and K_c = 84 GPa; m-$Ba_2MgSi_2O_7$: K_{T0} = 85, K_a = 96, K_b = 72, and K_c = 117 GPa) and compare them to those reported in the literature for åkermanite ($Ca_2MgSi_2O_7$). The results showed that, although the volume of Ba polyhedron in tetragonal polymorphs is larger than in the monoclinic forms, the interlayer compressibility is significantly lower in the former structures due to the occurrence of very short Ba–O distances. This unfavored Ba environment also makes tetragonal $Ba_2MgSi_2O_7$ a metastable phase at room conditions, possibly favored by high pressure. However, no phase transition occurs from monoclinic to tetragonal form due to kinetic hindrance in reconstructing the sheet topology.

► ***Introduction*** – The synthetic analogs of melilite structures have attracted considerable interest in different technological fields: e.g. ceramics (Dondi et al. 2011), glasses (Ochi, 2006), luminescent materials (Aitasalo et al. 2006), low-dimensional magnets (Adams et al. 1996), etc. Nevertheless, little attention has been paid to compounds having melilite stoichiometry, but reduced symmetry and, more important, different sheet topology [*see the general notes about these structures at the begin of this section*].

Although in the last decades many studies were dedicates to assess the behavior of these compounds, especially to interpret and solve the *IC* phase transition, very little effort has been devoted (with the exception of Armbruster et al. 1990) to solve the dichotomy among compounds with the same stoichiometry but with crystal structures based on different sheet topologies. Therefore, the first aim of this contribution is to provide a better understanding of the relationships among the $Ba_2TISi_2O_7$ polymorphs by means of a structural study along the join $Sr_{2-x}Ba_xMgSi_2O_7$, ($0 \leq x \leq 2$), where the two end-members have tetragonal melilite-type ($Sr_2MgSi_2O_7$) and monoclinic melilite-related ($Ba_2MgSi_2O_7$) features, respectively.

Furthermore, we report here the results of high-pressure X-ray diffraction experiments performed on the two end-members in order to explore the possible occurrence of phase transitions and investigate the difference in the elastic behavior of these compounds.

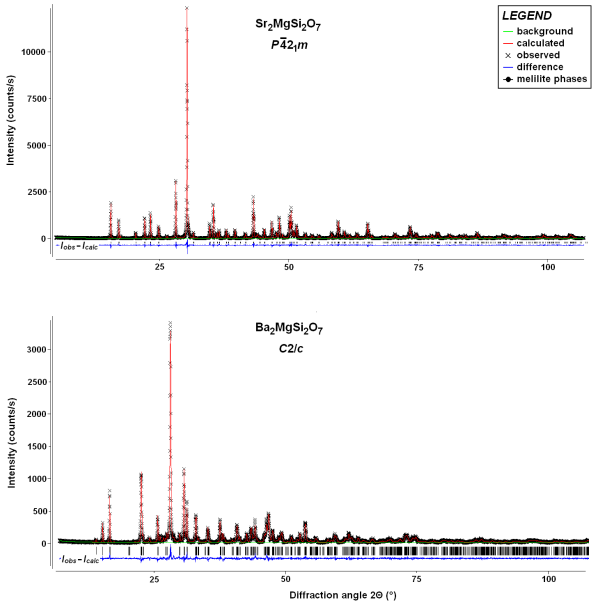

Figure D1. Final Rietveld fits for the $Sr_2MgSi_2O_7$ melilite-type (s.g. *P*-42$_1$*m*; top) and the $Ba_2MgSi_2O_7$ melilite-related (s.g. *C*2/*c*; bottom) samples. The experimental data are indicated by crosses (black), the calculated pattern is the continuous line (red) and the lower curve (blue) is the weighted difference between the calculated and observed patterns. Vertical ticks mark the position of reflections for melilite phases (black).

► ***Experimental procedures*** – [*for the experimental details (including: samples preparation, powder diffraction measurements at both ambient and high-pressure conditions, and Rietveld refinements strategy) readers are requested to refer to the chapter* ***2*** *of the present dissertation*].

During the refinements of the atomic coordinates, a soft constraint was applied to the Si–O distances with the constraint weight being progressively lowered until a minimal value. Quantitative phase analysis, agreement factors and refinement details, unit cell parameters, mean metal-oxygen bond distances, polyhedral volumes and mean interatomic angles are listed in Table D1, whereas final atomic coordinates, isotropic thermal parameters, and site fractions for samples along the $Sr_{2-x}Ba_xMgSi_2O_7$ ($0 \leq x \leq 2$) join are reported in Table D2. Furthermore, the Rietveld refinement plots of the two end-members are reported in Figure D1.

Table D1. Quantitative phase analysis, agreement factors and refinement details, unit cell parameters, mean metal-oxygen bond distances, polyhedral volumes. mean interatomic angles, and their standard deviations (within brackets) for the $Sr_{2-x}Ba_xMgSi_2O_7$ ($0 \leq x \leq 2$) samples.

Sample label	***Ba000***	***Ba100***	***Ba150***	***Ba160***	***Ba175***		***Ba200***	***Ba200****
Nominal Ba content $Sr_{2-x}Ba_xMgSi_2O_7$; *x* =	0.00	1.00	1.50	1.60	1.75		2.00	2.00
Main phases space group	*P*-42$_1$*m*	*P*-42$_1$*m*	*P*-42$_1$*m*	*P*-42$_1$*m*	*P*-42$_1$*m*	*C*2/*c*	*C*2/*c*	*P*-42$_1$*m*
Quantitative phase analysis								
Main phases:	94.70(1)	94.70(2)	95.40(1)	96.16(1)	63.52(9)	30.39(15)	95.34(1)	100.00
Other: $SrSiO_3$	5.30(8)	–	–	–	–		–	–
Sr_2SiO_4	–	5.30(21)	4.60(22)	3.84(26)	6.09(24)		–	–
$BaSiO_3$	–	–	–	–	–		4.66(10)	–
Effective Ba content (estimated from mass balance) $Sr_{2-x}Ba_xMgSi_2O_7$; *x* =	0.00	1.07	1.56	1.65	1.79	–	1.98	–
Agreement factors and refinement details								
R_{wp}	0.1146	0.1477	0.1533	0.1552	0.1616		0.1546	
R_p	0.0806	0.1007	0.1039	0.1066	0.1139		0.1128	
No. of data	6800	8333	8333	8333	8333		8000	
No. of variables	40	63	63	63	87		54	
R_F	0.0249	0.0291	0.0284	0.0317	0.0293	0.0340	0.0267	
R_F^2	0.0431	0.0484	0.0473	0.0552	0.0588	0.0679	0.0494	
No. of reflections	284	416	423	425	426	1196	1165	
Unit cell parameters								
a (Å)	8.0095(1)	8.1111(1)	8.1549(1)	8.1645(1)	8.1710(2)	8.4077(5)	8.4171(3)	8.2036(4)
b (Å)	–	–	–	–	–	10.7058(6)	10.7194(4)	–
c (Å)	5.1643(1)	5.2811(1)	5.3421(1)	5.3554(1)	5.3630(1)	8.4443(5)	8.4501(3)	5.4058(4)
β (°)	–	–	–	–	–	110.77(1)	110.77(1)	–
Unit cell volume (Å^3)	331.30(1)	347.44(1)	355.26(1)	356.99(1)	358.07(2)	710.69(7)	712.89(6)	363.81(2)
Mean metal-oxygen bond distances (Å)								
⟨*X*–O⟩	2.672(4)	2.736(6)	2.766(7)	2.769(6)	2.772(9)	–	2.820(12)	2.793(4)
⟨Mg–O⟩	1.941(3)	1.954(1)	1.958(2)	1.959(2)	1.962(2)	–	1.966(3)	1.966(4)
⟨Si–O⟩	1.617(4)	1.621(1)	1.626(2)	1.629(2)	1.632(2)	–	1.629(5)	1.635(4)
Mean interatomic angles (°)								
⟨O–Si–O⟩	109.3(3)	109.2(3)	109.2(3)	109.2(4)	109.2(5)	–	109.3(7)	109.3(2)
⟨Mg–O3–Si⟩	122.6(2)	124.0(2)	124.5(2)	124.5(2)	123.8(2)	–	119.0(5)	124.6(2)

*Data referred to the work of Shimizu et al. (1995).

Table D2. Final atomic coordinates (and their standard deviation within brackets), isotropic thermal parameters, and site fractions for samples along the $Sr_{2-x}Ba_xMgSi_2O_7$ ($0 \leq x \leq 2$) join.

$Sr_{2-x}Ba_xMgSi_2O_7$ (s.g. ***P*-42$_1$*m***)							
	Sr / Ba	Mg	Si	O1	O2	O3	
Ba000							
X	0.3345(1)	0	0.1386(2)	0.5	0.1418(4)	0.0784(4)	
Y	0.1655(1)	0	0.3614(2)	0	0.3582(4)	0.1922(4)	
Z	0.5070(2)	0	0.9437(5)	0.1617(14)	0.2527(9)	0.8060(7)	
Ueq. (Å^2 × 100)	0.87	0.89	0.54	1.28	1.36	1.56	
Site fraction (mol)	1 - 0	1	1	1	1	1	
Ba100							
X	0.3349(1)	0	0.1380(3)	0.5	0.1394(7)	0.0786(7)	
Y	0.1650(1)	0	0.3620(3)	0	0.3606(7)	0.1935(3)	
Z	0.5091(3)	0	0.9497(6)	0.1457(18)	0.2518(6)	0.8155(4)	
Ueq. (Å^2 × 100)	0.93	0.32	0.86	1.82	1.74	1.26	
Site fraction (mol)	0.5 / 0.5	1	1	1	1	1	
Ba150							
X	0.3351(1)	0	0.1376(3)	0.5	0.1403(9)	0.0764(8)	
Y	0.1648(1)	0	0.3624(3)	0	0.3597(9)	0.1943(4)	
Z	0.5094(4)	0	0.9505(7)	0.1418(21)	0.2493(7)	0.8190(5)	
Ueq. (Å^2 × 100)	0.69	0.34	0.38	2.11	3.21	1.40	
Site fraction (mol)	0.25 / 0.75	1	1	1	1	1	
Ba160							
X	0.3350(1)	0	0.1371(3)	0.5	0.1388(8)	0.0762(8)	
Y	0.1650(1)	0	0.3629(3)	0	0.3612(8)	0.1944(4)	
Z	0.5084(3)	0	0.9531(6)	0.1420(19)	0.2512(7)	0.8198(5)	
Ueq. (Å^2 × 100)	0.83	0.24	0.62	0.63	1.45	1.09	
Site fraction (mol)	0.20 / 0.80	1	1	1	1	1	
Ba175							
X	0.3351(1)	0	0.1382(4)	0.5	0.1379(11)	0.0745(14)	
Y	0.1648(1)	0	0.3618(4)	0	0.3621(11)	0.1946(5)	
Z	0.5065(6)	0	0.9536(8)	0.1336(29)	0.2517(8)	0.8182(5)	
Ueq. (Å^2 × 100)	0.85	0.11	0.82	1.04	1.16	2.29	
Site fraction (mol)	0.125 / 0.875	1	1	1	1	1	
$Ba_2MgSi_2O_7$ (s.g. ***C*2/*c***)							
	Ba	Mg	Si	O1	O2	O3	O4
Ba200							
X	0.2719(2)	0	0.8860(11)	0	0.6968(10)	0.9785(17)	0.8906(19)
Y	0.4567(1)	0.2598(10)	0.2834(5)	0.3307(13)	0.3455(9)	0.3502(9)	0.1348(5)
Z	0.0227(2)	0.25	0.8632(11)	0.75	0.7640(16)	0.0419(8)	0.8757(18)
Ueq. (Å^2 × 100)	0.83	0.6	1.01	2.2	1.25	2.04	2.41
Site fraction (mol)	1	1	1	1	1	1	1

Note: During the refinement of the sample *Ba175* the atomic coordinates for the monoclinic phase were kept fixed and equal to those refined for the monoclinic phase of the sample *Ba200*)

► ***Results and discussion*** − In our synthesis conditions, the major phases occurring in the samples are the *P*-42$_1$*m* melilite-type and the *C*2/*c* melilite-related structures. As reported in Table D1, the sample *Ba000* as well as all the other samples up to a barium concentration of 80 % (i.e. samples *Ba100*, *Ba150*, and *Ba160*) are almost monophasic,

mainly composed by the tetragonal melilite phase plus a very small amount of strontium silicates ($SrSiO_3$ and Sr_2SiO_4, ~4.9% on average). The occurrence of Sr silicates suggests that a less amount of MgO compared to the ideal stoichiometry ratio was actually available to the reaction leading to an excess of Sr an Si. This is clear in sample *Ba000* where, even in the absence of any Ba source, $SrSiO_3$ is found. The sample *Ba200* is also nearly monophasic and it is essentially composed by the monoclinic melilite-related phase, plus a ~4.7% of $BaSiO_3$ as minor phase.

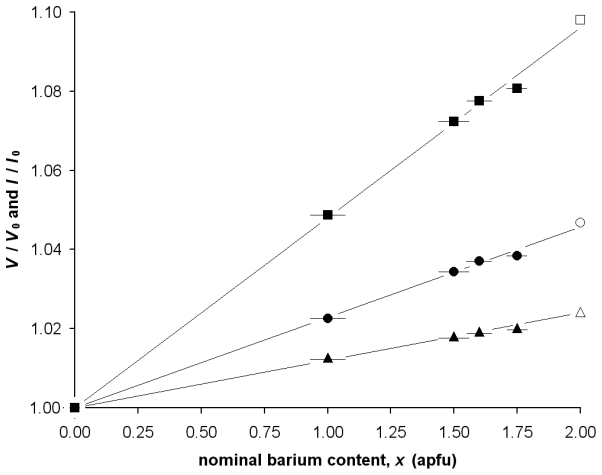

Figure D2. Unit-cell volume (V/V_0: squares) and lattice parameters (a/a_0 = b/b_0: triangles; c/c_0: circles) of melilite-type compounds along the join $Sr_{2-x}Ba_xMgSi_2O_7$ vs. the nominal barium content (black filled symbols). Data are normalized to the $Sr_2MgSi_2O_7$ parameters (V_0, a_0, b_0, c_0). $Ba_2MgSi_2O_7$ end-member (empty symbols) refers to the single-crystal refinement of Shimizu et al. (1995). Horizontal ticks refer to the difference between the nominal barium content and that calculated on the bases of the elemental composition of the main phases (see Table D1).

Sample *Ba175* describes a transitional situation. Apart the ~6.1% of Sr_2SiO_4 as minor phase, this sample is composed by both tetragonal (~63.5%) and monoclinic (~30.4%) forms. It is reasonable to estimate that with ~90% of barium concentration a compound, composed by half tetragonal and half monoclinic melilite phases, would form (e.g. sample *Ba180*).

In Figure D2 the normalized unit-cell axis lengths and volume of melilite-type phases (*Ba000*, *Ba100*, *Ba150*, *Ba160* and the melilite-type fraction of *Ba175*) are plotted vs. the barium content. The values scale linearly with the barium fraction, with the only exception of sample *Ba175*, which exhibits lattice parameters slightly smaller than those expected from the linear trend defined by the other samples. This is likely due to the coexistence in this sample of both the tetragonal and the monoclinic phases. The *c*-axis grows faster than the *a*-axis indicating that the crystal lattice mainly expands perpendicularly to the tetrahedral sheets (i.e. along [001]). This anisotropic lattice expansion is expected from the substitution of the larger Ba cation after Sr in the *X* site.

The anisotropic changes of the unit cell parameters along the join $Sr_{2-x}Ba_xMgSi_2O_7$ can be better understood by considering the variations in the metal-oxygen mean bond distances within the interlayer region. Figure D3 shows the mean bond distance of the eight-coordinated *X* site, ⟨*X*–O⟩, which increases linearly with Ba substitution. The trend defined by the ⟨*X*–O⟩ distances refined for the tetragonal phase in our samples nicely fits the value obtained by Shimizu et al. (1995) in their single crystal study of $Ba_2MgSi_2O_7$ melilite. In contrast, the ⟨*X*–O⟩ distance refined in the monoclinic $Ba_2MgSi_2O_7$ polymorph is about 0.03 Å larger than the one found in the tetragonal form. This suggests that the "5 + 3" - "3 + 5" ligand configuration in the former structure allows a less compressed environment than the "4 + 4" square antiprism in the latter. The absolute variation of the ⟨*X*–O⟩ distance between the Sr and Ba end-members is equal to ~0.12 Å (or ~0.15 Å, if the monoclinic polymorph is taken as the $Ba_2MgSi_2O_7$ end-member), corresponding to a relative increase of about 4.5 % (or 5.5 %) with respect to $Sr_2MgSi_2O_7$. This variation fully accounts for the expansion along the *c*-axis as observed in Figure D2.

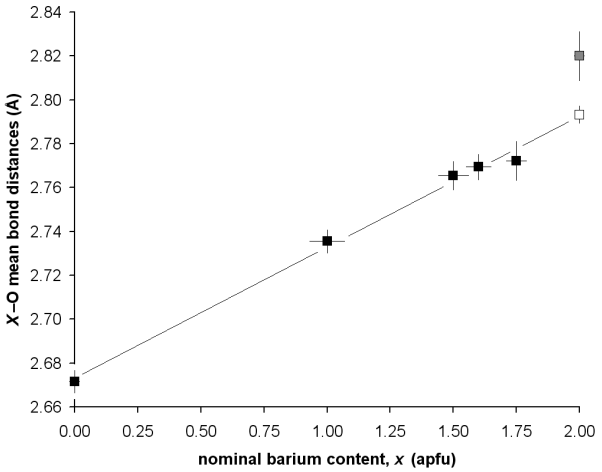

Figure D3. *X*–O mean bond distances as a function of barium content. Black filled symbols symbolize the melilite-type compounds, empty symbols refer to the $Ba_2MgSi_2O_7$ refined by Shimizu et al. (1995) in *P*-42$_1$*m* space group, whereas grey symbols represent the $Ba_2MgSi_2O_7$ refined in *C*2/*c* space group (*Ba200* this study). Vertical error bars represent the esd's. Horizontal ticks refer to the difference between the nominal barium content and that calculated on the bases of the elemental composition of the main phases (see Table D1).

The Ba for Sr substitution in the interlayer site also affects the dimensions of the tetrahedral sheet. This is evidenced by the variation of *T*–oxygen tetrahedral distances as plotted in Figure D4. Both the Mg–O and

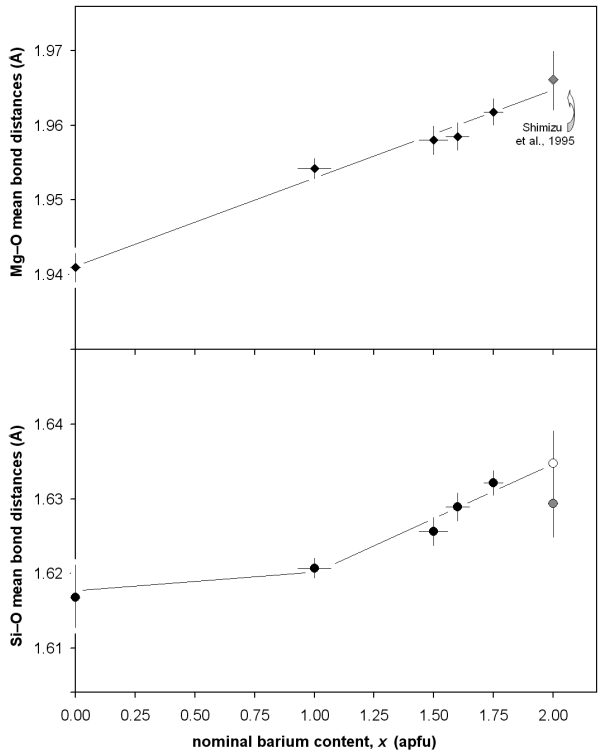

Figure D4. Mean metal-oxygen distances in tetrahedral sites *T1* (diamonds: on the top) and *T2* (circles: on the bottom) versus barium content. Black filled symbols symbolize the melilite-type compounds, empty symbols refer to the $Ba_2MgSi_2O_7$ refined by Shimizu et al. (1995) in *P*-42$_1$*m* space group, whereas grey symbols represent the $Ba_2MgSi_2O_7$ refined in *C*2/*c* space group (*Ba200*, this study). Vertical error bars represent the esd's. Horizontal ticks refer to the difference between the nominal barium content and that calculated on the bases of the elemental composition of the main phases (see Table D1).

⟨Si–O⟩ bond distances are stretched as a function of Ba increase although with different trends. Whilst the four symmetry equivalent Mg–O distances scale linearly with the barium fraction in the whole range, the variation of the mean Si–O distance is not linear: ⟨Si–O⟩ remains nearly constant (within the esd's) for samples *Ba000* and *Ba100*, while it shows a slight linear expansion with Ba content greater than 50%. Furthermore, both the Mg–O and ⟨Si–O⟩ tetrahedral distances show: (i) small absolute lengthening (~0.03 and ~0.01 Å for Mg–O and ⟨Si–O⟩, respectively), corresponding to a relative variation of an order of magnitude less that the one observed for the ⟨*X*–O⟩ distances; (ii) similar values when comparing the melilite-type and melilite-related barium end-members. More in detail, the Mg–O distances are equal within the esd's: 1.966(4) (*P*-42$_1$*m* s.g.; Shimizu et al. 1995) and 1.966(3) Å (*C*2/*c* s.g.; this work), while the ⟨Si–O⟩ distances are very close (the same within the esd's): 1.635(4) (*P*-42$_1$*m* s.g.; Shimizu et al. 1995) and 1.629(5) Å (*C*2/*c* s.g.; this work).

In order to compare the geometrical and bonding features of all samples along the $Sr_{2-x}Ba_xMgSi_2O_7$ join to those of other melilite-type and melilite-related compounds from the literature, the ⟨*T1*–*O*–*T2*⟩ angles (where *O* = "O3" and "O2 plus O3" for the tetragonal and the monoclinic structures, respectively) and the tetrahedral angle variance (σ^2) of *T2*, are plotted versus the *T*/*X* ratio (Figure D5). As previously pointed out by Giuli et al. (2000) these plots are well suited to predict the possible presence of an incommensurate modulation in these structures, because of the geometrical constraints in term of ionic size existing between the tetrahedral and interlayer cations.

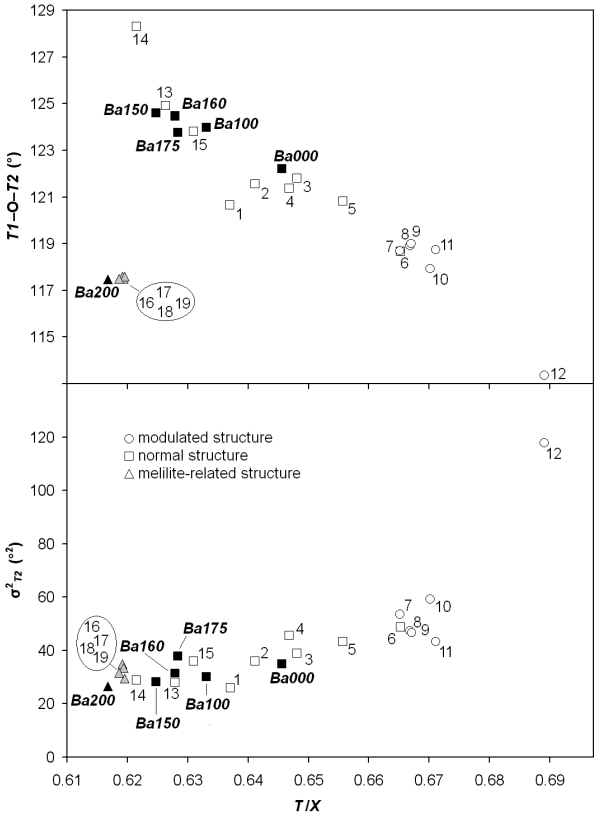

Figure D5. ⟨*T1*–*O*–*T2*⟩ angles (top) and *T2* angular distortion σ^2 (bottom) versus *T*/*X* ratio (see text for explanation). Circles, squares and triangles symbolize modulated, normal and melilite-related structures, respectively. Black filled symbols refer to structures studied in this work [*Ba200* is monoclinic $Ba_2MgSi_2O_7$ while *Ba175*-*Ba000* is the tetragonal $(Ba,Sr)_2MgSi_2O_7$ solid solutions]. Open symbols and numbers from the literature are as follows: (1) $Ca_2SiB_2O_7$ Giuli et al. 2000; (2) $Sr_2Al_2SiO_7$ Kimata 1984; (3) $Sr_2MgSi_2O_7$ Kimata 1983a; (4) $Sr_2ZnSi_2O_7$ Ardit et al. 2010a (5) $Sr_2MnSi_2O_7$ Kimata 1985; (6) $Ca_2Al_2SiO_7$ Kimata and Ii 1982; (7) $Ca_2CoSi_2O_7$ Kimata 1983b; (8) $Ca_2MgSi_2O_7$ Kimata and Ii 1981; (9) $Ca_2MgSi_2O_7$ Bindi et al. 2001b; (10) $Ca_2ZnSi_2O_7$ Bindi et al. 2001a; (11) $Ca_2ZnSi_2O_7$ Louisnathan 1969; (12) $Ca_2ZnGe_2O_7$ Armbruster et al. 1990; (13) tetragonal $Ba_2MgSi_2O_7$ Shimizu et al. 1995; (14) $Ba_2CuSi_2O_7$ Du et al. 2003; (15) $Ba_2CoSi_2O_7$ El Bali and Zavalij 2003; (16) monoclinic $Ba_2MgSi_2O_7$ Aitasalo et al. 2006; (17) $Ba_2CuSi_2O_7$ Malinovskii 1984; (18) $Ba_2CoSi_2O_7$ Adams et al. 1996; (19) $Ba_2ZnSi_2O_7$ Kaiser and Jeitschko 2002.

All plots in Figure D5 show that the melilite-type samples along the $Sr_{2-x}Ba_xMgSi_2O_7$ join always occur with unmodulated structures. Furthermore, excluding the Sr-åkermanite end-member (*Ba000*), each sample is characterized by a very low *T*/*X* ratio (~0.625 in average) revealing that structures with high concentration of Ba in *X* site have a low structural strain and consequently a small deformation of the tetrahedral sheets. As the tetragonal structures, the monoclinic compounds fall in a narrow field characterized by a very low structural strain, even lower than that of the melilite-type (i.e. < 0.620). Both $Ba_2MgSi_2O_7$ structural types are characterized by little *T2* distortion.

On the other hand, the values of ⟨*T1*–*O*–*T2*⟩ angles are very different for the two structure types. The tetragonal phases present almost flat tetrahedral sheets (high values of the ⟨*T1*–*O*–*T2*⟩ angles) with interlayer distance (equal to 5.406 Å) defined by the stacking periodicity along the *c*-axis, whereas the monoclinic compounds are characterized by wrinkled tetrahedral layers (low values of the ⟨*T1*–O–*T2*⟩ angles) with the interlayer spacing along the *b*-axis, calculated as the average distance between pairs of oxygen atoms across the interlayer (5.355 Å), slightly shorter than the halved axis length (5.360 Å). The wider interlayer spacing in the tetragonal polymorph, with respect to the monoclinic structure, appears in contrast with the shorter average ⟨*X*–O⟩ distance (2.793 Å), refined in the tetragonal melilite-type compound by Shimizu et al. (1995), as compared to what found in our study for the monoclinic end-member *Ba200* (⟨*X*–O⟩ = 2.820 Å). This apparent inconsistency is readily explained by the different tetrahedral sheet topologies and ligand environment of the *X* cation in the interlayer sites.

As already pointed out, in the *P*-42_1m structures the *X* polyhedron is enclosed between two tetrahedral sheets with upper and lower equal distribution of ligands (4 + 4), whereas in the *C*2/*c* compounds the *X*-cation connects two tetrahedral sheets with a different number of ligands (5 + 3 and 3 + 5). It follows that, while the *X* polyhedral shape in the former structure appears more regular than that in the latter, the volume of *X* polyhedron in the monoclinic structure is more tight than in the tetragonal one, the *X*-site volume being equal to 36.28 and 33.41 $Å^3$ for the *P*-42_1m and *C*2/*c* structural types of $Ba_2MgSi_2O_7$, respectively (the first value refers to Shimizu et al. 1995). Again, the apparent inconsistency of the shorter average bond distance associated to the larger polyhedral volume of the *X* site, found in the tetragonal

polymorph (⟨*X*–O⟩ = 2.793 Å and V_X = 36.28 Å^3) as compared to the monoclinic one (⟨*X*–O⟩ = 2.820 Å and V_X = 33.41 Å^3), is explained by the more compact arrangement of the interlayer space in the latter structure. Moreover, it is worth noting that bond distances down to 2.648 Å and 2.627 Å are found in the tetragonal $Ba_2MgSi_2O_7$ (Shimizu et al. 1995) and $Ba_2CoSi_2O_7$ (El Bali and Zavalij 2003), respectively, whereas Ba–O distances less then 2.69 Å do not occur in the monoclinic Ba_2*T1*Si_2O_7 compounds (*T1* = Mg, Co, Zn, Cu). In other words, the Ba polyhedron in the tetragonal structure, compared to the monoclinic one, is characterized at the same time by wider dimension along the stacking direction, larger polyhedral volume, and shorter average and minimal individual bond distances. Recalling that the ideal $^{[VIII]}$Ba–O bond distance, as calculated from the sum of ionic radii (Shannon 1976), is about 2.77 Å and that the ideal coordination number of Ba, as given by Brown (2002), is around ten (ideal $^{[X]}$Ba–O distance about 2.87 Å), we infer that the Ba environment in the tetragonal polymorph of $Ba_2MgSi_2O_7$ makes this structure less stable at ambient conditions than the monoclinic form. The larger ⟨Ba–O⟩ distance (2.818 Å) along with one individual distance of 2.70 Å, resulting from the single crystal refinement of $Ba_2MgGe_2O_7$, for which only tetragonal symmetry has been reported (Kamiskii et al. 2008), suggests that the average ⟨Ba–O⟩ and single Ba–O distances larger than 2.80 and 2.69 Å, respectively, is the stabilizing factor for the tetragonal or the monoclinic polymorphs of Ba_2*T1T2*$_2O_7$ compounds. Such a lower threshold on ⟨*X*–O⟩ and *X*–O distances appears more effective than the upper threshold on the *X* site volume (V_X is equal to 37.68 Å^3 in $Ba_2MgGe_2O_7$). These considerations suggest that the tetragonal structures of Ba_2*T1*Si_2O_7 (with *T1* = Mg, Co, Zn, Cu), which crystallize from a melt (i.e. at high temperature conditions) as metastable phases, would be favored by high pressure conditions. The existence of a lower threshold on *X–O* distances in monoclinic melilite-related structures also highlights the important role played by the interlayer cation in stabilizing/destabilizing the incommensurately modulated structures in both polymorphs. In fact, it has been recognized from superspace refinements that the presence of sixfold coordinated Ca cations is a distinct feature of modulated tetragonal melilite structures having the *X* site only occupied by Ca while its substitution with a small fraction of Sr increases the minimal coordination to seven- and eightfold (Bindi et al. 2001b). The stabilization effect on the *IC* structure from the reduced coordination numbers of the *X* cation would be less favored in the monoclinic polymorphs compared to the tetragonal ones.

Aiming to get further insights into the effects of pressure induce change in coordination a the *X* cation, *in situ* high pressure XRPD experiments on the tetragonal $Sr_2MgSi_2O_7$ and monoclinic $Ba_2MgSi_2O_7$ end-members were performed. Figure D6 shows that the unit-cell parameters refined from the HP data decrease smoothly with pressure in both Sr-åkermanite (*Ba000*) and barium melilite-related structure (*Ba200*).

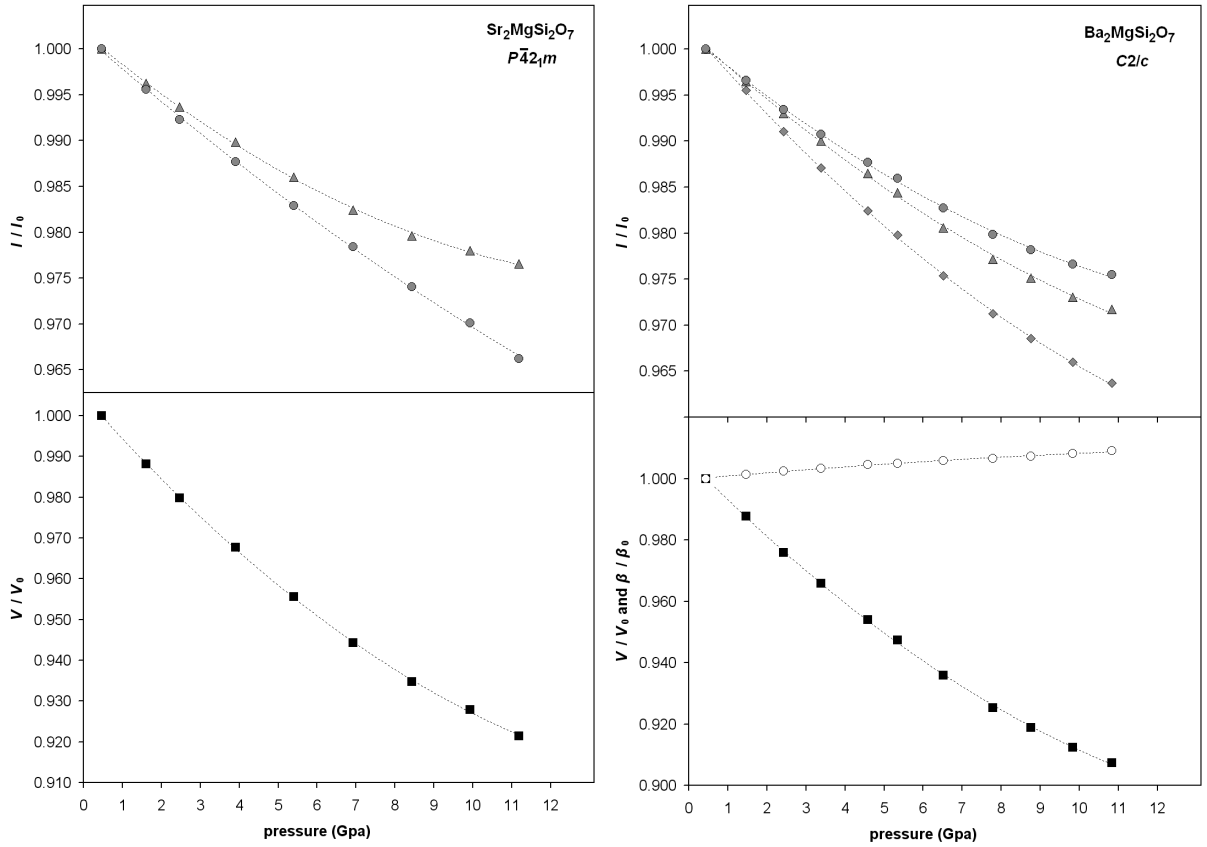

Figure D6. Variation of normalized unit-cell parameters of $Sr_2MgSi_2O_7$ melilite-type on the left side and $Ba_2MgSi_2O_7$ melilite-related compound on the right side, as a function of pressure. Triangles, diamonds, circles and squares symbolize *a*-, *b*-, *c*-axes and volume, respectively. Empty circles refer to *β* angle in the monoclinic structure.

The pressure–volume data, fitted with a Birch-Murnagham equation of state (EoS), yielded a bulk modulus of 107(3) and 85(2) GPa for tetragonal and the monoclinic structures, respectively. The elastic moduli of the individual crystallographic axes, obtained by fitting the measured data with the same EoS to the cubes of each of the cell axes, are: 121(6) and 84(1) GPa for the *Ba000 a*- and *c*-axis, respectively, while 96(2), 72(1) and 117(3) GPa for the *Ba200 a*-, *b*-, and *c*-axis, respectively.

Table D3. Elastic moduli of the melilite N structures determined from high-pressure X-ray diffraction.

Compound	s.g.	K_{T0}	K_a	K_b	K_c	Ref.
*$Ca_2MgSi_2O_7$	*P*-42$_1$*m*	90(2)	105(8)	–	78(4)	Yang et al. 1997
*$Ca_2MgSi_2O_7$	*P*-42$_1$*m*	94(1)	99(1)	–	84(1)	Merlini et al. 2009
$Sr_2MgSi_2O_7$	*P*-42$_1$*m*	107(3)	121(6)	–	84(1)	This study
$Ba_2MgSi_2O_7$	*P*-42$_1$*m*	*122*	*146*	–	*84*	This study (*extrapolated values*)
$Ba_2MgSi_2O_7$	*C*2/*c*	85(2)	96(2)	72(1)	117(3)	This study

*the reported values were obtained for pressure higher than 1.7 GPa

These data are compared with other melilite compounds in Table D3. Data listed in this table refer to normal structures (N). Indeed, åkermanite ($Ca_2MgSi_2O_7$), an incommensurately modulated structure (*IC*) at ambient condition, transforms into a normal structure at a pressure of about 1.7 GPa (Yang et al. 1997; Merlini et al. 2009) due to the stabilizing effect of high pressure for the unmodulated N structure. Therefore, no pressure induced transition from *N* to *IC* structures is expected in both $Sr_2MgSi_2O_7$ and $Ba_2MgSi_2O_7$. This is confirmed by the absence of any discontinuity in the behavior of cell parameters in Figure D6. The volumetric bulk modulus of the melilite-type and melilite-related compounds here considered always presents intermediate values between the compressibilities calculated along the tetrahedral sheets and along perpendicular directions. Furthermore, as already pointed out by Merlini et al. (2009), the compressibility along the *c*-axis for each melilite-type structure is the same (within the esd's) irrespectively of the compound composition (i.e. K_c ~84 GPa). On the other hand, the compressibility along *ab* planes decreases as a function of the ionic radius (i.r.) of cations in the *X*-site. Since no data are available for melilite-type structure with formula $Ba_2MgSi_2O_7$, following the previous observations it is possible to extrapolate the volumetric and lattice bulk moduli of such a compound by the equations K_{T0} (GPa) = [92.86 × i.r. (Å)] - 10, and K_a (GPa) = [157.14 × i.r.(Å)] - 77, resulting: K_{T0} ~122, K_a ~146 and K_c ~84 GPa. This data estimation is useful in order to compare the two $Ba_2MgSi_2O_7$ structural types and to describe the pressure evolution along the $X_2MgSi_2O_7$ series, where *X* = Ca, Sr, and Ba.

A comparison of the elastic moduli shows that tetragonal $Ba_2MgSi_2O_7$ is the less compressible among the structures reported in Table D3. Furthermore, it appears that in general the melilite-type structure is stiffer than the melilite-related (monoclinic) one. A more important feature is that the elastic

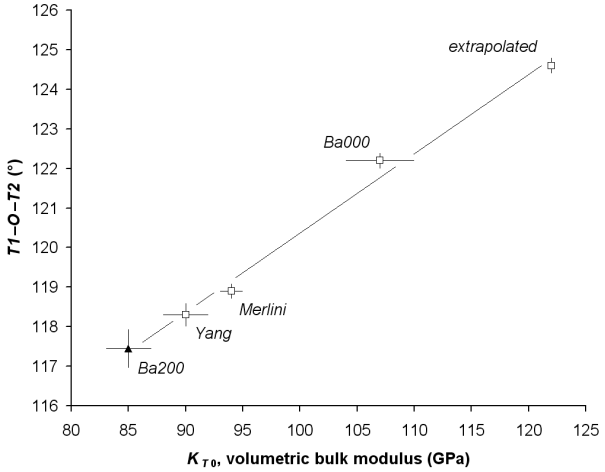

Figure D7. ⟨*T1*–*O*–*T2*⟩ angles as a function of the volumetric bulk modulus, K_{T0}. Black filled triangle and empty squares symbolize monoclinic (*C*2/*c*) and tetragonal (*P*-42$_1$*m*) structures, respectively. Symbol labels are the same as the references in Table D3.

properties of all compounds are strongly correlated with the distortion within the tetrahedral sheet at ambient condition. The tetrahedral wrinkling, as quantified by the ⟨*T1*–*O*–*T2*⟩ angles, is plotted in Figure D7 as a function of the volumetric bulk modulus.

In order to evaluate the elasticity along the tetrahedral sheets for both kind of structures in a same way, the K_a and K_c bulk moduli of the melilite-related compound (*Ba200*) were rearranged to obtain a single value as for the melilite-type compounds. To achieve this compressibility value, the *c*-axis was orthogonalized by multiplying its value for the sine of the corresponding β angle for each measured pressure. The resulting bulk modulus (fitted with a Birch-Murnagham EoS as for the other lattice parameters) was averaged to that of the *a*-axis, to yield a K_{ac} = 91 GPa. Such a value with all the other lattice compressibilities along the tetrahedral sheets scale linearly with the volumetric bulk modulus, highlighting the high dependence of the structures in their whole on the tetrahedral sheet arrangement, irrespective of which kind of topology is involved (melilite-type rather than melilite-related).

Therefore, the major difference between melilite-type and melilite-related structures can be ascribed to the different compressibility perpendicular to the tetrahedral sheet/interlayer stacking (i.e. along *c* for the tetragonal and along *b* for the monoclinic structures). Indeed, while the same compressibility along *c* (i.e. K_c = 84 GPa) is found for most of the different tetragonal compounds in Table D3, the monoclinic structure exhibits a smaller bulk modulus in the *b* direction (K_b = 72 GPa). This observation helps to understand the apparently contrasting features previously discussed when considering the ⟨*X*–O⟩ cubic distances and corresponding polyhedral volumes for the two $Ba_2MgSi_2O_7$ structure types: the shorter ⟨Ba–O⟩ distance is associated, in the tetragonal form, to a larger polyhedral volume, while the opposite occurs in the monoclinic structure. The bulk and axial compressibilities of different polymorphs are mostly defined by the different Ba coordination geometry. The interlayer region is stiffer in the tetragonal structure, despite the larger volume of Ba polyhedron, because the very short average and individual bond distances make the coordination around Ba tightly constrained. Similarly, the different degree of space confinement around Y ions in $YAlO_3$ and $YCrO_3$ perovskites has been recently found to explain their contrasting evolution under pressure (Ardit et al. 2010b).

► ***Conclusions*** − The crystal structure investigation of the $Sr_{2-x}Ba_xMgSi_2O_7$ ($0 \leq x \leq 2$) solid solution, combined to the high pressure study of the two end-members, are able to explain the relationships between the structures of tetragonal (melilite-type) and monoclinic (melilite-related) polymorphs reported in many systems ($Ba_2T1Si_2O_7$, *T1* = Mg, Co, Zn, Cu) and not clarified yet. In the tetragonal form, the tetrahedral sheet topology based on five-membered rings provides a regular "4 up + 4 down" coordination for Ba cations, which is favored in the crystallization from a melt. However, these regular Ba polyhedra imply the occurrence of very short Ba–O bond distances, which make the tetragonal structure less preferred when crystals are formed by solid-state reactions. In this case, the sheet topology of the melilite-related structure, made by alternating six- and four-membered tetrahedral rings, provides an additional degree of freedom which stabilizes the monoclinic polymorphs. The offset between two successive tetrahedral sheets (with doubling of the stacking axis length) allows the Ba cation to be hosted in the interlayer with a more compact coordination (i.e. with smaller polyhedral volume) based on the alternating "5 + 3" and "3 + 5" ligands configuration. We suggest that the high-pressure, inducing a shortening of the Ba–O distances, potentially increases the stability of Ba ligands configuration in the tetragonal structure. However, as expected and observed in HP experiments, no phase transition from monoclinic to tetragonal occurs, due to a kinetic hindrance in the reconstructive process necessary to vary the sheet topology from the melilite-related structure to the melilite-type one.

3. Section II. E. ♦ Local structural investigation along the Ca–Sr–Ba-åkermanite solid solution doped with a fixed amount of tetrahedrally coordinated Co^{2+}

► ***Introduction*** − This study is the first attempt, and the sole in this dissertation, to obtain information on the structural relaxation through a "*tracer cation*". The other cases of structural relaxation reported in this thesis (i.e. Cr-doped $YAlO_3$ perovskite [*A*] and $AlNbO_4$ alumoniobite [*C*], and Co-doped $Ca_2ZnSi_2O_7$ hardystonite [*G*]) were based on the calculation of the relaxation coefficient ε around a chromophore cation. In these studies, the chromofore substitutes the starting cation in the same polyhedron (i.e. octahedron or tetrahedron) where the structural relaxation is evaluated. In the study here presented, on the other hand, the structural relaxation along the Ca- to Sr-, and Sr- to Ba-åkermanite *extended* solid solution (i.e. calculated around the eight-fold coordinated Sr^{2+} and Ba^{2+}, in the first and second part of the join, respectively) will be achieved by evaluating the second shell effects of a fixed amount of Co^{2+} (i.e. the "*tracer cation*") which substitutes for Mg in the tetrahedral *T1* site [*for further detail on melilite structure, readers are requested to see the introductive description on melilite compounds at the begin of this section*].

The previous work of this section [*see the first work,* ***D***] explored the relationship between tetragonal melilite-type and monoclinic melilite-related polymorphs by means of a X-ray powder diffraction structural investigation along the $Sr_{2-x}Ba_xMgSi_2O_7$ ($0 \leq x \leq 2$) solid solution, and by a synchrotron high-pressure study of the two end-members. The main conclusion of the latter study was that, although the volume of Ba polyhedron in tetragonal polymorphs is larger than in the monoclinic forms, the interlayer compressibility is significantly lower in the former structures due to the occurrence of very short Ba–O distances. This Ba environment also makes tetragonal $Ba_2MgSi_2O_7$ a metastable phase at room conditions, possibly favoured by high pressure.

In the present study the previous Sr–Ba solid solution has been extended till the Ca-åkermanite end-member, and each synthesized sample (i.e. obtained by the solid-state reaction route) was yielded optically sensible by substituting 30% of the four-fold coordinated Mg^{2+} with Co^{2+}. The chemical formulation of such a join, $(Ca–Sr–Ba)_2(Mg_{0.7}Co_{0.3})Si_2O_7$,

opens a deeper access to the "melilite world" giving us the possibility to explore the effects induced by the cationic substitution, by means of a X-ray powder diffraction (XRPD) and electronic absorption spectroscopy (EAS) combined approach.

► ***Experimental*** – [*for the experimental details (including: synthesis procedure, X-ray powder diffraction data collection, Rietveld refinements, and optical spectroscopy) readers are requested to refer to the chapter **2** of the present dissertation*]. In addition to what reported in chapter ***2***, during the refinements of the atomic coordinates, a soft constraint was applied to the *T1*–O and Si–O bond distances with the constraint weight being progressively lowered until a minimal value (i.e. the final constraint weight ranges from 5 to 15). Quantitative phase analysis, agreement factors and refinement details, unit-cell parameters, mean metal–oxygen bond distances, bond angles, and tetrahedral distortion indices are listed in Table E1.

► ***Results and discussion***

● *Phase composition* – The major phase occurring in all samples is the $P\text{-}42_1m$ melilite-type structure. As reported in Table E1, the amount of this phase ranges from a minimum of 61.7% (sample $\mathbf{Sr_{0.25}Ba_{1.75}}$) to a maximum of 100% (sample **Sr**). A sample with stoichiometry $Ba_2MgSi_2O_7$ (hypothetical label **Ba**) was synthesized but not listed in Table E1, because mainly composed by the $C2/c$ melilite-related structure (i.e. 97.4%; *for a comparison reader are requested to refer to the sample Ba200 listed in Table D1 of the previous work, **D***). For this reason, the $P\text{-}42_1m$ $Ba_2MgSi_2O_7$ melilite-type structure solved by Shimizu et al. (2005) was selected as barium end-member of the join here studied (i.e. sample **Ba(S)** in Table 1). A note is needed for the sample $\mathbf{Sr_{0.25}Ba_{1.75}}$ which represents a transitional case. In fact, apart the ~9.9% of Sr_2SiO_4 as minor phase, this sample is composed by a large amount of tetragonal melilite-type structure (~61.7%) and by the first appearance of the monoclinic melilite polymorph (~28.4%). As stated in the previous work (***D***) of this section, the formation of barium-enriched tetragonal melilite is less favoured when crystals are obtained via solid-state reactions (as in the case of the samples synthesized for this study). For this reason samples with a nominal barium content greater than 1.75 apfu have a growing amount of monoclinic melilite, function of barium content.

With the only exception of sample **Sr**, therefore, all samples are not strictly monophasic, and contain variable amounts of minor phases deriving from unreacted precursors, such as: diopside ($CaMgSi_2O_6$), strontium silicate ($SrSiO_3$ and Sr_2SiO_4), and barium silicate ($BaSiO_3$).

Table E1. Quantitative phase analysis, agreement factors and refinement details, unit-cell parameters, mean metal–oxygen bond distances, bond angles, and tetrahedral distortion indices for the $(Ca,Sr,Ba)_2(Mg_{0.7}Co_{0.3})Si_2O_7$ samples. Standard deviations are reported within brackets.

$(Ca,Sr,Ba)_2(Mg_{0.7}Co_{0.3})Si_2O_7$							
nominal ionic radius of the cations hosted in X site, ir_X (Å):	1.12	1.19	1.26	1.34	1.38	1.40	1.42
			$^X(Sr_{2-x}Ba_x)^{T1}(Mg_{0.7}Co_{0.3})Si_2O_7$				
sample label	**Ca**	**CaSr**	**Sr**	**SrBa**	**$Sr_{0.5}Ba_{1.5}$**	**$Sr_{0.25}Ba_{1.75}$**	**Ba(S)***
main phases space group	*P*-42$_1$*m*	*P*-42$_1$*m*	*P*-42$_1$*m*	*P*-42$_1$*m*	*P*-42$_1$*m*	*P*-42$_1$*m*	*P*-42$_1$*m*
quantitative phase analysis							
main phases:	92.52(4)	100.00	97.19(1)	88.24(3)	91.59(2)	61.74(10)	100.00
other:							
$CaMgSi_2O_6$	7.48(5)	–	–	–	–	–	–
$SrSiO_3$	–	–	2.81(1)	–	–	–	–
Sr_2SiO_4	–	–	–	11.76(3)	8.41(3)	9.89(39)	–
$Ba_2MgSi_2O_7$ (*C*2/*c*)	–	–	–	–	–	28.37(17)	–
agreement factors and refinement details							
Chi^2	1.524	1.485	1.438	2.227	2.080	2.600	
R_{wp}	0.1278	0.1375	0.1185	0.1118	0.1140	0.1297	
R_p	0.0965	0.1006	0.0857	0.0777	0.0761	0.0900	
No. of Data	6250	8000	6800	6250	6250	6250	
No. of variables	63	41	46	63	63	88	
R(*F*)	0.0543	0.0446	0.0307	0.0306	0.0265	0.0245	
R(F^2)	0.0889	0.0737	0.0574	0.0509	0.0449	0.0437	
No. of reflections	364	356	284	415	422	426	
unit-cell parameters							
a = *b* (Å)	7.8325(3)	7.9291(2)	8.0161(1)	8.1070(1)	8.1532(1)	8.1730(2)	8.2036(4)
c (Å)	5.0124(2)	5.0837(1)	5.1648(1)	5.2666(1)	5.3273(1)	5.3549(1)	5.4058(4)
V (Å^3)	307.51(3)	319.62(2)	331.88(1)	346.14(1)	354.13(2)	357.69(2)	363.81(2)
mean metal-oxygen bond distances (Å)							
⟨*X*–O⟩	2.580(4)	2.624(4)	2.673(4)	2.732(6)	2.758(7)	2.778(11)	2.793(4)
⟨*T1*–O⟩	1.915(1)	1.929(2)	1.942(1)	1.952(2)	1.960(2)	1.960(2)	1.966(4)
⟨Si–O⟩	1.616(2)	1.618(1)	1.617(2)	1.620(2)	1.626(2)	1.629(2)	1.635(4)
bond angles (°)							
O3–*T1*–O3 [x4]	108.02(4)	106.64(5)	105.22(4)	104.24(7)	103.89(7)	104.35(8)	103.8(1)
O3–*T1*–O3 [x2]	112.42(7)	115.29(12)	118.36(8)	120.54(17)	121.33(17)	120.28(17)	121.6(2)
⟨O3–*T1*–O3⟩	109.49(5)	109.52(8)	109.60(6)	109.67(11)	109.70(11)	109.66(12)	109.7(1)
T1–O3–Si	118.90(10)	120.99(14)	122.85(11)	124.13(20)	124.63(21)	123.88(23)	124.6(2)
tetrahedral distortion indices							
λ_{T1}	1.0013	1.0052	1.0124	1.0194	1.0224	1.0185	1.0232
σ^2_{T1} (°^{2})	5.17	19.95	46.12	70.89	81.26	67.69	84.11
λ_{Si}	1.0103	1.0088	1.0079	1.0059	1.0065	1.0082	1.0065
σ^2_{Si} (°^{2})	44.48	38.38	34.00	26.06	28.29	32.96	28.26
T/*X* ratio	0.668	0.658	0.646	0.633	0.630	0.626	0.625

*Data referred to the work of Shimizu et al. (1995).

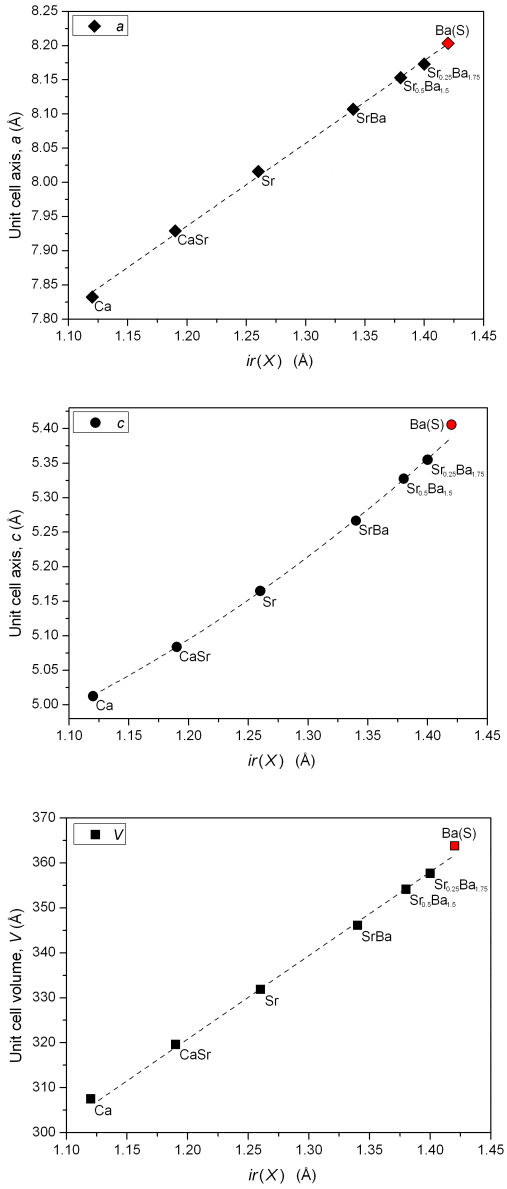

Figure E1. Lattice parameters (*a* and *c* axes) and unit-cell volume of melilite-type structures as a function of the nominal ionic radius of the cations hosted in the *X* site, *ir*(*X*). Red symbols refer to data achieved by the single-crystal refinement of tetragonal $Ba_2MgSi_2O_7$ (Shimizu et al. 1995). Standard deviation is within the symbol size.

● *Crystal structure of melilite* – Figure E1 shows the variation of the unit-cell parameter of melilite-type phases (including the sample **Ba(S)**, which refers to the *P*-42$_1$*m* $Ba_2MgSi_2O_7$ structure solved by Shimizu et al. 2005) as a function of the nominal ionic radius of the cations hosted in the *X* site, *ir*(*X*). As expected, both lattice parameter (*a* and *c* axes) and unit-cell volume (*V*) increase as a function of the cation size in *X* site. Although *a* and *V* have linear trends (i.e. follow the Vegard's law), data points for the *c*-axis present a just noticeable negative excess and must be fitted with a quadratic equation (i.e. the dashed line in Figure E1 fits the data points with $R^2 = 0.999$).

In order to estimate the possible axial anisotropy due to the cubic site expansion, in Figure E2 the *c*/*a* axial ratio (i.e. the most common evaluation of the anisotropy among the three orthogonal dimensions of the unit-cell for *P*-42$_1$*m* melilite-type compounds) is plotted against the nominal ionic radius of the cations hosted in the *X* site, *ir*(*X*). Data points plotted in Figure E2 show a cubic correlation ($R^2 = 0.994$), which means that the rate of growth of the *c*-axis is greater than that of the *a*-axis. Thus, the melilite lattice undergoes a greater expansion perpendicularly to the tetrahedral layers as bigger is the size of the cation in the *X* site.

Further information on the melilite structural variation, as a consequence to the lattice incorporation of cations progressively larger in the cubic *X* site, can be obtained by

considering the bond distance variations within the tetrahedral layers. As expected, the mean bond length ⟨*X*–O⟩ is linearly correlated to the size cations hosted in the cubic *X* site (Figure E3). Thus, the ⟨*X*–O⟩ mean bond distances strongly increase from **Ca** to **Ba(S)** samples with a maximum lengthening $\delta_{\langle X\text{–O}\rangle}$ = ⟨*X*–O⟩$_{\mathbf{Ca}}$ - ⟨*X*–O⟩$_{\mathbf{Ba(S)}}$ = 0.213 Å, corresponding to a relative increase of about 8.26 % with respect to $Ca_2MgSi_2O_7$ structure. This variation fully accounts for the expansion along the *c*-axis (i.e. 7.85 %) as observed, between the same **Ca** and **Ba(S)** samples, in Figure E1.

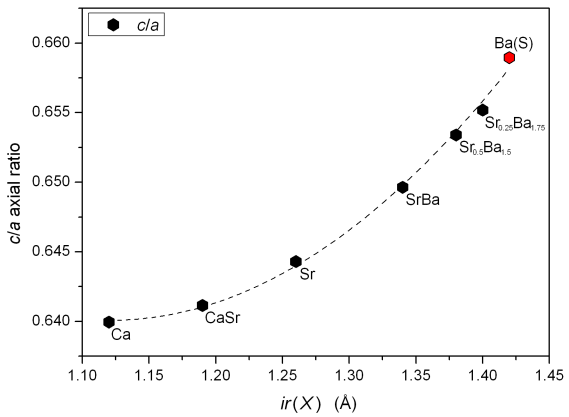

Figure E2. Plot of the (*c*/*a*) axial ratio versus *ir*(*X*). Red symbol refers to data achieved by the single-crystal refinement of tetragonal $Ba_2MgSi_2O_7$ (Shimizu et al. 1995). Standard deviation is within the symbol size.

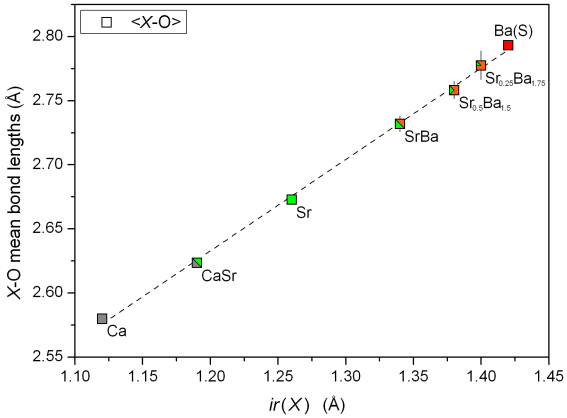

Figure E3. Plot of the ⟨*X*–O⟩ mean bond distances as a function of *ir*(*X*). Red symbol refers to data achieved by the single-crystal refinement of tetragonal $Ba_2MgSi_2O_7$ (Shimizu et al. 1995). Vertical error bars represent the esd's.

Although to a lesser manner, the cationic incorporation in the cubic site also affects the dimensions of the tetrahedral layers (Figure E4). Specifically, while the ⟨Si–O⟩ tetrahedral bond distances undergo a small lengthening, $\delta_{\langle\text{Si–O}\rangle}$ = ⟨Si–O⟩$_{\mathbf{Ca}}$ - ⟨Si–O⟩$_{\mathbf{Ba(S)}}$ = 0.019 Å, particularly centered on the last part of the solid solution (i.e. ⟨Si–O⟩$_{\mathbf{SrBa}}$ - ⟨Si–O⟩$_{\mathbf{Ba(S)}}$ = 0.015 Å), the *T1*–O bond distances scale linearly with the nominal ionic radius of the cations hosted in the *X* site, *ir*(*X*), highlighting an absolute stretching of about 2.5 times on respect to that of T2 bond lengths (i.e. $\delta_{T1\text{–O}}$ = *T1*–O$_{\mathbf{Ca}}$ - *T1*–O$_{\mathbf{Ba(S)}}$ = 0.051 Å).

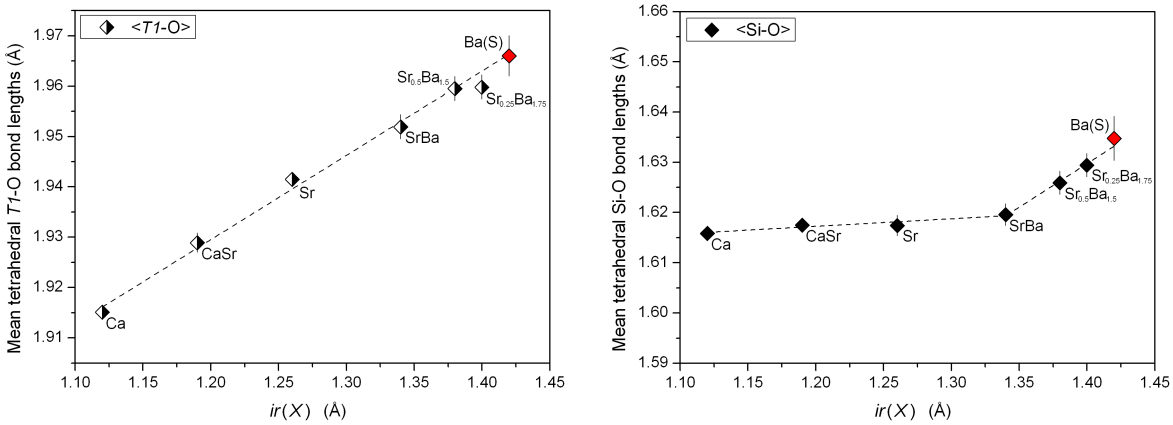

Figure E4. Mean metal-oxygen bond distances in tetrahedral sites versus the nominal ionic radius of the cations hosted in the *X* site, *ir*(*X*). Red symbols refer to data achieved by the single-crystal refinement of tetragonal $Ba_2MgSi_2O_7$ (Shimizu et al. 1995). Vertical error bars represent the esd's.

In the previous work, ***D***, the ⟨*T1*–O–*T2*⟩ angles and the tetrahedral angle variance (σ^2) of *T2* of all samples along the $Sr_{2-x}Ba_xMgSi_2O_7$ join were plotted versus the *T*/*X* ratio [*readers are requested to refer to the Figure D5 and the explanation throughout the text*] in order to predict the possible presence of an incommensurate modulation in the studied structures and to evaluate their geometrical and bonding features by comparison to those of other melilite-type and melilite-related compounds.

Besides these characteristics (i.e. for the samples in this study, the values of ⟨*T1*–O–*T2*⟩, σ^2(*T2*) and *T*/*X* ratio are equivalent, within the standard deviation, to those of samples with the same stoichiometry, if the Co doping is excluded), it is significant to observe the variation of the tetrahedral distortion, here estimated by means of the bond angle variance (σ^2; Robinson et al. 1971). In particular, Figure E5 shows that the tetrahedra *T1*, when compared with the adjacent corner-sharing tetrahedra *T2*, undergo a stronger distortion as bigger is the cation hosted in the cubic site proportional to the wrinkling of the tetrahedral sheets (i.e. increasing of the ⟨*T1*–O–*T2*⟩ angle values).

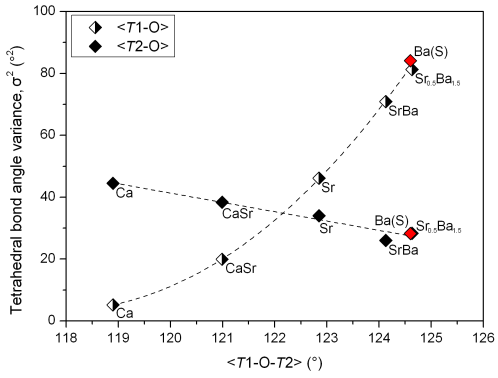

Figure E5. Plot of the tetrahedral distortion, bond angle variance(σ^2), as a function of the ⟨*T1*–O–*T2*⟩ angles. Red symbols refer to data achieved by the single-crystal refinement of tetragonal $Ba_2MgSi_2O_7$ (Shimizu et al. 1995).

● *Optical spectroscopy* – The optical spectra of Co-bearing melilites vary conspicuously by substituting Sr for Ca then Ba for Sr at the X site of åkermanite, despite the occupancy of the tetrahedral site *T1* remains unchanged. Spectra are dominated by intense bands due to electronic transitions of Co^{2+} in four-fold coordination (Figure E6).

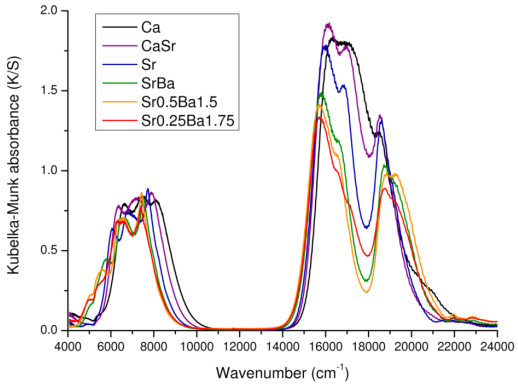

Figure E6. Optical spectra of Co^{2+}-bearing melilites.

Since the tetrahedral site *T1* has constant occupancy ($Mg_{0.7}Co_{0.3}$) all along the Ca-Sr-Ba series, no significant variation occurs to absorbance, as expected. On the other hand, quite unexpectedly, strong changes concern the energy and number of Co^{2+} bands (Figure E7). There is an overall shift of the main bands from higher wavenumbers for the Ca-åkermanite to lower and lower values for Sr- and (Ba,Sr)-åkermanites. Along with such a red-shift, some bands appear to be "activated", like those at 5000–6000 cm^{-1} (Figure E7a), while others turn to be "suppressed", like at ~18000 cm^{-1} (Figure E7b).

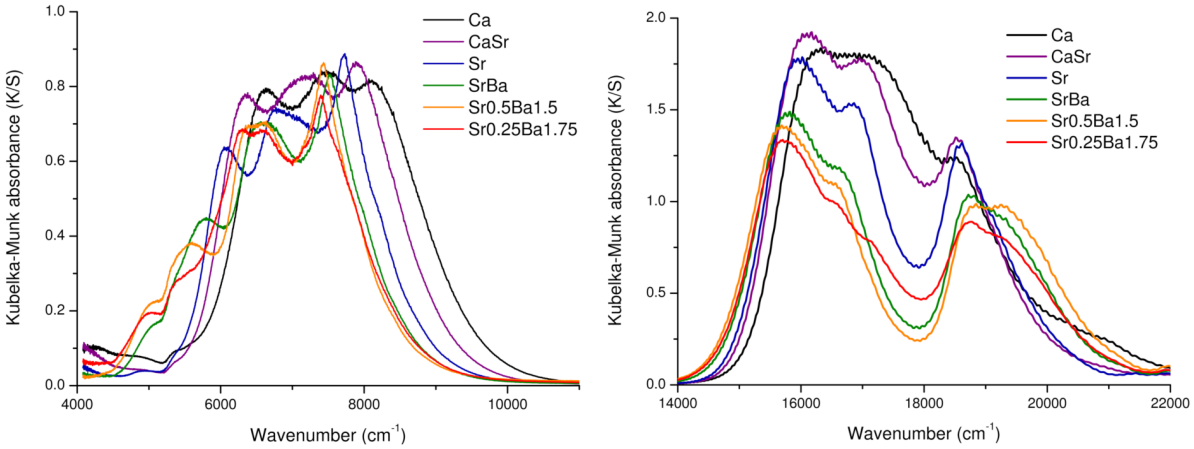

Figure E7. Optical spectra of Co^{2+}-bearing melilites: detail of the 4000–11000 cm^{-1} range (on the left) and the 14000–22000 cm^{-1} one (on the right).

In any case, all bands are attributable to Co^{2+} – on the basis of the Tanabe-Sugano diagram for d^3 ions (by the d^{10-N} rule when in tetrahedral coordination) – although they are originated by different transitions (Ferguson et al. 1969; Brunold et al. 1996):

- Spin-allowed transitions, three-fold split due to the strong spin-orbit coupling stemming from the d^7 electronic configuration of Co^{2+}, occurring as intense bands around 4000 cm^{-1}, $^4A_2 \rightarrow {}^4T_2$ (^4F) and in the 5600–8000 cm^{-1}, $^4A_2 \rightarrow {}^4T_1$ (^4F), and 15600-17000 cm^{-1}, $^4A_2 \rightarrow {}^4T_1$ (^4P), ranges.
- Spin-forbidden transitions, giving rise to low intensity bands at energy higher than 18000 cm^{-1}, due to several ^2G, ^2P and ^2H terms.
- Vibronic effects, mostly occurring as sidebands of the spin-allowed transitions, causing the remarkable complexity of the spectral features in the 5000–8000 and 15000–17000 cm^{-1} ranges; some appear to be "suppressed" or "activated" along with the shift of the spin-allowed bands.

The deconvolution of spectra gave satisfactory results by using several Gaussian bands to account for all the spin-allowed, spin-forbidden and vibronic transitions (Table E2). In such complex spectra, the interpretation is robust enough for some intense and well-defined bands (e.g. the high- and low-energy subbands of spin-allowed triplets) but it is rather uncertain for minor bands or the more structured spectral area; for example, the mid-energy subband of the $^4A_2 \rightarrow {}^4T_1$ (^4P) transition is often practically overlapping the others (Figure E8).

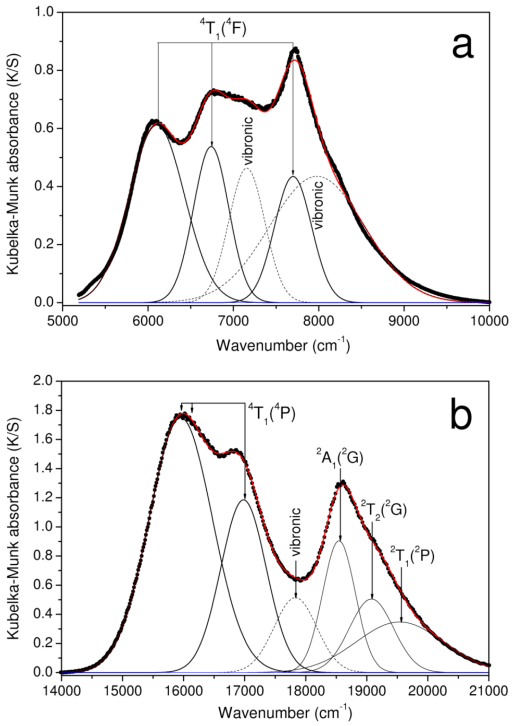

Figure E8. Deconvolution of optical spectra: example of $Sr_2Mg_{0.7}Co_{0.3}Si_2O_7$ melilite for the 4000–11000 cm^{-1} (a) and 14000–22000 cm^{-1} ranges (b).

Both the crystal field strength and Racah parameters were calculated by fitting the $^4T_1$ (^4F) and $^4T_1$ (^4P) spin-allowed bands in the Tanabe-Sugano diagram, taking the average energy of the three-fold transition by the barycentre method (Burns 1993), as the $^4T_2$ (^4F) one, which would have directly given the 10*Dq* value, falls out the investigated range for most samples (Table E3).

Table E2. Energy and intensity of optical bands of Co^{2+} in tetrahedral coordination at the *T1* site of Ca-Sr-Ba melilites. Spin-allowed transitions are **in bold**, uncertain interpretation is *in italic*.

sample label	**Ca**		**CaSr**		**Sr**		**SrBa**		**$Sr_{0.5}Ba_{1.5}$**		**$Sr_{0.25}Ba_{1.75}$**	
optical transition	energy (cm^{-1})	energy (cm^{-1})	energy (cm^{-1})	energy (cm^{-1})	energy (cm^{-1})	energy (cm^{-1})	energy (cm^{-1})	energy (cm^{-1})	energy (cm^{-1})	energy (cm^{-1})	energy (cm^{-1})	energy (cm^{-1})
$^4T_2(^4F)$	**4210**	**0.04**	**4000**	**0.08**	*<4000*		*<4000*		*<4000*		*<4000*	
vibronic	4830	0.01	4830	0.01			4960	0.08	4990	0.17		
vibronic							5350	0.03	5380	0.06		
$^4T_1(^4F)$	**6660**	**0.73**	**6370**	**0.76**	**6120**	**0.62**	**5780**	**0.43**	**5670**	**0.35**	***5650***	
vibronic	7160	0.08	6920	0.33								
$^4T_1(^4F)$	**7450**	**0.31**	**7260**	**0.42**	**6720**	**0.52**	**6490**	**0.55**	**6360**	**0.61**	***6650***	
vibronic					7050	0.52	6850	0.39	6740	0.44		
vibronic							7180	0.25	7090	0.40		
$^4T_1(^4F)$	**8030**	**0.61**	**7830**	**0.49**	**7680**	**0.60**	**7520**	**0.22**	**7420**	**0.38**	***7400***	
vibronic							7600	0.41	7660	0.31		
vibronic			8220	0.41	8040	0.40	8020	0.21	7890	0.22		
vibronic	8730	0.27			8600	0.14						
$^4T_1(^4P)$ + $^2E(^2G)$	**16170**	**1.73**	**16030**	**1.86**	**15950**	**1.74**	**15800**	**1.45**	**15690**	**1.35**	***15730***	***1.30***
$^4T_1(^4P)$											*16620*	*0.19*
$^4T_1(^4P)$	**16880**	**0.49**	**17070**	**1.39**	**16980**	**1.19**	**16780**	**0.79**	**16690**	**0.71**	***17170***	***0.67***
vibronic	17440	1.36	17700	0.73	17830	0.51	17520	0.27	17590	0.22		
$^2A_1(^2G)$	18520	1.08	18510	0.98	18550	0.90	18640	0.38	18660	0.66	*18600*	*0.38*
$^2T_2(^2G)$	19540	0.21	19150	0.53	19080	0.50	19170	0.78	19260	0.72	*19270*	*0.65*
$^2T_1(^2P)$	20500	0.26	20100	0.15	19540	0.35	20170	0.18	20680	0.18	*20340*	*0.16*
$^2T_2(^2H)$					21790	0.05	21910	0.05	21950	0.03	*21940*	*0.01*
$^2E(^2H)$							22830	0.04	22880	0.01	*22950*	*0.01*
$^2T_1(^2H)$	24530	0.01	24270	0.01	24170	0.01	23860	0.02				

Table E3. Average energy and splitting of spin-allowed transitions, crystal field strength and Racah *B* parameter of Co^{2+} in tetrahedral coordination at the *T1* site of Ca-Sr-Ba melilites.

sample label	**Ca**	**CaSr**	**Sr**	**SrBa**	**$Sr_{0.5}Ba_{1.5}$**	**$Sr_{0.25}Ba_{1.75}$**
nominal ionic radius of cations at X site, ir_X (Å):	1.12	1.19	1.26	1.34	1.38	1.40
parameter	cm^{-1}	cm^{-1}	cm^{-1}	cm^{-1}	cm^{-1}	cm^{-1}
average energy of the $^4T_1(^4F)$ transition (baricentre)	7345	7100	6900	6650	6545	*6525*
average energy of the $^4T_1(^4P)$ transition (baricentre)	16525	16550	16465	16290	16190	*16450*
crystal field strength, 10*Dq*	**4263**	**4108**	**3985**	**3834**	**3771**	***3754***
Racah *B* parameter	**739**	**755**	**761**	**763**	**762**	***781***
Racah *C* parameter (C=4.2*B)	**3103**	**3171**	**3195**	**3203**	**3199**	***3279***
spin-orbit coupling, as $^4T_1(^4F)$ transition splitting	1370	1460	1560	1740	1750	*1750*
spin-orbit coupling, as $^4T_1(^4P)$ transition splitting	710	1040	1030	980	1000	*1440*
spin-orbit coupling, average splitting	**1040**	**1250**	**1295**	**1360**	**1375**	***1595***

The 10*Dq* values decrease from Ca-åkermanite to the Sr- and (Ba,Sr)-åkermanites, showing a linear trend with the average cation radius at site *X* (Figure E9). In contrast, the Racah *B* parameter grows with the increasing mean size of *X* cation, so denoting a slight decrease of the covalency degree of Co–O bonding along with the Sr for Ca and Ba for Sr substitutions.

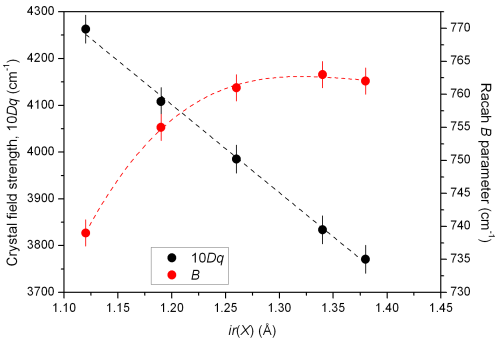

Figure E9. Crystal field strength and Racah *B* parameter of Co^{2+} in function of the average *X* cation radius.

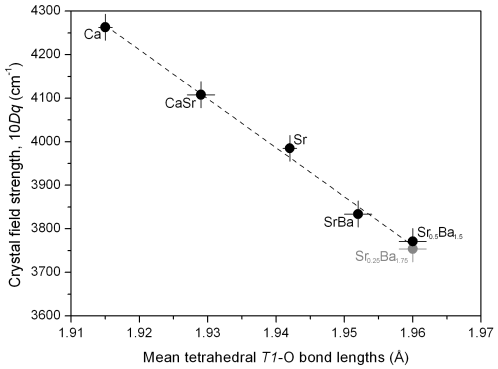

Figure E10. Crystal field strength of Co^{2+} in function of the *T1*–O distance.

Both the crystal field strength and Racah *B* parameter well reflect the progressive expansion of *T1* site along the Ca-Sr-Ba series: the longer the *T1*–O distance, the lower the 10*Dq* value (Figure E10) as expected from the Crystal Field Theory (Burns 1993). On the other hand, the longer the *T1*–O distance, the lower the Co and O orbitals overlapping, so explaining the slight decrease in covalency of the Co–O bond (Lever 1984). A way to estimate the spin-orbit coupling in complex electronic configurations, like that of Co^{2+}, is that of measuring the extent by which the $^4T_1$ (^4F) and $^4T_1$ (^4P) spin-allowed transitions are three-fold split (Torres et al. 2007). Such an estimation is more reliable by taking the difference between the high-energy and the low-energy subbands, when the mid-energy one is not easily discernible. The splitting measured by this way is increasing with the *T1*–O distance, i.e. going from Ca-åkermanite to Sr- and (Ba,Sr)-åkermanites, although the values are different from the $^4T_1$ (^4F) transition to the $^4T_1$ (^4P) one; a reasonable value is obtained by averaging the two transitions (Table E3). The band splitting, and

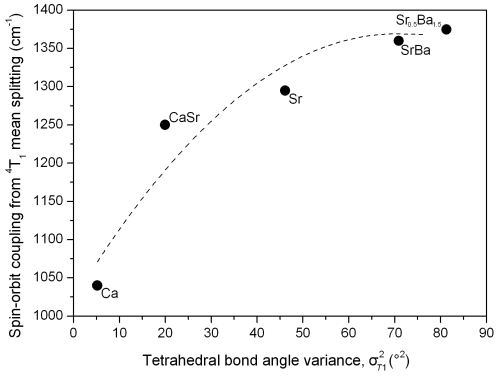

Figure E11. Co^{2+} spin-orbit coupling, gathered from spin-allowed band splitting, in function of the *T1*–O bond angle variance (σ^2).

therefore the spin-orbit coupling, grows with increasing bond angle distortion of *T1* tetrahedron (Figure E11).

Such a change to O–*T1*–O angles, by affecting the crystal field strength on the *e* and t_2 orbitals, has repercussions beyond the effect on spin-orbit coupling, i.e. the band splitting, likely affecting the vibronic transitions. Along with the Sr→Ca and Ba→Sr substitutions at site *X* – and the consequent angular distortion of tetrahedron *T1* – some vibronic bands are apparently "suppressed", like those occurring around 8000 and 17000 cm^{-1}, while others seem to be "activated", like those close to 5000 cm^{-1} (Figure E12).

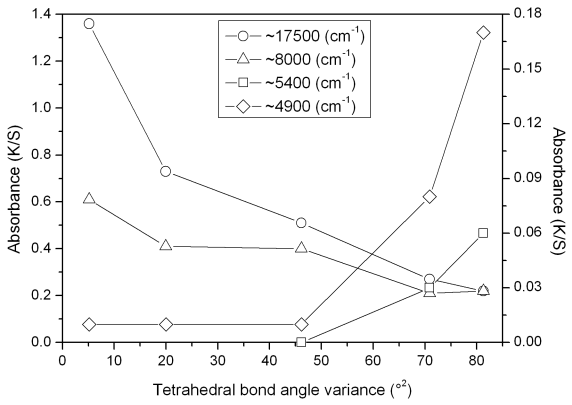

Figure E12. Intensity of some Co^{2+} vibronic bands in function of the *T1*–O bond angle variance (σ^2).

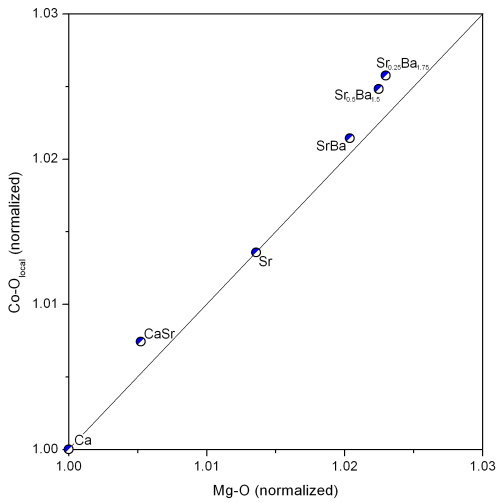

Figure E13. Comparison between normalized Mg–O and Co–O_{local} distances from undoped (see the value reported in the previous work, ***D***) and Co-doped (this work) (Ca,Sr,Ba)-åkermanite solid solutions, respectively.

● *Structural relaxation* – Taking into account the *Eq. (1.5)* [*reported in the introductive chapter of this dissertation*], by which $10Dq = \text{const} \cdot \langle \text{Co–O} \rangle^{-5}$, the value for the Co–O local distance in Co-åkermanite can be calculated (constant = 115504). Using such a constant and the different $10Dq$ values, it is possible to get the Co–O_{local} distances along the Ca-Sr-Ba series.

In order to evaluate the effect of the second next neighbours (Ca,Sr,Ba) on the *T1* site, the increase of the *T1*–O distance (in the undoped series where *T1* = Mg) can be compared with the increase of the Co–O_{local} distance (as inferred from DRS data, see Table E4). Comparing data normalized to åkermanite and Co-åkermanite = 1, it appears that the Co–O_{local} distance increases slightly more than the Mg–O distance (Figure E13). In other words, the melilite structure tends to relax more around Co^{2+} than Mg^{2+} once the *T1* tetrahedron turns increasingly more distorted (bond angles).

3. Section II. F. ♦ The inverse high temperature/high pressure relationship in the monoclinic $Ba_2MgSi_2O_7$ melilite-related structure

Note: This is a "*satellite*" study written in the 2011 by Ardit, M., Zanelli, C., Dondi, M., and Cruciani, G., reported as published (with few variations, if any, as described in the premise of this chapter) in the "*Periodico di Mineralogia*, 80, 155–165".

Abstract

High-temperature study of the synthetic melilite-related $Ba_2MgSi_2O_7$ (s.g. $C2/c$) was performed up to 1273 K. Linear thermal expansion coefficients along the unit cell edges and of the volume are $\alpha_a = 8.7 \times 10^{-6}$ K^{-1}, $\alpha_b = 11.0 \times 10^{-6}$ K^{-1}, $\alpha_c = 8.5 \times 10^{-6}$ K^{-1}, and $\alpha_V = 31.1 \times 10^{-6}$ K^{-1}, respectively, showing an anisotropic expansion behaviour characterized by $\alpha_a \approx \alpha_c < \alpha_b$. High-temperature data were then combined with high-pressure data (taken from the literature) for the same monoclinic sample. The "*inverse relationship*" of variation against temperature and pressure is observed for both the unit cell parameters and the (c/a) axial ratio as a function of the molar volume. A further comparison with melilite-type compound at ambient condition along the join $(Ca\text{-}Sr\text{-}Ba)_2MgSi_2O_7$ reveals that the tetragonal polymorph of the barium compound ($Ba_2MgSi_2O_7$) should be a metastable phase favoured by high pressure conditions.

► ***Introduction*** − In the last decade, many studies were dedicated to assess the high- and low-temperature behavior of melilite-type structures, especially to interpret and solve the phase transition from an incommensurately modulated (*IC*) to a normal (*N*) crystal structure occurring in melilite-type compounds with calcium occupying the eight-fold coordinated *X* site (e.g. Hemingway et al. 1986; Webb et al. 1992; Riester and Böhm 1997; McConnell et al. 2000; Kusaka et al. 2001; Bagautdinov et al. 2002; Merlini et al. 2005; Merlini et al. 2008). On the other hand, few works have been devoted to understand the high-pressure response of melilite structures (e.g. Yang et al. 1997; Haussühl and Liebertz 2004; Merlini et al. 2009), and no studies have been done about melilite-related compounds at non-ambient conditions.
In this paper, data on the thermal expansion of $Ba_2MgSi_2O_7$ melilite-related compound up to 1273 K and its structural response are presented. Furthermore, high-temperature data are combined with high-pressure data (Ardit et al. 2012) in order to test the "*inverse relationship*"

between structural variations due to temperature versus pressure (Hazen and Finger 1984), and to better understand the difference occurring between the two polymorph families.

► ***Experimental*** – [*for the experimental details (including: samples synthesis, data collection at both ambient and high-temperature conditions, and refinements strategy) readers are requested to refer to the chapter **2** of the present dissertation*].

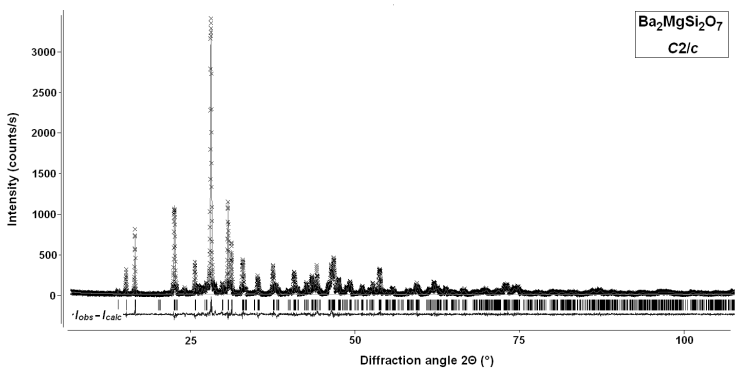

Figure F1. Plot of the Rietveld fitting of $Ba_2MgSi_2O_7$ melilite-related (s.g. *C*2/*c*) at ambient condition. The experimental data are indicated by crosses, the calculated pattern is the continuous line (among the crosses) and the lower curve is the weighted difference between the calculated and observed patterns. Vertical ticks mark the position of reflections for melilite phases.

In addition to the almost pure $Ba_2MgSi_2O_7$ melilite-related compound, a small amount of barium silicate ($BaSiO_3$) was detected, but quantitative Rietveld analysis indicates it is a minor phase with a mass fraction of ~4.7%. The presence of such minor compound was accounted for by running a multiphase refinement in which only the scale factor and the cell parameters were varied for the $BaSiO_3$ phase. Additionally, during the refinement of the atomic coordinates, a soft constraint was applied to the Si–O distances (i.e. Si–O1 = Si–O2 = 1.660 ± 0.010 Å, and Si–O3 = Si–O4 = 1.600 ± 0.005 Å), with the constraint weight being progressively lowered until a minimal value. The plot of the Rietveld refinement for the synthesized sample collected at ambient conditions is reported in Figure F1. The data obtained from this structural refinement and those previously reported by Aitasalo et al. (2006) for a same polycrystalline compound, are reported in Table F1 for comparison.

Table F1. Comparison of selected parameters for $Ba_2MgSi_2O_7$ melilites-related (s.g. *C*2/*c*) at ambient condition. Unit cell parameters, mean metal-oxygen bond distances, polyhedral volumes, mean interatomic angles, and their standard deviations (in parentheses) are listed.

	$Ba_2MgSi_2O_7$ (this study)	**$Ba_2MgSi_2O_7$** (Aitasalo et al. 2006)
Unit cell parameters		
a (Å)	8.4171(3)	8.4128(1)
b (Å)	10.7194(4)	10.7101(1)
c (Å)	8.4501(3)	8.4387(1)
β (°)	110.77(1)	110.71(1)
V (Å^3)	712.89	711.21
Mean metal-oxygen bond length (Å)		
⟨Ba–O⟩	2.820(12)	2.813(8)
⟨Mg–O⟩	1.966(3)	1.965(9)
⟨Si–O⟩	1.629(5)	1.630(8)
Polyhedral volume (Å^3)		
V_{BaO8}	33.41	33.19
V_{MgO4}	3.78	3.80
V_{SiO4}	2.19	2.19
Mean interatomic angles (°)		
⟨O–Si–O⟩	109.3(7)	109.2(5)
⟨Mg–O–Si⟩	117.5(5)	117.6(4)

► ***Results and discussion*** – The lattice parameters *a*, *b*, *c*, *β*, the unit cell volume *V*, and the thermal expansion coefficients (*TECs*) for the monoclinic $Ba_2MgSi_2O_7$ in the temperature range 303-1273 K are reported in Table F2. The coefficients of thermal expansion are given by

$$\alpha_l(T) = 1/l(\partial l / \partial T)_{X,P} \qquad \text{(F1)}$$

with composition and pressure held constants. Normalized unit-cell axes and volume plotted in Figure F2 scale linearly with increasing temperature. As expected from its layered nature, $Ba_2MgSi_2O_7$ does not exhibit an isotropic expansion behaviour (which would imply $\alpha_V \approx 3\alpha_{edge}$), but is characterized by $\alpha_a \approx \alpha_c$

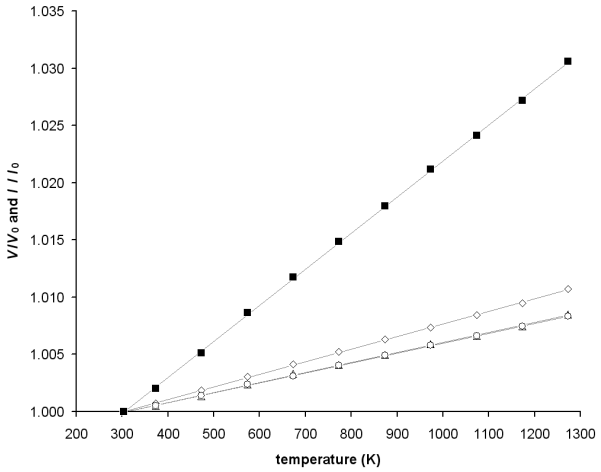

Figure F2. Unit cell volume (V/V_0: black filled squares) and lattice parameters (a/a_0: triangles; b/b_0: diamonds; and c/c_0: circles) of $Ba_2MgSi_2O_7$ melilite-related compound as a function of temperature. Lines through data-points are the fitting curves obtained from [Eq. (F1)] and TECs in Table F2.

$< \alpha_b$, namely the thermal expansion coefficient along the *b*-axis is higher than those along the tetrahedral layers which are almost equal. The same anisotropy is commonly found in melilite-type compounds studied under high-temperature, that always show a higher coefficient of thermal expansion perpendicularly to the tetrahedral layers.

Table F2. Thermal expansion data for the monoclinic $Ba_2MgSi_2O_7$, and their standard deviations (in brackets).

T (K)	*a* (Å)	*b* (Å)	*c* (Å)	*β* (°)	*V* (Å^3)	(*c*/*a*)*
303	8.4144(5)	10.7165(5)	8.4475(5)	110.76(1)	712.27(8)	0.6572(1)
373	8.4188(5)	10.7246(5)	8.4520(5)	110.73(1)	713.71(8)	0.6573(1)
473	8.4257(5)	10.7363(5)	8.4592(5)	110.68(1)	715.91(8)	0.6574(1)
573	8.4344(5)	10.7492(5)	8.4675(5)	110.64(1)	718.42(8)	0.6574(1)
673	8.4422(5)	10.7609(5)	8.4740(5)	110.59(1)	720.63(8)	0.6575(1)
773	8.4489(5)	10.7726(5)	8.4817(5)	110.55(1)	722.86(9)	0.6575(1)
873	8.4562(5)	10.7841(5)	8.4891(5)	110.51(1)	725.08(9)	0.6576(1)
973	8.4642(5)	10.7955(6)	8.4964(5)	110.47(1)	727.34(9)	0.6576(1)
1073	8.4704(6)	10.8071(6)	8.5034(6)	110.43(1)	729.45(9)	0.6577(1)
1173	8.4773(6)	10.8182(6)	8.5104(6)	110.38(1)	731.62(10)	0.6577(2)
1273	8.4857(6)	10.8316(6)	8.5178(6)	110.35(1)	734.06(10)	0.6579(2)
TEC ($\alpha \times 10^{-6}$ K^{-1})	*8.67(3)*	*11.01(4)*	*8.51(3)*		*31.05(9)*	

In numerous crystalline materials, structural changes are mainly function of the molar volume. For these materials the structural answers with decreasing temperature are the same to those with increasing compression (i.e. the so-called "*inverse relationship*" previously described by Hazen and Finger 1984). Therefore, it is interesting to compare the measured high-temperature data with those recently collected and described under high-pressure conditions by Ardit et al. (2012) for the melilite-related $Ba_2MgSi_2O_7$ compound.

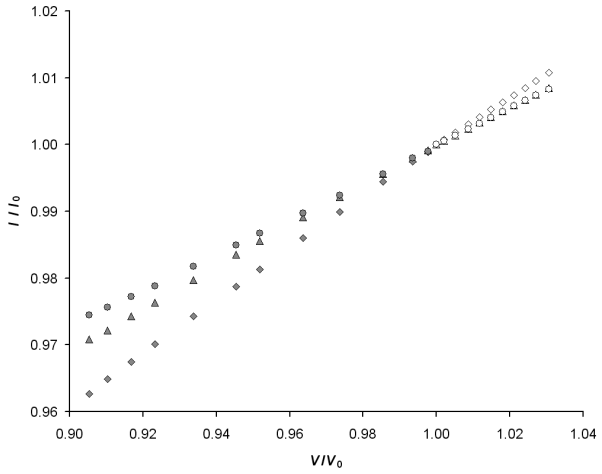

Figure F3. Almost ideal inverse relationship with pressure (grey filled symbols) and temperature (empty symbols), characterized by the continuous variation of the lattice parameters ($a/a_0 = b/b_0$: triangles; c/c_0: circles) versus V/V_0.

In Figure F3 is reported the variation of the normalized lattice parameters (a/a_0, b/b_0 and c/c_0) as a function of the normalized cell volume (V/V_0). For these parameters an almost ideal inverse relationship exists and both the pressure and temperature data sets describe almost linear trends along the same parameter.

The *c*/*a* axial ratio is a common way to estimate the anisotropy among the three orthogonal dimensions of the unit cell in tetragonal melilite-type compounds,

relating the tetrahedral layer corrugation (out of the *ab*-plane) with the dimension of the cation in the *X* site (along the *c*-axis). In order to obtain a similar and meaningful value also for the monoclinic melilite-related compounds we propose the $(c/a)^*$ axial ratio where: $c^* = \frac{b_{mon.}}{2}$ and $a^* = \sqrt{a_{mon.} \times c_{mon.} sen\beta}$. The resulting values of a such calculated $(c/a)^*$ ratio are plotted in Figure F4 as a function of the normalized cell volume (V/V_0).

Even if the inverse relationship is still maintained the high-pressure/high-temperature data sets show two distinct trends. The evolution of the axial ratio clearly highlights the subtle difference which exists and is expected in the anisotropic response of the melilite-related lattice towards high pressure vs. high temperature conditions.

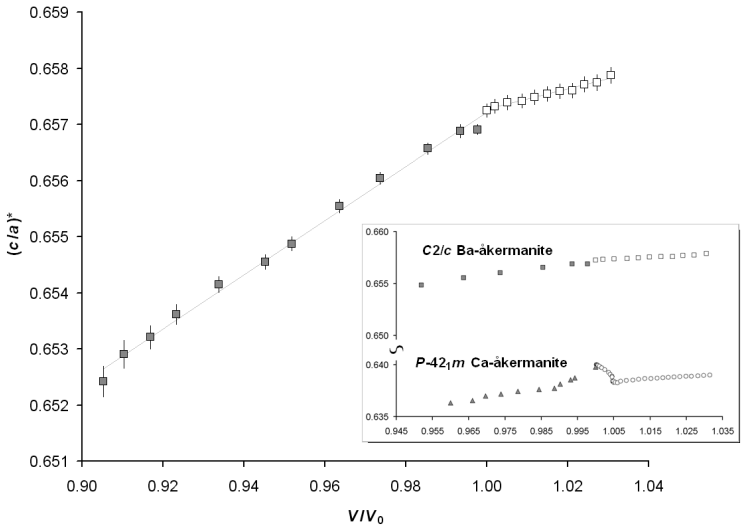

Figure F4. The inverse relationship for the monoclinic $Ba_2MgSi_2O_7$. Plot of the $(c/a)^*$ ratio versus normalized volume V/V_0 (pressure; grey filled symbols; temperature: empty symbols). The inset shows the comparison with the tetragonal Ca-åkermanite structure (HP and HT data from Yang et al. 1997 and Merlini et al. 2005, respectively). The two trends have very similar linear slopes, except within the region where Ca-åkermanite behaves as an incommensurately modulated structure.

The axial ratio in melilite-type (c/a) and related structures $(c/a)^*$ also varies as a function of the composition as described by the *T*/*X* dimensional misfit parameter. The latter is calculated as the ratio of the average tetrahedral bond distances over the ⟨*X*–O⟩ bond distances and reflects the geometrical constraints existing on the ratio of ionic radii of *T* and *X* cations for the occurrence of stable melilite-type structures. Therefore, the *T*/*X* parameter best defines the compositional field of existence for the different kinds of $X_2T1T2_2A_7$ compounds (e.g. Rothlisberger et al. 1990). The relationship between $(c/a)^*$ and *T*/*X* is illustrated in Figure F5 considering Ca- and Sr-åkermanites (tetragonal symmetry), the (Ba,Sr) solid solution term, which marks the transition from tetragonal to monoclinic symmetry (Ardit et al. 2012), and both monoclinic and tetragonal $Ba_2MgSi_2O_7$.

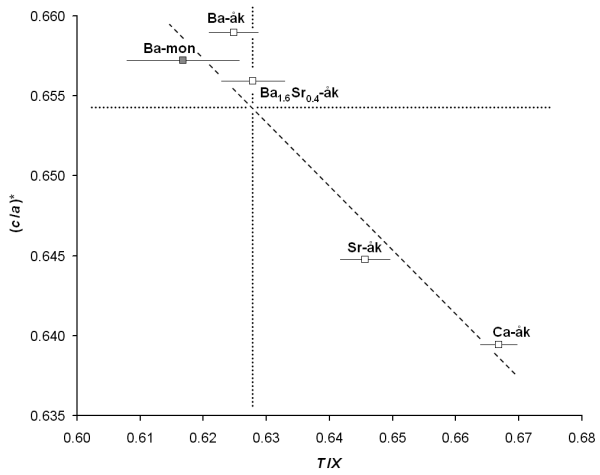

Figure F5. $(c/a)^*$ ratio as a function of the T/X ratio (see text for explanation). Grey filled symbol refers to the structure studied in this work.
Empty symbols and labels are as follows: [Ca-åk] = $Ca_2MgSi_2O_7$ Kimata and Ii 1981; [Sr-åk] = $Sr_2MgSi_2O_7$ and [$Ba_{1.6}Sr_{0.4}$-åk] = ($Ba_{1.6}Sr_{0.4}$)$MgSi_2O_7$ Ardit et al. 2012; [Ba-åk] = $Ba_2MgSi_2O_7$ Shimizu et al. 1995.

We suggest that when moving along this trend from the high T/X and low $(c/a)^*$ region [i.e. $T/X > 0.627$ and $(c/a)^* < 0.654$] to lower T/X and higher $(c/a)^*$, the $X_2MgSi_2O_7$ compounds are no longer stable with tetragonal symmetry (i.e. with melilite-type structure) and are favoured to adopt the monoclinic $Ba_2CuSi_2O_7$-type structure. It must be pointed out that, while the tetragonal Ca-, Sr- and ($Ba_{1.6}Sr_{0.4}$)-åkermanites, and the monoclinic $Ba_2MgSi_2O_7$ are stable forms which can be synthesized by solid state reactions, the tetragonal polymorph of $Ba_2MgSi_2O_7$ is a metastable form only obtained from melt crystallization under very carefully controlled conditions (Shimizu et al. 1995).

The above considerations allow some speculations to be made on the possible occurrence of a phase transition from monoclinic to lower (triclinic) or higher (e.g. tetragonal) symmetry induced by pressure or temperature in $Ba_2MgSi_2O_7$. If the $(c/a)^*$ limit of ~0.654 is taken as a boundary at which the changes of T/X dimensional misfit affects the relative stabilities of the monoclinic vs. tetragonal structure, then we expect that such a limit might also be reflected by a discontinuity on the trend of $(c/a)^*$ as a function of pressure and temperature. As a matter of fact, a careful inspection of Figure F5 reveals a subtle jump at about $(c/a)^* = 0.6545$ which occurs on the compression side. Examination of powder patterns around this value does not provide any indication for the occurrence of a phase transition. On the other hand, due to kinetic hindrances, it is unlikely that a reconstructive transformation as the one relating the layer topology of the two $Ba_2MgSi_2O_7$ polymorphs would take place under high pressure conditions at room temperature. Concerning the structural reasons why the tetragonal polymorph should be favoured by high pressure, besides the reduced dimensional misfit between the tetrahedral layer and the interlayer, we note that the most significant difference in the bond distances of the two $Ba_2MgSi_2O_7$ polymorphs is in the average ⟨Ba–O⟩ distance. In fact, ⟨Ba–O⟩ is equal to 2.793 Å for the tetragonal form (Shimizu et al. 1995) while is 2.820 Å

in the monoclinic form (Ardit et al. 2012). Furthermore, the monoclinic structures of $Ba_2T1Si_2O_7$ compounds (*T1* = Mg, Co, Zn, Cu) do not show Ba–O distances less then ~2.69 Å, while bond distances down to 2.648 Å and 2.627 Å are found in tetragonal $Ba_2MgSi_2O_7$ (Shimizu et al. 1995) and $Ba_2CoSi_2O_7$ (El Bali and Zavalij 2003), respectively. In other words, the Ba coordination environment in the tetragonal polymorph would be strongly favoured by high pressure compared to the monoclinic situation.

We also argue that the more intuitively conceivable transition from monoclinic to tetragonal at high temperature would never occur, as a solid state transformation, because Figure F5 clearly shows that the $(c/a)^*$ axial ratio increases with temperature, leading to *T*/*X* misfit values which are not compatible with the tetragonal melilite structure. This observation explains the many unsuccessful attempts we made in order to obtain the tetragonal phase by heating the synthesized monoclinic powder at high temperatures.

As a final remark, the present study represents a nice application of the comparative *P*-*T*-*X* (pressure-temperature-composition) approach in the sense of Hazen and Finger (1984).

3. Section III.

Structural relaxation around four-fold coordinated Co^{2+}: the case of the $Ca_2ZnSi_2O_7$–$Ca_2CoSi_2O_7$ melilite solid solution

***

3. Section III. G. ♦ Structural relaxation in tetrahedrally-coordinated Co^{2+} along the hardystonite–Co-åkermanite melilite solid solution

Note: This is a "*key*" study, by Ardit, M., Cruciani, G., and Dondi, M., in preparation for the "*Physics and Chemistry of Minerals*".

► ***Introduction*** − A recent work (Dondi et al. 2011, *see the next work, **H**, reported in this section*) promoted the Co-doped hardystonite structure as a new blue-coloured ceramic pigment. Although containing a much lower amount of cobalt (i.e. the best compromise between cobalt concentration and optical response was reached with a nominal cobalt doping of 0.3 apfu) than the traditional blue colorants (i.e. $CoAl_2O_4$ spinel and Co_2SiO_4 olivine), hardystonite-based pigments impart a deep blue colour on glazes and glassy coatings, by resisting aggressive media rich in CaO and ZnO, and avoiding specking defects of highly staining colorants. As previously illustrated [*see the description of melilite compounds at the beginning of the second section, **3. Section 2***], hardystonite ($Ca_2{}^{T1}Zn^{T2}Si_2O_7$) is a melilite-type structure with only one tetrahedral site (i.e. *T1*) where Co^{2+} can be hosted. This structural feature averts complications deriving from the order-disorder mechanisms in Co-Zn distribution between different tetrahedral sites (as, for instance, in willemite pigments, *see the third work, **I**, reported in this section*), or among different polyhedra (e.g. the intersite cation exchange occurring in spinel structures).

The aim of this work is to obtain deeper information on the mechanisms of coloration, and consequently discover why the same chromophore ion with the same valence state (i.e. Co^{2+}) hosted in the same polyhedral environment (i.e. tetrahedron) should bestow an enhanced colorimetric performance on a hardystonite-based structure compared to conventional blue colorants (i.e. cobalt aluminate spinel and cobalt silicate olivine) and Co-doped willemite

(Ozel et al. 2010). In order to disclose this point a series of samples along the $Ca_2ZnSi_2O_7$–$Ca_2CoSi_2O_7$ melilite-type solid solution were synthesized by solid-state reaction route and investigated by combining X-ray powder diffraction and electronic adsorption spectroscopy methods. Furthermore, in the introductive chapter of this dissertation it was been reported that several studies demonstrate that the stability of isostructural solid solutions, at the atomic scale, is affected by a structural relaxation around substituting cations. Although evidences of a large deviation from the Vegard's rule in tetrahedral site were already reported for simple binary solid solution (e.g. Levelut et al. 1991), all of the mentioned studies about silicate and oxide solid solutions of geological interest are mainly focused on cation substitution in octahedral coordination sites. The only exception is represented by the work of Hålenius et al. (2011) where the effects of the tetrahedral Mn^{2+}–Mg substitution were assessed along the $(Mg_{1-x}Mn_x)Al_2O_4$ spinel join.

Hence, considering the growing importance of this latter topic, the present study is also devoted to assess the degree of structural relaxation around four-fold coordinated Co^{2+} by combining the double viewpoint deriving from the long- (*XRPD*) and short-range (*EAS*) approaches.

► ***Experimental*** – [*for the experimental details (including: synthesis procedure, X-ray powder diffraction data collection, Rietveld refinements, and optical spectroscopy) readers are pleased to refer to the chapter **2** of the present dissertation*]. In addition to what reported in chapter ***2***, it is to point out that, during refinement of the atomic coordinates, a set of soft constraints were applied to the Zn–O and Si–O bond distances (i.e. 1.918 ± 0.003 ≤ Zn–O ≤ 1.938 ± 0.003 Å, and Si–O1 = 1.948 ± 0.005 Å, Si–O2 = 1.593 ± 0.003 Å, and Si–O3 = 1.615 ± 0.003 Å), with

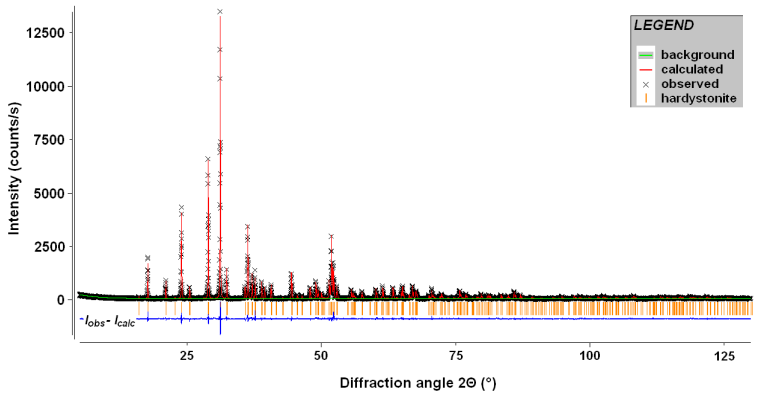

Figure G1. Final Rietveld fit for the $Ca_2Zn_{0.75}Co_{0.25}Si_2O_7$ melilite-type (s.g. *P*-42$_1$*m*) H25 sample. The experimental observed data are indicated by crosses (black), the calculated pattern is the continuous line (red) and the lower curve (blue) is the weighted difference between the calculated and observed patterns. Vertical ticks mark the position of reflections for the melilite phase (orange).

the constraint weight being progressively lowered until a minimal value. This procedure was done because of the incommensurately modulated character of the structures under investigation. The values of the *T*/*X* ratio, *T1*–O3–Si bond angle and σ^2_{Si} tetrahedral angular variance obtained through the Rietveld refinement of the samples here studied and listed in Table F1 would be located in *Figure E5* [*third chapter, section II, work **E***] between circles "7" ($Ca_2CoSi_2O_7$; Kimata 1983b) and "10" ($Ca_2ZnSi_2O_7$; Bindi et al. 2001a), stating the presence of an incommensurate modulation in these structures [*see text of the work **E*** (*third chapter, section II*) *for a more detailed explanation*].

The plot of the Rietveld refinement for the synthesized sample H25 is reported in Figure G1. Furthermore, agreement factors, refinement details, and structural parameters of the refined samples along the $Ca_2Zn_{1-x}Co_xSi_2O_7$ solid solution are summarized in Table G1.

Table G1. Goodness of fit (agreement factors), refinement details, and structural parameters with their standard deviations (in parentheses).

$Ca_2ZnSi_2O_7$–$Ca_2CoSi_2O_7$ (s.g. *P*-42_1m; Z = 2)					
Sample label	**H0**	**H25**	**H50**	**H75**	**H100**
nominal cobalt content (*apfu*)	0.00	0.25	0.50	0.75	1.00
agreement factors and refinement details					
Chi^2	1.849	1.678	1.473	1.577	1.499
R_{wp}	0.1150	0.1085	0.1010	0.0927	0.0967
R_p	0.0846	0.0824	0.0769	0.0706	0.0725
No. of Data	8333	8333	8333	8333	8333
No. of variables	96	90	90	90	90
R(*F*)	0.0377	0.0506	0.0539	0.0543	0.0615
R(F^2)	0.0625	0.0736	0.0841	0.0695	0.0814
No. of reflections	363	363	364	364	366
unit cell parameters					
a (Å)	7.8273(1)	7.8285(1)	7.8311(1)	7.8348(1)	7.8394(1)
c (Å)	5.0159(1)	5.0167(1)	5.0189(1)	5.0217(1)	5.0247(1)
V (Å^3)	307.31(1)	307.45(1)	307.79(1)	308.26(1)	308.80(1)
metal–oxygen bond distances (Å)					
Ca–O1	2.513(6)	2.501(8)	2.501(8)	2.532(12)	2.541(15)
Ca–O2	2.472(5)	2.477(7)	2.499(7)	2.470(12)	2.473(16)
Ca–O2' [x2]	2.697(4)	2.695(5)	2.688(6)	2.714(9)	2.720(12)
Ca–O3 [x2]	2.382(4)	2.382(5)	2.383(5)	2.411(7)	2.426(8)
Ca–O3' [x2]	2.743(4)	2.742(4)	2.734(4)	2.692(6)	2.663(7)
⟨Ca–O⟩	2.579(4)	2.577(6)	2.576(6)	2.580(9)	2.579(11)
T1–O3 [x4]	1.920(1)	1.924(1)	1.929(1)	1.933(1)	1.938(1)
Si–O1	1.644(2)	1.642(2)	1.645(1)	1.647(2)	1.648(2)
Si–O2	1.592(1)	1.592(1)	1.593(1)	1.593(1)	1.593(1)
Si–O3 [x2]	1.611(1)	1.614(1)	1.614(1)	1.615(1)	1.615(1)
⟨Si–O⟩	1.615(1)	1.615(1)	1.616(1)	1.617(1)	1.618(1)
bond angles (°)					
O3–*T1*–O3 [x4]	107.49(3)	107.59(3)	107.93(3)	108.42(3)	108.55(3)
O3–*T1*–O3 [x2]	113.51(6)	113.31(6)	112.59(5)	111.59(6)	111.34(5)
⟨O3–*T1*–O3⟩	109.50(4)	109.49(4)	109.48(4)	109.48(4)	109.48(4)
T1–O3–Si	118.69(8)	118.53(9)	118.13(9)	117.31(11)	117.28(13)
polyhedral distortion parameters					
λ_{T1}	1.0025	1.0023	1.0015	1.0007	1.0005
σ^2_{T1} (°^{2})	9.66	8.73	5.79	2.67	2.08
λ_{Si}	1.0115	1.0114	1.0116	1.0127	1.0147
σ^2_{Si} (°^{2})	50.92	50.69	51.56	54.79	61.70
T/*X* ratio	0.666	0.667	0.668	0.668	0.669

► *Results and discussion* –

● *Crystal structure* – Five compounds of Co-doped hardystonite with melilite-type structure were obtained through solid-state reaction synthesis; no impurities were detected. The variation of the normalized unit cell lattice (i.e. a/a_0 and c/c_0, respectively) and of the unit cell

volume (V/V_0) with composition across the hardystonite–Co-åkermanite solid solution is shown in Figure G2. A non-linear variation of the lattice constants as a function of the cobalt increasing is evident. Indeed, each data set presents a negative excess that can be perfectly fitted by the following quadratic equation:

$$a = 7.82727(5) + 0.00300(30) \cdot x_{Co} + 0.00926(33) \cdot x_{Co}^2 \qquad (R^2 = 0.999);$$
$$c = 5.01584(4) + 0.00278(23) \cdot x_{Co} + 0.00631(24) \cdot x_{Co}^2 \qquad (R^2 = 0.990);$$
$$V = 307.302(6) + 0.3961(32) \cdot x_{Co} + 1.1287(35) \cdot x_{Co}^2 \qquad (R^2 = 0.997).$$

On the other hand, both *a*- and *c*-axis show trends almost superimposed (within the *sd*) meaning that the structure accounts for the doping effect in a fairly isotropic way. As a matter of fact, the *c*/*a* axial ratio (i.e. the most common way to estimate the anisotropy among the three orthogonal dimensions of the unit cell in a tetragonal melilite structure) is constant for all the solid solution members ($c/a \approx 0.641$), meaning that the cell expansion, as a consequence to the Co for Zn substitution, is equally distributed through the tetrahedral layer (i.e. the *ab*-plane) and along the *c*-axis.

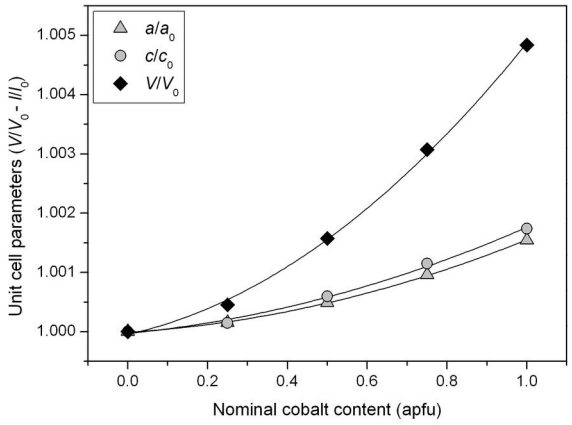

Figure G2. Variation of the normalized unit cell axes and volume of the Co-doped hardystonite samples along the $Ca_2Zn_{1-x}Co_xSi_2O_7$ solid solution as a function of the nominal cobalt content. Standard deviation is within the symbol size.

Similarly to what previously found in other structures, such as Co-doped gahnite (e.g. Tristan et al. 2005; Gaudon et al. 2009; Popović et al. 2009; Duan et al. 2011) and Co-doped willemite (Ozel et al. 2010), when the smaller Co^{2+} (0.58 Å) substitutes for the bigger Zn^{2+} (0.60 Å, Shannon 1976) in tetrahedral coordination, an unexpected lattice edges lengthening is observed. As already pointed out (Louisnathan 1969; Ozel et al. 2010), such behaviour can be interpreted as an evidence for the enhanced covalent character of the four-fold oxygen coordinated Zn^{2+} due to the strong hybridization of the sp^3 orbitals. With the cobalt doping increasing the covalence degree is lowered, promoting more ionic tetrahedral metal-oxygen bond distances.

Despite the nonlinear variation of the unit cell dimensions, the tetrahedral mean metal–oxygen bond distances scale linearly with the nominal cobalt amount increasing.

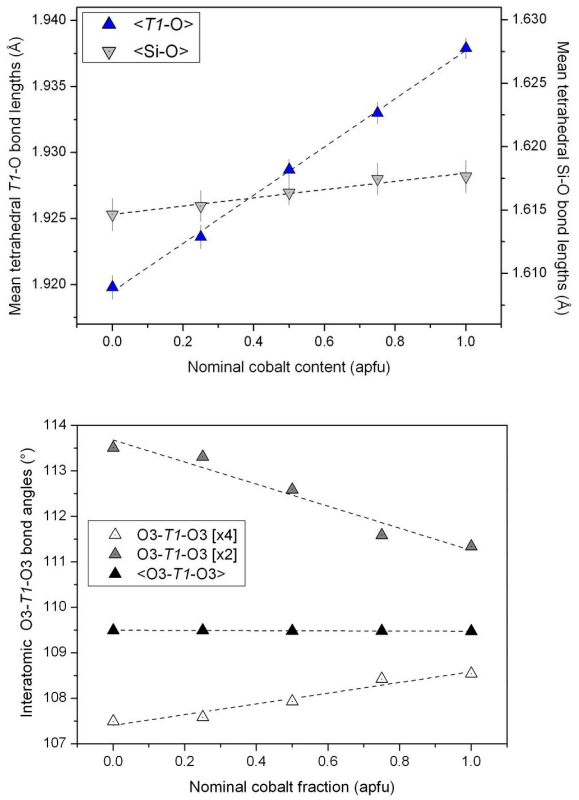

Figure G3. Variation of the mean tetrahedral metal-oxygen bond lengths (a) and of the interatomic O3–*T1*–O3 (b) as a function of the nominal cobalt doping. In figure b the standard deviation is within the symbol size.

Data shown in Figure G3a indicate that the Zn for Co replacement almost exclusively affects the *T1* site (i.e. maximum tetrahedral lengthening $\delta_{T1–O} = (T1–O)_{H100} - (T1–O)_{H0} = 0.018$ Å), whereas *T2* tetrahedral site, hosting the Si cation, undergoes a regular but lower lengthening of bond lengths (i.e. $\delta_{Si–O} = 0.003$ Å). Furthermore, data on the mean bond distances of the eight-coordinated *X* site, ⟨Ca–O⟩, listed in Table G1, show no variation within the standard deviation. A so defined variation of polyhedral bond lengths clearly indicates that the cobalt incorporation in the hardystonite structure mainly involves the first coordination shell (i.e. the *T1* tetrahedral site) where the cation substitution takes place.

Another important evidence, indicating the mechanism of cobalt incorporation in the hardystonite *T1* tetrahedral site, stems from the variation of the interatomic bond angles (Figure G3b). The analysis of the O3–*T1*–O3 angles (i.e. one pair of O3–*T1*–O3 angles different from the other two) reveals that, moving toward the Co-åkermanite end-member, the tetrahedral arrangement of the oxygen anions around the *T1* metal becomes more regular, tending to form a "*platonic solid*" (i.e. in our case an isometric tetrahedron). As a matter of fact, the three pairs of O3–*T1*–O3 angles converge to the ideal value of 109.47°.

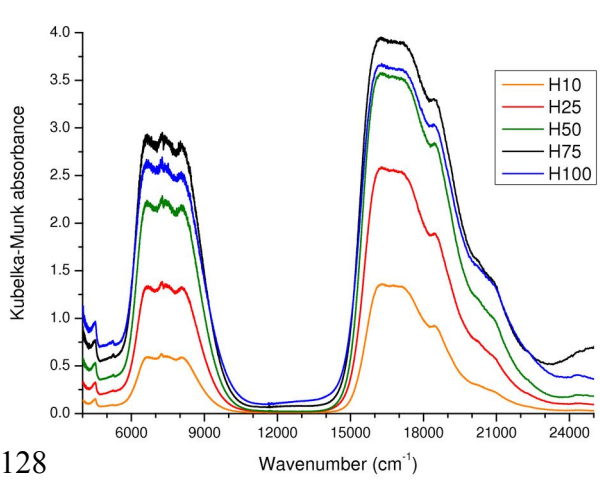

Figure G4. Optical spectra of the Co-doped hardystonite samples along the $Ca_2Zn_{1-x}Co_xSi_2O_7$ (with $0.1 \leq x \leq 1$) solid-solution.

● *Optical properties* – The optical spectra of Co-doped hardystonite samples exhibit

several strong absorption bands (Figure G4) with an optical density increasing in function of the nominal cobalt content. Such absorption bands originate from d-d transitions of Co^{2+} in tetrahedral coordination (and to a minor extent from vibronic effects).

Going in detail in the spectra interpretation, three regions can be distinguished (see Figure G5 and Table G2):

I) In the 4000–5500 cm^{-1} range, low intensity bands occur as a consequence of vibronic transitions and one of the three subbands caused by the splitting of the $^4T_2$ (^4F) transition (around 4500 cm^{-1}).

II) In the 5500–10500 cm^{-1} interval, the $^4T_1$ (^4F) transition is three-fold split and is found with some vibronic sidebands at higher energy (Figure G5A).

III) The optical spectra are particularly complex in the 14000–25000 cm^{-1} region (Figure G5B) where the $^4T_1$ (^4P) transition, split in three subbands, occurs together with several spin-forbidden transitions in the high energy part of spectra (over 18000 cm^{-1}).

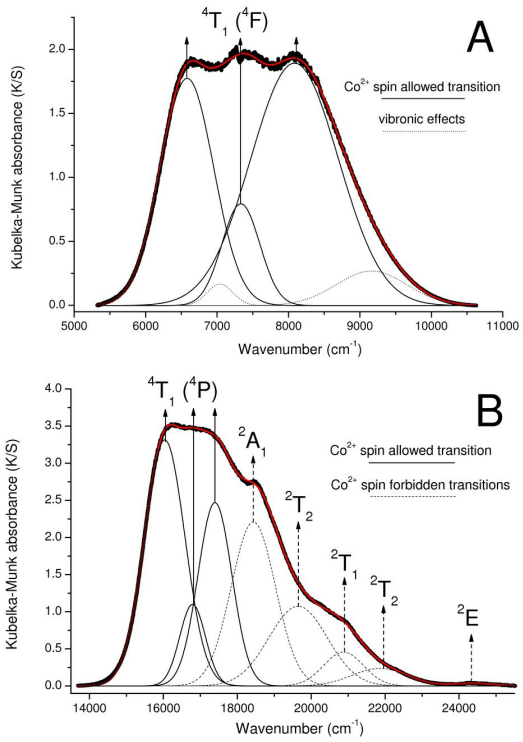

Figure G5. Optical spectra interpreted by deconvolution of individual bands in the 5500–10500 (A) and 14000–25000 cm^{-1} ranges (B). Electronic and vibronic transitions are indicated. Examples refer to sample $CaZn_{0.5}Co_{0.5}Si_2O_7$.

Averaging the energy of the three subbands attributable to $^4T_1$(^4F) and $^4T_1$(^4F) transitions of Co^{2+} in tetrahedral coordination, both the crystal field strength $10Dq$ and the Racah B_{35} parameter can be estimated. The value of $10Dq$ is increasing from 4225 cm^{-1} (Co end-term) to 4273 cm^{-1} (Co = 0.1 apfu) while Racah B_{35} parameter fluctuates in the 742-757 cm^{-1} range without any apparent relationship with the Co for Zn substitution (Table G2).

These trends imply that the mean local cobalt-oxygen distance, $\langle Co–O \rangle^{local}$, increases along the join with the amount of cobalt, while the degree of covalency does not significantly change.

Table G2. Optical properties of the hardystonite–Co-åkermanite solid solution.

Sample label	**H10**	**H25**	**H50**	**H75**	**H100**
Nominal cobalt content (apfu)	0.10	0.25	0.50	0.75	1.00
Energy of transition bands (cm^{-1})					
vibronic	4470	4460	4470	4460	4460
$^4T_2(^4F)$	4520	4530	4520	4530	4530
vibronic	7190	7170	7040	7160	7200
$^4T_1(^4F)$	6690	6660	6580	6570	6500
$^4T_1(^4F)$	7450	7450	7330	7300	7370
$^4T_1(^4F)$	8080	8090	8090	8070	8070
$^4T_1(^4P)$	15990	15980	16040	15920	15960
$^4T_1(^4P)$	16640	16510	16790	16680	16290
$^4T_1(^4P)$	17580	17300	17400	17330	17310
$^2A_1$	18370	18600	18440	18500	18670
$^2T_2$	19310	19860	19650	19840	19810
$^2T_1$	20860	21020	20880	20930	20830
$^2T_2$	*N.D.*	22100	21850	22080	22070
^2E	*N.D.*	24010	24440	24630	24280
$^4T_1(^4F)$ average	**7385**	**7375**	**7335**	**7320**	**7285**
$^4T_1(^4P)$ average	**16737**	**16597**	**16743**	**16643**	**16520**
Crystal field strength, $10Dq$ (cm^{-1})	**4273**	**4270**	**4228**	**4230**	**4225**
Racah B_{35} *parameter* (cm^{-1})	**752**	**743**	**757**	**750**	**742**
$\langle Co–O \rangle^{local}$ (Å)	**1.933**	**1.933**	**1.936**	**1.937**	**1.938**

● *Structural relaxation* – Local metal–oxygen lengths in the hardystonite–Co-åkermanite solid solution were achieved by means of the crystal field parameter $10Dq$ *according to Eq. (1.5)* [*reported in the introductive chapter of this dissertation*]. The obtained local distances are listed in Table G2.

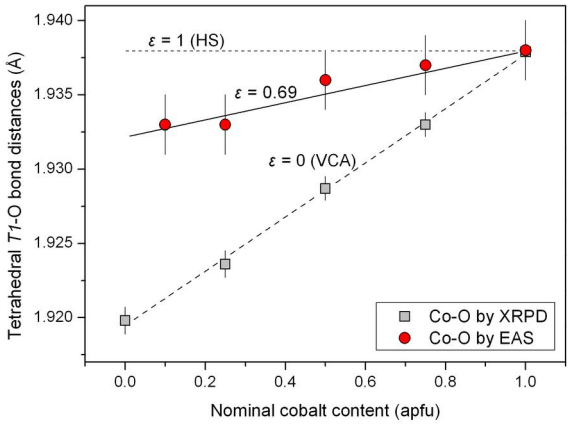

Figure G6. Coefficient of structural relaxation around $^{[IV]}Co^{2+}$ in the hardystonite–Co-åkermanite melilite-type solid solution.

The relaxation of the hardystonite structure around tetrahedrally coordinated Co^{2+} can be appreciated plotting both *T1*–O and $\langle Co–O \rangle^{local}$ tetrahedral bond distances versus nominal cobalt amount (Figure G6). The relaxation coefficient, calculated *according to Eq.(1.2)* [*see the introductive chapter of this dissertation*], yields ε = 0.69, implying an ideal tetrahedral bond length of ~1.932 Å for an infinite dilution of the cobalt in the solid solution (i.e. $\varepsilon_{\lim x(Co)\to 0}$). The relaxation coefficient here obtained is far from the requirements of the addivity Vegard's law where the structural relaxation is absent ($\varepsilon = 0$). On the other hand, such local relaxation value is the lowest found among those previously reported for other structures where the structural relaxation is considered for cations hosted in tetrahedral coordination. Specifically:

- $\varepsilon = 0.83$ for the spinel *sensu strictu*–galaxite ss (Hålenius et al. 2011);
- $\varepsilon = 0.89$ for the Co-doped willemite structure.

3. Section III. H. ♦ Co-doped hardystonite, $Ca_2(Zn,Co)Si_2O_7$, a new blue ceramic pigment

Note: This is a "*satellite*" with "*technological*" character study written in the 2011 by Dondi, M., Zanelli, C., Ardit, M., and Cruciani, G., reported as published (with few variations, if any, as described in the premise of this chapter) to the "*Journal of the American Ceramic Society*, 94, 1025–1030".

Abstract

Raising cost, limited reserves, and toxicity make a pressing need to reduce the consumption of cobalt in the ceramic industry, trying to improve efficiency and sustainability of pigments. A novel blue colorant, based on the melilite structure, has been developed by searching for a ceramic pigment stable in very aggressive media, like the calcium- and zinc-rich glazes used in porous tiles (stoneware and monoporosa). Hardystonite was selected as a typical crystalline compound found in these coatings, which has just one four-fold crystallographic site where Co^{2+} ions can be accommodated, thus ensuring its unrivalled blue colour. Five samples ($Ca_2Zn_{1-x}Co_xSi_2O_7$ with x = 0.05, 0.1, 0.2, 0.3 and 0.4) were prepared by solid state synthesis in industrial-like conditions (~95% yield) and characterized by XRD, DRS, SEM-EDS and technological testing. Increasing cobalt doping gives rise to a gradual expansion of the hardystonite unit cell, unexpected on the basis of Zn^{2+} and Co^{2+} ionic radii, attributed to a change of the covalent character of M–O bonding. Optical spectra are dominated by the strong absorption bands of Co^{2+} in tetrahedral coordination (crystal field strength Dq = 421 cm^{-1}, Racah B parameter = 793 cm^{-1}). The best compromise between cobalt concentration and optical response was found to be around x = 0.3. The hardystonite pigment bestows a deep blue colour on glazes and glassy coatings, withstanding aggressive media rich in CaO and ZnO better than industrial blue pigments (cobalt aluminate, spinel) with similar colour efficiency than industrial blue dyes (cobalt silicate, olivine) but with the advantage to avoid specking defects of highly staining colorants.

► ***Introduction*** − The blue colorants currently used by the ceramic industry are spinels $(Co,Zn)Al_2O_4$ and $Co(Cr,Al)_2O_4$ (DCMA numbers 13-26-2, 13-28-2 and 13-29-2), olivine Co_2SiO_4 (DCMA 5-08-2), phosphates $Co_3(PO_4)_2$ and $CoLiPO_4$ (DCMA 8-11-1 and 8-12-1, respectively) and borate $(Co,Mg)B_2O_5$ (DCMA 2-02-1) (Eppler 1998; DCMA 1982;

ICS 2003). Only spinels generally behave as a true pigment, bestowing colour on glazes and vitrified bodies by a heterogeneous mixture of crystals dispersed in the vitreous phase formed during firing, while olivine, borate and phosphates act as dyes, as their crystals dissolve in the glassy matrix (Eppler 1987 and 1998). Cobalt appears to be hardly replaceable in order to achieve a deep blue coloration, since alternative chromophores, as in the case of V-doped zircon (DCMA 14-42-2), impart a turquoise colour. However, raising cost and limited reserves are turning cobalt into a strategic commodity, which the ceramic industry has an increasing difficulty to access (Eppler 1987; Llusar et al. 2001). From here stems the demand for enhanced efficiency of blue colorants in order to lower as much as possible the cobalt consumption. New structures have been proposed for this purpose: willemite Zn_2SiO_4 and hibonite $CaAl_{12}O_{19}$, where Co doping imparts a blue hue and Ni doping gives rise to turquoise shades (Forés et al. 2000; Forés et al. 2001; Costa et al. 2009; Leite et al. 2009), or Al_2O_3-MoO_x, a greyish-blue mordent pigment (Dondi et. al 2008). On the other hand, new dyes have been recently developed: $(Co,Cu)FeOPO_4$ and $FeCoOPO_4$ (Meseguer et al. 2008), or $CoNH_4PO_4$ (Jonynaitë et al. 2008). Moreover, there is a growing interest on blue nanopigments, suitable for digital decoration techniques, like ink-jet printing (Ahmed et al. 2008; Gardini et al. 2008; Cavalcante et al. 2009).

Another aspect needing to be improved is the pigment behaviour in glazes for porous wall and floor tiles (monoporosa and stoneware bodies). As a matter of fact, conventional pigments suffer a deterioration of their colouring performance in such Zn- and Ca-rich glazes due to chemical attack during fast firing from 1100 to 1170 °C (Eppler 1987; Monari and Manfredini 1996; Escardino et al. 2002; Dondi et al. 2007).

The present study was undertaken to search for a new crystal structure suitable to act as a blue pigment especially in glazes rich in zinc and calcium. This target was pursued combining two criteria: (i) having a structure with the unrivalled colouring efficiency of Co^{2+} ions tetrahedrally coordinated by oxygens (Burns 1993), and (ii) finding a crystal phase chemically stable in the aggressive environment of a Zn-Ca-borosilicate melt at high temperature. In this kind of glazes, there are phases which crystallize during firing, like willemite, gahnite ($ZnAl_2O_4$), anorthite ($CaAl_2Si_2O_8$), wollastonite ($CaSiO_3$), diopside ($CaMgSi_2O_6$) and hardystonite ($Ca_2ZnSi_2O_7$) (Knowles and Freeman 2004; Sorlí et al. 2004; Siligardi et al. 2009). This latter has attracted our attention because it is a calcium zinc silicate – therefore

presumably more stable in systems rich in Ca and Zn than calcium silicates or zinc silicate – having only one single tetrahedral site where Co^{2+} ions can be accommodated (Hagiya et al. 1993), so avoiding the order-disorder complications in Co-Zn distribution between different tetrahedral sites, as occurs for instance in willemite pigments (Ozel et al. 2010). In fact, hardystonite crystallizes in the tetragonal system, space group $P\text{-}42_1m$, with general formula $X_2T1T2_2A_7$, where X is a typically a large monovalent to trivalent cation (e.g. Na^+, Ca^{2+}, Y^{3+}), $T1$ and $T2$ are small divalent to tetravalent cations (e.g. Zn^{2+}, Mg^{2+}, Al^{3+} in $T1$; Si^{4+}, Al^{3+} in $T2$); and A is O^{2-}, but also F^-, S^{2-} or N^{3-}. Its structure is characterized by layers of linked tetrahedra ($T2_2O_7$ dimers and four-fold coordinated $T1$ cations) connected by X cations in a distorted eight-coordinated antiprismatic site (Bindi et al. 2001). Tetrahedral site $T1$ represents a quasi-regular environment with 4 identical metal–oxygen lengths, but one pair of O–M–O angles different from the other two, so resulting in an intermediate point symmetry (-4) with respect to the regular tetrahedral site of spinel (T_d) and the strongly distorted fourfold coordinated site in glasses.

Hardystonite is not new for technological applications: it has been recently proposed as host lattice for phosphors (Hao and Wang 2007; Kamioka et al. 2007), and as biomaterial (Wu et al. 2005). Another melilite (åkermanite, $Ca_2MgSi_2O_7$) was proposed as blue pigment with a cobalt doping up to 24% in weight (Bystrikov et al. 1982). [*for further details on melilite-type structures readers are requested to refer to the general notes at the begin of the* ***SectionII*** *- chapter* ***3***].

This work is aimed at assessing the potential as ceramic pigment of cobalt-doped hardystonite by solid state synthesis, powder characterization (crystal structure and optical properties) and testing its technological behaviour in ceramic coatings.

► ***Experimental*** – [*for the experimental details (including: samples synthesis, data collection by X-ray powder diffraction, Rietveld*

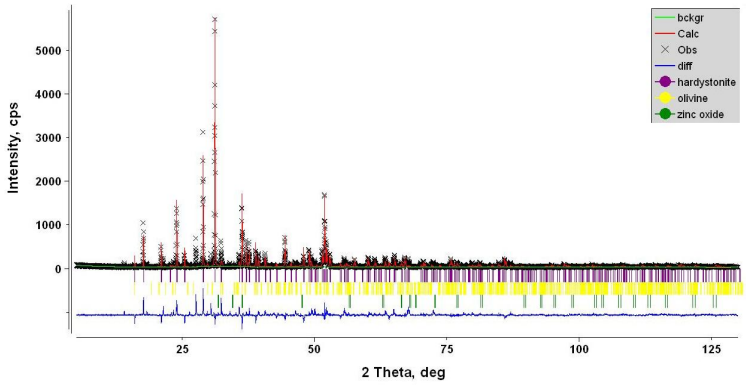

Figure H1. Plot of Rietveld refinement performed on X-ray powder diffraction data of sample H30. The experimental data are indicated by crosses, the calculated pattern is the continuous line and the lower curve is the weighted difference between the calculated and observed patterns. Vertical ticks mark the position of allowed reflections for the hardystonite phase present in the sample and of minor phases.

*refinements, and UV-visible-NIR spectroscopy) readers are requested to refer to the chapter **2** of the present dissertation*].

Unit cell parameters of the hardystonite samples and pigment phase composition are listed in Table H1, while the Rietveld refinement plots of the sample H30, $Ca_2(Zn_{0.70}Co_{0.30})Si_2O_7$, is reported in Figure H1.

● The microstructure of the as-synthesized hardystonite pigment H30 was observed under SEM (Cambridge StereoScan 360, graphite sputtered powders, Leica, Cambridge, U.K.). In situ chemical analyses were performed using Link Analytical electron microprobe (High Wycombe, U.K.) (average of 38 spots).

● Technological behavior was assessed by adding the pigment different ceramic glazes (S2 and S5) and glassy coatings (F2 and F5) for porous wall and floor tiles, whose chemical and physical properties are reported in Table 2.6 [*Chapter **2***]. Hardystonite pigment was contrasted with high-quality industrial blue colorants: cobalt aluminate (spinel) and cobalt silicate (olivine). In order to compare the same amount of cobalt in the coating (0.35% CoO), the hardystonite pigment H30 was added into coatings at 5 wt%, while spinel and olivine additions were 1.2% and 0.5%, respectively. Coating application was carried out by wet mixing, sprinkling the slip on a porous ceramic tile, that was dried in oven and fast fired in an electric roller kiln (1100 °C maximum temperature, 45 min cold-to-cold). Color was measured by diffuse reflectance spectroscopy (HunterLab Miniscan MSXP4000, Reston, VA, 400–700 nm, D_{65} standard illuminant, 10° observer, white glazed tile reference x = 31.5, y = 33.3) and expressed as CIE-Lab coordinates.

Table H1. Unit cell parameters and pigment phase composition.

Sample	Unit	H5	H10	H20	H30	H40
Cobalt fraction	apfu (*x*)	0.05	0.10	0.20	0.30	0.40
Hardystonite unit cell						
a	Å	7.8208(2)	7.8206(2)	7.8210(3)	7.8224(4)	7.8253(3)
c	Å	5.0154(2)	5.0165(2)	5.0174(2)	5.0181(3)	5.0193(2)
Volume	Å^3	306.76(2)	306.81(2)	306.91(3)	307.06(4)	307.36(3)
Pigment phase composition						
Hardystonite	% wt.	95.1	94.2	95.3	95.6	95.9
Olivine	% wt.	3.0	3.6	3.6	3.9	3.5
Zincite	% wt.	1.9	2.2	1.1	0.5	0.6

► ***Results and discussion*** – The lattice parameters and the unit cell volume of the refined crystal structures are reported in Table H1. Cobalt doping gives rise to a progressive lattice parameters and unit cell volume increasing (Figure H2). This expansion is unpredictable on the basis of ionic radii (Zn^{2+} 0.60 Å, Co^{2+} 0.58 Å, in tetrahedral coordination) but, as reported by Louisnathan (1969), it can be explained by a varying covalent character of the *M*–O bonding. In fact, the strong hybridization of sp^3 orbitals enhances the Zn–O bond covalent nature, so particularly short Zn–O distances are promoted (Torres et al. 2007). The result of the Co → Zn substitution implies a more ionic bond and longer *M*–O distance, as observed also in willemite and gahnite (Gaudon et al. 2009; Ozel et al. 2010).

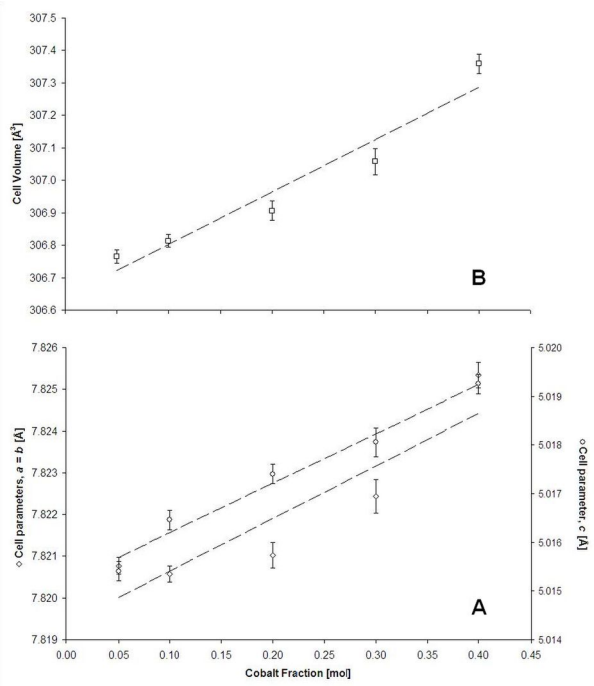

Figure H2. Variation of the unit cell parameters (A), and unit volume cell (B) of hardystonite pigments as a function of cobalt doping. The parameters are represented by the following symbols: *a* = *b* (diamonds), *c* (circles), and *V* (squares).

The micrograph of hardystonite sample H30 reveals a heterogeneous distribution of the particle size, ranging from 5 μm to the submicrometer range, mostly with botryoidal grains and rounded lamellae (Figure H3). The composition of the hardystonite pigment H30, as determined by in situ EDS analysis, is summarized in Table H2; the actual Co content is close to the nominal value.

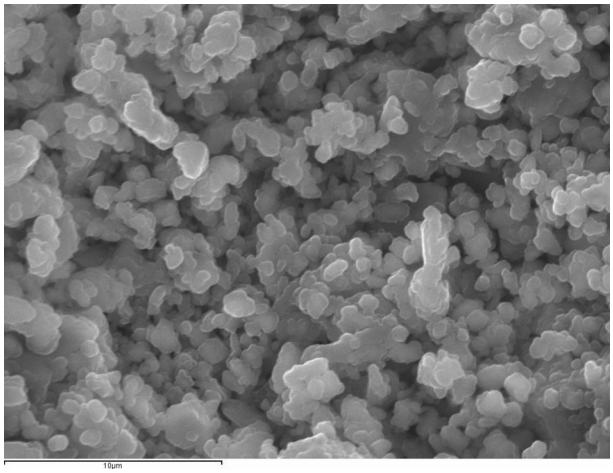

Figure H3. SEM micrograph of the as-synthesized hardystonite pigment H30; scale bar is 10 µm.

Table H2. Chemical composition of the hardystonite pigment H30. (SD, standard deviation).

Chemical composition	% wt.	s.d.
SiO_2	40.23	0.55
ZnO	18.01	1.58
CoO	5.72	0.46
CaO	35.13	5.86
Crystallochemical composition	*apfu*	*SD*
O	14	
Si	4.145	0.057
Zn	1.371	0.120
Co	0.471	0.039
Ca	3.869	0.645
Cobalt doping	*Molar fraction*	*SD*
Co/(Zn+Co)	0.26	0.020

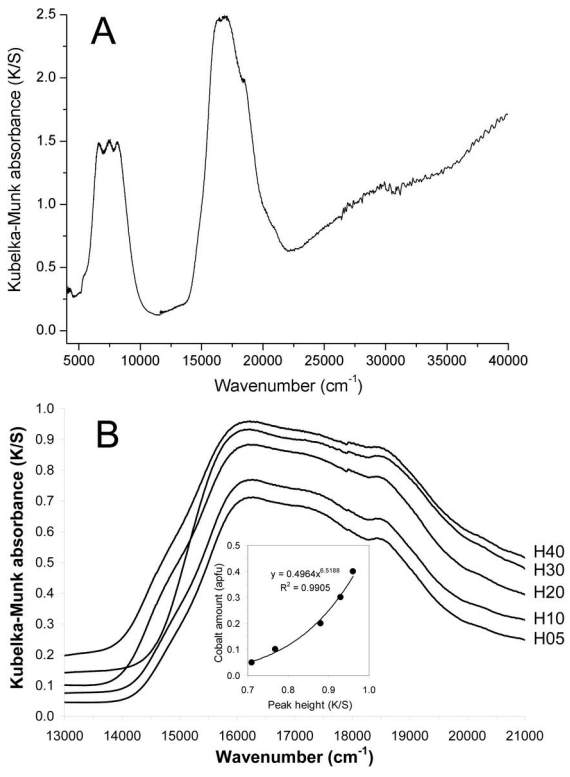

Figure H4. Diffuse reflectance spectra of hardystonite pigments: (A) full UV-visible-NIR spectrum of sample H30; (B) visible spectra of pigments with increasing cobalt content (in the inset: relationship of cobalt amount versus intensity of peak at ~16000 cm^{-1}).

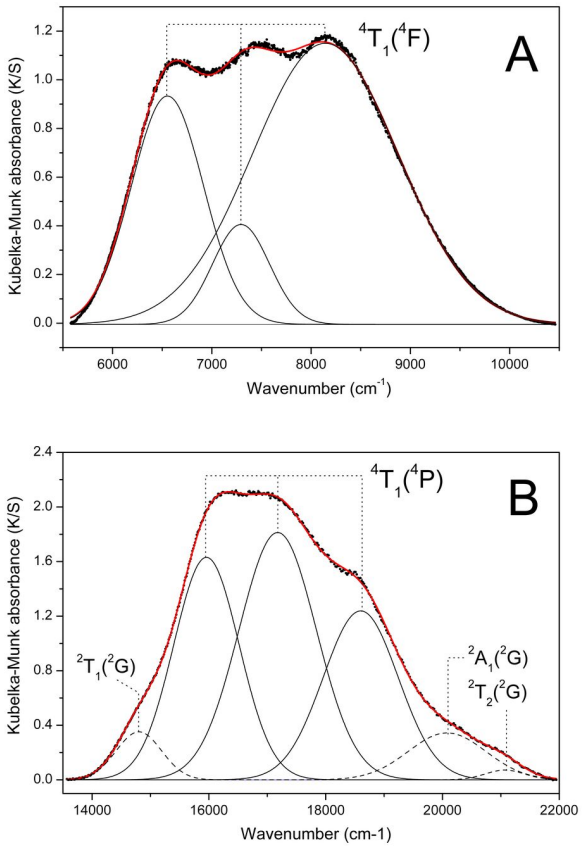

Figure H5. Optical spectrum of pigment H30 and its deconvolution in the electron absorption bands of Co^{2+} in tetrahedral coordination in the NIR (A) and visible (B) ranges.

Optical spectra of hardystonite pigments are dominated by the very strong absorption bands (Figure H4A), which exhibit an increasing optical density as a function of the nominal cobalt content by an expected power law dependence (Figure H4B). These bands are attributable to electron transitions of Co^{2+} in tetrahedral coordination: $^4T_2(^4F)$ and $^4T_1(^4F)$ in the near infrared (Figure H5A) as well as $^4T_1(^4P)$, associated to spin-forbidden transitions, in the visible spectrum (Figure H5B). The optical properties of hardystonite H30 are the following: crystal field strength $10Dq$ = 4210 cm^{-1}, interelectronic repulsion Racah parameter B = 793 cm^{-1} and the spin-orbit parameter λ = -126 cm^{-1}. The $10Dq$ value is slightly higher than known values for Co^{2+} in fourfold coordination in oxides and silicates (3900–4100 cm^{-1}) while the Racah B parameter falls within the variation range in the same compounds (700–830 cm^{-1}) suggesting a similar degree of covalence of the Co–O bonding (Burns 1993; Lever 1984).

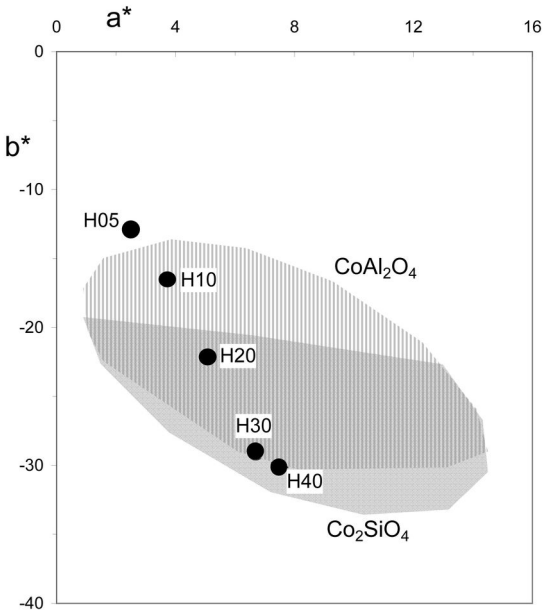

Figure H6. Colour of cobalt-doped hardystonite pigments, dispersed in glassy coating F2, compared with conventional cobalt aluminate (spinel) and cobalt silicate (olivine) pigments (this work and Eppler 1987).

The best compromise between cobalt concentration and optical response was searched for by contrasting colorimetric parameters of hardystonite pigments with those of industrial colorants (Figure H6). A deep blue coloration (i.e. b* > 25) is obtained for a cobalt concentration around x = 0.3; for this reason, the sample H30 was selected for the technological characterization.

The hardystonite pigment behaves satisfactorily in ceramic applications by developing a deep blue colour, so withstanding to aggressive media containing high to very high amounts of calcium and zinc (Table H3). In particular, hardystonite exhibits a colouring performance comparable with that of olivine, which acts as a dye resulting totally dissolved in the glassy phase, and distinctly better than that of spinel (Figure H7). Hardystonite pigments, thanks to their limited cobalt concentration, have the advantage to be added in suitable amounts

(usually 3–5% in weight of the coating) so avoiding specking defects that occur using low amounts of highly staining dyes and pigments (Eppler 1987 and 1998).

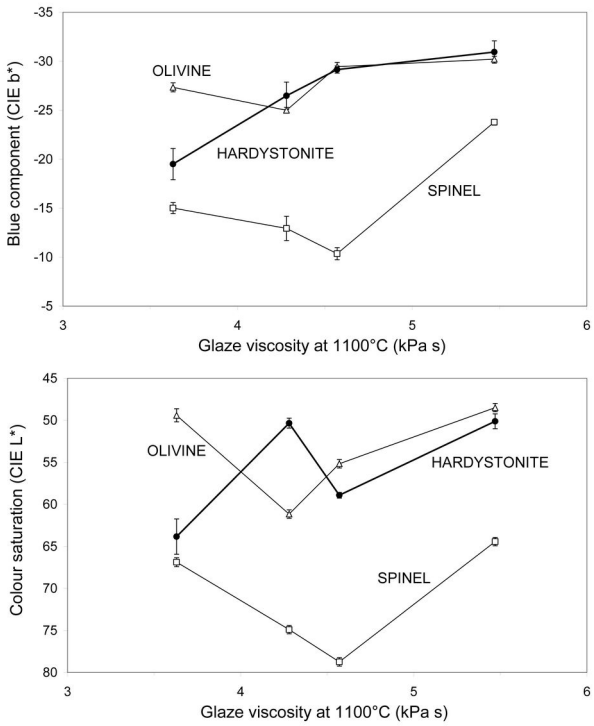

Figure H7. Colour performance of hardystonite pigment in ceramic glazes of different viscosity (Table 2.6) in comparison with cobalt aluminate (spinel) and cobalt silicate (olivine).

Table H3. CIE $L^*a^*b^*$ colour of glazes (S2 and S5) and glassy coatings (F2 and F5) containing blue colorants (0.35% wt. CoO). [L^* (100 = white, 0 = black); a^* (+red, -green); b^* (+yellow, -blue); SD, standard deviation].

Colorant	Coating	*L**	SD	*a**	SD	*b**	SD
Hardystonite (H30)	F2	63.8	2.1	4.8	0.5	-19.5	1.6
$Ca_2Zn_{0.7}Co_{0.3}Si_2O_7$	S2	50.1	0.9	8.2	0.3	-30.9	0.6
	F5	50.3	0.6	5.0	0.2	-26.5	0.7
	S5	58.9	0.3	4.5	0.1	-29.2	0.2
Olivine (O)	F2	49.4	0.8	8.3	0.2	-27.3	0.2
Co_2SiO_4	S2	48.5	0.2	8.6	0.2	-30.2	0.1
	F5	61.2	0.1	5.6	0.1	-25.0	0.1
	S5	55.2	0.2	7.5	0.1	-29.4	0.2
Spinel (S)	F2	66.9	0.5	2.7	0.1	-15.0	0.3
$CoAl_2O_4$	S2	64.4	0.1	1.2	0.0	-23.8	0.1
	F5	74.9	0.1	0.8	0.1	-12.9	0.6
	S5	78.7	0.1	-0.7	0.1	-10.4	0.3

► ***Conclusion*** − A new blue-coloured ceramic pigment, based on the hardystonite structure, was developed looking especially at application in highly aggressive glazes and glassy coatings for stoneware and monoporosa tiles. Containing a much lower amount of cobalt than conventional ceramic colorants, the hardystonite pigment is able to significantly reduce the Co consumption, improving manufacturing cost and sustainability, also thanks to its easy synthesis at a rather low temperature.

Hardystonite pigments exhibit a colouring performance, once the same amount of cobalt is used, that is better than cobalt aluminate spinel and equal to cobalt silicate olivine, but with the advantage to avoid defects typical of highly staining dyes.

The wide range of isomorphic substitutions allowed in the melilite structure makes it particularly suitable for tailoring structural modifications and optical properties. Work is in

progress involving substitution of Mg or Al after Zn on the one side, and Sr, Ba or Y after Ca on the other side, as well as using further chromophore ions beyond Co^{2+}.

3. Section III. I. ♦ Co-doped willemite ceramic pigments: technological behaviour, crystal structure and optical properties

Note: This is a "*satellite*" with "*technological*" character study written in the 2010 by Ozel, E., Yurdakul, M., Turan, S., Ardit, M., Cruciani, G., and Dondi, M., reported as published (with few variations, if any, as described in the premise of this chapter) in the "*Journal of the European Ceramic Society*, 30, 3319–3329".

Abstract

Cobalt-doped willemite is a promising blue ceramic pigment, but some important aspects concerning crystal structure, optical properties and technological behaviour are still undisclosed. In order to get new insight on these features, willemite pigments ($Zn_{2-x}Co_xSiO_4$, $0 < x < 0.3$) were synthesized by the ceramic route and characterized from the structural (XRPD with Rietveld refinement), optical (DRS and colorimetry), microstructural (SEM, STEM, TEM, EDX, EELS) and technological (simulation of the ceramic process) viewpoints. The incorporation of cobalt in the willemite lattice, taking preferentially place in the Zn1 tetrahedral site, induces an increase of unit cell parameters, metal-oxygen distances, and inter-tetrahedral tilting. It causes shifting and enhanced splitting of spin-allowed bands of Co^{2+} in tetrahedral coordination, implying slight changes of crystal field strength *Dq* and Racah *B* parameter, but increasing spin-orbit coupling parameter λ. Willemite pigments impart deep blue hue to ceramic glazes and glassy coatings with a colouring performance better than commercial Co-bearing colorants in the 800–1200 °C range. Detailed SEM-TEM investigation and microanalysis proved that no diffusion phenomena occur at the pigment-glassy coating interface and that willemite pigments are chemically inert during firing at 1050 °C.

► ***Introduction*** − Willemite, Zn_2SiO_4 (trigonal, *R*-3H) with phenakite structure is an orthosilicate with all atoms in general position and composed by a framework of tetrahedra accommodating zinc and silicon in three different fourfold crystallographic sites: two slightly different zinc sites Zn1 (⟨Zn–O⟩ 1.950 Å) and Zn2 (⟨Zn–O⟩ 1.961 Å), and Si (⟨Si–O⟩ 1.635 Å), so resulting in rhombohedral symmetry with lattice parameters $a = b$ ~13.948 Å, and c ~9.315 Å(Bragg and Zachariasen 1930; Hang et al. 1970; Klaska et al. 1978; McMurdie et al. 1986)

Such a rigid lattice, with only non-centrosymmetric cationic sites, gives the chance to get special optical properties; in fact, synthetic willemite is meeting an increasing interest for its potential as phosphor host (e.g. with Eu^{3+}, Mn^{2+}, Tb^{3+}, Ce^{3+} doping) (Brunold et al. 1996; Ahmadi et al. 2000; Van der Kolk et al. 2000; Sreekanth Chakradhar et al. 2004; Wan et al. 2006; Yan and Huang 2007), glass-ceramics (Rudkovskaya et al. 2003; Hu et al. 2005), dielectric ceramics for wireless applications (Ohsato 2005), and it has been proposed, because of its high-temperature stability, as ceramic pigment (Chandrappa et al. 1999; Forés et al. 2000; Llusar et al. 2001). As in the case of the well known spinel pigments $(Zn,Co)Al_2O_4$ (DCMA 13-26-2 and 13-28-2), a deep blue colour is obtained by doping the willemite structure with cobalt, that replaces zinc ions in tetrahedral positions. The advantage of willemite pigments comes from suitably saturated hues that can be obtained with a lower Co amount with respect to spinel $CoAl_2O_4$ or olivine (Co_2SiO_4, DCMA 5-08-2) colorants(Forés et al. 2000).

In this study, production and characterization of willemite ceramic pigments, obtained by using ZnO powders which are industrial by-products, were undertaken. Different pigment compositions, having $Zn_{2-x}Co_xSiO_4$ stoichiometry (where $0 < x < 0.3$), were designed and synthesized in order to get a new insight into the interrelationships between crystal structure, coloration and technological behaviour. In particular, structural features (XRD), optical properties (DRS) and thermal stability and pigment-glaze interactions (SEM, TEM, EELS) were appraised investigating the $Zn_{2-x}Co_xSiO_4$ join before the transition to the olivine structure-type.

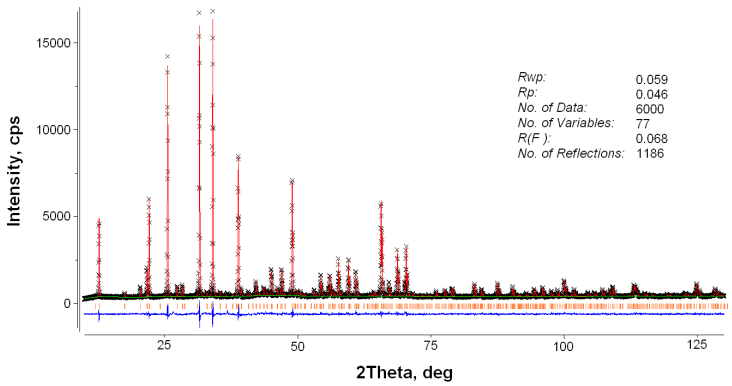

Figure I1. Plot of Rietveld refinement performed on X-ray powder diffraction data of sample *W*30. The experimental data are indicated by cross signs, the calculated pattern is the continuous line and the lower curve is the weighted difference between the calculated and observed patterns. The rows of vertical tick marks shows the allowed reflections for the crystalline phase present in the sample.

► ***Experimental procedure*** – [*for the experimental details (including: sample preparation, X-ray powder diffraction and structural characterization, Rietveld refinements,*

*and UV-visible-NIR diffuse reflectance spectroscopy) readers are requested to refer to the chapter **2** of the present dissertation*].

Reagent grade SiO_2 (Riedel-de Haën) and Co_3O_4 (Ferro) plus ZnO from industrial metal slag were used as raw materials (Table I1). No mineralizer was added.

● Technological performance of willemite pigments was evaluated by adding 5 wt% of pigment *W*30 into different types of glassy coatings (i.e. frit giving rise to a transparent coating) and glazes (i.e. mix of frit and minerals giving rise to an opaque vitro-crystalline coating) for ceramic tiles and sanitary-ware (Matteucci et al. 2006a; Tenorio Cavalcante et al. 2007; *see Table 2.6, chapter **2***). Every batch was wet mixed and the slip sprinkled on porous ceramic tiles, then dried in oven and fired with different schedules in electric roller kiln (800–1200 °C, 1 h cold-to-cold) or chamber furnace (1250 °C, 12 h cold-to-cold). The colour stability was evaluated by measuring the CIELab parameters of coatings by MSXP4000 Miniscan spectrometer (Hunterlab, white glazed tile reference x = 31.5, y = 33.3, illuminant D_{65}, 10° observer). The colouring performance of willemite pigment was compared with commercial Co-olivine and Co-aluminate colorants, that were added taking care that the Co amount be the same in all glazes/glassy coatings.

Table I1. Chemical composition of raw materials used in pigment preparation. The chemical composition of raw materials (Co_3O_4 and ZnO) were determined by X-ray floresans spectrometer (XRF, Rigaku RZS Primus).

% wt.	ZnO (from slag)	Co_3O_4 (Ferro)	SiO_2 (Riedel-de Haen)	ZnO (Fluka)
ZnO	95.5	–	–	≥ 99.0 %
Co_3O_4	–	96.7	–	–
PbO	1.62	–	–	–
NiO	0.02	–	–	–
CuO	0.53	–	–	–
Fe_2O_3	0.14	0.053	–	–
Al_2O_3	–	0.105	–	–
CaO	0.07	0.024	–	–
K_2O	0.25	–	–	–
Na_2O	–	1.49	–	–
MgO	–	0.034	–	–
SiO_2	0.12	0.043	≥ 98.0 %	–
SO_3	1.74	1.56	–	–

● In order to evaluate its chemical stability, the *W*30 Co-willemite pigment was admixed to glassy coating F1 and fired at 1050 °C with dwell time of 30 min. The pigment was selected since it has the most intense blue colour and the coating was selected since it contains the lowest amount of ZnO among the compositions here considered. Samples were polished with

cross section polisher (Jeol SM-09010, Japan) for scanning electron microscope (SEM) examinations (Zeiss, Supra 50 VP, Germany). Focus ion beam lift out method (FEI-Nova 600 NanoLab DualBeam™, USA) was used for transmission electron microscope (TEM) sample preparation. Electron transparent samples were characterised by using 200 kV field emission TEM (Jeol 2100F, Japan) attached with an energy filter (Gatan GIF Tridiem), parallel electron energy loss spectrometer (PEELS), a high angle annular dark field scanning transmission electron microscope (STEM-HAADF) detector (Fishione) and an energy dispersive X-ray (EDX) spectrometer (Jeol JED-2300T, Japan). In the STEM-EDX/EELS analysis, an electron spot with 1–2 nm in diameter was used and the acquisition time was chosen as 40-s live time. Furthermore, a drift corrector was used to avoid any possible drifts that may occur at nano-scale during acquisition of STEM-EDX spot and line scan elemental analysis. In STEM-EELS analysis, the convergence and collection semi-angles were 9.2 and 15.7 mrad, respectively. The spectrometer energy dispersions were 0.2 and 0.5 eV/channels. The backgrounds of all acquired EEL and reference spectra were subtracted according to power-law in this study (Thomas and Midgley 2002).

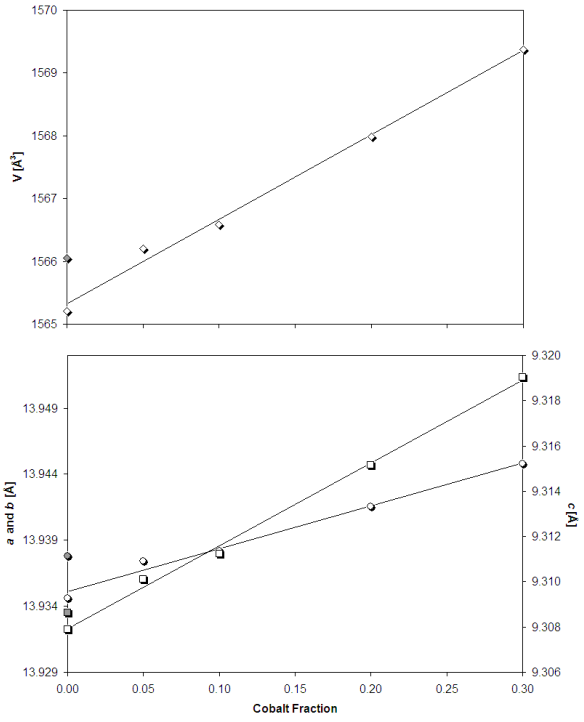

Figure I2. Unit cell volume (*V*: diamonds) and lattice parameters (*a* = *b*: circles; *c*: squares) of willemite pigments as a function of cobalt doping (white symbols); reference sample *WR* (grey symbols).

► *Results and discussion*

● *Crystal structure* – In our synthesis conditions, the major phase occurring in all samples is willemite plus a small amount of residual phases due to the low purity ZnO raw material.

The incorporation of cobalt in the willemite lattice is clearly proved by the increase of the unit cell parameters and volume, proportional to the cobalt doping (Figure I2). This fact is unexpected on the basis of ionic radii (Zn^{2+} 0.60 Å, Co^{2+} 0.58 Å, in tetrahedral coordination) but is readily explained by a varying covalency degree of the *M*–O bonding. In fact, it is known that

the Zn–O bonding exhibits an enhanced covalency, due to the strong hybridization of sp^3 orbitals, that promotes particularly short Zn-O distances (Louisnathan 1969). The result of the Co → Zn substitution implies a more ionic bond and longer *M*–O distance.

Doping up to 0.1 apfu produces small crystal structural changes, but appreciable increasing of unit-cell volume occurs for Co additions ≤ 0.2 apfu (Figure I2).

Nevertheless, the refined mean ⟨Zn1–O⟩ and ⟨Zn2–O⟩ distances, even with a narrow range of variation, suggest that cobalt takes place in both Zn1 and Zn2 sites, but with a different preference: an expansion can be recognized for the Zn1 tetrahedron (the one with originally shorter distances), while the Zn2 tetrahedron remains constant or slightly contracts (Table I2). As reported for different doping of the willemite structure, ions with smaller ionic radii should be hosted in the smaller zinc cation site (Klaska et al. 1978; Ericsson and Filippidis 1986; Krause et al. 1995; Brunold et al. 1996). On this basis, Co^{2+} is expected to be mainly hosted in the Zn1 sites (average polyhedral volume = 3.770 Å^3) with a maximum tetrahedral deviation δ(Zn1–O) = 0.018 Å, while zinc atoms should be preferentially placed on the Zn2 site (average polyhedral volume = 3.910 Å^3) with a smaller tetrahedral deviation δ(Zn2–O) = 0.006 Å (Figure I3).

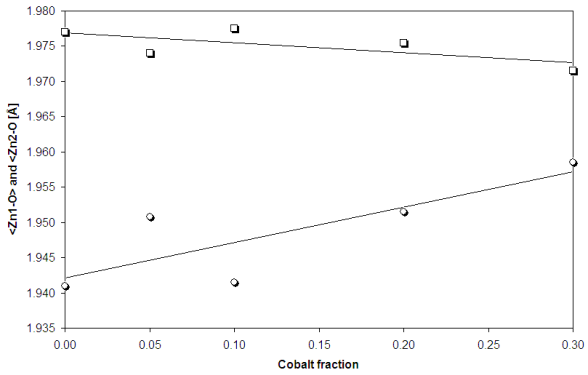

Figure I3. Mean metal–oxygen distances in the tetrahedral sites Zn1 (circles) and Zn2 (squares) of willemite pigments as a function of cobalt doping.

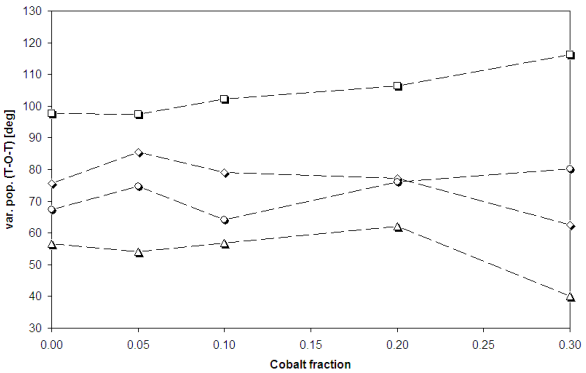

Figure I4. Variance of *T*–O–*T* angles in willemite pigments as a function of cobalt doping: *T*–O1–*T* (diamond), *T*–O2–*T* (circle), *T*–O3–*T* (triangle), *T*–O4–*T* (square).

Another important evidence, indicating the mechanism of cobalt incorporation in the willemite tetrahedral sites, stems from inter-tetrahedral tilting. The analysis of variance among the three *T*–O–*T* angles hinged on each oxygen site shows that the tetrahedral tilting mostly involves the O4 and O3 hinges. The *T*–O4–*T* angles become more dissimilar with increasing Co content, while the opposite occurs for the *T*–O3–*T*

angles. This means that the tilting arrangement around the O3 and O4 hinges are made progressively less equivalent by the Co substitution (Figure I4).

Table I2. Batch composition, X-ray diffraction details, unit cell parameters, metal-oxygen distances, effective volume and *T*–O–*T* angles in willemite structures analyzed.

Sample Lable	***WR***	***W*0**	***W*5**	***W*10**	***W*20**	***W*30**
Nominal cobalt content						
$Zn_{2-x}Co_xSiO_4$; x =	0.00	0.00	0.05	0.10	0.20	0.30
Agreement factors and refinement details						
R_{wp}	0.1242	0.0812	0.0630	0.0442	0.0294	0.0592
R_p	0.0818	0.0520	0.0411	0.0297	0.0213	0.0455
No. of data	6250	6000	6000	6000	6000	6000
R_F^2	*0.0427*	*0.0378*	*0.0457*	*0.0490*	*0.0545*	*0.0679*
No. of Reflections	1184	1184	1184	1186	1186	1186
No. of variables	77	77	77	77	77	77
Unit cell parameters ($\alpha = \beta = 90°$; $\gamma = 120°$)						
$a = b$ (Å)	13.9378(1)	13.9346(1)	13.9374(1)	13.9382(1)	13.9415(1)	13.9448(1)
c (Å)	9.30867(1)	9.30791(1)	9.31012(1)	9.31125(1)	9.31514(1)	9.31903(1)
Unit cell volume (Å^3)	1566.05	1565.21	1566.21	1566.58	1567.98	1569.37
Tetrahedral metal–oxygen mean distances (Å)						
Zn1–O	1.956	1.941	1.951	1.942	1.952	1.959
Zn2–O	1.971	1.977	1.974	1.978	1.976	1.972
Si–O	1.620	1.626	1.620	1.627	1.620	1.619
			Polyhedral volume (Å^3)			
Zn1	3.81	3.72	3.77	3.72	3.77	3.82
Zn2	3.90	3.92	3.90	3.92	3.91	3.90
Si	2.18	2.20	2.18	2.20	2.18	2.17
			T–O–T angles			
Zn2–O1–Zn2	108.6(5)	110.5(6)	109.5(6)	110.0(7)	110.0(6)	109.3(5)
Zn2–O1–Si	131.5(7)	131.5(8)	132.0(9)	131.6(10)	131.4(10)	128.2(8)
Zn2–O1–Si	119.9(7)	117.9(8)	118.5(9)	118.3(10)	118.6(10)	122.4(9)
Av.	120.0	120.0	120.0	120.0	120.0	120.0
Variance	*87.4*	*75.6*	*85.5*	*79.1*	*77.3*	*62.5*
Zn1–O2–Zn1	109.9(6)	110.4(7)	110.4(8)	111.0(8)	111.0(7)	110.6(6)
Zn1–O2–Si	132.1(8)	130.4(9)	131.3(10)	130.4(11)	131.7(11)	132.0(9)
Zn1–O2–Si	118.0(7)	118.6(8)	117.9(9)	118.1(10)	116.8(10)	117.1(9)
Av.	120.0	119.8	119.9	119.8	119.8	119.9
Variance	*84.1*	*67.4*	*74.7*	*64.2*	*76.0*	*80.2*
Zn1–O3–Zn2	112.4(5)	110.5(5)	110.3(5)	110.3(6)	109.6(6)	111.2(6)
Zn1–O3–Si	127.4(7)	128.9(7)	128.1(8)	128.7(9)	128.7(10)	126.0(10)
Zn2–O3–Si	120.2(7)	120.5(8)	121.5(8)	120.8(9)	121.5(10)	122.6(10)
Av.	120.0	120.0	120.0	119.9	119.9	119.9
Variance	*37.5*	*56.6*	*54.0*	*56.8*	*62.0*	*40.1*
Zn1–O4–Zn2	105.0(4)	105.9(4)	106.1(4)	105.8(5)	105.4(4)	104.6(5)
Zn1–O4–Si	128.4(10)	129.1(10)	129.5(13)	129.9(11)	129.5(11)	129.9(9)
Zn2–O4–Si	123.5(10)	123.5(10)	123.1(12)	122.8(11)	124.0(11)	123.8(9)
Av.	119.0	119.5	119.6	119.5	119.6	119.4
Variance	*101.5*	*97.7*	*97.5*	*102.2*	*106.3*	*116.2*

Note: Figures in parentheses are standard deviations in the last decimal figure. The polyhedral volume is calculated as reported by Swanson and Peterson (1980). The variance of the *T*–O–*T* angles is defined by: $\sum(x - \langle x \rangle)^2 / n$, where x is the mean value of the sample average and n is the sample dimension.

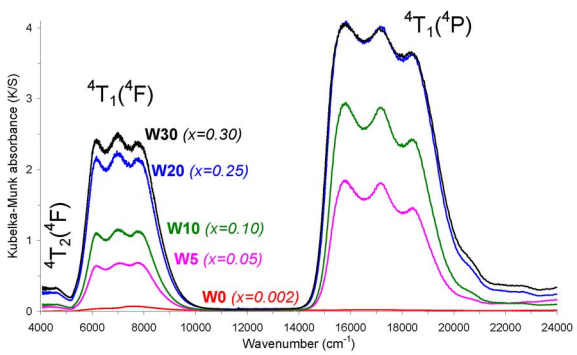

Figure I5. Optical spectra of cobalt-bearing willemite pigments (x=cobalt content, apfu).

● *Optical properties* – The optical spectra of cobalt-bearing willemite pigments are characterized by electron transitions of Co^{2+} in tetrahedral coordination (Figure I5) which exhibit increasing absorbance values matching fairly well with the nominal cobalt occupancies. Sample *W*0, even if nominally Co-free, in reality contains cobalt traces as low as $x = 0.002$ (likely due to contamination in unsealed crucible).

The spectra are dominated by the spin-allowed, three-fold split $^4T_1(^4F) \leftarrow {}^4A_2(^4F)$ and $^4T_1(^4P) \leftarrow {}^4A_2(^4F)$ transitions, occurring at about 6000-8000 cm^{-1} and 16000-18500 cm^{-1} respectively, together with the low intensity band around 4600 cm^{-1} attributable to the $^4T_2(^4F) \leftarrow {}^4A_2(^4F)$ transition (Figure I5).

The $^4T_2(^4F)$ transition was fitted with a single band (Figure I6a). The $^4T_1(^4F)$ triple band is almost symmetrical (Figure I6b) and was easily deconvoluted in three components ($^4A_2$, $^4A_2$, $^4A_2$) originating by the splitting due to both low point symmetry of tetrahedral sites in willemite and spin-orbit coupling of Co^{2+} ions (Lever 1984; Brunold et al. 1996; Duan et al. 2003). Deconvolution of the complex band at 16000-18500 cm^{-1} (Figure I6c) required five peaks: the main three are attributed to splitting of the $^4T_1(^4P)$ transition ($^4A_2$, $^4B_{1/2}$, $^4B_{2/1}$). The others are likely due to spin-forbidden transitions, four of which originate from the ^2G term and are expected to occur, according to the Tanabe-Sugano diagram built with the experimental 10*Dq* and *B* values, around ~16200 cm^{-1} (^2E), ~16900 cm^{-1} ($^2T_1$), ~18400 cm^{-1} ($^2A_1$) and ~19400 cm^{-1} ($^2T_2$).

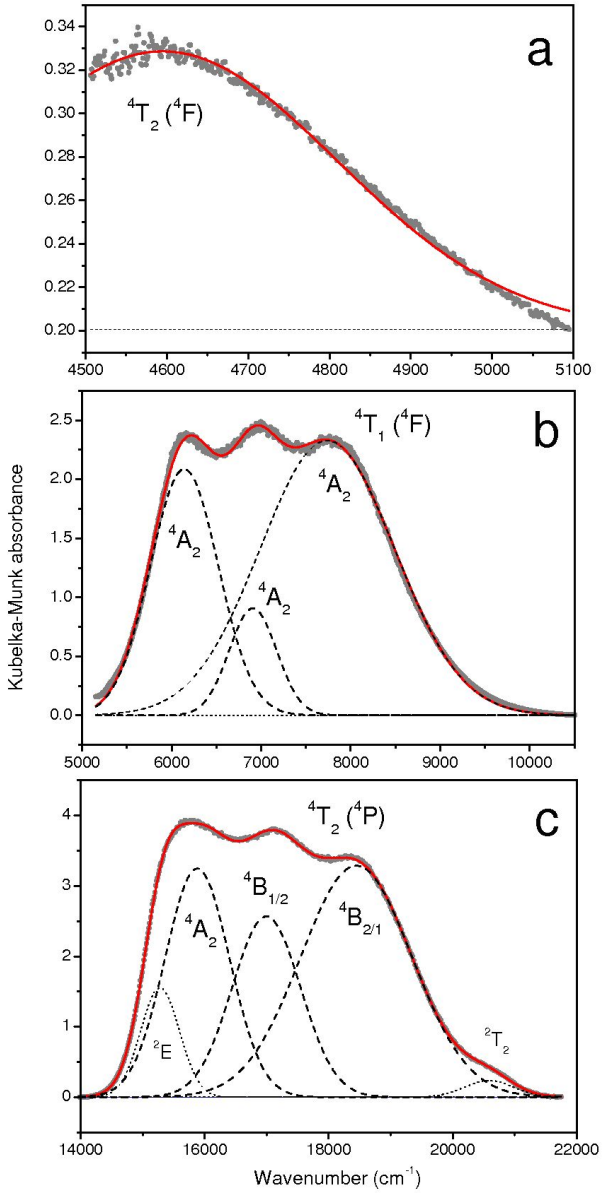

Figure I6. (a-c) Deconvolution of the optical spectra of willemite pigment *W*30.

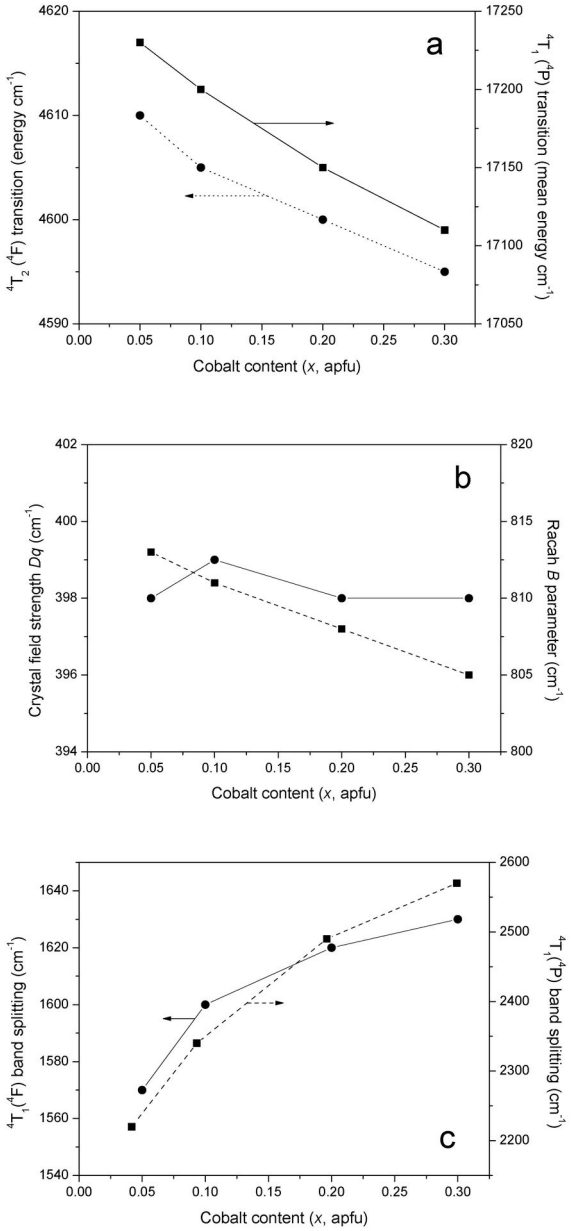

Figure I7. Optical parameters of willemite pigments as a function of the cobalt content: (a) energy of the Co^{2+} transitions; (b) crystal field strength *Dq* and interelectronic repulsion Racah *B* parameter; (c) Co^{2+} band splitting.

The Co^{2+} spin-allowed transitions exhibit a progressive shift toward lower energy with increasing cobalt content, particularly evident for the $^4T_2$ and $^4T_1(^4P)$ bands (Table I3 and Figure I7a). The crystal field strength *Dq* and Racah *B* parameter are nearly constant around *Dq* = 398 cm^{-1} and *B* = 810 cm^{-1} (Figure I7b); these values are close to willemite with Co

doping as low as 0.01 apfu (Dq = 404 cm^{-1} and B = 792 cm^{-1}) (Brunold et al. 1996). This implies that little changes of covalency degree and Co–O local distance occur going toward the Co end-member. However, the increase of the $^4T_1$ band splitting and spin-orbit parameter λ, occurring in the same direction, confirms the change in the local symmetry of ligands observed by XRD in terms of O–Co–O angles (Figure I7c).

Table I3. Optical properties of willemite pigments.

Sample			***W*0**	***W*5**	***W*10**	***W*20**	***W*30**
Co concentration (*x*)			*(0.002)*	0.05	0.10	0.20	0.30
Spin-allowed transitions		SFT[a]	cm^{-1}	cm^{-1}	cm^{-1}	cm^{-1}	cm^{-1}
T_d symmetry	C_v symm.						
$^4T_2$ (^4F)	$^4A_2$		*4750*	4610	4605	4600	4595
	$^4A_2$		*5700*	6150	6150	6130	6120
$^4T_1$ (^4F)	$^4A_2$		*6300*	6880	6880	6870	6870
	$^4A_2$		*7500*	7720	7750	7750	7750
				15520	15450	15340	15280
		^2E					
	$^4A_2$	$^2T_1$	*15300*	16130	16050	15950	15880
$^4T_1$ (^4P)	$^4B_{1/2}$		*17000*	17210	17160	17060	17000
	$^4B_{2/1}$	$^2A_1$	*18700*	18350	18390	18440	18450
		$^2T_2$					
				20500	20500	20530	20590
$^4T_1$ (^4F) band mean energy			*6500*	6917	6927	6917	6913
$^4T_1$ (^4P) band mean energy							
$^4T_1$ (^4F) band splitting (δ)							
$^4T_1$ (^4P) band splitting (δ)							
Crystal field strength (*Dq*)							
Racah *B* parameter							
Racah *C* parameter							

[a]Spin-forbidden transitions

● *Technological behaviour of willemite pigments* – Co-doped willemite behaves successfully in the ceramic process, imparting intense blue colour to various glazes and glassy coatings. When compared with commercial Co-aluminate and Co-olivine colorants, willemite pigments exhibit similar trends in function of coating composition and firing temperature, but

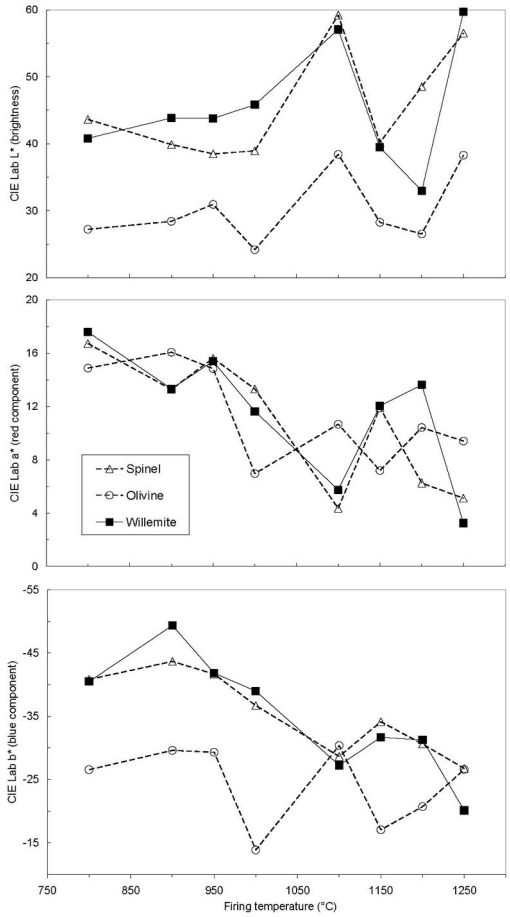

Figure I8. Colour change vs. maximum firing temperature of pigments when used in different glassy coatings (F1 to F4) and glazes (S1 to S4).

present the best colouring performance in the 800–1200 °C range, as shown by the best value of the parameter *b** (Figure I8). The strong blue shade of willemite implies a characteristic colour, that is as saturated as that of cobalt aluminate, but less saturated than that of cobalt silicate, as shown by the lower value of *L**. These results strengthen previous indications on the technological behaviour of willemite pigments (Forés et al. 2000; Llusar et al. 2001).

The thermal stability of both willemite and commercial pigments appears to be reduced in high temperature glazes. Passing from 1100 °C to over 1200 °C, willemite pigments become gradually less blue, as a consequence of the converging action of increasing firing temperature and aggressive chemical environments due to high concentration of calcium, magnesium and zinc in molten glazes (for example S1 composition).

Table I4. Chemical composition of willemite pigment dispersed in glassy coating (see Figure I9a for the localization of analyzed points).

	Glassy Coating	Pigment	Pigment
% wt.	Point 1	Point 2	Point 3
SiO_2	63.36	46.70	40.89
Al_2O_3	9.29	6.08	5.20
CaO	1.52	0.65	0.64
CoO	2.00	4.95	6.43
ZnO	13.49	31.83	38.48
PbO	4.04	1.67	1.26
Na_2O	5.07	7.65	6.72
K_2O	1.23	0.48	0.43

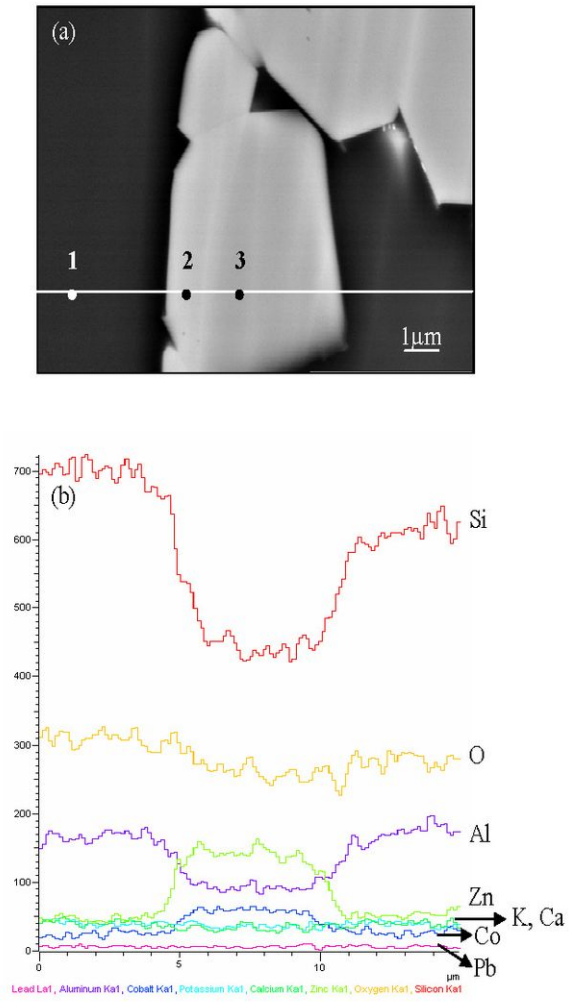

Figure I9. (a) Backscattered SEM image of pigment grains embedded in the glassy coating and (b) line scan analysis of Al, Si, K, Ca, Zn, Co and Pb elements along the white line shown in (a).

● *Pigment-coating interactions* – In order to assess the chemical stability of Co-willemite pigments, backscattered images of *W*30 particles dispersed in the glassy coating F1 were taken at high magnification under SEM and composition of elements in pigment particles were determined by line scan EDX analysis (Figure I9). The absence of image contrast indicates that there is no reaction layer between the pigment particle and the matrix within the resolution limit of SEM (Figure I9a). Looking at the line scan analysis, the Ca, K and Pb concentration is almost the same in both pigment and glass, implying that a diffusion of Ca and K occurred from glass to willemite; Co and Zn amounts seem to decrease when the edge of the pigment grain is reached (Figure I9b). Spot analysis at different points, shown in Figure I9a, partially

confirms that glass contains Zn and Co, likely diffusing from the pigment particle (Table I4), but a certain effect of electron beam broadening during EDX analysis cannot be ruled out. Therefore, TEM is needed to go in depth in the pigment-glass interactions during firing at 1050 °C (Figure I10). The whole length size of sample prepared with focused ion beam technique was approximately 15 µm x 6 µm, which was limited to only the glass region around one single pigment particle to avoid underneath grain effect causing misleading results in chemical analysis (Kyser and Murata 1974). Prior to chemical analysis, STEM-HAADF imaging technique was carried out to highlight any chemical contrast to assess whether there is any reaction layer at the interface, since in STEM-HAADF the image intensity is approximately proportional to the square of the atomic number (Z^2; Varela et al. 2005), which means that any chemical difference would create an atomic number contrast to chemically visualise diffusion layer formation at the interface (Figure I11).

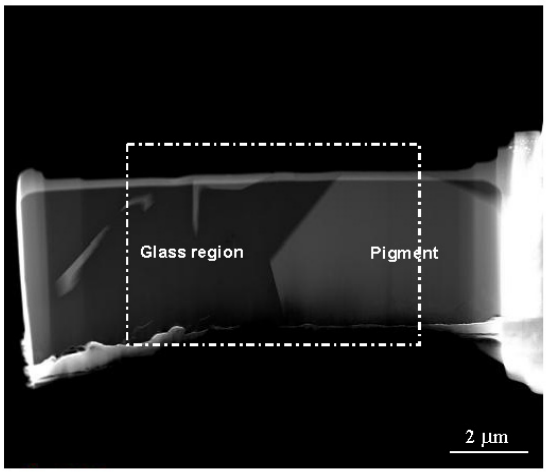

Figure I10. Z-contrast STEM-HAADF image of FIB prepared sample showing a pigment grain in glassy coating at low magnification.

As a result of the number of electrons inelastically scattered from higher atomic number elements, such as Co (Z = 27) and Zn (Z = 30), present in the pigment, the glass appears black coloured and willemite grey. From the STEM-HAADF image shown in Figure I11a, it can be deduced that no diffusion layer is present at the

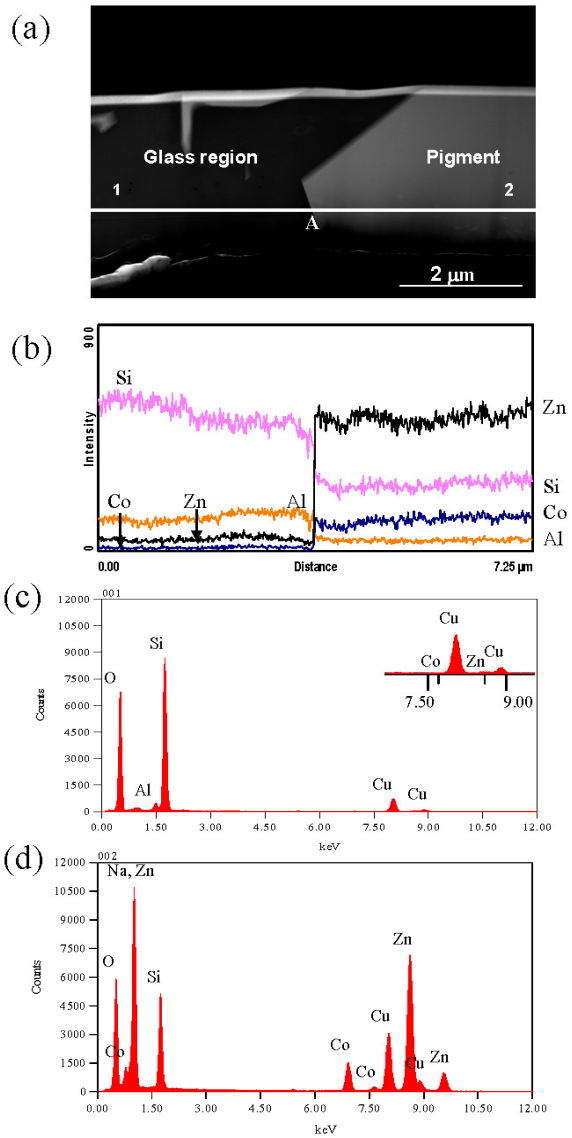

Figure I11. (a) The STEM-HAADF image of pigment dispersed in glassy coating, magnified image of dashed rectangular area in Figure I10, (b) STEM-EDX line scan analysis of Zn, Si, Co, Al elements along the white line shown in (a), (c) STEM-EDX spot analysis of glass region (point 1) and (d) pigment grain (point 2) shown in (a).

interface. At this point, the question to be answered is whether there is any diffusion between glass and pigment or not. For this purpose, EDX analysis at STEM mode was performed due to the fact that the spatial resolution of this technique is around a few nanometres, so much better than EDX under SEM (Williams et al. 2003). STEM-EDX line scan analysis confirms that the pigment composition contains only Co, Zn, Si, and O, while in the left hand side of Figure I11b the intensity profiles of Co-K and Zn-K characteristic x-ray lines are almost zero up to a specific point (marked with A) plotting in the glass region, whereas going closer to the pigment grain a little increase of Co and Zn is observed. EDX spot analyses were acquired from glass and pigment (points 1 and 2 in Figure I11a) and shown in Figure I11c and I11d, respectively. Comparing these line scans end point analysis, it can be deduced that no elements diffused and particularly Co and Zn did not migrate from the pigment to the glass.

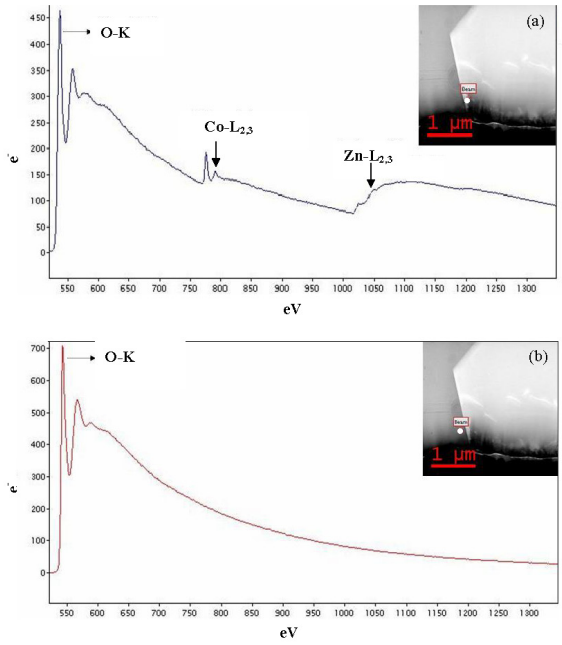

Figure I12. EEL spectra of (a) pigment, and (b) glassy coating in the 525-1350 eV energy loss rangef.

Electron energy loss spectroscopy (EELS) was also applied to appraise if cobalt doped willemite is chemically inert in contact with the glassy coating at 1050 °C. The spectrum acquired on the pigment (Figure I12a) exhibits the Co-$L_{3,2}$ (779 and 794 eV) and Zn-$L_{3,2}$ (1020 and 1043 eV) edges along with O K edges; in contrast, the EEL analysis performed very close to the pigment grain neither Co nor Zn edges are visible (Figure I12b). This confirms the STEM/EDX data in Figures I11, leading to the conclusion that no diffusion layer is present at the pigment-glass interface, which means that the cobalt doped willemite pigment produced in this work was chemically inert, at least at 1050 °C.

About the valence of Co ions in Zn_2SiO_4, a fingerprinting analysis was performed comparing the EEL spectra of the pigment and CoO taken as reference (Figure I13). It can be appreciated that the energy of Co-L_3 and Co-L_2 edges is the same in both EEL spectra and the intensity ratio of the Co-L_3 to Co-L_2 is 1.76 ± 0.03 for the pigment and 1.75 ± 0.03 for CoO. Thus, the oxidation state of cobalt ion in the blue willemite pigment is Co(II+) (Wang et al. 2000; Yu-Zhang et al. 2003), confirming the previous results on the Zn_2SiO_4 crystal structure obtained by using a different technique (Brunold et al. 1996).

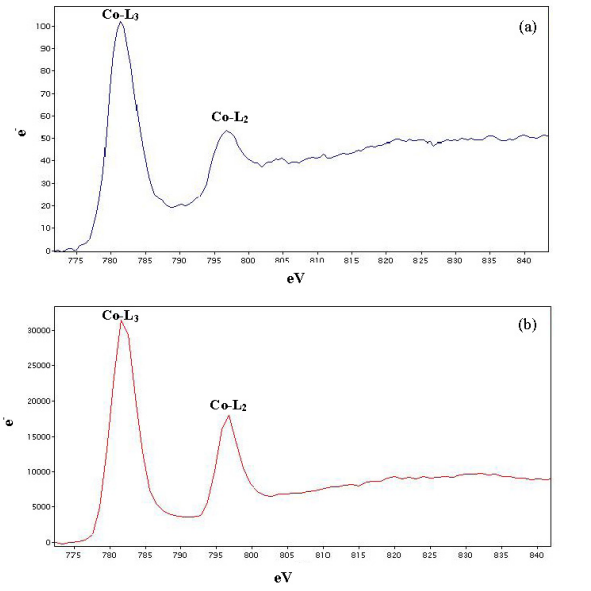

Figure I13. The EEL spectra showing Co-L3,2 edges of (a) pigment grain and (b) reference CoO.

► ***Conclusions*** – Cobalt-doped willemite performs successfully as ceramic pigment, bestowing intense blue coloration to a wide range of glazes and glassy coatings. Thanks to its satisfactory chemical stability and optical features, willemite exhibits a colouring performance – comparing the same Co amount in the ceramic coating – better than conventional blue colorants, such as spinel $CoAl_2O_4$ or olivine Co_2SiO_4.

A detailed microstructural investigation – involving SEM-EDX, STEM-HAADF and TEM-EELS – supports technological tests, confirming that willemite pigments are chemically inert in contact with the ceramic matrix in which they are dispersed. No interface layer was formed and no diffusion phenomena were revealed between pigment and glassy coating at 1050 °C.

Cobalt incorporation in the willemite structure occurs with increasing unit cell volume and parameters. Besides the ionic radius of Co^{2+} is smaller than that of the Zn^{2+} ion, cobalt doping causes an elongation of the mean metal-oxygen distance at the Zn1 site, which implies a preferential Co occupancy of this tetrahedral site. Growing the amount of cobalt induces an important change of the local symmetry of ligands – witnessed by the change of intertetrahedral tilting and *T*–O–*T* angles – confirmed by increasing splitting of Co^{2+} optical bands and spin-orbit coupling parameter. This enhances the distortion of tetrahedral site,

which low point symmetry is likely to be the reason of the best optical properties of willemite with respect to cobalt aluminate spinel and cobalt silicate.

A deeper understanding of properties and behaviour of Co-doped willemite is gained from these insights which, on one side, prove that high quality pigments can be actually obtained using secondary precursors, e.g. ZnO recovered from slag, and on the other side that $(Zn,Co)SiO_4$ does is a promising pigment for novel ceramic applications, particularly new decoration techniques (Gardini et al. 2008; Cavalcante et al. 2009).

4.
CONCLUSION
(*On the structural relaxation around octahedrally coordinated Cr^{3+}*)

Structural relaxation around octahedrally coordinated Cr^{3+} is very common and well documented for minerals and synthetic compounds (e.g. ruby (Al_2O_3) vs. eskolaite (Cr_2O_3), grossular ($Ca_3Al_2Si_3O_{12}$) vs. uvarovite ($Ca_3Cr_2Si_3O_{12}$) and pyrope ($Mg_3Al_2Si_3O_{12}$) vs. knorringite ($Mg_3Cr_2Si_3O_{12}$) garnets, spinel ($MgAl_2O_4$) vs. magnesiochromite ($MgCr_2O_4$) and gahnite ($ZnAl_2O_4$) vs. zincochromite ($ZnCr_2O_4$) spinels. Furthermore, in the first section of the previous chapter [*Results and discussion*], the structural relaxation along $YAlO_3$–$YCrO_3$ perovskite and $AlNbO_4$–$Al_{0.5}Cr_{0.5}NbO_4$ alumoniobite solid solutions was calculated by combining X-ray powder diffraction and diffuse reflectance optical absorption techniques.
With respect to the structural relaxation caused by the chromium for aluminium replacement mechanism a discussion will be addressed in this conclusive chapter by comparing the values of the relaxation coefficients of the previous listed structures with their different structural features.

4.1. Packing efficiency and symmetry lowering

Every crystal structure tends to follow the fundamental concept of *sphere packing*. The spherical concept of atoms in crystal structures devised by Goldschmidt, followed by the formulation of Goldschmidt's ionic model into Pauling's rules (Pauling 1927), led Laves to enunciate the principles of space-filling in crystal structures. Laves' idea can be summarized on the basis of three principles (Borchardt-Ott 1993):

(i) *The Principle of Closest Packing*. Atoms in a crystal structure attempt to arrange themselves in a manner which fills space most efficiently;

(ii) *The Symmetry Principle*. Atoms in a crystal structure attempt to achieve an environment of the highest possible symmetry;

(iii) *The Interaction Principle*. Atoms in a crystal structure attempt to achieve the highest coordination (i.e. the maximum possible number of nearest neighbours with which they can interact).

By following the first of these three principles, in Table 4.1 are reported the *atomic packing factors* (*APF*) obtained by calculating the oxygen-packing (by assuming 1.35 Å as the ionic radius of oxygen ion; Shannon 1976) for the considered structures through the following equation:

$$APF = \frac{N° Atoms \times VAtoms}{Vcell} \tag{4.1}$$

Table 4.1. Structural relaxation coefficients (ε), unit cell volumes (V), atomic packing factors (*APF*), octahedral features (i.e. internal variables *M*–O and O–*M*–O) and connectivity (*M*–*M*), and volumetric bulk moduli.

	s.g.	ε	Ref.	V_{cell} (Å^3)	APF	*M*–O	O–*M*–O	*M*–*M*	K_{T0} (GPa)	Ref.
$AlNbO_4$– $Al_{0.8}Cr_{0.2}NbO_4$	*C*2/*m*	0.00	[*]	280.73 284.08	0.59 0.58	5	11	2+1	191(9) –	[6]
Rutile-type	$P4_2/mnm$	–		65.07	0.63	2	4	2+1	225(2)	[6]
$YAlO_3$– $YCrO_3$	*Pnma*	0.54	[*]	203.49 218.27	0.61 0.57	3	7	1	192(2) 208(1)	[7] [8]
Al_2O_3– Cr_2O_3	*R*-3*cH*	0.58	[1]	255.06 287.94	0.73 0.64	2	5	3	257(6) 238(4)	[9] [10]
$ZnAl_2O_4$– $ZnCr_2O_4$	*Fd*-3*m*	0.60	[2]	529.71 577.82	0.62 0.57	1	3	2	202(1) 183(4)	[11] [12]
$MgAl_2O_4$– $MgCr_2O_4$	*Fd*-3*m*	0.68	[3]	529.44 557.32	0.62 0.57	1	3	2	194(6) 209(9)	[13] [14]
$Ca_3Al_2Si_3O_{12}$– $Ca_3Cr_2Si_3O_{12}$	*Ia*-3*d*	0.74	[4]	1666.07 1697.42	0.59 0.58	1	3	0	169(1) 160(1)	[15] [16]
$Mg_3Al_2Si_3O_{12}$– $Mg_3Cr_2Si_3O_{12}$	*Ia*-3*d*	0.77	[5]	1502.89 1562.51	0.66 0.63	1	3	0	171(2) –	[17]

References: [*] This study; [1] Neuhaus and Richartz 1958 – Schmitz-DuMont and Reinen 1959 – Poole and Itzel 1963 – Reinen 1969; [2] Hålenius et al. 2010; [3] Reinen 1969 – Hålenius et al. 2010; [4] Andrut and Wildner 2001 – Langer et al. 2004; [5] Taran et al. 2004; [6] Duan et al. 1999; [7] Ross et al. 2004b; [8] Ardit et al. 2010b; [9] Finger and Hazen 1978; [10] Finger and Hazen 1980; [11] Levy et al. 2001; [12] Levy et al. 2005; [13] Finger et al. 1986; [14] Fan et al. 2008; [15] Pavese et al. 2001; [16] Diella et al. 2004; [17] Zhang et al. 1998.

By definition the *packing efficiency* of close-packed structures ranges from 0.52 (i.e. simple cubic, *sc*, structures), to 0.68 (i.e. body-centred cubic, *bcc*, structure), to the highest value of 0.74 (i.e. cubic closest-packed, *ccp*, corresponding to the face-centred cubic lattice, *fcc*, and hexagonal closest-packed, *hcp*, structures).

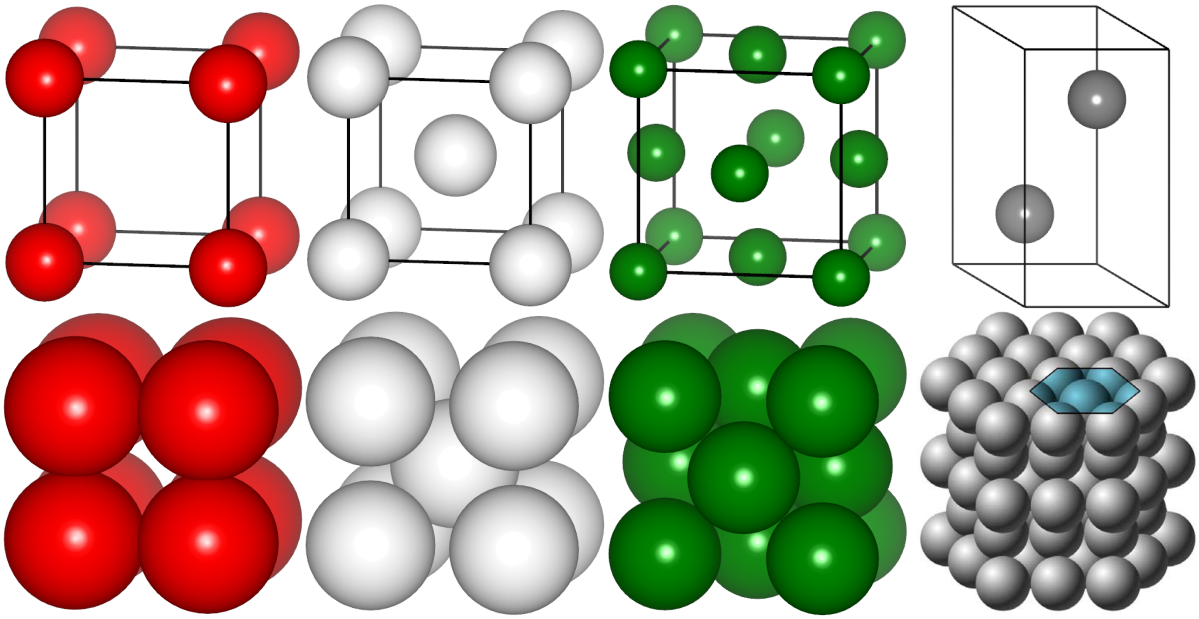

Figure 4.1. Schematic representation of packing efficiency of so defined close-packed structures.

Although not all the structure under comparison can be formally defined as "close-packed structures" (e.g. the garnet structure is out of this definition), all of them show a very high *packing efficiency* which varies from 0.57 (i.e. Cr-member of both perovskite and spinel structures) to 0.73 (i.e. corundum).

Even if characterized by a high packing efficiency, it is noteworthy that perovskite (orthorhombic) as well as alumoniobite (monoclinic) structures are far away to follow the second of the above enunciated principles. In fact, their symmetry is lower than that of the spinel- and garnet-type structures (both with cubic symmetry). On the other hand, both orthorhombic perovskite and monoclinic alumoniobite originate from an archetype structure with a cubic symmetry (s.g. *Pm*-3*m*). Hence, both perovskite and alumoniobite archetype, as well as spinel and garnet structures, belong to the hexoctahedral class of the cubic system, and show holohedral symmetry.

The reason of the symmetry lowering for $YAl_{1-x}Cr_xO_3$ perovskite and $Al_{1-x}Cr_xO_4$ alumoniobite structures stems from the chemical nature of the cations hosted in the oxygen-based polyhedra. Mismatch in sublattice (cation or anion) size, local charge balance requirements, electronic configuration, and other factors may induce strong intra- and interpolyhedral lattice distortions leading to lowering of symmetry from the archetype structure, in order to minimize the potential lattice energy. The resulting structures are characterized by more distorted polyhedra, in which the coordination numbers are usually reduced (e.g. the cubic site A (C.N. = 8 or 12) of the perovskite structure has an *ECoN* ~7, and the octahedral site *M2* (C.N. = 6) of the alumoniobite structure presents an *ECoN* drastically reduced to about 4; *for further details readers are requested to refer to the first, **A**, and the third, **C**, works of the first section of chapter 3*).

4.2. Structural relaxation coefficient as a function of the structural features

Back to Table 4.1, it is remarkable that the structures characterized by the largest departure from cubic symmetry due to lattice distortions are also those behaving as completely constrained structures (e.g. $\varepsilon = 0$ for alumoniobite) or nearly so (e.g. $\varepsilon = 0.54$ for the perovskite) in terms of lattice relaxation. The strongest long range lattice constraints force the bond lengths to adjust locally (i.e. at the short range of the first coordination shell) to the value predicted by Vegard's law. On the other hand, structures characterized by an undistorted lattice are more prone to relax (i.e. $\varepsilon = 0.58$, 0.60 and 0.68, 0.74 and 0.77 for corundum, spinel and garnet structures, respectively), consequently the lattice results more flexible, and every bond tends to adjust to its natural length in order to maintain distances similar to those occurring in the end-members.

From such a statement, two questions arise:

1) How can a "constrained" structure, as those of alumoniobite, be able to incorporate 0.24 mol of chromium (*see the third, **C**, work of the first section of chapter 3*), whose ionic radius is about 15% larger than that of aluminium (0.615 and 0.535 Å, respectively)?, and

2) How is it the degree of structural relaxation related to the structural features of the considered structures?

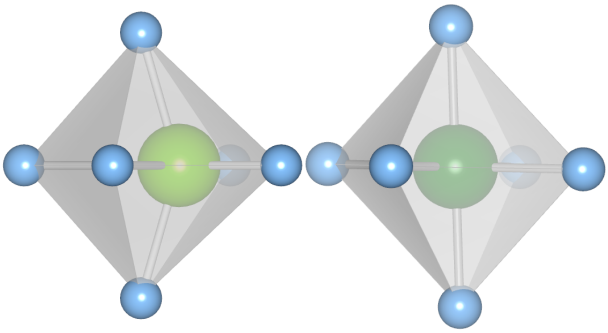

Figure 4.2. The highly distorted octahedron *M*2 of Cr-doped alumoniobite (on the left) against the regular octahedron of the garnet structure (on the right).

The answer to the first question brings us back to the lowering of symmetry for structures whose archetype had a cubic symmetry. For instance, the symmetry of the alumoniobite is monoclinic *C*2/*m*, and its octahedra are highly distorted (Figure 4.2-left) and characterized by 5 non-equivalent metal-oxygen bond distances, *M*–O, and 11 non-equivalent oxygen–metal–oxygen bond angles, O–*M*–O. On the other hand, the cubic symmetry of both spinel (s.g. *Fd*-3*m*) and garnet (s.g. *Ia*-3*d*) structures implies a higher point symmetry of the octahedral site and therefore the octahedron of these structures is more regular (Figure 4.2-right) and characterized by a smaller number of degrees of freedom (i.e. for both spinel and garnet structural types, the octahedra are characterized by the variation of a unique bond distance *M*–O, and 3 non-equivalent bond angles O–*M*–O).

The increasing of the internal octahedral flexibility (i.e. more degrees of freedom) of alumoniobite (and perovskite) structure, due to the lowering of the archetype symmetry, allows a partial (or complete in the case of the perovskite structure) Cr→Al substitution with an increasing of the octahedral distortion, but with no (or partial) effects on the structural relaxation. In the "extreme" case of the alumoniobite structure, the replacement above is limited to 24% since the octahedron is no longer deformable, and an additional phase transition is necessary in order to minimize the lattice energy (i.e. the monoclinic $AlNbO_4$ structure transforms into the tetragonal rutile-type $CrNbO_4$ structure).

In order to explain the problem raised in the second question, the octahedral connectivity (reported as *M*–*M* in Table 4.1) must be considered in addition to the octahedral degree of freedom (*M*–O + O–*M*–O) and the structural symmetry.

Although all the structures here considered have a high packing efficiency (see the previous paragraph), their octahedral connectivity is very variable. It ranges from isolated octahedra

(*M*–*M* = 0) for the garnet structures, corner-shared octahedra (*M*–*M* = 1) for perovskite structures, edge-shared octahedra (*M*–*M* = 2) for spinel structures, to the face-shared octahedra (*M*–*M* = 3) of the corundum structures.

It results very interesting that, if the internal distortion of the octahedra (i.e. the octahedral degrees of freedom, *M*–O + O–*M*–O) and the octahedral connectivity (*M*–*M*) for the structures under comparison are considered together and plotted versus the structural relaxation coefficient, an interesting trend is defined. If such trend, in a first approximation, is considered by itself, a crystal structure should be more relaxed as smaller is the sum of its degrees of freedom plus its interoctahedral connectivity. Obviously, this is a physical nonsense. On the other hand, if the symmetry of the structure is considered as the main factor, and the structural features (i.e. the octahedral degrees of freedom and connectivity) as the direct consequences of the general symmetry, then this trend can be physically related to the concept of the lattice distortion.

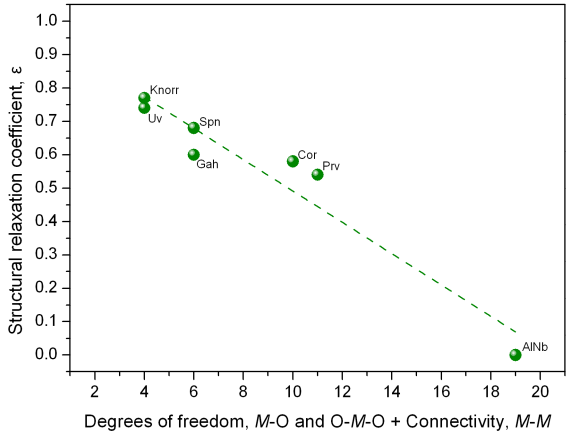

Figure 4.3. Coefficient of structural relaxation (ε) as a function of structural features (i.e. octahedral degrees of freedom and connectivity). Data labels are as follows: (AlNb) $Al_{1-x}Cr_xO_4$ This study; (Prv) $YAl_{1-x}Cr_xO_3$ This study; (Cor) $(Al_{1-x}Cr_x)_2O_3$ Neuhaus and Richartz 1958 – Schmitz-DuMont and Reinen 1959 – Poole and Itzel 1963 – Reinen 1969; (Gah) $Zn(Al_{1-x}Cr_x)_2O_4$ Hålenius et al. 2010; (Spn) $Mg(Al_{1-x}Cr_x)_2O_4$ Reinen 1969 – Hålenius et al. 2010; (Uv) $Ca_3(Al_{1-x}Cr_x)_2Si_3O_{12}$ Andrut and Wildner 2001 – Langer et al. 2004; (Knorr) $Mg_3(Al_{1-x}Cr_x)_2Si_3O_{12}$ Taran et al. 2004.

Furthermore, aimed to provide a different viewpoint, a brief note on the elastic properties of the selected solid solutions, will be given in the next few lines.

The difference between the end-members bulk moduli, K_{T0}, of the selected structures (see Table 4.1 and references therein) decrease with the increasing of the structural relaxation coefficient. Taking into account the two extreme cases, garnet vs. alumoniobite, it is possible to observe that, while grossular and uvarovite have almost the same compressibility (i.e. K_{T0} = 169 and 160 GPa, respectively; with ΔK_{T0} ~5%) the monoclinic alumoniobite and the tetragonal rutile have compressibility that are substantially different (i.e. K_{T0} = 191 and 225 GPa, respectively; with ΔK_{T0} ~18%). This is very interesting, because it means that the Cr

acceptance for the garnet structure does not induce any lattice constraint (i.e. the structure is relaxed). On the contrary, the difference in terms of compressibility, and the phase transition from the alumoniobite to the rutile-type $CrNbO_4$ structure, means that the Cr increasing in the alumoniobite structure is a further lattice constraint that the crystal structure cannot withstand (the structure is stiffer and does not relax).

References

Adams, R., Layland, R., Payen, C., and Datta, T. (1996) Syntheses, structural analyses, and unusual magnetic properties of $Ba_2CoSi_2O_7$ and $BaCo_2Si_2O_7$. *Inorganic Chemistry*, **35**, 3492–3497.

Ahmadi, T., Haase, M., and Weller, H. (2000) Low-temperature synthesis of pure and Mn-doped willemite phosphor (Zn_2SiO_4:Mn) in aqueous medium. *Materials Research Bulletin*, **35**, 1869–1879.

Ahmed, I., Dessouki, H., and Ali, A. (2008) Synthesis and characterization of new nano-particles as blue ceramic pigment. *Spectrochimica Acta* A, **71**, 616–620.

Aitasalo, T., Hölsä, J., Laamanem, T., Lastusaari, M., Letho, L., Niittykoski, J., and Pellé, F. (2006) Crystal structure of the monoclinic $Ba_2MgSi_2O_7$ persistent luminescence material. *Zeitschrift für Kristallographie Supplement*, **23**, 481–486.

Andrault, D. and Poirier, J. (1991) Evolution of the distortion of perovskites under pressure: An EXAFS study of $BaZrO_3$, $SrZrO_3$ and $CaGeO_3$. *Physics and Chemistry of Minerals*, **18**, 91–105.

Andrut, M. and Wildner, M. (2001) The crystal chemistry of birefringent natural uvarovites: Part I. Optical investigations and UV-VIS-IR absorption spectroscopy. *American Mineralogist*, **86**, 1219–1230.

Andrut, M., Wildner, M., and Rudiwicz, C. (2004) Optical absorption spectroscopy in geosciences. Part II: Quantitative aspects of crystal fields. *In* Beran, A. and Libowitzky, E. (Eds.). *Spectroscopic methods in mineralogy*. EMU Notes in Mineralogy, **6**, 145–188. Eötvös University Press, Budapest.

Angel, R. (2000) Equations of state. *In* Hazen, R. and Downs, R. (Eds.). *High-Temperature and High-Pressure crystal chemistry*. Reviews in Mineralogy and Geochemistry, **41**, 35–60. MSA, Washington DC.

Angel, R., Zhao, J., and Ross, N. (2005) General rules for predicting phase transitions in perovskites due to octahedral tilting. *Physical Review Letters*, **95**, 025503, 1–4.

Ardit, M., Cruciani, G., and Dondi, M. (2010a) The crystal structure of Sr-hardystonite, $Sr_2ZnSi_2O_7$. *Zeitschrift für Kristallographie*, **225**, 298–301.

Ardit, M., Dondi, M., Merlini, M., Bouvier, P., and Cruciani, G. (2010b) Elastic properties of $YCrO_3$ perovskite up to 60 GPa. *Physical Review* B, **82**, 064109, 1–7.

Ardit, M., Zanelli, C., Dondi, M., and Cruciani, G. (2011) The inverse high temperature/high pressure relationship in the monoclinic $Ba_2MgSi_2O_7$ melilite-related structure. *Periodico di Mineralogia*, **80**, 155–165.

Ardit, M., Dondi, M., and Cruciani, G. (2012) Lattice distortion upon compression in orthorhombic perovskites: Review and development of a predictive tool. *In* Krivovichev, S. (Ed.). *Minerals as Advanced Materials II*, 305–318. Springer, Berlin.

Ardit, M., Dondi, M., and Cruciani, G. (2012) Structural instability, cation ordering, and local relaxation along the join $AlNbO_4$–$CrNbO_4$. Accepted for the *American Mineralogist*.

Ardit, M., Dondi, M., and Cruciani, G. (2012) Melilite-type and melilite-related compounds: structural variations along the join $Sr_{2-x}Ba_xMgSi_2O_7$ ($0 \leq x \leq 2$) and high-pressure behaviour of the two end-members. *Physics and Chemistry of Minerals*, DOI 10.1007/s00269-011-0475-7.

Armbruster, T., Röthlisberger, F., and Seifert, F. (1990) Layer topology, stacking variation, and site distortion in melilite-related compounds in the system CaO-ZnO-GeO_2-SiO_2. *American Mineralogist*, **75**, 847–858.

Armstrong, T., Stevenson, J., Hasinska, K., and McCready, D. (1998) Synthesis and properties of mixed lanthanide chromite perovskites. *Journal of the Electrochemical Society*, **145**, 4282–4289.

Bagautdinov, B., Hagiya, K., Noguchi, S., Ohmasa, M., Ikeda, N., Kusaka, K., and Iishi, K. (2002) Low-temperature studies on the two-dimensional modulations in åkermanite-type crystals: $Ca_2MgSi_2O_7$ and $Ca_2ZnSi_2O_7$. *Physics and Chemistry of Minerals*, **29**, 346–350.

Baldi, G. and Dolen, N. (1999) Synthesis of a new class of red pigments based on perovskite type lattice $A_xB_{(2-x-y)}Cr_yO_3$ with x = 0.9-1.1, y = 0.05-0.12, A = Y, lanthanides, B = Al for use in body stain and high temperature glazes. effect of Cr^{+++} and metal a on the colour of ceramic pigment. *Materials Engineering*, **10**, 151–164.

Baur, W. (1974) The geometry of polyhedral distortions. Predictive relationships for the phosphate group. *Acta Crystallographica* B, **30**, 1195–1215.

Bindi, L., Czank, M., Röthlisberger, F., and Bonazzi, P. (2001) Hardystonite from Franklin furnace: a natural modulated melilite. *American Mineralogist*, **86**, 747–751.

Bindi, L., Bonazzi, P., Dusěk, M., Petříček, V., and Chapuis, G. (2001) Five-dimensional structure refinement of natural melilite, $(Ca_{1.89}Sr_{0.01}Na_{0.08}K_{0.02})(Mg_{0.92}Al_{0.08})(Si_{1.98}Al_{0.02})O_7$. *Acta Crystallographica* B, **57**, 739–746.

Blosi, M., Albonetti, S., Costa, A., Dondi, M., Ardit, M., and Cruciani, G. (2009) Sol–gel combustion synthesis of chromium doped yttrium aluminum perovskites. *Journal of Sol-Gel Science and Technology*, **50**, 449–455.

Borchardt-Ott, W. (1993) Crystallography. Springer, Berlin.

Bouvier, P. and Kreisel, J. (2002) Pressure-induced phase transition in $LaAlO_3$. *Journal of Physics: Condensed Matter*, **14**, 3981–3992.

Bragg, W. and Zachariasen, W. (1930) The crystalline structure of phenakite, Be_2SiO_4, and willemite, Zn_2SiO_4. *Zeitschrift für Kristallographie*, **72**, 518–528.

Brown, I. and Altermatt, D. (1985) Bond-valence parameters obtained from a systematic analysis of the inorganic crystal structure database. *Acta Crystallographica* B, **41**, 244–247.

Brown, I. (2002) The chemical bond in inorganic chemistry: The bond valence model. IUCr Monographs on Crystallography, **12**. Oxford Univ. Press, New York.

Brunold, T., Gudel, H., and Cavalli, E. (1996) Absorption and luminescence spectroscopy of Zn_2SiO_4 willemite crystals doped with Co^{2+}. *Chemical Physics Letters*, **252**, 112−120.

Burdett, J., Hughbanks, T., Miller, G., Richardson, J. Jr., and Smith, J. (1987) Structural–electronic relationships in inorganic solids: powder neutron diffraction studies of the rutile and anatase polymorphs of titanium dioxide at 15 and 295 K. *Journal of the American Chemical Society*, **109**, 3639–3643.

Burns, R. (1993) Mineralogical applications of crystal field theory (2nd Edition). Cambridge University Press, Cambridge.

Bystrikov, A., Gorbachev, V., Orlov, D., Petrakov, V., and Shishkin, I. (1982) Decorative materials based on cobalt-containing åkermanite. *Glass and Ceramics*, **39**, 128–130.

Carini II, G., Anderson, H., Nasrallah, M., and Sparlin, D. (1991) Defect structure, nonstoichiometry, and phase stability of Ca-doped $YCrO_3$. *Journal of Solid State Chemistry*, **94**, 329–336.

Carlson, W. and Rossman, G. (1988) Vanadium- and chromium-bearing andalusite: Occurrence and optical-absorption spectroscopy. *American Mineralogist*, **73**, 1366–1369.

Chandrappa, G., Ghosh, S., and Patil, K. (1999) Synthesis and properties of willemite, Zn_2SiO_4, and M^{2+}:Zn_2SiO_4 (M = Co and Ni). *Journal of Materials Synthesis and Processing*, **7**, 273–279.

Chavan, S., Patwe, S., and Tyagi, A. (2003) Bulk and lattice thermal expansion in $Ce_{1-x}Sr_xO_{2-x}$ ($0.0 \leq x \leq 0.10$). *Journal of Alloys and Compounds*, **360**, 189–192.

Chavan, S., Mathews, M., and Tyagi, A. (2004) Phase relations and thermal expansion studies in the ceria-yttria system. *Journal of the American Ceramic Society*, **87**, 1977–1980.

Christensen, A., Johansson, T., and Lebech, B. (1976) Magnetic properties and structure of chromium niobium oxide and iron tantalum oxide. *Journal of Physics C: Solid State Physics*, **9**, 2601–2610.

Costa, G., Ribeiro, M., Labrincha, J., Dondi, M., Matteucci, F., and Cruciani, G. (2009) A new turquoise blue ceramic pigment based on Ni-doped hibonite ($CaAl_{12}O_{19}$). *Journal of the European Ceramic Society*, **29**, 2671–2678.

Cruciani, G., Matteucci, F., Dondi, M., Baldi, G., and Barzanti A. (2005) Structural variations of Cr-doped (Y,REE)AlO3 perovskites. *Zeitschrift für Kristallographie*, **220**, 930–937.

Cruciani, G., Ardit, M., Dondi, M., Matteucci, F., Blosi, M., Dalconi, M.C., and Albonetti, S. (2009) Structural relaxation around Cr^{3+} in $YAlO_3$–$YCrO_3$ perovskites from electron absorption spectra. *Journal of Physical Chemistry* A, **113**, 13772–13778.

Deer, W., Howie, R., and Zussman, J. (1986) Rock-forming minerals. Volume 1B: Disilicates and ring silicates. (2nd Edition). Longman, London.

Denton, A. and Ashcroft, N. (1991) Vegard's law. *Physical Review* A, **43**, 3161–3164.

Diella, V., Sani, A., Levy, D., and Pavese, A. (2004) High-pressure synchrotron X-ray diffraction study of spessartine and uvarovite: A comparison between different equation of state models. *American Mineralogist*, **89**, 371–376.

Dondi, M., Cruciani, G., Guarini, G., Matteucci, F., and Raimondo, M. (2006) The role of counterions (Mo, Nb, Sb, W) in Cr-, Mn-, Ni- and V-doped rutile ceramic pigments. Part 2. Colour and technological properties. *Ceramics International*, **32**, 393–405.

Dondi, M., Matteucci, F., Zama, I., and Cruciani, G. (2007) High-performance yellow ceramic pigments $Zr(Ti_{1-x-y}Sn_{x-y}V_yM_y)O_4$ (M = Al, In, Y): crystal structure, colouring mechanism and technological properties. *Materials Research Bulletin*, **42**, 64–79.

Dondi, M., Matteucci, F., Baldi, G., Barzanti, A., Cruciani, G., Zama, I., and Bianchi, C. (2008) Gray-blue Al_2O_3-MoO_x ceramic pigments: crystal structure, colouring mechanism and technological performance. *Dyes and Pigments*, **76**, 179–186.

Dondi, M., Lyubenova, T., Carda, J., and Ocaña, M. (2009) M-doped Al_2TiO_5 (M=Cr, Mn, Co) solid solutions and their use as ceramic pigments. *Journal of the American Ceramic Society*, **92**, 1972–1980.

Dondi, M., Zanelli, C., Ardit, M., and Cruciani, G. (2011) Co-doped hardystonite, $Ca_2(Zn,Co)Si_2O_7$, a new blue ceramic pigment. *Journal of the American Ceramic Society*, **94**, 1025–1030.

Dry Colour Manufacturer's Association (1982) Classification and chemical description of the mixed metal oxide inorganic coloured pigments - Metal oxides and ceramics colours subcommittee. DCMA (2nd Edition), Washington DC.

Du, J., Zeng, H., Song, L., Dong, Z., Ma, H., Guo, G., and Huang, J. (2003) Synthesis and structure of a new polymorph $Ba_2CuSi_2O_7$. *Chinese Journal of Structural Chemistry*, **22**, 33–36.

Duan, W., Wentzcovitch, R., and Chelikowsky, J. (1999) First-principles search for high-pressure phases of $GaAsO_4$. *Physical Review B*, **60**, 3751−3756.

Duan, X., Yuan, D., Cheng, X., Sun, Z., Sun H., Xu, D., and Lv, M. (2003) Spectroscopic properties of Co^{2+}: $ZnAl_2O_4$ nanocrystals in sol-gel derived glass-ceramics. *Journal of Physics and Chemistry of Solids*, **64**, 1021−1025.

Duan, X., Yuan, D., Cheng, X., and Yu, F. (2011) Cation distribution in Co-doped $ZnAl_2O_4$ nanoparticles studied by X-ray photoelectron spectroscopy and ^{27}Al solid-state NMR spectroscopy. *Inorganic Chemistry*, **50**, 5460−5467.

Dunn, T., McClure, D., and Pearson, R. (1965) Some aspects of crystal field theory. Harper and Row Eds., New York.

Efremov, V., Trunov, V., and Evdokimov, A. (1981) Refinement of the structure of aluminum niobate. *Kristallografiya*, **26**, 305–311.

El Bali, B. and Zavalij, P. (2003) Tetragonal form of barium cobalt disilicate, $Ba_2CoSi_2O_7$. *Acta Crystallographica* E, **59**, 59–61.

Eppler, R. (1987) Selecting ceramic pigments. *American Ceramic Society Bulletin*, **66**, 1600–1604.

Eppler, R. (1998) Colorants for ceramics. *In* Kirk, R., and Othmer, D. (Eds.) *Encyclopedia of chemical technology*, **8**, 877–892. Wiley, New York.

Ercit, T., Hawthorne, F., and Černý P. (1992) The crystal structure of alumotantite: its relation to the structures of simpsonite and the $(Al,Ga)(Ta,Nb)O_4$ compounds. *Canadian Mineralogist*, **30**, 653–662.

Ericsson, T. and Filippidis, A. (1986) Cation ordering in the limited solid solution Fe_2SiO_4-Zn_2SiO_4. *American Mineralogist*, **71**, 1502–1509.

Escardino, A., Mestre, A., Feliu, C., Jodar, P., and Díaz, L. (2002) Stability of (Cr)CaO SnO_2 SiO_2 pink pigment in ceramic frits. *British Ceramic Transactions*, **101**, 213–220.

Fan, D., Zhou, W., Liu, C., Liu, Y., Jiang, X., Wan, F., Liu, J., Li, X., and Xie, H. (2008) Thermal equation of state of natural chromium spinel up to 26.8 GPa and 628 K. *Journal of Materials Science*, **43**, 5546–5550.

Faure, G. (1998) Principles and applications of geochemistry (2^{nd} Edition). Prentice Hall, New Jersey.

Ferguson, J., Wood, D., and Van Uitert, L. (1969) Crystal-field spectra of $d^{3,7}$ ions. V. Tetrahedral Co^{2+} in $ZnAl_2O_4$ spinel. *Journal of Chemical Physics*, **51**, 2904–2910.

Finger, L. and Hazen, R. (1978) Crystal structure and compression of ruby to 46 kbar. *Journal of Applied Physics*, **49**, 5823–5826.

Finger, L. and Hazen, R. (1980) Crystal structure and isothermal compression of Fe_2O_3, Cr_2O_3, and V_2O_3 to 50 kbars. *Journal of Applied Physics*, **51**, 5362–5367.

Finger, L., Hazen, R., and Hofmeister, A. (1986) High-pressure crystal chemistry of spinel ($MgAl_2O_4$) and magnetite (Fe_3O_4): comparisons with silicate spinels. *Physics and Chemistry of Minerals*, **13**, 215–220.

Forés, A., Llusar, M., Badenes, J., Calbo, J., Tena, M., and Monrós, G. (2000) Cobalt minimisation in willemite ($Co_xZn_{2-x}SiO_4$) ceramic pigments. *Green Chemistry*, **2**, 93–100.

Forés, A., Llusar, M., Badenés, J., Calbo, J., Tena, M., and Monros, G. (2001) Alternative turquoise blue pigment for glazes. *American Ceramic Society Bulletin*, **80**, 47–52.

Forman, R., Piermarini, G., Barnett, J., and Block, S. (1972) Pressure measurement made by the utilization of ruby sharp-line luminescence. *Science*, **176**, 284–285.

Galoisy, L. (1996) Local versus average structure around cations in minerals from spectroscopic and diffraction measurements. *Physics and Chemistry of Minerals*, **23**, 217–225.

Garcia-Lastra, J., Aramburu, J., Barriuso, M., and Moreno M. (2006) Optical properties of Cr^{3+}-doped oxides: Different behaviour of two centres in alexandrite. *Physical Review* B, **74**, 115118, 1–5.

Garcia-Lastra, J., Buzaré, J., Barriuso, M., Aramburu, J., and Moreno M. (2007) 3*d* impurities in normal and inverted perovskites: Differences are not explained by ligand field theory. *Physical Review* B, **75**, 155101, 1–6.

Gardini, D., Dondi, M., Costa, A., Matteucci, F., Blosi, M., Galassi, C., Baldi, G., and Cinotti, E. (2008) Nano-sized ceramic inks for drop-on-demand ink-jet printing in quadrichromy. *Journal of Nanoscience and Nanotechnology*, **8**, 1979–1988.

Gaudon, M., Apheceixborde, A., Ménétrier, M., Le Nestour, A., and Demourgues, A. (2009) Synthesis temperature effect on the structural features and optical absorption of $Zn_{1-x}Co_xAl_2O_4$ oxides. *Inorganic Chemistry*, **48**, 9085–9091.

Gaudry, É., Kiratisin, A., Sainctavit, Ph., Brouder, Ch., Mauri, F., Ramos, A., Rogalev, A., and Goulon, J. (2003) Structural and electronic relaxations around substitutional Cr^{3+} and Fe^{3+} ions in corundum. *Physical Review* B, **67**, 094108, 1–10.

Gaudry, É., Sainctavit, Ph., Juillot, F., Bondioli, F., Ohresser, P., and Letard, I. (2006) From the green color of eskolaite to the red color of ruby: an X-ray absorption spectroscopy study. *Physics and Chemistry of Minerals*, **32**, 710–720.

Geiger, C. (2001) Solid solutions: Background, history and scientific perspective. *In* Geiger C. (Ed.) *Solid solutions in silicate and oxide systems*. EMU Notes in Mineralogy, **3**, 3–7. Eötvös University Press, Budapest.

Geller, S. and Wood, A. (1956) Crystallographic studies of perovskite-like compounds. I. Rare earth orthoferrites and $YFeO_3$, $YCrO_3$, $YAlO_3$. *Acta Crystallographica*, **9**, 563–568.

Giuli, G., Bindi, L., and Bonazzi, P. (2000) Rietveld refinement of okayamalite, $Ca_2SiB_2O_7$: Structural evidence for the B/Si ordered distribution. *American Mineralogist*, **85**, 1512–1515.

Goldschmidt, V. (1937) The principles of distribution of chemical elements in minerals and rocks. *Journal of the Chemical Society*, 655–673.

Greis, O., Ziel, R., Garcia, D., Claussen, N., Breidenstein, B., and Haase, A. (1996) Crystal structure and morphology of disordered $AlNbO_4$ from X-ray powder diffraction. *Materials Science Forum*, **228**, 825–830.

Griffen, D. and Ribbe, P. (1979) Distortions in the tetrahedral oxyanions of crystalline substances. *Neues Jahrbuch für Mineralogie-Abhandlungen*, **137**, 54–73.

Grinberg, M., Sikorska, A., Sliwinski, A., Barzowska, J., Shen, Y., Ubizskii, S., and Melnyk, S. (2003) Photoacoustic and optical absorption spectroscopy studies of luminescent Cr^{3+} and Cr^{4+} centers in yttrium aluminum garnet. *Physical Review* B, **67**, 045113, 1–9.

Hagiya, K., Ohmasa, M., and Iishi, K. (1993) The modulated structure of synthetic Co-åkermanite, $Ca_2CoSi_2O_7$. *Acta Crystallographica* B, **49**, 172–179.

Hålenius, U., Andreozzi, G., and Skogby H. (2010) Structural relaxation around Cr^{3+} and red-green color change in the spinel (sensu stricto)-magnesiochromite ($MgAl_2O_4$-$MgCr_2O_4$) and gahnite-zincochromite ($ZnAl_2O_4$-$ZnCr_2O_4$) solid-solution series. *American Mineralogist*, **95**, 456–462.

Hålenius, U., Bosi, F., and Skogby, H. (2011) A first record of strong structural relaxation of TO_4 tetrahedra in a spinel solid solution. *American Mineralogist*, **96**, 617–622.

Hammersley, A., Svensson, S., Hanfland, M., Fitch, A., and Hausermann, D. (1996) Two-dimensional detector software: From real detector to idealised image or two-theta scan. *High Pressure Research*, **14**, 235–248.

Hang, C., Simonov, M., and Belov, N. (1970) Crystal structures of willemite $Zn_2[SiO_4]$ and its germanium analog $Zn_2[GeO_4]$. *Soviet Physics - Crystallography*, **15**, 387–390.

Hao, Y. and Wang, Y. (2007) Synthesis and photoluminescence of new phosphors $M(Mg, Zn)Si_2O_7:Mn^{2+}$ (M = Ca, Sr, Ba). *Materials Research Bulletin*, **42**, 2219–2223.

Haussühl, S. and Liebertz, J. (2004) Elastic and thermoelastic properties of synthetic $Ca_2MgSi_2O_7$ (åkermanite) and $Ca_2ZnSi_2O_7$ (hardystonite). *Physics and Chemistry of Minerals*, **31**, 565–567.

Hazen, R. and Finger, L. (1984) Comparative crystal chemistry. Wiley, New York.

Hemingway, B., Evans, H., Nord, G., Haselton, H., Robie, R., and McGee, J. (1986) Åkermanite: phase transitions in heat capacity and thermal expansion, and revised thermodynamic data. *Canadian Mineralogist*, **24**, 425–434.

Henderson, B., Gallagher, H., Han, T., and Scott M. (2000) Optical spectroscopy and optimal crystal growth of some Cr^{4+}-doped garnets. *Journal of Physics: Condensed Matter*, **12**, 1927–1938.

Hoppe, R. (1979) Effective coordination numbers (ECoN) and mean active fictive ionic radii (MEFIR). *Zeitschrift für Kristallographie*, **150**, 23–52.

Hoppe, R., Voigt, S., Glaum, H., Kissel, J., Müller, H., and Bernet, K. (1989) A new route to charge distributions in ionic solids. *Journal of the Less-Common Metals*, **156**, 105–122.

Hu, A., Li, M., Mao Dali, D., and Liang, K. (2005) Crystallization and properties of a spodumene-willemite glass ceramic. *Thermochimica Acta*, **437**, 110–113.

Ishihara, T. (2009) Perovskite oxide for solid oxide fuel cells. Springer, New York.

Italian Ceramic Society (2003) Colour, pigments and colouring in ceramics. SALA, Modena.

Jasper-Tönnies, B. and Müller-Buschbaum, H. (1983) Synthese und Struktur von $AlTaO_4$. *Zeitschrift für Anorganische und Allgemeine Chemie*, **504**, 113–116 (In german).

Jenkins, R. (2000) X-ray technique: Overview. *In* Meyers, R. (Ed.). *Encyclopedia of Analytical Chemistry*. 13269–13288. John Wiley & Sons Ltd, Chichester.

Jonynaitė, D., Jasaitis, D., Senvaitienė, J., and Kareiva, A. (2008) Synthesis of $CoNH_4PO_4$ pigment by co-precipitation method. *Chemija*, **19**, 23–26.

Juhin, A., Calas, G., Cabaret, D., and Galoisy, L. (2007) Structural relaxation around substitutional Cr^{3+} in $MgAl_2O_4$. *Physical Review* B, **76**, 054105-1–6.

Juhin, A., Calas, G., Cabaret, D., Galoisy, L., and Hazemann, J.-L. (2008) Structural relaxation around substitutional Cr^{3+} in pyrope garnet. *American Mineralogist*, **93**, 800–805.

Kaiser, J. and Jeitschko, W. (2002) Crystal structure of the new barium zinc silicate $Ba_2ZnSi_2O_7$. *Zeitschrift für Kristallographie - New Crystal Structures*, **217**, 25–26.

Kaminskii, A., Bohaty, L., Becker, P., Liebertz, J., Held, P., Eichler, H., Rhee, H., and Hanuza, J. (2008) Tetragonal $Ba_2MgGe_2O_7$ - a novel multifunctional optical crystal with numerous manifestations of nonlinear-laser effects: almost sesqui-octave Stokes and anti-Stokes combs and cascaded $\chi^{(3)}\leftrightarrow\chi^{(2)}$ lasing with involved second and third harmonic generation. *Laser Physics Letters*, **5**, 845–868.

Kamioka, H., Yamaguchi, T., Hirano, M., Kamiya, T., and Hosono, H. (2007) Structural and photo-induced properties of Eu^{2+}-doped $Ca_2ZnSi_2O_7$: a red phosphor for white light generation by blue ray excitation. *Journal of Luminescence*, **122**, 339–341.

Keppler, H. and Bagdassarov, N. (1999) The specification of Ni and Co in silicate melts from optical absorption spectra to 1500 ºC. *Chemical Geology*, **158**, 105–115.

Kimata, M. (1983a) The structural properties of synthetic Sr-åkermanite, $Sr_2MgSi_2O_7$. *Zeitschrift für Kristallographie*, **163**, 295–304.

Kimata, M. (1983b) The crystal structure and stability of Co-åkermanite, $Ca_2CoSi_2O_7$, compared with the mineralogical behaviour of Mg cation. *Neues Jahrbuch für Mineralogie-Abhandlungen*, **146**, 221–241.

Kimata, M. (1984) The structural properties of synthetic Sr-gehlenite, $Sr_2Al_2SiO_7$. *Zeitschrift für Kristallographie*, **167**, 103–116.

Kimata, M. (1985) The structural properties and mineralogical significance of synthetic $Sr_2MnSi_2O_7$ melilite with 4-coordinated manganese. *Neues Jahrbuch für Mineralogie-Monatshefte*, 83–96.

Kimata, M. and Ii, N. (1981) The crystal structure of synthetic åkermanite, $Ca_2MgSi_2O_7$. *Neues Jahrbuch für Mineralogie-Monatshefte*, 1–10.

Kimata, M. and Ii, N. (1982) The structural properties of synthetic gehlenite, $Ca_2Al_2SiO_7$. *Neues Jahrbuch für Mineralogie-Abhandlungen*, **144**, 254–267.

Klaska, K.-H., Eck, J., and Pohl, D. (1978) New investigation of willemite. *Acta Crystallographica* B, **34**, 3324–3325.

Knight, K., Marshall, W., Bonanos, N., and Francis, D. (2005) Pressure dependence of the crystal structure of $SrCeO_3$ perovskite. *Journal of Alloys and Compounds*, **394**, 131–137.

Knowles, K. and Freeman, F. (2004) Microscopy and microanalysis of crystalline glazes. *Journal of Microscopy*, **215**, 257–270.

König, E. and Kremer, S. (1977) Ligand field energy diagrams. Plenum Press, New York.

Körner, R., Ricken, M., Nölting, J. and Riess, I. (1989) Phase transformations in reduced ceria: determination by thermal expansion measurements. *Journal of Solid State Chemistry*, **78**, 136–147.

Krause, M., Sonntag, R., Kleint, C., Rönsch, E., and Stüsser, N. (1995) Magnetism and cation distribution in iron zinc silicates. *Physica* B, **213-214**, 230–232.

Kusaka, K., Hagiya, K., Ohmasa, M., Mukai, M., Iishi, K., and Haga, N. (2001) Determination of structures of $Ca_2CoSi_2O_7$, $Ca_2MgSi_2O_7$ and $Ca_2(Mg_{0.55}Fe_{0.45})Si_2O_7$ in incommensurate and normal phases and observation of diffuse streaks at high temperature. *Physics and Chemistry of Minerals*, **28**, 150–166.

Kyser, D. and Murata, K. (1974) Quantitative electron microprobe analysis of thin films on substrates. *IBM Journal* of Research and *Development*, **18**, 352–363.

Langer, K. (2001) A note on mean distances, $R_{[MO6]}$, in substituted polyhedra, $[(M_{1-x}M_x')O_6]$, in the crystal structures of oxygen based solid solutions: local *versus* crystal averaging methods. *Zeitschrift für Kristallographie*, **216**, 87–91.

Langer, K., Taran, M., and Platonov, A. (1997) Compression moduli of Cr^{3+}-centered octahedra in a variety of oxygen-based rock-forming minerals. *Physics and Chemistry of Minerals*, **24**, 109–114.

Langer, K., Platonov, A., and Matsyuk, S. (2004) Local mean chromium–oxygen distances in Cr^{3+}-centered octahedra of natural grossular-uvarovite garnet solid solutions from electronic absorption spectra. *Zeitschrift für Kristallographie*, **219**, 272–277.

Larson, A. and Von Dreele, R. (1988) General structure analysis system (GSAS). Los Alamos National Laboratory Report 86-748, Los Alamos, New Messico.

Leite, A., Costa, G., Hajjaji, W., Ribeiro, M., Seabra, M., and Labrincha, J. (2009) Blue cobalt doped-hibonite pigments prepared from industrial sludges: Formulation and characterization. *Dyes and Pigments*, **81**, 211–217.

Lenglet, M. and Hochu, F. (2000) Correlation between ionic-covalent parameters and infrared spectroscopic data in II-III transition metal spinel-type oxides. *Materials Research Bulletin*, **32**, 863–872.

Levelut, C., Ramos, A., and Petiau, J. (1991) EXAFS study of the local structure in CdS_xSe_{1-x} compounds. *Materials Science and Engineering* B, **8**, 251–263.

Lever, A. (1984) Inorganic electronic spectroscopy (2nd Edition). Elsevier, Amsterdam.

Levy, D., Pavese, A., Sani, A., and Pischedda, V. (2001) Structure and compressibility of synthetic $ZnAl_2O_4$ (gahnite) under high-pressure conditions, from synchrotron X-ray powder diffraction. *Physics and Chemistry of Minerals*, **28**, 612–618.

Levy, D., Diella, V., Pavese, A., Dapiaggi, M., and Sani, A. (2005) *P-V* equation of State, thermal expansion, and *P-T* stability of synthetic zincochromite ($ZnCr_2O_4$ spinel). *American Mineralogist*, **90**, 1157–1162.

Llusar, M., Forés, A., Badenes, J., Calbo, J., Tena, M., and Monrós, G. (2001) Color analysis of some cobalt-based blue pigments. *Journal of the European Ceramic Society*, **21**, 1121–1130.

Loa, I., Adler, P., Grzechnik, A., Syassen, K., Schwarz, U., Hanfland, M., Rozenberg, G., Gorodetsky, P., and Pasternak, M. (2001) Pressure-Induced Quenching of the Jahn-Teller Distortion and Insulator-to-Metal Transition in $LaMnO_3$. *Physical Review Letters*, **87**, 125501, 1–4.

Loa, I., Wang, X., Syassen, K., Roth, H., Lorenz, T., Hanfland, M., and Mathis, Y.-L. (2007) Crystal structure and the Mott–Hubbard gap in $YTiO_3$ at high pressure. *Journal of Physics: Condensed Matter*, **19**, 406223, 1–9.

Louisnathan, J. (1969) Refinement of the crystal structure of hardystonite, $Ca_2ZnSi_2O_7$. *Zeitschrift für Kristallographie*, **130**, 427–437.

Lufaso, M., Mugavero III, S., Gemmill, W., Lee, Y., Vogt, T., and zur Loye, H.-C. (2007) Pressure- and temperature-dependent X-ray diffraction studies of $NdCrO_3$. *Journal of Alloys and Compounds*, **433**, 91–96.

Malinovskii, Yu A. (1984) Crystal structure of $Ba_2CuSi_2O_7$. *Soviet Physics - Doklady*, **29**, 706–708.

Marfunin, S. (1979) Physics of minerals and inorganic materials. Springer, Berlin-Heidelberg-New York.

Marinova, Y., Hohemberger, J., Cordoncillo, E., Escribano, P., and Carda, J. (2003) Study of solid solutions, with perovskite structure, for application in the field of the ceramic pigments. *Journal of the European Ceramic Society*, **23**, 213–220.

Mathews, M., Ambekar, B., and Tyagi, A. (2000) Bulk and lattice thermal expansion of $Th_{1-x}Ce_xO_2$. *Journal of Nuclear Materials*, **280**, 246–249.

Matteucci, F., Lepri Neto C., Dondi M., Cruciani G., Baldi G., and Boschi A. (2006a) Colour development of red perovskite pigment $Y(Al,Cr)O_3$ in various ceramic applications. *Advances in Applied Ceramics*, **105**, 99–106.

Matteucci F., Cruciani G., Dondi M., and Raimondo M. (2006b) The role of counterions (Mo, Nb, Sb, W) in Cr-, Mn-, Ni- and V-doped rutile ceramic pigments. Part 1. Crystal structure and phase transformations. *Ceramics International*, **32**, 385–392.

McConnell, J., McCammon, C., Angel, R., and Seifert, F. (2000) The nature of the incommensurate structure in åkermanite, $Ca_2MgSi_2O_7$, and the character of its transformation from the normal structure. *Zeitschrift für Kristallographie*, **215**, 669–677.

McMurdie, H., Morris, M., Evans, E., Paretzkin, B., Wong-Ng, W., and Hubbard, C. (1986) Standard X-ray diffraction powder patterns from the JCPDS research associationship. *Powder Diffraction*, **1**, 265–275.

Merlini, M., Gemmi, M., and Artioli, G. (2005) Thermal expansion and phase transitions in åkermanite and gehlenite. *Physics and Chemistry of Minerals*, **32**, 189–196.

Merlini, M., Gemmi, M., Cruciani, G., and Artioli, G. (2008) High-temperature behaviour of melilite: in situ X-ray diffraction study of gehlenite–åkermanite–Na melilite solid solution. *Physics and Chemistry of Minerals*, **35**, 147–155.

Merlini, M., Gemmi, M., Hanfland, M., and Crichton, W. (2009) High-pressure behaviour of åkermanite and gehlenite and phase stability of the normal structure in melilites. *American Mineralogist*, **94**, 704–709.

Meseguer, S., Tena, M., Gargori, C., Galindo, R., Badenés, J., Llusar, M., and Monrós, G. (2008) Development of blue ceramic dyes from cobalt phosphates. *Ceramics International*, **34**, 1431–1438.

Mezouar, M., Crichton, W., Bauchau, S., Thurel, F., Witsch, H., Torrecillas, F., Blattmann, G., Marion, P., Dabin, Y., Chavanne, J., Hignette, O., Morawe, C., and Borel, C. (2005) Development of a new state-of-the-art beamline optimized for monochromatic single-crystal and powder X-ray diffraction under extreme conditions at the ESRF. *Journal of Synchrotron Radiation*, **12**, 659–664.

Milos M., Kairouani S., Rabaste S., and Hauser A. (2008) Energy migration within the ^{2}E state of Cr^{3+}. *Coordination Chemistry Reviews*, **252**, 2540–2551.

Mitchell, R.(2002) Perovskites: Modern and Ancient. Almaz Press, Thunder Bay-Ontario.

Momma, K. and Izumi, F. (2008) VESTA: a three-dimensional visualization system for electronic and structural analysis. *Journal of Applied Crystallography*, **41**, 653–658.

Monari, G. and Manfredini, T. (1996) Coloring effects of synthetic inorganic cobalt pigments in fast-fired porcelainized tiles. *Ceramic Engineering and Science Proceedings*, **17**, 167–172.

Montanari, G., Costa, A., Albonetti, S., and Galassi, C. (2005) Nb-doped PZT material by Sol-Gel combustion. *Journal of Sol-Gel Science and Technology*, **36**, 203–211.

Moreno M., Garcia-Lastra, J., Aramburu, J., and Barriuso, M. (2007) Transition metal impurities in wide gap materials: are the electronic properties well described through the ligand field theory? *Theoretical Chemistry Accounts*, **118**, 665–671.

Morosin, B. (1965) The crystal structure of $GaNbO_4$. *Acta Crystallographica*, **18**, 874–879.

Navrotsky, A. and D. Weidner, D. (1989) Perovskite: A structure of great interest to geophysics and materials science. Geophysical Monograph Series, **45**. AGU, Washington DC.

Neuhaus, A. and Richartz, W. (1958) Absorptionsspektrum und Koordination allochromatisch durch Cr^{3+} gefärbter natürlicher und synthetischer Einkristalle und Kristallpulver. *Angewandte Chemie*, **70**, 430–434.

Oberti, R. (2001) The diffraction experiment in the study of solid solutions: Long-range properties. *In* Geiger C. (Ed.) *Solid solutions in silicate and oxide systems*. EMU Notes in Mineralogy, **3**, 179–205. Eötvös Univiversity Press, Budapest.

Ochi, Y. (2006) Crystal structure of Sr-åkermanite glass–ceramics. *Materials Research Bulletin*, **41**, 1825–1834.

Ohsato, H. (2005) Research and development of microwave dielectric ceramics for wireless communications. *Journal of the Ceramic Society of Japan*, **113**, 703–711.

Ozel, E., Yurdakul, M., Turan, S., Ardit, M., Cruciani, G., and Dondi, M. (2010) Co-doped willemite ceramic pigments: Technological behaviour, crystal structure and optical properties. *Journal of the European Ceramic Society*, **30**, 3319–3329.

Paszkowicz, W. (2006) Ninety years of powder diffraction. *Synchrotron Radiation in Natural Science*, **5**, 115–126.

Pauling, L. (1927) The sizes of ions and the structure of ionic crystals. *Journal of the American Chemical Society*, **49**, 765–790.

Pavese, A., Levy, D., and Pischedda, V. (2001) Elastic properties of andradite and grossular, by synchrotron X-ray diffraction at high pressure conditions. *European Journal of Mineralogy*, **13**, 929–937.

Pedersen, B. (1962) The crystal structure of aluminum niobium oxide. *Acta Chemica Scandinavica*, **16**, 421–430.

Petersen, A. and Müller-Buschbaum, H. (1992) Ein Beitrag über Oxide vom Typ AMO_4 (A= Ti^{3+}, Cr^{3+}; M= Nb^{5+}, Ta^{5+}). *Zeitschrift für Anorganische und Allgemeine Chemie*, **609**, 51–54.

Poole, C. and Itzel, J. (1963) Optical reflection spectra of chromia-alumina. *Journal of Chemical Physics*, **39**, 3445–3455.

Popović, J., Tkalčec, E., Gržeta, B., Kurajica, S., and Rakvin, B. (2009) Inverse spinel structure of Co-doped gahnite. *American Mineralogist*, **94**, 771–776.

Putnis, A. (1992) Introduction to mineral sciences. Cambridge University Press, Cambridge.

Ramesha, K., Llobet, A., Proffen, Th., Serrao, C., and Rao, C. (2007) Observation of local non-centrosymmetry in weakly biferroic $YCrO_3$. *Journal of Physics: Condensed Matter*, **19**, 102202, 1–8.

Reinen, D. (1969) Ligand-field spectroscopy and chemical bonding in Cr^{3+}-containing oxidic solids. *Structure and Bonding*, **6**, 30–51.

Riester, M. and Böhm, H. (1997) Phase transition of modulated Co-åkermanite, $Ca_2CoSi_2O_7$. *Zeitschrift für Kristallographie*, **212**, 506–509.

Rietveld, H. (1967) Line profiles of neutron powder-diffraction peaks for structure refinement. *Acta Crystallographica*, **22**, 151–152.

Rietveld, H. (1969) A profile refinement method for nuclear and magnetic structures. *Journal of Applied Crystallography*, **2**, 65–71.

Ringwood, A. (1955) The principles governing trace element distribution during magmatic crystallization Part I: The influence of electronegativity. *Geochimica et Cosmochimica Acta,* **7**, 189–202.

Robinson, K., Gibbs, G., and Ribbe, P. (1971) Quadratic elongation; a quantitative measure of distortion in coordination polyhedra. *Science*, **172**, 567–570.

Ross, N. (1998) High pressure study of $ScAlO_3$ perovskite. *Physics and Chemistry of Minerals*, **25**, 597–602.

Ross, N. and Angel, R. (1999) Compression of $CaTiO_3$ and $CaGeO_3$ perovskites. *American Mineralogist*, **84**, 277–281.

Ross, N. and Chaplin, T. (2003) Compressibility of $CaZrO_3$ perovskite: Comparison with Ca-oxide perovskites. *Journal of Solid State Chemistry*, **172**, 123–126.

Ross, N., Zhao, J., Burt, J., and Chaplin, T. (2004a) Equations of state of $GdFeO_3$ and $GdAlO_3$ perovskites. *Journal of Physics: Condensed Matter*, **16**, 5721–5730.

Ross, N., Zhao, J., and Angel, R. (2004b) High-pressure single-crystal X-ray diffraction study of $YAlO_3$ perovskite. *Journal of Solid State Chemistry*, **177**, 1276–1284.

Röthlisberger, F., Seifert, F., and Czank, M. (1990) Chemical control of the commensurate-incommensurate phase transition in systematic melilites. *European Journal of Mineralogy*, **2**, 585–594.

Rudkovskaya, N., Mikhailenko, N., Lisinenkova, S., and Levin, Y. (2003) Diffusion processes in firing willemite glaze on quartz glass ceramics. *Glass and Ceramics*, **60**, 226–228.

Salinas-Sanchez, A., Garcia-Muñoz, J., Rodriguez-Carvajal, J., Saez-Puche, R., and Martinez J. (1992) Structural characterization of R_2BaCuO_5 (R = Y, Lu, Yb, Tm, Er, Ho, Dy, Gd, Eu and Sm) oxides by X-ray and Neutron diffraction. *Journal of Solid State Chemistry*, **100**, 201–211.

Sameshima, S., Ichikawa, T., Kawaminami, M., and Hirata, Y. (1999) Thermal and mechanical properties of rare earth-doped ceria ceramics. *Materials Chemistry and Physics*, **61**, 31–35.

Sasaki, S., Prewitt, C., and Liebermann, R. (1983) The crystal structure of $CaGeO_3$ perovskite and the crystal chemistry of the $GdFeO_3$-type perovskites. *American Mineralogist*, **68**, 1189–1198.

Schmitz-DuMont, O. and Reinen, D. (1959) Farbe und Konstitution bei anorganischen Feststoffen. III Die Lichtabsorption des dreiwertigen chroms. *Zeitschrift für Elektrochemie*, **63**, 978–987.

Schmetzer, K. and Berdesinski, W. (1978) Das Absorptionsspektrum von Cr^{3+} in Zoisit. *Neues Jahrbuch für Mineralogie-Monatshefte*, 197–202.

Segal, D. (1997) Chemical synthesis of ceramic materials. *Journal of Materials Chemistry*, **7**, 1297–1305.

Seifert, F., Czank, M., Simons, B., and Schmahl, W. (1987) A commensurate-incommensurate phase transition in iron-bearing åkermanite. *Physics and Chemistry of Minerals*, **14**, 26–35.

Serrao, C., Kundu, A., Krupanidhi, S., Waghmare, U., and Rao, C. (2005) Biferroic $YCrO_3$. *Physical Review* B, **72**, 220101, 1–4.

Shannon, R. (1976) Revised effective ionic radii and systematic studies of interatomic distances in halides and chalcogenides. *Acta Crystallographica* A, **32**, 751–767.

Shannon, R. and Fischer, R. (2006) Empirical electronic polarizabilities in oxides, hydroxides, oxyfluorides, and oxychlorides. *Physical Review* B, **73**, 235111, 1–28.

Shimizu, M., Kimata, M., and Iida, I. (1995) Crystal structure of $Ba_2MgSi_2O_7$ melilite: the longest tetrahedral Mg–O distance. *Neues Jahrbuch für Mineralogie-Monatshefte*, 39–47.

Shuk, P. and Greenblatt, M. (1999) Hydrothermal synthesis and properties of mixed conductors based on $Ce_{1-x}Pr_xO_{2-\delta}$ solid solutions. *Solid State Ionics*, **116**, 217–223.

Siligardi, C. Mugoni, C., Corradini, D., Venturelli, D., Montorsi, M., and Novaes de Oliveira, A. (2009) Nova frita pertencente ao sistema CaO-ZnO-SiO_2 para aplicações cerâmicas. *Cerâmica Industrial*, **14**, 20–27.

Smirnov, Yu.E. and Zvereva, I. (2003) Cation distribution and interatomic interactions in oxides with heterovalent isomorphism: VII. $CrNbO_4$ and $LiFeO_2$ oxides. *Russian Journal of General Chemistry*, **73**, 165–168.

Sorlí, S., Tena, M., Mestre, A., Llusar, M., and Monrós, G. (2004) Effect of the major devitrifying phase on ceramic glaze microstructure and mechanical properties. Proceeding QUALICER 2004, Castellón, Spain, 99–110.

Sreekanth Chakradhar, R., Nagabhushana, B., Chandrappa, G., Ramesh, K., and Rao, J. (2004) Solution combustion derived nanocrystalline Zn_2SiO_4:Mn phosphors: a spectroscopic view. *Journal of Chemical Physics*, **121**, 10250–10259.

Sugahara, M., Yoshiasa, A., Komatsu, Y., Yamanaka, T., Bolfan-Casanova, N., Nakatsuka, A., Sasaki, S., and Tanaka, M. (2006) Reinvestigation of the $MgSiO_3$ perovskite structure at high pressure. *American Mineralogist*, **91**, 533–536.

Swanson, D. and Peterson, R. (1980) Polyhedral volume calculation. *Candian Mineralogist*, **18**, 153–156.

Tabero, P. (2007) Thermal expansion of *M*NbO4 phases where *M* = Al, Cr, Fe, Ga. *Journal of Thermal Analysis and Calorimetry*, **88**, 269–272.

Tachiwaki, T., Kunifusa, Y., Yoshinaka, M., Hirota, K., and Yamaguchi, O. (2001) Formation, powder characterization and sintering of $YCrO_3$ prepared by a sol–gel technique using hydrazine. *International Journal of Inorganic Materials*, **3**, 107–111.

Tanabe, Y. and Sugano, S. (1954) On the absorption spectra of complex ions. I and II. *Journal of the Physical Society of Japan*, **9**, 753–779.

Taran, M., Langer, K., Platonov, A., and Indutny, V. (1994) Optical absorption investigation of Cr^{3+} ion-bearing minerals in the temperature range. *Physics and Chemistry of Minerals*, **21**, 360–372.

Taran, M., Langer, K., Abs-Wurmbach, I., Frost, D., and Platonov, A. (2004) Local relaxation around $^{[6]}Cr^{3+}$ in synthetic pyrope-knorringite garnets, $^{[8]}Mg_3{}^{[6]}(Al_{1-X}Cr_X{}^{3+})_2{}^{[4]}Si_3O_{12}$, from electronic absorption spectra. *Physics and Chemistry of Minerals*, **31**, 650–657.

Taran, M., Koch-Müller, M., and Feenstra, A. (2009) Optical spectroscopic study of tetrahedrally coordinated Co^{2+} in natural spinel and staurolite at different temperatures and pressures. *American Mineralogist*, **94**, 1647−1652.

Tenorio Cavalcante, P., Dondi, M., Guarini, G., Barros, F., and da Luz, A. (2007) Ceramic application of mica titania pearlescent pigments. *Dyes and Pigments*, **74**, 1–8.

Tenorio Cavalcante, P., Dondi, M., Guarini, G., Raimondo, M., and Baldi, G. (2009) Colour performance of ceramic nano-pigments. *Dyes and Pigments*, **80**, 226–232.

Thomas, N. (1998) A new global parameterization of perovskite structures. *Acta Crystallographica* B, **54**, 585–599.

Thomas, P. and Midgley, P. (2002) An introduction to energy-filtered transmission electron microscopy. *Topics in Catalysis*, **21**, 109–138.

Toby, H. (2001) EXPGUI, a graphical user interface for GSAS. *Journal of Applied Crystallography*, **34**, 210–213.

Torres, F., Rodriguez-Mendoza, U., Lavin, V., de Sola, E., and Alarcon, J. (2007) Evolution of the structural and optical properties from cobalt cordierite glass to glass-ceramic based on spinel crystalline phase materials. *Journal of Non-Crystalline Solids*, **353**, 4093−4101.

Tristan, N., Hemberger, J., Krimmel, A., Krug von Hidda, H.-A., Tsurkan, V., and Loidl, A. (2005) Geometric frustration in the cubic spinel $M Al_2O_4$ (*M*=Co, Fe, and Mn). *Physical Review* B, **72**, 174404, 1–9.

Urusov, V. (1992) A geometric model of deviations from Vegard's rule. *Journal of Solid State Chemistry*, **98**, 223–236.

Urusov, V. (2001) The phenomenological theory of solid solutions. *In* Geiger C. (Ed.) *Solid solutions in silicate and oxide systems*. EMU Notes in Mineralogy, **3**, 121–153. Eötvös University Press, Budapest.

Urusov, V. and Taran, M. (2011) Structural relaxation and crystal field stabilization in Cr3+-containing oxides and silicates. *Physics and Chemistry of Minerals*, DOI 10.1007/s00269-011-0456-x.

Van Der Kolk, E., Dorenbos, P., Van Eijk, C., Bechtel, H., Jüstel, T., Nikol, H., Ronda, C., and Wiechert, D. (2000) Optimised co-activated willemite phosphors for application in plasma display panels. *Journal of Luminescence*, **87-89**, 1246–1249.

Varela, M., Lupini, A., Van Benthem, K., Borisevich, A., Chisholm, M., Shibata, N., Abe, E., and Pennycook, S. (2005) Materials characterization in the aberration-corrected scanning transmission electron microscope. *Annual Review of Materials Research*, **35**, 539–569.

Vegard, L. (1921) Die konstitution der mischkristalle und die raumfüllung der atome. *Zeitschrift für Physik*, **5**, 17–26.

Vegard, L. and Dale, H. (1928) Untersuchungen ueber mischkristalle und legierungen. *Zeitschrift für Kristallographie*, **67**, 148–162.

Voloshin, A., Men'shikov, Y., and Pakhomovskii, Y. (1981) Alumotantite and natrotantite, new tantalum minerals in granitic pegmatites. *Zapiski Vsesoyuznogo Mineralogicheskogo Obshchestva*, **110**, 338–345 (in Russian). - *American Mineralogist* (1982), **67**, 413 (abstract only).

Wan, J., Wang, Z., Chen, X., Mu, L., Yu, W., and Qian, Y. (2006) Controlled synthesis and relationship between luminescent properties and shape/crystal structure of Zn_2SiO_4:Mn^{2+} phosphor. *Journal of Luminescence*, **121**, 32–38.

Wang, S., Lin, B., Dong, Y., Fang, D., Ding, H., Liu, X., and Meng, G. (2009) Stable, easily sintered Ca–Zn-doped $YCrO_3$ as novel interconnect materials for co-fired yttrium-stabilized zirconia-based solid oxide fuel cells. *Journal of Power Sources*, **188**, 483–488.

Wang, Z., Yin, J., and Jiang, Y. (2000) EELS analysis of cation valence states and oxygen vacancies in magnetic oxides. *Micron*, **31**, 571–580.

Warren, B. (1930) The structure of melilite $(Ca,Na)_2(Mg,Al)(Si,Al)_2O_7$. *Zeitschrift für Kristallographie*, **74**, 131–138.

Webb, S., Ross, C., and Liebertz, J. (1992) Thermal expansion and spontaneous strain associated with the Normal-Incommensurate phase transition in melilites. *Physics and Chemistry of Minerals*, **18**, 522–525.

Wildner, M., Andrut, M., and Rudowicz, C. (2004) Optical absorption spectroscopy in geosciences. Part I: Basic concepts of crystal field theory. *In* Beran, A. and Libowitzky, E. (Eds.). *Spectroscopic methods in mineralogy*. EMU Notes in Mineralagy, **6**, 93–140. Eötvös University Press, Budapest.

Williams, D., Watanabe, M., Papworth, A., and Li, J. (2003) Quantitative characterization of the composition, thickness and orientation of thin films in the analytical electron microscope. *Thin Solid Films*, **424**, 50–55.

Wolfram, T. and Ellialtioglu, S. (2006) Electronic and optical properties of *d*-band perovskites. Cambridge University Press, Cambridge.

Wu, C., Chang, J., and Zhai, W. (2005) A novel hardystonite bioceramic: preparation and characteristics. *Ceramics International*, **31**, 27-31.

Wu, X., Qin, S., and Wu, Z. (2006) Generalized gradient approximation calculations of the pressure-induced phase transition of $YAlO_3$ perovskite. *Journal of Physics: Condensed Matter*, **18**, 3907–3916.

Yan, B. and Huang, H. (2007) Matrix-inducing synthesis and luminescence of Zn_2SiO_4:xTb^{3+} submicrometer phosphors derived from the Sol-Gel assembling of different multicomponent hybrid precursors. *Journal of Alloys and Compounds*, **429**, 338–342.

Yang, H., Hazen, R., Downs, R., and Finger, L. (1997) Structural change associated with the incommensurate-normal phase transition in åkermanite, $Ca_2MgSi_2O_7$, at high pressure. *Physics and Chemistry of Minerals*, **24**, 510–519.

Young, R. (1995) The Rietveld method. Oxford University Press, New York.

Yu-Zhang, K., Imhoff, D., Leprince-Wang, Y., Roy, E., Zhou, S., and Chien, C. (2003) Multiscale analysis of the nanostructured granular solid CoO–Ag by TEM and EELS. *Acta Materialia*, **51**, 1157–1166.

Zen, E. (1956) Validity of "Vegard's law". *American Mineralogist*, **41**, 523–524.

Zhao, J., Ross, N., and Angel, R. (2006) Estimation of polyhedral compressibilities and structural evolution of $GdFeO_3$-type perovskites at high pressures. *Acta Crystallographica* B, **62**, 431–439.

Zhang, L., Ahsbahs, H., and Kutoglu, A. (1998) Hydrostatic compression and crystal structure of pyrope to 33 GPa. *Physics and Chemistry of Minerals*, **25**, 301–307.